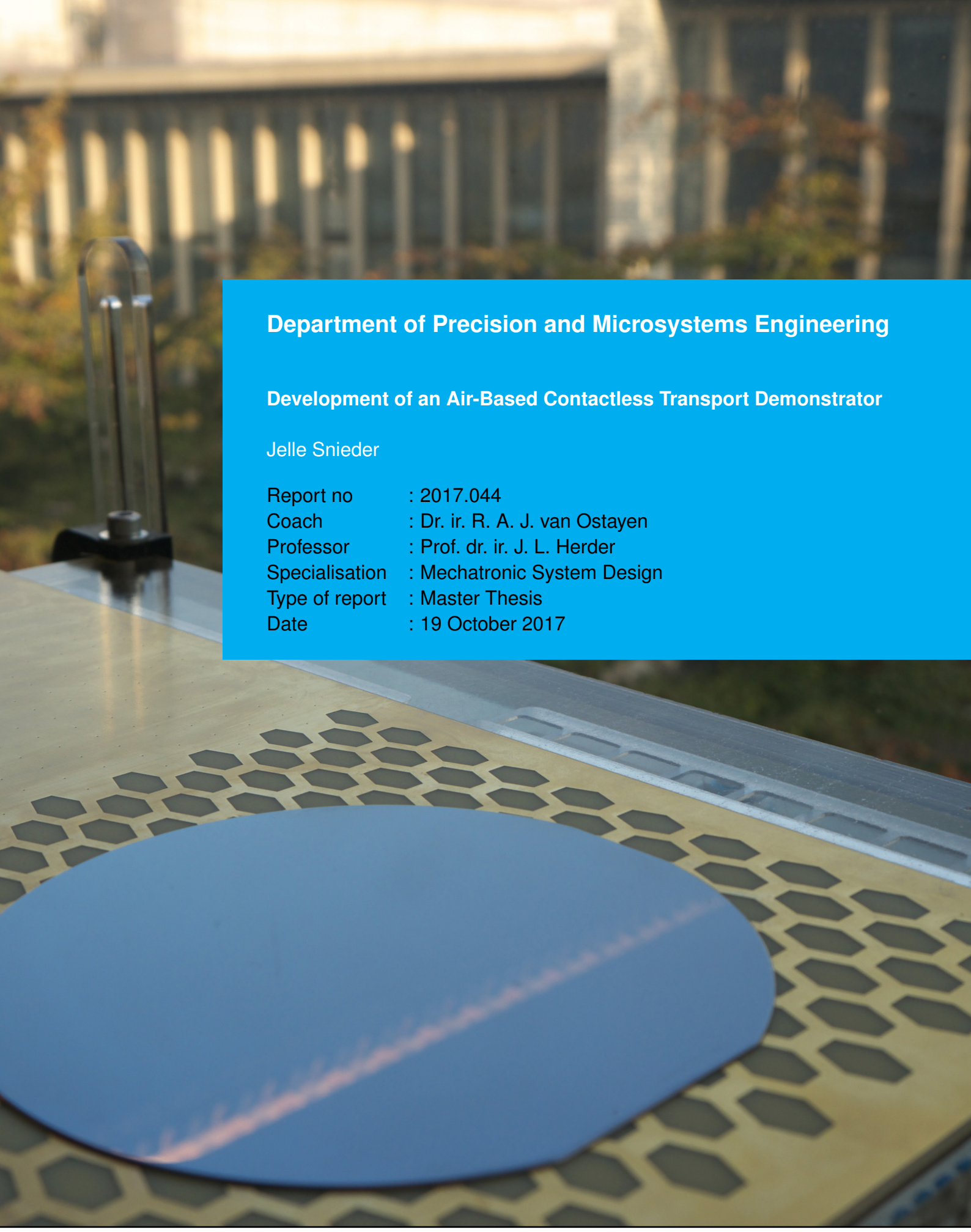

Department of Precision and Microsystems Engineering

Development of an Air-Based Contactless Transport Demonstrator

Jelle Snieder

Report no	: 2017.044
Coach	: Dr. ir. R. A. J. van Ostayen
Professor	: Prof. dr. ir. J. L. Herder
Specialisation	: Mechatronic System Design
Type of report	: Master Thesis
Date	: 19 October 2017

Development of an Air-Based Contactless Transport Demonstrator

by

J. Snieder

to obtain the degree of Master of Science
at the Delft University of Technology,
to be defended publicly on Thursday October 19, 2017 at 14:00 AM.

Student number:	4111397	
Supervisor:	Dr. ir. R. A. J. van Ostayen	
Thesis committee:	Prof. dr. ir. J. L. Herder,	TU Delft
	Dr. ir. M. Langelaar,	TU Delft
	Dr. ir. D. L. Schott,	TU Delft
	Ir. S. G. E. Lampaert,	TU Delft

This thesis is confidential and cannot be made public until October 19, 2019.

TU Delft

Abstract

In many industries, for example the semi-conductor and solar cell industry, production processes have to handle thin substrates such as wafers or solar cells. For economical reasons, the thickness of these substrates shows a decreasing trend over the years. This results in an increasing breakage rate of the substrates during the production process. A solution to this problem could be contactless handling. This research focuses on air-based contactless handling of thin substrates. A simple, vacuum pre-loaded air bearing surface is able to levitate a substrate to a well-defined fly height, due to the high air film stiffness. A net flow in a specified direction is realised by creating pockets in the surface, as visualised in the schematic cross-section in Figure 1. The net flow generates a viscous traction force on the substrate. This principle can be used to actuate thin substrates in a contactless manner.

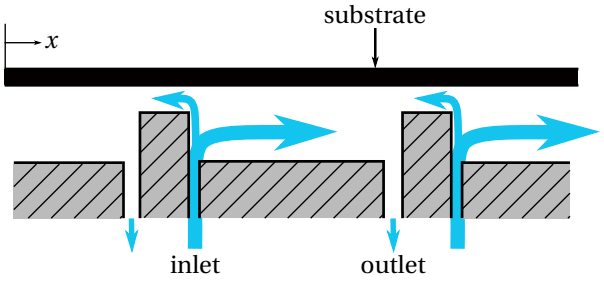

Figure 1: By creating pockets in the air bearing surface, a net flow in the positive x-direction is realised.

The state of the art in contactless positioning using a thin film of air is mainly focused on the positioning of the substrate. The next step in thin substrate handling is transporting them. In this project, two transport demonstrators are designed and fabricated, using different manufacturing methods. To limit the total mass flow in the transport demonstrator, an active air bearing surface is combined with a passive air bearing surface. The active air bearing surface is able to actuate and levitate the substrate, while the passive air bearing surface is only able to levitate the substrate and guide its motion. The top view of the design and the thin substrate, which is a 100 mm diameter wafer, are shown in Figure 2. The fly height and air film stiffness of the active surface and the passive surface are matched to realise a smooth transition of the wafer between the surfaces.

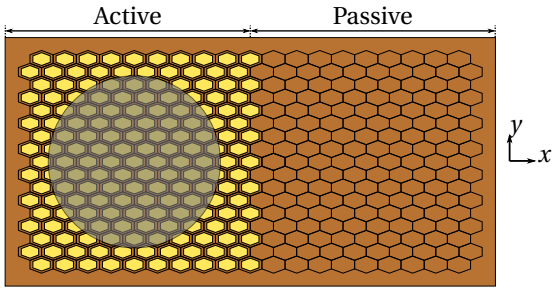

Figure 2: Top view of the demonstrator design, which consists of an active surface and a passive surface. The wafer is visualised partially transparent on top of the active surface.

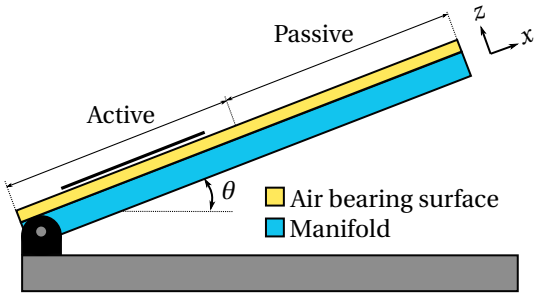

Figure 3: Side view of the demonstrator design, which can be placed at an angle θ. In combination with with gravity, the system is able to actuate the wafer in two degrees of freedom. The wafer is located on top of the active surface.

The active surface and passive surface of each demonstrator consist of separate cells. A tessellation study is done to find the optimal cell geometry for tiling the surfaces. The cell geometries are optimised for a high traction force over mass flow ratio. Stretched, hexagonally shaped cells, as shown in Figure 2, show the best performance. This cell geometry is used in both surfaces. The active cells have two feed pressure inlets and

one vacuum pressure outlet and are able to actuate in positive x-direction and both positive and negative y-direction. The air bearing surface can be placed at a certain angle, as shown in Figure 3. In combination with gravity, the active surface is able to actuate the wafer in two degrees of freedom.

The first demonstrator, which is shown in Figure 4, is designed and manufactured to validate the numerical model. Different manufacturing methods have been developed. The air bearing surface is realised by using PCB production techniques. The pockets with a pocket depth of 13 µm are created by removing parts of the thin copper layer on top of the PCB. The manifold is made of laser-cut PMMA plates. The flow restrictions are orifice holes, which are directly drilled in the PCB air bearing surface. The first demonstrator is able to actuate the wafer with 15 mN at a fly height of 30 µm. The air film stiffness could not be measured, due to the relatively large variations in the fly height measurements. The model and measurements are in the same order of magnitude and the trend lines show good agreement. Differences can be explained by the curvature of the air bearing surface and the non-uniform vacuum pressure, due to the pressure losses in the manifold.

The design of the second demonstrator is similar to the design of the first demonstrator. The main difference is the restriction diameters, which are designed for a higher air film stiffness. The inlet restrictions are laser-cut in an additional layer of steel. This layer is placed underneath the PCB air bearing surface. The second demonstrator shows a better performance than the first demonstrator. Smaller fly heights and larger traction forces are measured, due to the higher film stiffness. An actuation force of 32 mN is measured at a corresponding fly height of 23 µm. The fly heights in both demonstrators are higher than desired, which is caused by the curvature of the air bearing surface. The wafer must fly higher to float freely on the thin film of air. Model and measurements are in the same order of magnitude but with different trend lines, especially compared to the results of the first demonstrator. A better agreement is found by applying a smaller inlet discharge coefficient and small differences in the vacuum pressure and outlet discharge coefficient in the model. The fly height and stiffness of the active and passive surface are matched by making use of the numerical model. A smooth transition of the wafer between the active surface and the passive surface is observed. Based on this qualitative test, the demonstrator is a promising concept to realise an air-based contactless conveying line for thin substrates.

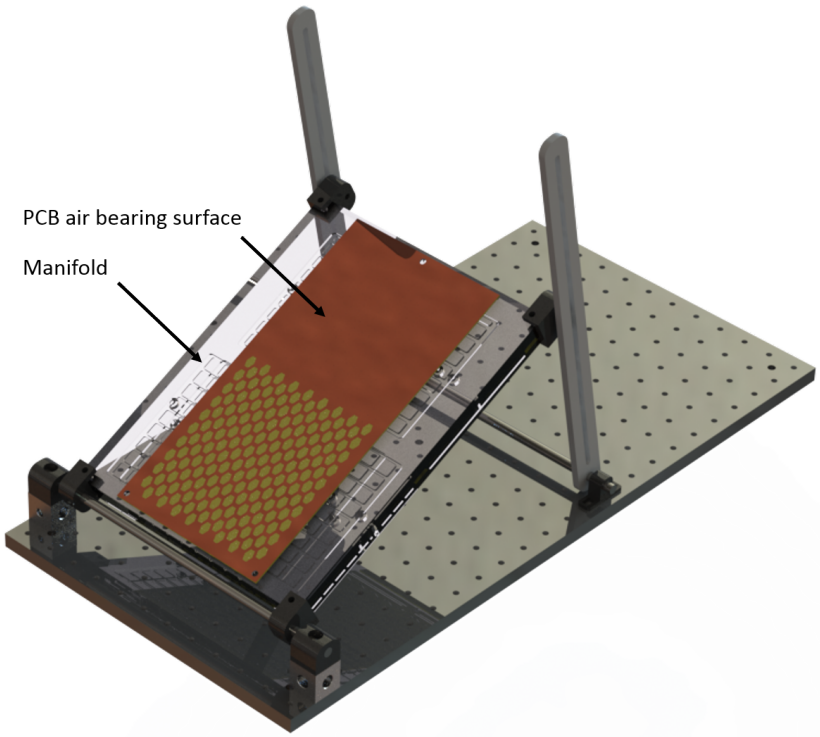

Figure 4: Render of the demonstrator.

Acknowledgements

This report is the result of my thesis study, which is the final stage of my master Precision and Microsystems engineering at the Delft University of Technology. After an exploratory discussion with Ron I decided to start this project on the principle of contactless handling of thin substrates. I have never regret this decision. The combination of theoretical and practical work made for an interesting final project. Especially the possibility to create a demonstrator yielded valuable experience, which I will not soon forget.

I would like to thank Ron for being my daily supervisor and for all the coaching during the project. You have been a great help during all aspects of this research. I especially appreciate that you are always able to see a solution or a new way to solve the numerous challenges, which occur during a thesis project. Thank you, for always having time to help me out. Here, I would also like to thank Just, Matthijs, Dingena and Stefan for completing my thesis committee.

The manufacturing of the demonstrators could not have been so successful, without the help of the technical support staff of PME. Rob, Spiridon, Patrick and Harry, thank you for all the guidance in the manufacturing of the demonstrators, helping me with the orders, and supplying me with all the materials and equipment I needed for the pneumatic connections and the measurement set-up. The realisation is also made possible by Gerard, Rene and Piet from the workshop, and Jos, from the 'meetshop'. Thank you for assisting me in all the conventional machining techniques, the numerous experiments with the laser and helping me out with the Labview programs.

It was great to have so many fellow students, with whom I shared the lab and our office. Special thanks to Ruud, Bart, Arjan, Eshan, Niek, Roy, Thomas, Ruben, Kaz, Jeroen, Arnoud and Martijn, for all the interesting discussions, drinks and keeping me healthy with the shared fruit and peppernuts. Also, I would like to thank Alexandra, Stefan, Tijn, Nils, Ruben, Joran, Jeroen, Roy, Jesper and Anne for proofreading parts of my draft report during the last month. It helped me a lot in making things more clear.

A warm thank you to my family and friends for your encouragement, support and helping me put things in perspective. And last but certainly not least, I would like to thank Alexandra for her patience and for listening to my stories about air bearings, pneumatic hammer, dynamic stability, and so much more.

J. Snieder
Delft, October 2017

Contents

1 Introduction

In this chapter, an introduction to contactless handling of thin substrates is presented. The relevance of, and motivation for the use of contactless handling techniques are discussed at first and the results of a literature study on contactless handling techniques is given, with a focus on pneumatic systems. Transport of thin substrates is discussed in more depth after which the chapter ends with an explanation of the focus and research objective of this thesis.

1.1. Motivation

In the high-tech industry, many processes are involved with the handling of thin substrates. Some examples are wafers in the semiconductor industry, solar panels in the photovoltaic industry, but also glass substrates for flat panel displays. Due to the thickness and material properties of the substrates they are often fragile and difficult to handle. Another issue is the sensitivity to contamination. The influence of both the fragility and contamination issues on contactless handling are discussed in more detail.

Solar Industry

The main driver for contactless handling in the solar cell industry is cost reduction. Up to 93% of the solar panels are produced with crystalline silicon [3]. The panels are generally made of thin mono- or polycrystalline silicon sheets. The silicon material accounts for approximately 61% of the cell price (data in 2015) [1]. A more efficient use of the silicon can be achieved by reducing the kerf of the cutting process or by reducing the thickness of the silicon substrate. The decreasing trend in the silicon substrate thickness, or wafer thickness, over the years can be seen in Figure 1.1.

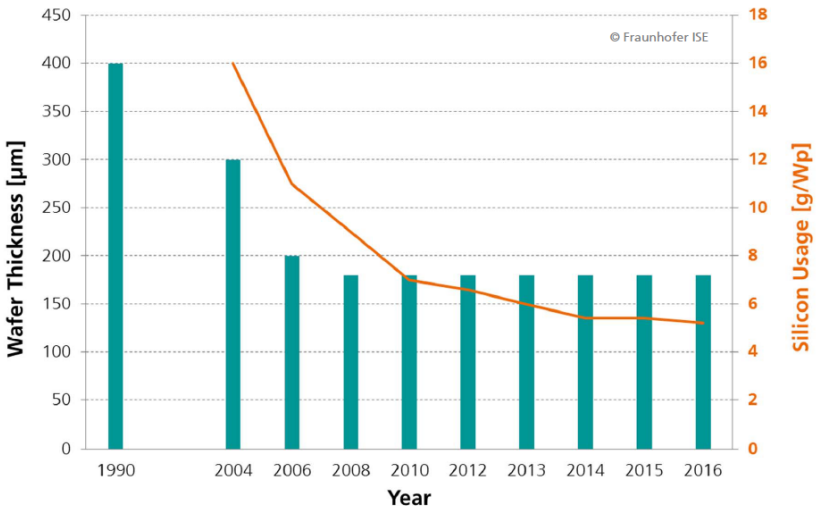

Figure 1.1: Evolution of the silicon substrate thickness [3].

It can be seen that the thickness has not decreased from 2008-2016. A substrate thickness of 180 µm is preferred, mainly due to reduced breakage of the substrates. A future reduction down to 100 µm is predicted but there is a need for innovative handling concepts to reduce the breakage rate.

Semiconductor Industry

In the semiconductor industry, integrated circuits are produced for the realisation of chips. Often, monocrystalline silicon substrates, also called wafers, are used. The wafers exist in many dimensions; up to a diameter of 450 mm. An example of a wafer can be seen in Figure 1.2. After they have been sliced from a grown silicon cylindrical ingot several processing steps are performed to pattern specific features and circuits on the wafer (lithography). In the final step the chips are separated from each other by cutting the wafer. Nowadays, the features on the wafer can be as small as 14 nm. With such small dimensions contamination of the wafer is a big issue as small dust or material particles can damage the small and fragile features. A lot of research is addressed to limit or to prevent the contamination. One of the identified contamination sources is the mechanical contact between the wafers and the handling tools [10]. The contaminated areas can be seen in Figure 1.3. The specific pattern is created by three mechanical pins which handle the wafer from the backside. Small metal-ion contaminations are created by the mechanical contact. During the processing steps, 30% of this metal-ion contamination is transferred from the backside to the front side of the wafer, resulting in a yield loss of about 0.5-1%. One of the methods to solve this type of contamination is to avoid the mechanical contact. Contact-less handling could be a solution.

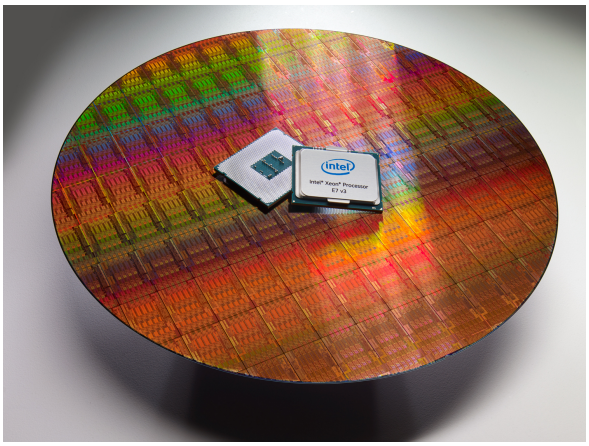

Figure 1.2: A wafer is used for the production of chips (Intel).

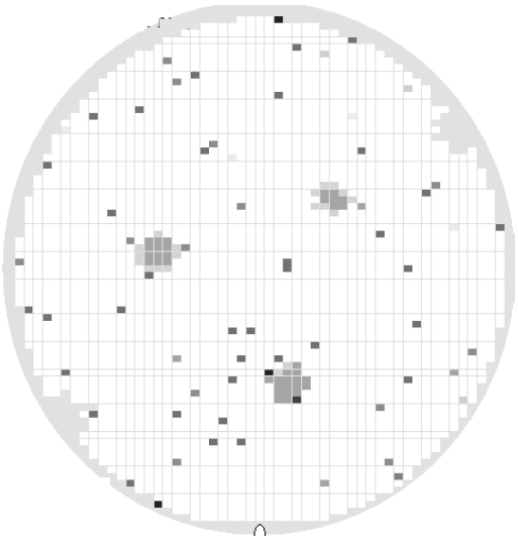

Figure 1.3: Metal-ion contamination on a wafer [10].

These two examples give an impression of the benefits of contactless handling. Many research groups are working on contactless handling techniques, for numerous reasons. The different handling techniques are discussed in the next section.

1.2. State of the Art

Contactless handling of products is employed for several reasons. It all started with the demand of reducing the friction between two solids. Friction is eliminated in a contactless handling system. The absence of friction, which also means an absence of stick-slip, is beneficial for the precise positioning of objects. The contactless handling of objects can be divided into two main functions: levitation and propulsion. The levitation, or bearing function, eliminates the contact between the object and its surroundings. Gravity has to be overcome to achieve this. The propulsion, or motor function, is about controlling the objects motion, which requires some sort of actuation principle. An overview of air-based contactless handling principles is presented in Appendix A.

Within the Mechatronic System Design group of Delft University of Technology, research is conducted on exploiting the viscous traction force of a thin film of air for handling thin substrates. Since the start in 2006,

three generations of contactless, air-based actuators have been developed: the variable pressure concept, the deformable surface concept and the outlet variation concept. They are all discussed briefly.

Gen-1: Variable Pressure Concept

Wesselingh [51] developed the first generation, which is called the step surface actuator. The bearing surface of a simple air bearing surface is modified by partly recessing it to a depth of 20 µm, hereby creating dams. The high pressure inlets and vacuum outlets are positioned at the sides of the dams, as can be seen in the cross-section in Figure 1.4. If the average pressure in the thin air film exceeds ambient pressure the object is lifted from the actuator surface to a typical fly height of 15 µm. Air will flow from the high pressure inlets to the vacuum outlets, hereby generating viscous traction forces on the object. As the thin film resistance in the direction of the pockets is lower than the thin film resistance in the direction of the dam more air will flow towards the right into the pocket, resulting in a net traction force on the object in the same direction. The traction force is controlled by varying the pressure difference with valves below the actuator surface.

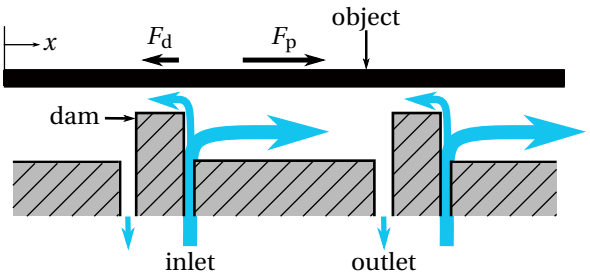

Figure 1.4: Schematic cross-section of the step surface actuator cell. Air will flow from the inlet to the outlets. Because the flow restriction above the dam is higher than the flow restriction of the recess, more air will flow in the direction of the latter. A net traction is generated on the object.

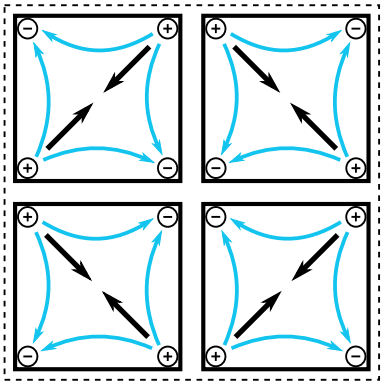

Figure 1.5: A cluster of actuator cells. Pressure inlets and vacuum outlets from pairs to be able to actuate three degrees of freedom. Each in- and outlet is connected to a proportional valve.

The actuator cell, consisting of a recess and a surrounding dam, has a square shape of 10 mm×10 mm with a recess of 8 mm×8 mm. Each actuator cell is equipped with a pair of inlets and outlets. In the final design clusters are formed to be able to actuate in three degrees of freedom. A cluster consists of four actuator cells, as can be seen in Figure 1.5. The design is formed by 3×3 clusters and the object to be actuated is a 100 mm diameter silicon wafer of 525 µm thickness. Accelerations up to 600 mm s^{-2} have been reached, together with a maximum velocity of 30 mm s^{-1}. Moreover, a positioning bandwidth of 50 Hz and a servo error of 6 nm (1σ) have been measured.

Gen-2: Deformable Surface Concept

Instead of controlling the viscous traction force on the object by controlling the pressures, as has been done in the step surface actuator, Vuong [49] developed an air-based, contactless actuator in which the force is controlled by deforming the surface. The final design, called the flowerbed, uses hexagonal shaped actuator cells, which are found to be the most beneficial with respect to the mass flow and the surface coverage. The working principle can be seen in the cross-section in Figure 1.6, and the top view of the system is shown in Figure 1.7. The shape of the actuator cells reminds of flowers, which explains the name of the system. The pressure inlet, which is connected to a capillary, is located at the centre of the flower and vacuum can be found in between them. The flowers are held by two spring steel membranes. When the actuators are in upright position, the system works just like an air bearing surface and no net traction is generated. By moving the bottom membrane with respect to the top membrane, the actuator heads tilt, thereby deforming the bearing surface and generating a net traction force on the object in the direction of tilting.

The final system has 61 flowers and is designed for positioning 300 mm diameter silicon wafers. The lack of time delay in the supply lines improves the bandwidth significantly. The theoretical bandwidth between actuating the membrane and the force generation on the object is equal to 1000 Hz, but has only been verified up to 400 Hz due to practical limitations. Krijnen [25] designed variable reluctance actuators to actuate

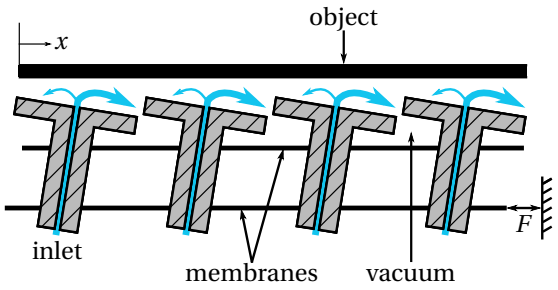

Figure 1.6: Schematic cross-section of the flowerbed. The "flowers" can be tilted by moving the membranes with respect to each other, thereby directing the flow and generating a net traction on the object. Vacuum is located in between the flowers.

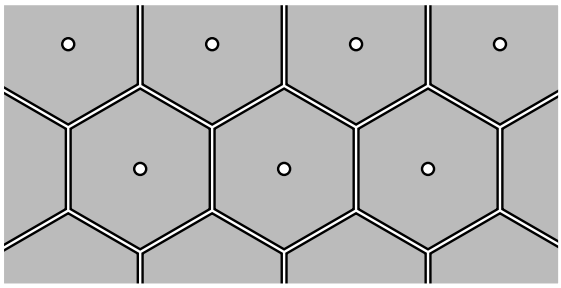

Figure 1.7: Top view of the flowerbed. A pressure inlet is located in the middle of the flower and there is a vacuum in between the hexagon cells.

the membrane and applied fractional order control to position the wafer. A bandwidth of 60 Hz has been achieved. This is lower than expected and can be explained by the relatively high mass and low response time of the reluctance actuators. At the moment, research is going on to improve the bandwidth by redesigning the actuators. Accelerations up to 1.17 $\mathrm{m\,s^{-2}}$ have been measured, in combination with a positional accuracy of a 0.1 µm positional accuracy (2σ).

Gen-3: Outlet Variation Concept

The last concept has recently been developed by Verbruggen [48]. In this concept the viscous traction force is controlled by varying the outlet restrictions. A cross-section of the design can be seen in Figure 1.8. The design is made out of a plate, coloured in light-grey, with circular holes. Pillars, coloured in dark-grey, are inserted in the holes on a lower level, hereby creating dams and recesses. The inlets are positioned at the centre of the pillars, while the outlets are formed by the circular gap between the pillars and the holes. In the neutral situation the pillars are centred in the hole and no net force on the object is generated. By moving the dams with respect to the recess surface, which is done by moving the plate with respect to the pillars, the outlet resistances will change. More air will flow to the side where the outlet resistance becomes smaller, which will create a net viscous traction force on the object in the same direction. This is visualised in Figure 1.9. An open-loop demonstrator has been realised, which shows a reasonable match with the numerical model. An average angular acceleration of 11.1 $\mathrm{rad\,s^{-2}}$ has been achieved.

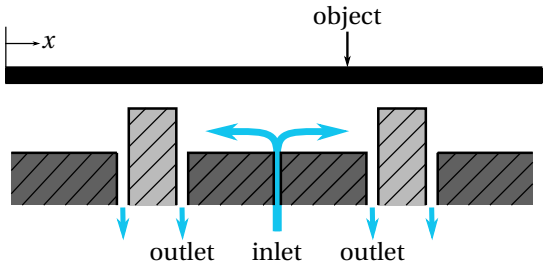

Figure 1.8: Schematic cross-section of the outlet variation concept. In the neutral position no net viscous traction force is generated.

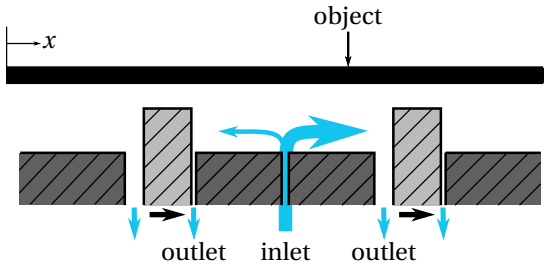

Figure 1.9: Schematic cross-section of the outlet variation concept. If the dams are moved with respect to the recess surface a net viscous traction force is generated.

1.3. Transport

Up to now, the developed contactless air based demonstrators [52][49][48] have been designed for the positioning of thin substrates. However, there is a need for contactless transportation solutions from industry to prevent breakage of the substrates and minimise contamination, as has been explained in Section 1.1. Therefore, the focus of this thesis is on exploiting the principle of using a viscous traction force of a thin film of air for transporting thin substrates. The transportation of a circular substrate is visualised in the conveying line in Figure 1.10. The set-up consists of active contactless air-based actuator surfaces and passive air bearing

surfaces. The actuator surfaces are able to generate a force on the substrate and make it move in a certain direction. The passive bearing surfaces are only able to levitate the substrate and guide its motion. Passive surfaces are used to reduce the mass flow of the system, as they consume less air. A second actuator surface can catch the substrate and send it to the next active surface. It is believed that the combination of active and passive surfaces is the solution for transporting a thin substrate to the desired location in a contactless way.

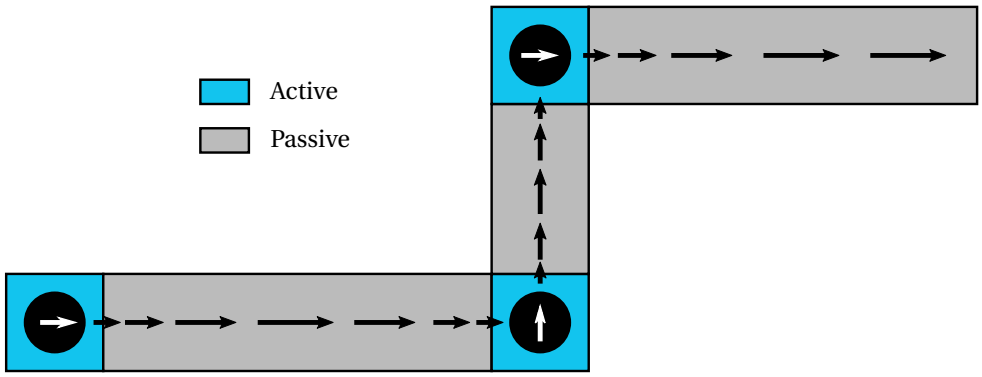

Figure 1.10: Schematic overview of a conveying line with active and passive surfaces.

An essential element in transporting thin substrates over these conveying lines is a smooth transition between the active and passive surfaces. It is believed that a smooth transition can be realised if the fly height of the two surfaces are matched. If the substrates are perfectly flat, it moves smoothly from one surface to another. In reality, the substrates are not flat and it has a certain bow and warp, which are the measures for its flatness. The stiffness of the air film deforms the wafer to the actuator surface shape. If the stiffness of the different surfaces are not matched, the substrate will experience a change in its deformation. Therefore, it is proposed to also match the stiffness of each surface. If the fly height and film stiffness are matched, a smooth transition over the surfaces can be realised.

In the previous positioning demonstrators the actuator surfaces have always been covered by the substrate. The created thin film acts as a flow resistance and limits the mass flow through the outlets. In the transport demonstrator this will not be the case. As the substrate travels over the surfaces it will leave the vacuum outlets open to ambient air. The mass flow through the outlets must be limited in some way.

1.4. Research Objective

In this project, a transport demonstrator will be designed and built, in order to show the possibilities of using the viscous traction force of a thin film of air for transport purposes. The research objective is stated as follows:

"Design and realisation of a contactless air-based and efficient transport demonstrator for thin substrates."

One of the reasons behind the contactless actuation systems is to minimise the contamination due to mechanical contact. The air must therefore also be clean, and clean air is costly. The system should therefore be efficient in terms of mass flow. The mass flow will be reduced by combining the active surfaces with passive surfaces. Both surfaces will be designed to be efficient. The active surface will be optimised for a high force over mass flow ratio, which is a measure for the performance of the actuator [49]. The passive surface will be optimised for minimum mass flow. The mass flow through the outlet will be limited by increasing the outlet resistance.

Manufacturability will become a challenge for the realisation of large conveying lines. The previous demonstrators have all proven it is difficult to manufacture flat surfaces with small pockets in the order of

10 µm at a low roughness (sub-micrometer). One of the goals of this project is to find a cost effective way to realise these systems on a large scale.

The demonstrator must be able to actuate a thin substrate in at least two degrees of freedom (DoF): x and y. The transported object is chosen to be a 100 mm diameter silicon wafer with a thickness of 525 µm. The focus will be on the transition between the active surface and the passive surface. It is proposed to achieve a smooth transition by matching the fly height and air film stiffness of each surface.

1.5. About This Study

A theoretical analysis of a simple air bearing and an air bearing actuator is presented in Chapter 2. This chapter also includes the theoretical background on orifice restrictions and the dynamic analysis of an air bearing system. Two demonstrators will be designed and manufactured. Chapter 3 contains the conceptual design of both demonstrators. Chapter 4 describes the design of the first demonstrator. Its realisation and validation can be found in Chapter 5. The results of the realisation and validation of the first demonstrator will be used to design the second demonstrator in Chapter 6. The realisation and validation of the second demonstrator are presented in Chapter 7. Chapter 8 contains the conclusion and the recommendations are presented in Chapter 9. Multiple appendices on different subjects are present in Appendix A-I, and are referred to if more information on a certain subject is required.

2

Theoretical Analysis

In this chapter, the concept of using the viscous traction force of a thin film of air to actuate a substrate is explained in more detail. The theory, which describes the load carrying capacity and traction, has been well described in the work of Vuong [49] and Verbruggen [48]. The main results of their work are presented here and a full description and derivation of the equations is presented in Appendix C. What is new however, is the study on the restrictions and the related stiffness and stability of the system. These are presented in this chapter as well. First, the optimality criteria are discussed and applied to a simple vacuum pre-loaded air bearing. By changing the design of the passive air bearing it can be made active. The active air bearing is analysed in depth. All expressions are given for both the incompressible and compressible flow and differences between those two are discussed. The chapter continues with the restriction theory and a dynamic analysis, in which the frequency dependent stiffness and damping of an air bearing surface are analysed. The dynamic analysis is also used to check the stability of the system.

2.1. Optimal Design Criteria

The modelling of an air-based actuator and the calculations of the relevant parameters are explained by making use of a simple air bearing in two dimensions: x and z. The air bearing has an infinite width in y-direction. It can be seen in Figure 2.1.

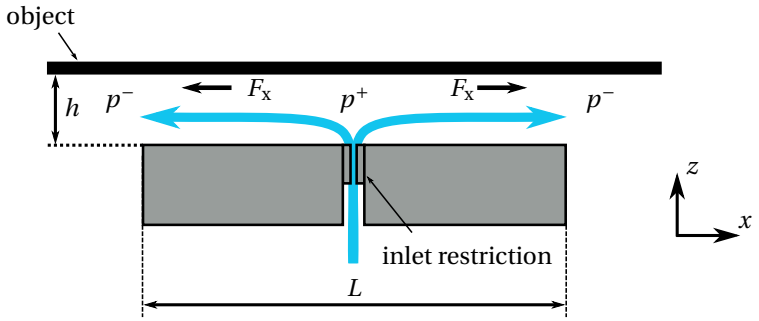

Figure 2.1: Schematic view of a two-dimensional air bearing.

The object, which is a thin substrate, is carried by a thin film of air. Typically in air bearing applications, the fly height h is in the order of 10 µm, while the length L is in the order of millimetres. Air flows from below the bearing surface through an inlet restriction to the outlets of the system. The pressure downstream the inlet is equal to p^+ and decays to a pressure p^- at the outlets of the air bearing. The pressure distribution in the thin film in x-direction can be calculated with the Reynolds equation:

$$\frac{d}{dx}\left(\frac{\rho H^3}{12\eta}\frac{dp}{dx}\right) = 0 \tag{2.1}$$

The pressure p depends on the coordinate x and is the variable to be solved. The dynamic viscosity of air is represented by η. The variable ρ is the air density. The derivation of the Reynolds equation and a physical

interpretation of all its terms can be found in Appendix B. For now, it is important to know the following assumptions have been made [20]:

1. Body forces are neglected. A body force is a force that acts throughout the volume of the whole body due to for example gravity, electric fields and magnetic fields.
2. As the film height is very small compared to the film length, a constant pressure over the film height is assumed.
3. At the boundaries between the air film and the surfaces no slip is assumed. The air film and the surface have the same velocity at the interface.
4. The flow is assumed to be laminar: fluid inertia is neglected.
5. The lubricant, which is air in this case, is assumed to behave as a Newtonian fluid. The shear stress is linear proportional to the velocity gradient and the viscosity.
6. The air film is assumed to be isothermal.
7. The viscosity of the air film is assumed to be constant.

For the specific form of the Reynolds equation in Equation 2.1, the velocities of both surfaces are assumed to be negligibly small compared to the air film velocities [49]. Moreover, dynamic effects have been removed from the equation. The static pressure distribution is calculated. The required load capacity can be calculated as well. As the carried object is a thin substrate, its weight can be neglected and the required load capacity per unit area can be assumed to be exactly zero:

$$\overline{w} = \frac{1}{L}\int_0^L \left(p - p_\mathrm{a}\right) \mathrm{d}x = 0 \tag{2.2}$$

The variable L is the length of the air bearing application. The zero load capacity of the air bearing shows that the substrate is levitated with zero acceleration in the normal direction z. The Reynolds equation is calculated while satisfying the boundary conditions and the zero load capacity. If the pressure distribution is found the force density (force per unit area) can be calculated:

$$\overline{F}_\mathrm{x} = \frac{1}{L}\int_0^L -\frac{H}{2}\frac{\partial p}{\partial x}\,\mathrm{d}x \tag{2.3}$$

In this equation, H is the film thickness function, which - for this specific air bearing example in Figure 2.1 - is equal to h over the entire length. For this specific example, the net force density is equal to zero, as will be shown in the next section. However, non-zero net force densities can be created by modifying the air bearing surfaces. This is explained in detail in Section 2.3. The mass flow density (the mass flow per unit area) can be obtained from the pressure distribution as well. It is decided to calculate the mass flow density at the inlet as the sum of the mass flows through the left and right domains:

$$\overline{\dot{m}} = \frac{1}{12\eta L}\rho\left(H^3\frac{\partial p}{\partial x}\bigg|_\mathrm{left} - H^3\frac{\partial p}{\partial x}\bigg|_\mathrm{right}\right) \tag{2.4}$$

2.2. Air Bearing

The motor function and bearing function of the passive air bearing surface are analysed first. This is done for the incompressible flow and compressible flow situation. Figure 2.2 shows a cross-section of one passive cell, which is dark-coloured. The cell is modelled with an infinite width in the y-direction, pointing out of the paper. The cell has a length L and the inlet is positioned at a distance of αL from the right outlet, $0 < \alpha < 1$. The film height H is constant and equal to the fly height h. The inlet and outlet grooves are assumed to be infinitely small, resulting in a flow path length which is equal to the cell length L. As a last assumption, the outlet restriction is assumed to be negligibly small. In practice this restriction is chosen to be small, such that the pressure p^- is close to the vacuum pressure p_v, in order to make full use of the vacuum source. In a simple air bearing, such as in Figure 2.1, the force density is equal to zero. Therefore, only the mass flow density are optimised for realising an efficient system.

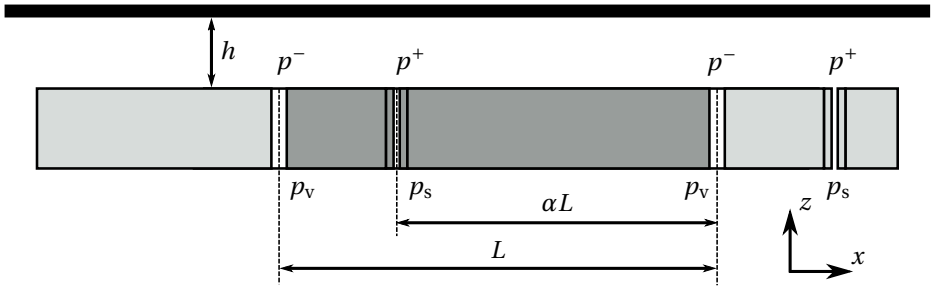

Figure 2.2: Schematic cross-section of a passive cell.

2.2.1. Incompressible Flow Case

In the incompressible flow model, the density is assumed to be constant. This is a valid assumption if the pressure difference in the system is relatively small compared to ambient pressure. The vacuum pressure p_v must therefore be close to ambient pressure. As the flow is assumed to be incompressible, the pressure distribution shows a linear decrease from the inlet pressure p^+ to the outlet pressures p^-. This is visualised in Figure 2.3. The zero load condition from Equation 2.2, is then used to determine the inlet pressure p^+. The outlet pressure p^- can be substituted with the vacuum pressure p_v, because the outlet restriction is assumed to be negligibly small:

$$p^+ = 2p_a - p^- = 2p_a - p_v \tag{2.5}$$

The maximum value of p^+ for the incompressible flow assumption is equal to 2 bar, in the case that the vacuum pressure p_v is equal to 0 bar. The zero load condition shows that, because the weight of the thin substrate is neglected, vacuum pressure is necessary for having a pressure difference between the inlet and outlet. If the outlet pressure is equal to ambient pressure, there is no pressure difference and thus no flow.

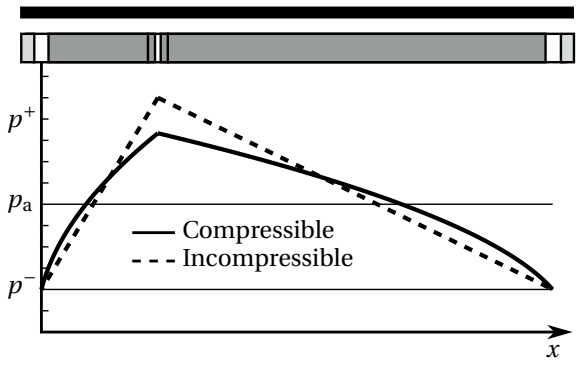

Figure 2.3: Pressure distribution passive cell.

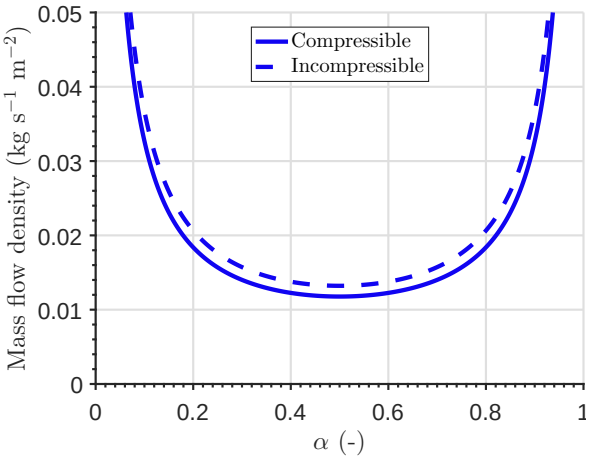

Figure 2.4: Optimisation of variable α for minimum mass flow.

Motor Function

The motor function of the cell is characterised by the force density. The force density of the passive cell from Figure 2.2 is calculated by integrating the shear traction over the cell length L. The force density turns out to be equal to zero; no in-plane force is generated. Viscous traction forces are created in the left and right x-direction, but the net force is equal to zero as they cancel each other out. The mass flow density can be derived as well, based on Equation 2.4 and the expression for the inlet pressure p^+ from Equation 2.5:

$$\overline{m} = \frac{p_a}{R_g T}\frac{h^3}{6\eta L^2}\left(\frac{1}{1-\alpha}+\frac{1}{\alpha}\right)(p_a - p_v) \tag{2.6}$$

In this equation the density ρ is calculated by using the ideal gas law at ambient pressure: $\frac{p_a}{R_g T}$. The parameter R_g is the specific gas constant of air and T is the absolute temperature. The variable α is optimised for minimum mass flow. The mass flow is minimum when $\alpha = 0.5$, which means a centrally positioned inlet. The optimisation can be seen in Figure 2.4. In this figure, the mass flow density is calculated for a passive cell with a length of 10 mm and a film height of 10 µm. The vacuum pressure is set at 0.7 bar. The outcome makes sense because, with this value of α, the thin film restrictions in both directions are equal and the sum of the two restrictions is at a maximum.

Bearing Function

The bearing function of the thin air film has two functionalities: the load capacity and the bearing stiffness. The load capacity has been discussed before. It should be big enough to be able to lift the substrate to the defined fly height. The second property of the bearing function is the bearing stiffness. A positive bearing stiffness can be realised by placing a restriction at the inlet. This is explained in Appendix D. The bearing stiffness enables a stable fly height of the substrate. The analogy of air flow with electric circuits is useful to determine the analytical bearing stiffness of the system. This is explained in detail in Appendix C. The resulting stiffness at the fly height h_0 is equal to:

$$\overline{k}(h_0) = -\left.\frac{\partial R_e(h)}{\partial h}\right|_{h=h_0} \frac{R_i - R_o}{2\left(R_e(h_0) + R_i + R_o\right)^2}\left(p_s - p_v\right) \tag{2.7}$$

The resistance $R_e(h_0)$ is the equivalent thin film resistance. It depends on the cell geometry, as well as its derivative $\left.\frac{\partial R_e(h)}{\partial h}\right|_{h=h_0}$, and it is derived in Appendix C. The resistances R_i and R_o are respectively the inlet and outlet resistance of the air bearing. A positive stiffness is realised if the inlet resistance R_i is larger than the outlet resistance R_o. The stiffness increases if the pressure difference increases. The resistance R_i can be chosen. This is explained in Appendix C as well. The stiffness per unit area is visualised in Section 2.4, together with the results from the compressible analysis.

2.2.2. Compressible Flow Case

If the pressure difference in the system becomes larger, the assumptions for incompressible flow are no longer valid and the air density in the Reynolds equation of Equation 2.1 has a high dependency on the film pressure. The pressure distribution for the compressible flow can be seen in Figure 2.3. There is no longer a linear decrease from the inlet pressure p^+ to the outlet pressures p^-. The zero load capacity can be used to derive an expression for the inlet pressure p^+:

$$p^+ = -\frac{1}{2}p_v + \frac{3}{4}p_a + \frac{1}{4}\sqrt{-12{p_v}^2 + 12p_a p_v + 9{p_a}^2} \tag{2.8}$$

The derivation can be found in Appendix C. In this equation, the pressure p^- is substituted with the vacuum pressure p_v. The maximum value of p^+ for the compressible flow assumption is equal to 1.5 bar, in the case that the vacuum pressure p_v is equal to 0 bar.

Motor Function

Similar to the incompressible flow calculations the net force density of the passive cell is equal to zero. The mass flow density is equal to:

$$\overline{m} = \frac{\left(p^+ + p_v\right)}{2R_g T}\frac{h^3}{12\eta L^2}\left(\frac{1}{1-\alpha} + \frac{1}{\alpha}\right)\left(p^+ - p_v\right) \tag{2.9}$$

In which the expression for the inlet pressure p^+ from Equation 2.8 can be inserted. For minimum mass flow the variable α is equal to 0.5, similar to the incompressible flow situation. This can be seen in Figure 2.4. In this figure the simulating conditions for both the incompressible and compressible flow are identical. The cell length L is 10 mm, the film height h is 10 µm and the vacuum pressure p_v is 0.7 bar. It can be noticed that the mass flow for the compressible flow is slightly smaller than the mass flow for the incompressible flow.

Bearing Function

In the case of the incompressible flow assumption the stiffness has been derived analytically by setting up a system of volume flow equations, as explained in Appendix C. For the compressible flow situation it is no longer valid to state that the volume flow through each restriction is equal as the density of the air is dependent of the pressure. The resulting mass flow equations are non-linear in terms of the pressure variables. To avoid long analytical derivations, the stiffness for the compressible flow is determined numerically. The load capacity per unit area is determined for a small perturbation in the film height, both negative and positive. The stiffness per unit area can then be calculated:

$$\bar{k} = -\frac{\overline{w}_{\mathrm{h}+\delta\mathrm{h}} - \overline{w}_{\mathrm{h}-\delta\mathrm{h}}}{2\delta h} \tag{2.10}$$

The stiffness per unit area is visualised in Section 2.4, together with the results from the incompressible analysis.

2.3. Air Bearing Actuator

Vuong [49] and Verbruggen [48] analysed and compared different geometries and concepts: the stepped surface, the tilted surface and the variable outlet restriction concept. They have both confirmed that for actuation in a single degree of freedom the step surface actuator performs best. Therefore, this concept is discussed in depth. A schematic overview of the system can be seen in Figure 2.5. The concept is very similar to the passive cell from Figure 2.2. The main difference is the varying air bearing surface, which is created by lowering the bearing surface at certain locations, forming so called pockets and dams. The cell has a length L and the inlets and outlets are positioned next to the dams at a distance αL, $0 < \alpha < 1$. The parameter β represents the pocket depth as a factor times the fly height above the dam, $\beta \geq 1$. The motor function and bearing function of the active cell are analysed for incompressible flow and compressible flow.

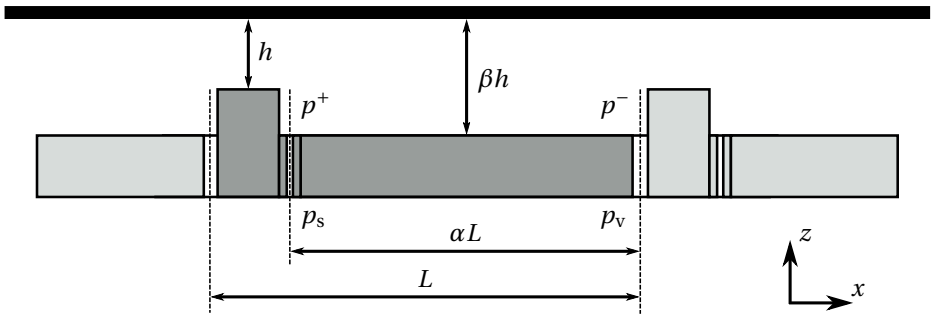

Figure 2.5: Schematic cross-section of an active cell: the stepped surface actuator.

Vuong [49] suggested to measure the performance of a contactless, air-based actuator by looking at the force squared over mass flow ratio: the **performance limit** $\left(\overline{F}^2/\overline{\dot{m}}\right)$. The performance limit gives the maximum force density for a specific mass flow density. Verbruggen [48] suggested to measure the performance by looking at the force over mass flow ratio: the **performance ratio** $\left(\overline{F}/\overline{\dot{m}}\right)$. Verbruggen compared the performance limit and performance ratio in a detailed analysis and concluded that the performance ratio is the best measure to optimise for a limited mass flow. As one of the goals of this project is to design an efficient demonstrator, the performance ratio is used in the design process. In other words, if a system gives a higher force for a given mass flow, it can be seen as more efficient.

2.3.1. Incompressible Flow Case

For the active cell, the film height H is not constant any more, contrary to the passive cell. However, it does not change the pressure distribution in the cell. The incompressible pressure distribution in the active cell can be seen in Figure 2.6. The figure shows the pressure decreases linearly from the inlet pressure p^+ to the outlet pressures p^-. As the pressure profile is similar to the pressure distribution of the passive cell, the inlet pressure can be expressed as in Equation 2.5.

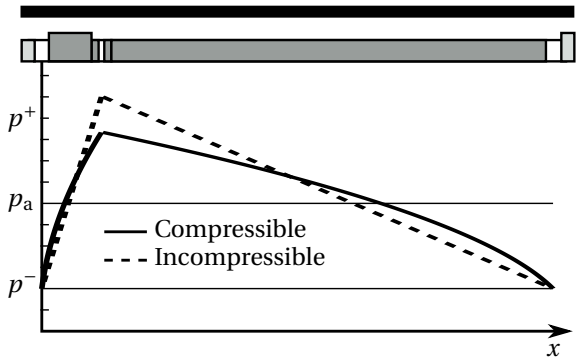

Figure 2.6: Pressure distribution active cell.

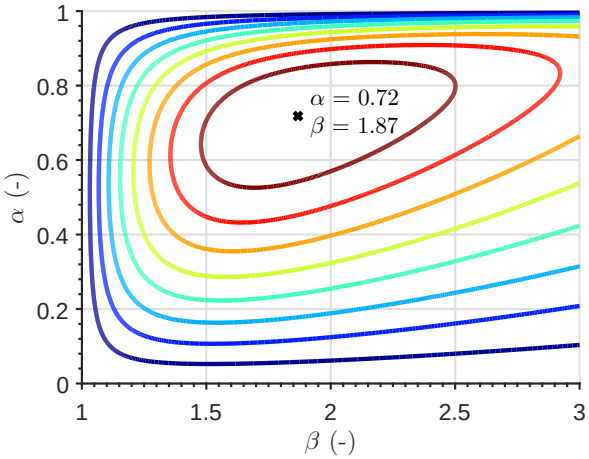

Figure 2.7: Optimisation of the performance ratio (force over mass flow) with the variables α and β.

Motor Function

The motor function can be characterised by the force density. Using Equation 2.3 and the expression for the inlet pressure $p^+$the force density is determined:

$$\overline{F} = \frac{(\beta - 1)\, h}{L} \left(p_a - p_v\right) \tag{2.11}$$

The difference between the active cell and the passive cell is clear. A net force density is generated, which scales with the pressure difference $p_a - p_v$, the pocket depth $(\beta - 1)\, h$ and the length of the cell L. The force density does not depend on the variable α. If the variable β is equal to 1, the pocket depth goes to zero and the force density is equal to zero as well. In addition, the mass flow density for the active cell can be derived:

$$\overline{\dot{m}} = \frac{p_a}{R_g T} \frac{h^3}{12\eta L^2} \left(\frac{1}{1-\alpha} + \frac{\beta^3}{\alpha} \right) \left(p_a - p_v\right) \tag{2.12}$$

In this equation, the expression for the inlet pressure p^+ is already inserted. Due to the factor β the mass flow density is larger than the mass flow of the active cell, which has been determined in Equation 2.6. If β is larger than 1 the thin film resistance is lowered, which results in a larger mass flow. With the expressions for the force density and the mass flow density known, the performance ratio (force over mass flow ratio) can be calculated:

$$\frac{\overline{F}}{\overline{\dot{m}}} = \frac{R_g T}{p_a} \frac{6\eta L}{h^2} \frac{\beta - 1}{\frac{1}{1-\alpha} + \frac{\beta^3}{\alpha}} \tag{2.13}$$

The first term in the performance ratio is the inverse of the air density and is constant in the incompressible flow situation. The second term shows the influence of the variables L and h. It is clear that the performance ratio increases for an increasing length L and a decreasing film height h. This is purely due to the fact that the mass flow density scales with the film height to the power three and the inverse of the cell length squared, while the force density scales with simply the fly height and the inverse of the cell length. The third part of the performance ratio equation consists of the variables α and β. This part can be optimised for the highest performance ratio. The results can be seen in Figure 2.7, in which the performance ratio (force over mass flow) is plotted for different values of α and β. The highest performance ratio is found for $\alpha = 0.72$ and $\beta = 1.87$. These values are also used in calculations later in this section.

Bearing Function

The stiffness per unit area for the active cell can be calculated the same way as the passive cell, resulting in the same formula as in Equation 2.7. The only difference with the passive cell is that the flow resistances of the thin film are different, due to the varying fly height in the active cell. The equivalent film resistance $R_e(h)$ and its derivative $\frac{\partial R_e(h)}{\partial h}$ are derived in Appendix C. The results are shown in Section 2.4.

2.3.2. Compressible Flow Case

In the compressible flow case, the density is not constant and can no longer be removed from the Reynolds equation, similar to the passive cell. Solving the Reynolds equations results in the same pressure distribution and load capacity as the passive cell. The pressure distribution is visualised in Figure 2.6. The pressure does not decrease in a linear fashion any more. Furthermore, the inlet pressure p^+ has become smaller, compared to the incompressible situation. The inlet pressure p^+ can be expressed in the same way as in Equation 2.8.

Motor Function

The force density and mass flow density of the active cell can be calculated, using Equation 2.3 and Equation 2.4, respectively:

$$\overline{F} = \frac{1}{L}\frac{(\beta-1)\,h}{2}\left(p^+ - p_\mathrm{v}\right) \tag{2.14}$$

$$\overline{\dot{m}} = \frac{\left(p^+ + p_\mathrm{v}\right)}{2R_\mathrm{g}T}\frac{h^3}{12\eta L^2}\left(\frac{1}{1-\alpha}+\frac{\beta^3}{\alpha}\right)\left(p^+ - p_\mathrm{v}\right) \tag{2.15}$$

In both equations the inlet pressure p^+ can be taken from Equation 2.8. As the force density and mass flow density are known, the performance ratio for the compressible flow situation can be determined:

$$\frac{\overline{F}}{\overline{\dot{m}}} = \frac{2R_\mathrm{g}T}{p^+ + p_\mathrm{v}}\frac{6\eta L}{h^2}\frac{\beta-1}{\frac{1}{1-\alpha}+\frac{\beta^3}{\alpha}} \tag{2.16}$$

The difference between the performance ratio in the compressible and incompressible situation (Equation 2.13) can be found in the first term. It has no influence on the optimisation for finding the optimal α and β regarding performance ratio. They are identical to the values, which are found in the incompressible flow situation.

Bearing Function

Similar to the passive cell, the stiffness of the active cell for the compressible flow situation is determined numerically. The results are shown in Section 2.4.

2.4. Performance

The performance of the system is visualised by comparing the motor function and bearing function of both the passive cell from Figure 2.2 and the active cell from Figure 2.5. Each function is shown for the incompressible flow and compressible flow situation. The cells have a length L of 10 mm and a fly height h of 10 µm. The cells are optimised as mentioned in the previous sections. For the passive cell, the variable α is equal to 0.5, and for the active cell the variable α is equal to 0.72, and the variable β is equal to 1.87.

2.4.1. Motor Function

The motor function of the system is characterised by the force density and the mass flow density. First, the mass flow densities of the passive cell and active cell are compared with each other for the incompressible and compressible flow. The mass flow densities for the passive cell are calculated with Equation 2.6 (incompressible) and Equation 2.9 (compressible). The mass flow densities of the active cell are calculated with Equation 2.12 (incompressible) and Equation 2.15 (compressible). The results for a varying pressure difference $\left(p_\mathrm{a} - p_\mathrm{v}\right)$ can be seen in Figure 2.8. For the incompressible flow assumption, the mass flow densities increase linearly with the pressure difference. For this specific example, the mass flow density of the active cell is more than three times the mass flow of the passive cell. The compressible flow can be seen in the figure as well. For small pressure differences, up to approximately 0.1 bar, the incompressible and compressible mass flow densities match fairly well. For larger pressure differences, the difference between the mass flow densities becomes significant. However, for the compressible flow the mass flow density of the active cell is also more than three times the mass flow density of the passive cell. Figure 2.8 illustrates the benefit of combining an active surface with a passive surface in a transport demonstrator for reducing the total mass flow.

Only the active cell has a net force density. The performance of the active cell is visualised in Figure 2.9. This figure shows the force density of the active cell for varying mass flow densities for both the incompressible and compressible flow. The pressure difference $\left(p_\mathrm{a} - p_\mathrm{v}\right)$ is fixed at at a few values. The force density

and mass flow density are calculated with Equation 2.11 and Equation 2.12, respectively, (incompressible) and Equation 2.14 and Equation 2.15 (compressible), respectively. For a given pressure difference, the curves represent the performance of the optimal active cell. Assuming an ambient pressure of 1 bar, the limit performance curve is found for a pressure difference of 1 bar, as vacuum cannot go below 0 bar. The performance curves are obtained by varying the cell length L. In practice, the cell length is fixed. The mass flow density and force density for a fixed cell length of 10 mm are shown in the figure as well. These curves are found by varying the pressure difference $(p_a - p_v)$. The curves stop at the limit performance curve. Similar to the mass flow plot in Figure 2.8, the difference between the performance curves for the incompressible and compressible flow becomes larger when the pressure difference $(p_a - p_v)$ increases. For a pressure difference of 1 bar, the curves seem to be similar, but the results are different as the actuator lengths for a certain mass flow and force density are not the same. This is also the reason why the lines of the incompressible and compressible flow for the fixed actuator length of 10 mm have a different end point on the limit performance curve.

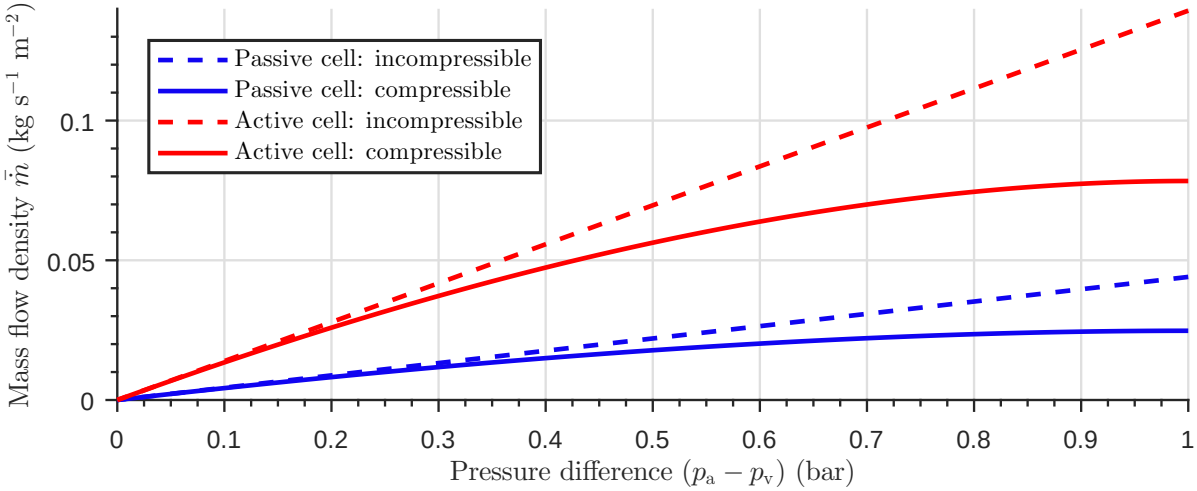

Figure 2.8: Modelled mass flow density of the passive and active cell for the incompressible and compressible flow.

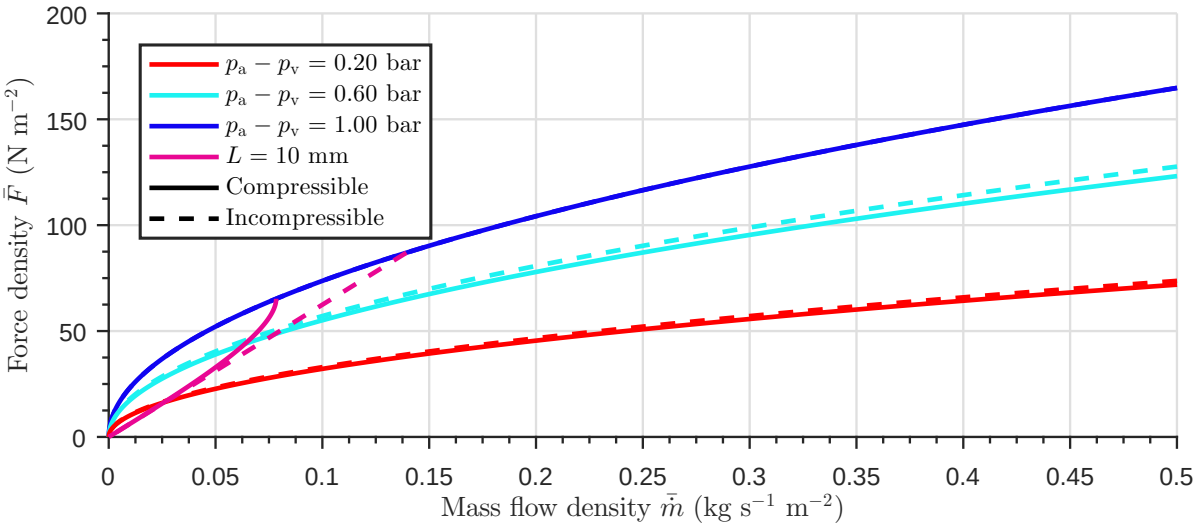

Figure 2.9: Performance curves of the active cell for the incompressible and compressible flow.

2.4.2. Bearing Function

The stiffness for the incompressible flow assumption has been calculated using Equation 2.7. The inlet restriction and equivalent thin film restrictions are calculated using the equations, which are derived in Appendix C. The feed pressure p_s is equal to 3 bar and the vacuum pressure p_v is equal to 0.7 bar. The stiffness densities can be seen in Figure 2.10, which shows the modelled stiffness per unit area for a changing fly height.

In practice, the fly height can change due to an out-of-plane external force for example. For the calculation of the stiffness densities of the active cell, the pocket depth is fixed at a value of $(\beta - 1)\,h$, in which the fly height h is equal to 10 µm. The stiffness density of the passive cell is negligibly small for very low fly heights. After reaching an optimum above the $1 \times 10^{10}\,\mathrm{N\,m^{-1}\,m^{-2}}$, it slowly decreases with increasing fly height. A small difference between the incompressible flow and the compressible flow can be noticed. The stiffness density of the active cell starts at a high stiffness, even for a zero fly height. For this fly height there is still air present in the pocket, which results in a positive stiffness. Again, the stiffness reaches an optimum and decreases slowly with increasing fly height. In general the stiffness of the passive cell is higher than the stiffness of the active cell.

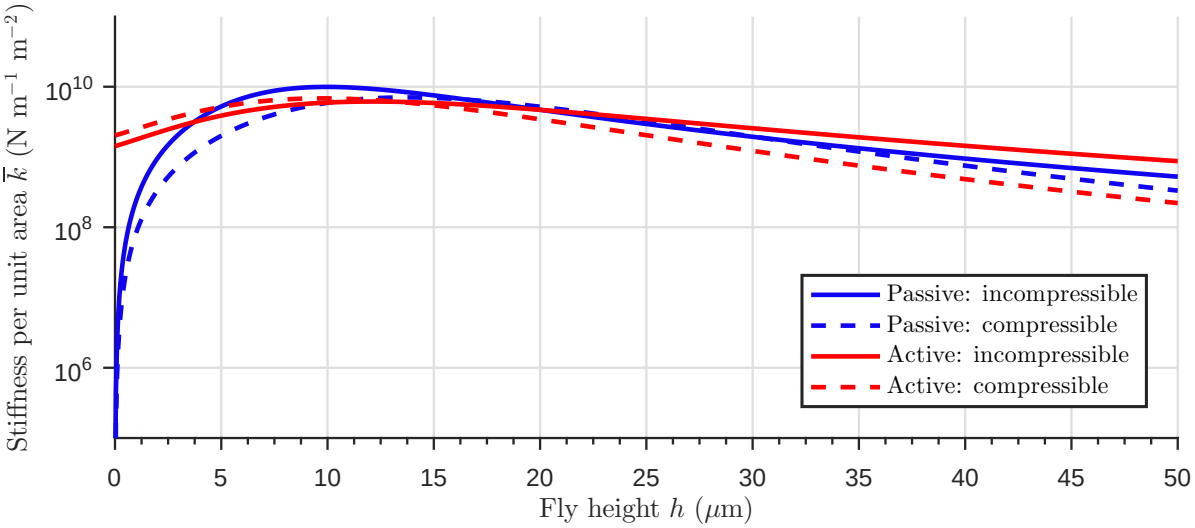

Figure 2.10: Modelled stiffness per unit area for varying fly height for the incompressible and compressible flow.

2.5. Restrictions

In the previous sections, the inlet restriction R_i and outlet restriction R_o have been modelled as constant parameters. This is often not true and the restriction values depend on the pressure difference over the restriction. There are different type of flow restrictions, such as capillaries, porous restrictions, and orifice restrictions. The first two are discussed in more detail in Appendix D. In this project orifice restrictions are used. The reasons behind this choice are presented in Chapter 3.

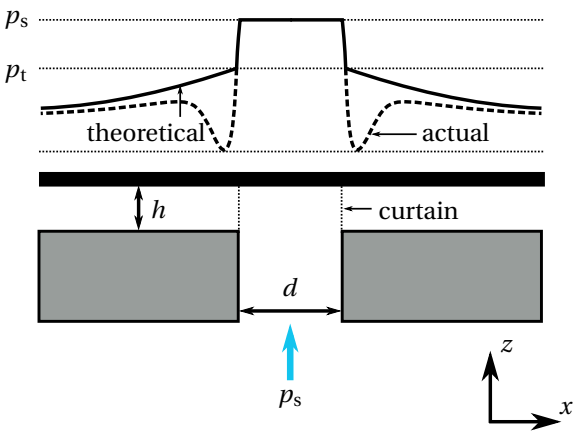

Figure 2.11: Schematic cross-section of an inherent orifice restriction and the corresponding pressure profile.

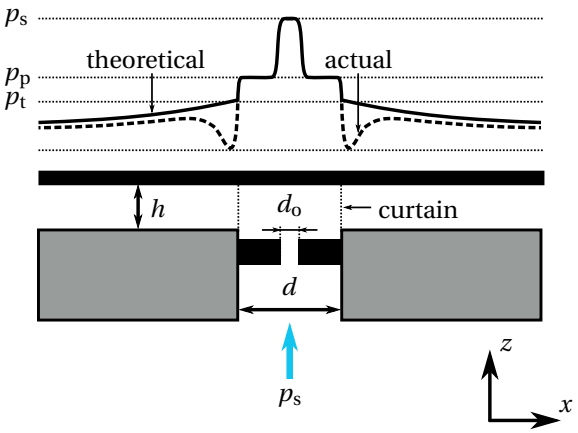

Figure 2.12: Schematic cross-section of a pocketed orifice restriction and the corresponding pressure profile.

There are two main types of orifice restrictions. They are both discussed in depth. Most of the theory is

taken from [42]. The first type is the inherent orifice restriction, which is also called an annular orifice. It is shown in Figure 2.11. These orifices are often realised by drilling a hole through the air bearing surface. The air flows through the orifice into the bearing film. The surface area which separates the orifice feed hole from the air bearing film is called the curtain. As the curtain area πdh is usually very small compared to the orifice feed area, it is the main flow restriction for this type of orifices. A typical pressure profile of the inherent orifice restriction is visualised above the schematic cross-section. Directly at the location of the orifice the pressure equals the feed pressure p_s. The air accelerates when it enters the air bearing film, which results in a reduced pressure. In theory, the static pressure is reduced to the throat pressure p_t. From there, the pressure reduces smoothly due to viscous pressure losses. The theoretical pressure profile can be seen in Figure 2.11 as well. In practice, the pressure drop at the entrance of the bearing film is larger, as a consequence of dynamic effects. A vena contracta occurs when the air enters the bearing film: the area of the air flow is at its minimum, which is smaller than the curtain area. The air velocity is at its maximum, resulting in a static pressure drop. As the flow continues, the air recovers some of its dynamic pressure. Assuming the expansion of the gas to be an isentropic process, the mass flow through the inherent orifice is given by:

$$\dot{m} = \begin{cases} C_d A p_s \sqrt{\frac{\kappa}{\kappa-1}\left[\left(\frac{p_t}{p_s}\right)^{2/\kappa} - \left(\frac{p_t}{p_s}\right)^{(\kappa+1)/\kappa}\right]\frac{2}{R_s T}}, & \text{if } \frac{p_t}{p_s} \geq \left(\frac{2}{\kappa+1}\right)^{\frac{\kappa}{\kappa-1}} \\ C_d A p_s \sqrt{\left(\frac{2}{\kappa+1}\right)^{2/(\kappa-1)}\left(\frac{\kappa}{\kappa+1}\right)\frac{2}{R_s T}}, & \text{if } \frac{p_t}{p_s} < \left(\frac{2}{\kappa+1}\right)^{\frac{\kappa}{\kappa-1}} \end{cases} \tag{2.17}$$

The mass flow depends on the curtain area A, the supply pressure p_s, the pressure ratio (p_t/p_s), the specific gas constant for dry air R_s, and the absolute temperature T. If the pressure ratio (p_t/p_s) is larger than or equal to the critical pressure ratio of 0.528, the mass flow is governed by the square root term. The critical pressure ratio depends on the specific heat ratio of air. If the pressure ratio is smaller than the critical pressure ratio, the flow becomes choked and the mass flow increases linearly with the upstream pressure p_s. Choked conditions in the flow of air though an orifice occur when the reduction in diameter causes the flow to accelerate to a maximum: it reaches supersonic velocity. Further reduction of the diameter will not allow the air to accelerate any further, so the flow becomes choked. The discharge coefficient C_d is a number between 0 and 1 and accounts for the vena contracta effect at the entrance to the bearing film and effects such as the sharpness of corners which the flow passes. A typical value for C_d is 0.8 [42].

The second type of orifice restrictions is the pocketed orifice, which is formed by recessing the area around the orifice, shown in Figure 2.12. Pocketed orifices are often realised by inserted jewels into a drilled hole. The jewels, which are used in watches and clocks, have well-defined holes in the centre. The recess results in a larger area where the pressure is equal to the inlet pressure. In comparison with inherent orifices, pocketed orifices have the advantage of a higher load capacity and stiffness. However, the recess also increases the chance on dynamic instabilities. This is explained in Section 2.6. A typical pressure profile is shown above the schematic cross-section in Figure 2.12. The air flows through the orifice, which is the main flow restriction. The acceleration of the air flow results in a pressure reduction from the feed pressure p_s to the pocket pressure p_p. When the air enters the bearing film, the pressure is reduced a bit more to the throat pressure p_t, due to the flow restriction of the curtain. In reality, a large pressure drop can be noticed at the location of the curtain, as a vena contracta occurs. The air recovers some of its dynamic pressure as it flows further into the bearing film. The theoretical mass flow can be expressed as follows:

$$\dot{m} = \begin{cases} \frac{C_d A p_s}{\sqrt{1+\delta_L^2}} \sqrt{\frac{\kappa}{\kappa-1}\left[\left(\frac{p_p}{p_s}\right)^{2/\kappa} - \left(\frac{p_p}{p_s}\right)^{(\kappa+1)/\kappa}\right]\frac{2}{R_s T}}, & \text{if } \frac{p_p}{p_s} \geq \left(\frac{2}{\kappa+1}\right)^{\frac{\kappa}{\kappa-1}} \\ \frac{C_d A p_s}{\sqrt{1+\delta_L^2}} \sqrt{\left(\frac{2}{\kappa+1}\right)^{2/(\kappa-1)}\left(\frac{\kappa}{\kappa+1}\right)\frac{2}{R_s T}}, & \text{if } \frac{p_p}{p_s} < \left(\frac{2}{\kappa+1}\right)^{\frac{\kappa}{\kappa-1}} \end{cases} \tag{2.18}$$

The mass flow equations differ slightly from the mass flow equations for the inherent orifice. The area A is in this case equal to the orifice hole area: $\frac{\pi}{4} d_0^2$. The inherent compensation factor δ_L is calculated in the following way:

$$\delta_L = \frac{d_0^2}{4dh} \tag{2.19}$$

It accounts for the effect of the resistances (orifice restriction and curtain restriction) in series. The mass flow equation is based on the pressure ratio between the feed pressure p_s and the pocket pressure p_p. As said

before, the pocketed orifice has a higher bearing stiffness than the inherent orifice, up to a factor of 1.5 [42].

2.6. Dynamic Analysis

In the previous sections, the static stiffness of a thin film of air has been determined for both the passive and active cell. In reality, the stiffness and damping of an air film are frequency dependent. A dynamic analysis is performed to determine the stiffness and damping of a thin film of air when subjected to a sinusoidal squeeze motion: a change of fly height in time. This is done by a linear perturbation technique in which the squeeze motion around the static solution of the Reynolds equation is studied. The dynamic analysis is then extended to check the influence of volumes on the dynamic stability. The volumes are located downstream the inlet restrictions. The dynamic analysis is performed on the passive cell, which can be seen in Figure 2.13. The inlet and outlet are positioned at a distance $L/2$, as a result of the optimisation in Section 2.2.1.

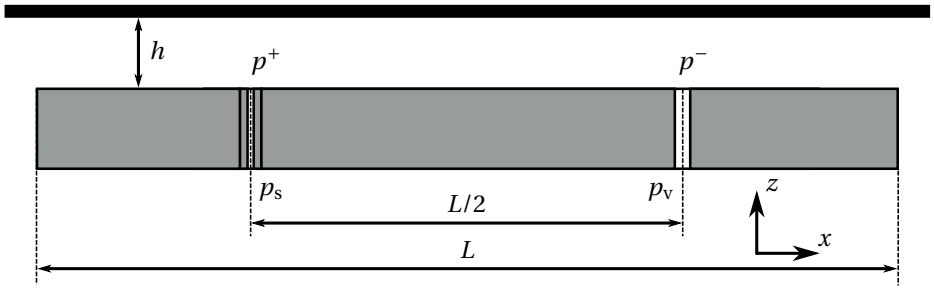

Figure 2.13: Passive cell for dynamic analysis.

2.6.1. Perturbed Reynolds Equation

The dynamic analysis is performed by perturbing the Reynolds equation. The perturbation technique is explained step by step. The static solution of the Reynolds equation is perturbed by a real and imaginary sinusoidal signal with a small amplitude. The static fly height h_0 is perturbed with a perturbation signal δh, leading to a small perturbation in the pressure:

$$\begin{aligned} h &= h_0 + \delta h(t),\ \delta h(t) = \tilde{h} e^{j\omega t} \\ p &= p_0 + \delta p(t),\ \delta p(t) = \tilde{p} e^{j\omega t} \end{aligned} \tag{2.20}$$

In these equations, the complex parameter j is equal to $\sqrt{-1}$. The perturbation signal δh and change in pressure δp are characterised by the amplitude of $\tilde{h}$ and $\tilde{p}$, respectively, and the frequency ω. The perturbed load capacity δW is found by integrating the real part of the perturbed pressure over the area of the cell. The stiffness can then be calculated:

$$k(\omega) = -\frac{\partial W}{\partial h} \approx -\frac{\delta W - W_0}{(h_0 - \delta h) - h_0} = -\frac{\int \Re\left(\tilde{p}\right) \mathrm{d}A}{\tilde{h}} \tag{2.21}$$

In this equation, W_0 is the unperturbed load capacity, which is equal to zero as the zero load condition applies. The damping is defined as the negative change of load with velocity, resulting in:

$$c(\omega) = -\frac{\partial W}{\partial \dot{h}} \approx -\frac{\delta W - W_0}{\left(\dot{h}_0 - \delta \dot{h}\right) - \dot{h}_0} = -\frac{\int \Im\left(\tilde{p}\right) \mathrm{d}A}{\omega \tilde{h}} \tag{2.22}$$

The damping can therefore be found by integrating the imaginary part of the perturbed pressure and dividing by the frequency and the fly height perturbation. Both stiffness and damping are frequency dependent, because the perturbed pressure is dependent on the frequency. Qualitative behaviour about the frequency dependent damping and stiffness is given by Al-Bender [4]:

- $c(\omega = 0)$ may be either positive (stable) or negative (unstable),

- $c(\omega = 0) > 0 \Leftrightarrow k$ is increasing and c is decreasing for increasing ω,
- $c(\omega = 0) < 0 \Leftrightarrow k$ is decreasing and c is increasing for increasing ω.
- $\lim_{\omega \to \infty} c(\omega) = 0$

If the damping starts at a positive value, it remains positive for all frequencies until it reduces to zero at infinite frequency. The stiffness increases for increasing frequency and settles at a certain stiffness for infinite frequency. If the static damping is negative, it increases to a positive value before decreasing to zero. The corresponding stiffness decreases for increasing frequency and settles at a certain stiffness for infinite frequency as well. The damping of the thin film of air will always approach zero for infinite frequency.

The time dependent Reynolds equation is perturbed with the perturbation signals. The time dependent Reynolds equation in one dimension is taken from Equation B.15. The sliding velocity of the bounding surfaces of the thin film of air are assumed to be negligibly small and therefore Couette flow is neglected. The equation can be written as:

$$-\frac{\partial}{\partial x}\left(\frac{ph^3}{12\eta R_s T}\frac{\partial p}{\partial x}\right)+\frac{\partial}{\partial t}\left(\frac{ph}{R_s T}\right)=0 \tag{2.23}$$

In this equation, the pressure p and the fly height h are a function of time. Both variables are perturbed with the perturbation signals from Equation 2.20, resulting in:

$$-\frac{1}{12\eta R_s T}\frac{\partial}{\partial x}\left[\left(p_0+\delta p\right)\left(h_0+\delta h\right)^3\frac{\partial}{\partial x}\left(p_0+\delta p\right)\right]+\frac{1}{R_s T}\frac{\partial}{\partial t}\left[\left(p_0+\delta p\right)\left(h_0+\delta h\right)\right]=0 \tag{2.24}$$

The higher terms in δ, like $\delta p \delta h$, are assumed to be negligibly small and can therefore be neglected. The complete equation can then be written as:

$$\begin{aligned}-\frac{1}{12\eta R_s T}\frac{\partial}{\partial x}\left(p_0 h_0^3\frac{\partial}{\partial x}p_0+p_0 h_0^3 e^{j\omega t}\frac{\partial}{\partial x}\tilde{p}+\tilde{p}h_0^3 e^{j\omega t}\frac{\partial}{\partial x}p_0+3p_0 h_0^2\tilde{h}e^{j\omega t}\frac{\partial}{\partial x}p_0\right)\\ +\frac{1}{R_s T}j\omega p_0\tilde{h}e^{j\omega t}+\frac{1}{R_s T}j\omega h_0\tilde{p}e^{j\omega t}=0\end{aligned} \tag{2.25}$$

The first part in brackets, $p_0 h_0^3 \nabla p_0$, describes the static solution and is equal to zero, as can be seen in Equation 2.1. Therefore, it can be removed from the equation. Both sides of the equations are multiplied by $e^{-j\omega t}$, such that the $e^{j\omega t}$ terms can be removed as well. The final equation is the perturbed Reynolds equation:

$$-\frac{1}{12\eta R_s T}\frac{\partial}{\partial x}\left(p_0 h_0^3\frac{\partial}{\partial x}\tilde{p}+\tilde{p}h_0^3\frac{\partial}{\partial x}p_0+3p_0 h_0^2\tilde{h}\frac{\partial}{\partial x}p_0\right)+\frac{1}{R_s T}j\omega\left(p_0\tilde{h}+h_0\tilde{p}\right)=0 \tag{2.26}$$

The perturbed Reynolds equation describes the change in pressure for a small deviation of the fly height. It contains the static solution, characterised by the 0 subscripts, and the perturbed solution. First, the static solution is solved, which is then substituted in the perturbed equation, such that the perturbed solution can be solved. The orifice mass flow equations are also perturbed. The mass flow equations are taken from Section 2.5. It is assumed that the pocket diameter is relatively large compared to the orifice diameter and fly height, resulting in a small inherent compensation factor δ_L, which is therefore neglected:

$$\begin{aligned}\text{inlet: } \dot{m}_i &= \begin{cases} C_{d,i}A_i p_s\sqrt{\frac{\kappa}{\kappa-1}\left[\left(\frac{p}{p_s}\right)^{2/\kappa}-\left(\frac{p}{p_s}\right)^{(\kappa+1)/\kappa}\right]\frac{2}{R_s T}}, & \text{if } \frac{p}{p_s}\geq\left(\frac{2}{\kappa+1}\right)^{\frac{\kappa}{\kappa-1}} \\ C_{d,i}A_i p_s\sqrt{\left(\frac{2}{\kappa+1}\right)^{2/(\kappa-1)}\left(\frac{\kappa}{\kappa+1}\right)\frac{2}{R_s T}}, & \text{if } \frac{p}{p_s}<\left(\frac{2}{\kappa+1}\right)^{\frac{\kappa}{\kappa-1}}\end{cases} \\ \text{outlet: } \dot{m}_o &= \begin{cases} C_{d,o}A_o p\sqrt{\frac{\kappa}{\kappa-1}\left[\left(\frac{p_v}{p}\right)^{2/\kappa}-\left(\frac{p_v}{p}\right)^{(\kappa+1)/\kappa}\right]\frac{2}{R_s T}}, & \text{if } \frac{p_v}{p}\geq\left(\frac{2}{\kappa+1}\right)^{\frac{\kappa}{\kappa-1}} \\ C_{d,o}A_o p\sqrt{\left(\frac{2}{\kappa+1}\right)^{2/(\kappa-1)}\left(\frac{\kappa}{\kappa+1}\right)\frac{2}{R_s T}}, & \text{if } \frac{p_v}{p}<\left(\frac{2}{\kappa+1}\right)^{\frac{\kappa}{\kappa-1}}\end{cases}\end{aligned} \tag{2.27}$$

In the equation, the pressure p is the pressure in the thin film, downstream the inlet restriction and upstream the outlet restriction. In the following equations, the inlet and outlet can be distinguished by the i

and *o* subscript, respectively. The perturbed variant of these mass flow equations are inconvenient to process because of the square roots. Therefore, the equation is linearised around the pressure p which is found in the static analysis. This is only done in the perturbed analysis and can be justified because the perturbation signals $\tilde{p}$ and $\tilde{h}$ are small compared to the static solution. The linearised mass flow equations are:

$$\begin{aligned} \dot{m}_{\mathrm{i,lin}} &= \left.\frac{\partial \dot{m}_{\mathrm{i}}}{\partial p}\right|_{\mathrm{p_{0,i}}} \left(p - p_{0,\mathrm{i}}\right) + \left.\dot{m}_{\mathrm{i}}\right|_{\mathrm{p_{0,i}}} \\ \dot{m}_{\mathrm{o,lin}} &= \left.\frac{\partial \dot{m}_{\mathrm{o}}}{\partial p}\right|_{\mathrm{p_{0,o}}} \left(p - p_{0,\mathrm{o}}\right) + \left.\dot{m}_{\mathrm{o}}\right|_{\mathrm{p_{0,o}}} \end{aligned} \tag{2.28}$$

The derivatives $\left.\frac{\partial \dot{m}_{\mathrm{i}}}{\partial p}\right|_{\mathrm{p_{0,i}}}$ and $\left.\frac{\partial \dot{m}_{\mathrm{o}}}{\partial p}\right|_{\mathrm{p_{0,o}}}$ are determined analytically and evaluated at the pressures in the thin film which are found in the static analysis. This is done at the location of the inlet and the outlet, respectively. The linearised mass flow equations are perturbed with the perturbations from Equation 2.20, resulting in:

$$\begin{aligned} \dot{m}_{\mathrm{i,lin}} &= \left.\frac{\partial \dot{m}_{\mathrm{i}}}{\partial p}\right|_{\mathrm{p_{0,i}}} \left(p_0 + \tilde{p}e^{j\omega t} - p_{0,\mathrm{i}}\right) + \left.\dot{m}_{\mathrm{i}}\right|_{\mathrm{p_{0,i}}} \\ \dot{m}_{\mathrm{o,lin}} &= \left.\frac{\partial \dot{m}_{\mathrm{o}}}{\partial p}\right|_{\mathrm{p_{0,o}}} \left(p_0 + \tilde{p}e^{j\omega t} - p_{0,\mathrm{o}}\right) + \left.\dot{m}_{\mathrm{o}}\right|_{\mathrm{p_{0,o}}} \end{aligned} \tag{2.29}$$

The static solution can be removed, as this is done in the perturbed Reynolds equation as well. The remaining part is multiplied by $e^{-j\omega t}$, such that the $e^{j\omega t}$ terms can be removed as well. The final perturbed mass flow equations for the inlets and outlet are:

$$\begin{aligned} \dot{m}_{\mathrm{i,lin}} &= \left.\frac{\partial \dot{m}_{\mathrm{i}}}{\partial p}\right|_{\mathrm{p_{0,i}}} \tilde{p} \\ \dot{m}_{\mathrm{o,lin}} &= \left.\frac{\partial \dot{m}_{\mathrm{o}}}{\partial p}\right|_{\mathrm{p_{0,o}}} \tilde{p} \end{aligned} \tag{2.30}$$

2.6.2. Solving the Perturbed Reynolds Equation

The perturbed Reynolds equation is solved by using the finite element package COMSOL Multiphysics™ [2]. The static solution is first calculated, which is then used in the perturbed Reynolds equation to calculate the perturbed solution. The passive cell is modelled with periodic boundary conditions. It has length L of 10 mm. The vacuum pressure p_{v} is set at 0.7 bar and the fly height h is equal to 10 µm. The inlet and outlet are orifice restrictions with a diameter of 0.1 mm and 0.3 mm, respectively, and the discharge coefficient for both restrictions is equal to 0.8. The perturbation on the height has a positive amplitude $\tilde{h}$ of 0.01 µm. The real and imaginary parts of the perturbed pressure are plotted in Figure 2.14. The top row represents the pressure profile when the frequency is equal to 1 Hz, while the pressure profiles in the bottom row are calculated for a frequency of 1×10^5 Hz. The graphs show clearly that the perturbed pressure varies with the frequency. Therefore, both stiffness and damping are frequency dependent. The values of the perturbed pressures are negative, because of the positive height perturbation. The small increase in height results in a small reduction in the film pressure.

The dynamic stiffness and damping of one cell are plotted in Figure 2.15 (solid lines). The dotted lines, representing the case with a volume downstream the inlet restriction, are discussed in the next subsection. The plots show the qualitative behaviour which has been discussed in the previous section. Up to a perturbation frequency of approximately 1×10^3 Hz the stiffness and damping are constant. For larger frequencies, the stiffness increases until it saturates at a constant value. The damping reduces to zero for increasing frequencies.

2.6.3. Pneumatic Hammer

Air bearing applications often make use of pocketed restrictions, because of their superior bearing stiffness over inherent orifices. The pocketed orifices, which have been discussed in Section 2.5, have a recess around the orifice, which is also called a pocket. The pocket should be designed carefully to prevent dynamic instabilities. Such a dynamic instability is called pneumatic hammer and it is a well known phenomena in air

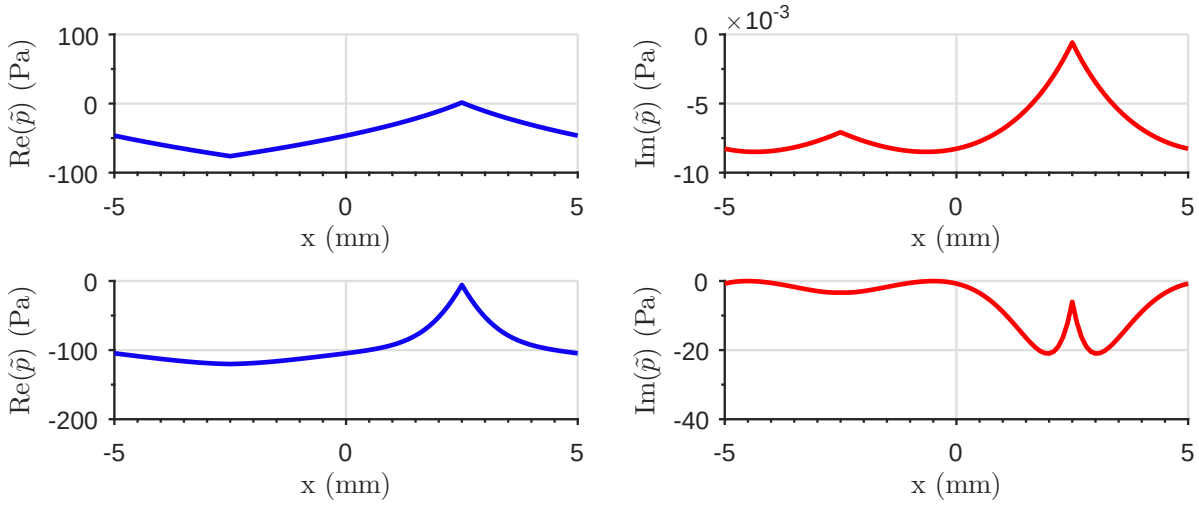

Figure 2.14: Dynamic pressure in the thin film at 1 Hz, top row, and 1×10^5 Hz, bottom row.

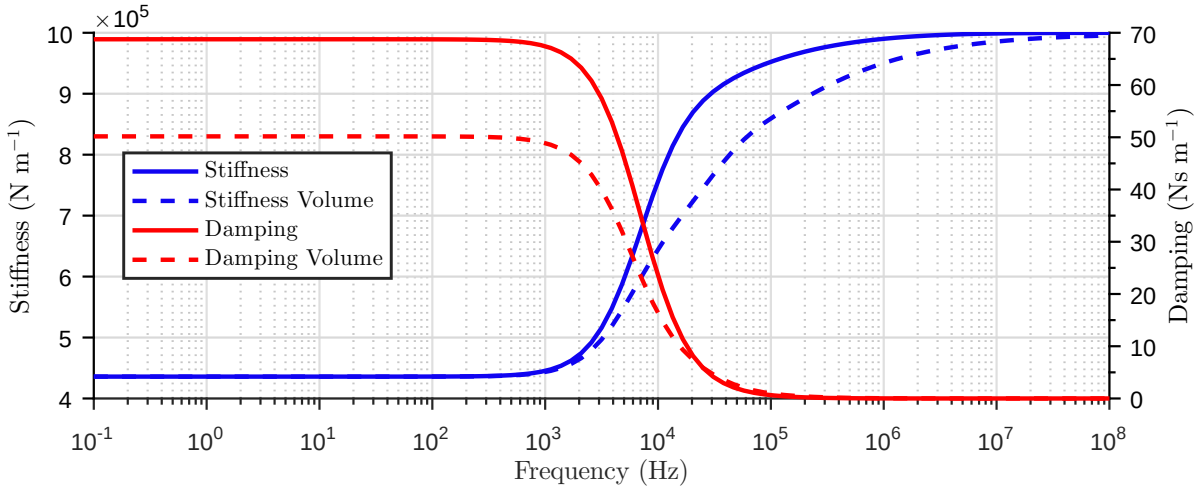

Figure 2.15: Dynamic stiffness and damping of one cell. The solid lines represent the variables without a volume and the dotted lines are calculated for a volume of $V = 0.45\,\text{mm}^3$.

bearing design. Pneumatic hammer is caused by the compressibility of air, which results in a time delay between changes in the fly height and the response to these changes through variations in the orifice pocket pressure. For example, if the fly height is decreased by some sort of perturbation, the pocket pressure will increase. This causes an increase in fly height, which results in a decreasing pocket pressure. Due to the decrease in pocket pressure the fly height reduces again. If the time delay is too long, overcompensation occurs and the system becomes unstable, resulting in a buzzing sound. The volumes provide the possibility of storing energy in the air film and releasing it in phase with the motion of the bearing system, leading to negative damping. A rule of thumb states that the pocket volume should be smaller than 1/20 of the volumes between the two bearing surfaces [42], in order to have a dynamically stable system. The influence of the volume of the pocketed orifice on the dynamic stability is investigated. This is done by adding the volume to the dynamic model. The orifice and the included volume V can be seen in Figure 2.16. In the worst case scenario, there is zero pressure drop over the volume, making it truly 'dead'. The mass balance over the volume of the pocket is:

$$V\frac{\partial \rho}{\partial t} = \dot{m}_{\text{i},1} - \dot{m}_{\text{i},2} \tag{2.31}$$

The mass flow $\dot{m}_{\text{i},1}$ is the flow through the orifice. The mass flow $\dot{m}_{\text{i},2}$ is the flow coming out of the volume, which is the actual flow entering the bearing film. Assuming constant temperature, the density can be written as $\rho = \frac{p}{R_s T}$:

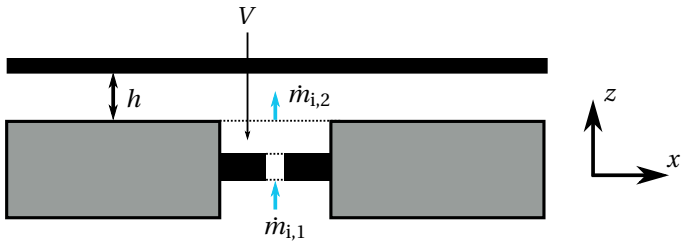

Figure 2.16: Modelling the mass flow through a pocketed orifice.

$$\frac{V}{R_s T}\frac{\partial p}{\partial t} = \dot{m}_{i,1} - \dot{m}_{i,2} \tag{2.32}$$

Similar to the previous perturbation technique, the mass flow through the orifice is linearised around the pressure at the inlet in the thin film. For the dynamic analysis, the perturbed pressure is substituted in the mass flow conservation equation:

$$\dot{m}_{i,2} = \left.\frac{\partial \dot{m}_i}{\partial p}\right|_{p_{0,i}} \left(p_0 + \tilde{p}e^{j\omega t} - p_{0,i}\right) + \dot{m}_i|_{p_{0,i}} - \frac{V}{R_s T}\frac{\partial\left(p_0 + \tilde{p}e^{j\omega t}\right)}{\partial t} \tag{2.33}$$

The static solution is removed as has been done before. The remaining part is multiplied by $e^{-j\omega t}$, which makes it possible to remove the $e^{j\omega t}$ terms. The resulting mass flow equations at the inlets are now equal to:

$$\dot{m}_{i,2} = \left.\frac{\partial \dot{m}_i}{\partial p}\right|_{p_{0,i}} \tilde{p} - \frac{V\tilde{p}}{R_s T} j\omega \tag{2.34}$$

The mass flow equation at the inlet of the system has been changed to the equation above. The dimensions of the passive cell are similar to the analysis in Section 2.6.2. Typical dimensions of the orifice jewels are outer dimensions in the range of 1.2 mm up to 2.2 mm[1]. As an example, the analysis is done with a 1.7 mm diameter pocket with a pocket depth of 0.2 mm, resulting in a volume of 0.45 mm^3. The influence of this volume on the dynamic behaviour of the cell can be seen in Figure 2.15. The damping at low frequencies is decreased. For increasing frequency it still reduces to zero. If the damping becomes negative, the system is unstable and pneumatic hammer will occur. Therefore, the volumes should not be too large. The stiffness shows the similar behaviour to the system without the volume for low frequencies, but the values start to differ from a frequency of about 1×10^3 Hz.

As said before, if the system is dynamically stable can be determined by analysing the damping. If the damping becomes negative, pneumatic hammer will occur. The damping of the system is influenced by the pressures, the bearing geometry, and the restrictions. To have a better understanding when the system becomes unstable, the damping is calculated when the pressure ratio between the feed pressure p_s and the pocket pressure p^+, and the volume of the pocket are both varied. The pressure ratio $\left(p^+/p_s\right)$ is a measure for the pressure drop over the inlet restriction. It is varied by varying the diameter of the orifice at the inlet. The other dimensions are fixed and are the same as in the previous analysis. It must be noted that the results do largely depend on the vacuum pressure and these results are calculated for a vacuum pressure of 0.7 bar. The results are shown in Figure 2.17. It can be seen that the system is more likely to become unstable if the pressure ratio is small, which means the pressure drop over the inlet restriction is large. For larger pressure ratios, the damping is positive and the system is stable. The dotted black line represents the rule of thumb, which states the system is stable if the pocket volume is less than 1/20 of the volume between the two bearing surfaces. For the case of a vacuum pressure of 0.7 bar, this seems to be a very good estimate. As the damping has a great dependency on the vacuum pressure, the analysis is done for multiple vacuum pressure Appendix E.1. From this extended analysis it can be concluded that the vacuum pressure has a negative influence on the dynamic stability of an air bearing. A decreasing vacuum pressure will result in a decreasing damping, which increases the chance of pneumatic hammer.

[1] http://www.swissjewel.com/2/orifice_jewels

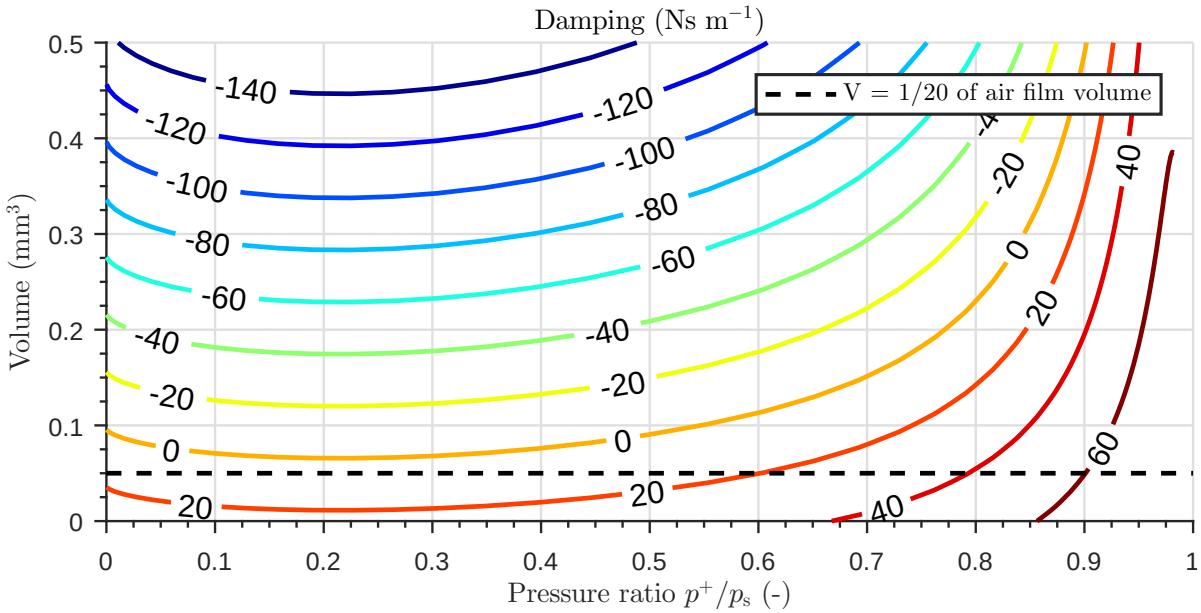

Figure 2.17: Damping as function of the pressure ratio (p^+/p_s) and the pocket volume. The dotted line represents the pocket volume of 1/20 of the volume between the two bearing surfaces.

The results of the study on pneumatic correspond with the analysis from Arghir [6] on journal bearings. He concludes that pneumatic hammer is less likely to happen if the orifice diameter is increased, resulting in a decrease in pressure drop over the restriction and a corresponding increase in pressure ratio (p^+/p_s).

2.7. Conclusion

In this chapter, the passive and active cell have been investigated analytically. The mass flow density, force density, and stiffness density of each cell have been determined and compared with each other. From the presented analysis, the optimal values for the parameters α and β can be obtained. The passive cell has a minimum mass flow density when α is equal to 0.5. The active cell has the highest performance ratio when α is equal to 0.72 and β is equal to 1.87. It is clear that for the same fly height, cell length and vacuum pressure a passive cell consumes less air than an active cell. Combining both in a transport demonstrator will reduce the total mass flow, compared to a transport demonstrator with only active cells. In general, the passive cell has a higher stiffness density than the active cell for the same fly height. As the geometries are fixed, the stiffness values should be matched by tuning the feed pressure, vacuum pressure or restrictions. The geometries have been studied using the incompressible flow and compressible flow assumption. For small pressure differences up to approximately 0.1 bar, the results for the incompressible and compressible flow match well. For larger pressure differences the incompressible flow results become inaccurate and the compressible flow model should be used. Lastly, a dynamic analysis has been performed on the passive cell to study the frequency dependent stiffness and damping of a thin film of air. The restrictions are chosen to be pocketed orifices, which results in a volume downstream the inlet restrictions. The influence of these volumes on the dynamic stability of the cell has been studied. Limiting the volumes to 1/20 of the volume between the bearing surfaces is a safe guide line for preventing pneumatic hammer. In general, the chance on pneumatic hammer can be reduced by increasing the orifice diameter or reducing the volume of the pockets.

3

General Conceptual Design

In this chapter, the conceptual design of the transport demonstrator is presented. A description of all the design steps can be found in the design overview in the next section. This is followed by the surface design, which is based on the tessellation of the surface. Different options are optimised and compared with each other. The last step is the design of the flow restrictions, after which the chapter ends with the surface matching and the design plan of the demonstrators.

3.1. Design Overview

The goal of this project is to develop a contactless air-based efficient transport demonstrator. The focus will be on a smooth transition of the wafer when travelling from the active surface to the passive surface or the other way around. Therefore, the demonstrator consists of one active surface and one passive surface. It should be able to actuate a 100 mm diameter silicon wafer by an acceleration of 1G and it should prove a smooth transition can be realised by matching the fly height and air film stiffness of both surfaces. A side-view of the conceptual design can be seen in Figure 3.1. The top view of the conceptual design is shown in Figure 3.2. The geometry of the cells in this figure is explained in Section 3.2.

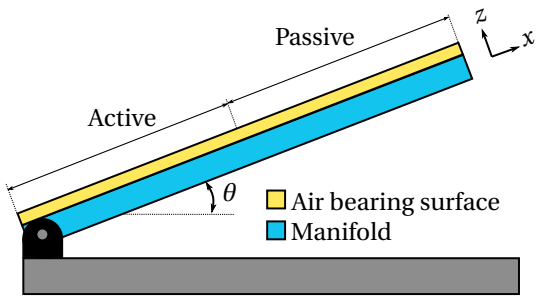

Figure 3.1: Side-view of the conceptual design. The wafer is not shown.

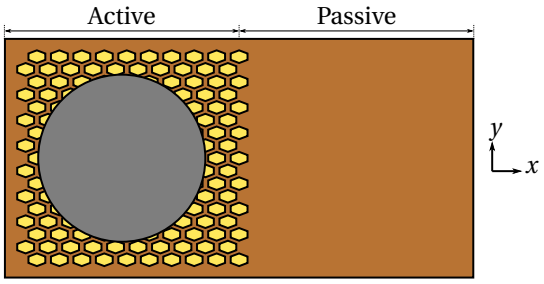

Figure 3.2: Top-view of the conceptual design. The wafer is shown on top of the active surface.

To exploit gravity, the bearing surfaces are placed at an angle θ. The actuator cells are designed in such a way that they can actuate in the positive x-direction, against gravity. When the actuator force is larger than the gravitational force the substrate will move in positive x-direction. However, by decreasing the pressure difference in the actuator cells, the gravitational force exceeds the actuator force and the substrate will move in negative x-direction. Besides the actuation in positive x-direction, which is the main transport direction, the actuator cells are to actuate in the positive and negative y-direction. In this way, the substrate is able to move in two degrees of freedom. In the neutral position, when the angle θ is equal to 0°, the demonstrator should be able to actuate the substrate by an acceleration of 1G. This means that the angle θ can be increased to 90°, for which angle the demonstrator is able to maintain the substrate at a certain position. At smaller angles, an actuation force is available to accelerate the substrate. The system is designed in a layer approached way. Each layer has its own function. The advantage of this design method is that the layers can be manufac-

tured separately. By stacking all the layers the complete functional system is realised. The following layers or functions can be identified.

1. Air bearing surface
The air bearing surface is the layer on which the wafer floats. It consists of an active surface, which is able to actuate the wafer, and a passive surface, which can only levitate the wafer. It can be seen in Figure 3.2 that the air bearing surface consists of cells. The choice for this cell geometry is discussed in detail in Section 3.2.

2. Restrictions
The restrictions are the inlets and outlets of the system and can be found all over the air bearing surface. The inlet restrictions are essential for having air bearing stiffness. In the demonstrator, the wafer will fly from the active surface to the passive surface and the other way around. This means that the cells of the active and passive are not always covered by the wafer, and part of the outlets are left open to ambient air. Therefore, the outlet restrictions must be designed in such a way that the air flow to the vacuum pump is limited.

3. Manifold
The last layer is the manifold, which consists of numerous holes and channels. They connect the feed pressure and vacuum pressure supplies to the correct inlets and outlets. It has been decided to manufacture the manifold out of laser-cut PMMA plates, which are bonded together with double sided tape. The reason behind this choice is explained in Chapter 5.

The total system is designed in several steps:

- The design process starts with the requirements and conceptual design from this section. The requirements have already been set in the introduction in Section 1.4.
- The next step in the design is to determine the surface design, which is done in Section 3.2. Similar to the 1D situation in Chapter 2 the surface consists of cells. Different cells, or geometries, for tiling the surfaces are compared with each other. The geometry of the cells of the active surface is chosen first. This geometry is used for the passive surface as well.
- The type of flow restrictions are chosen in Section 3.3. Based on the characteristics of the available vacuum pump, the outlet restrictions are designed. The next step is to develop a guide line for the dimensioning of the inlet restrictions. This is done by making a trade-off between the required feed pressure and the achievable air film stiffness. A high stiffness is preferred, because it compensates for the possible waviness of the air bearing surface. This is explained in Section 3.3.
- The last step of the conceptual design is the explanation of the design plan, which is based on the preceding sections.

3.2. Surface Design

In this section, the cells of the active and passive surfaces are designed. The principle of tiling a surface is explained first, after which different geometries are compared with each other. In the last step, the passive surface is designed.

3.2.1. Tessellation

The active and passive surface are divided in separate cells, similar to the 1D cells of Chapter 2. Each cell performs a levitation and an actuation function, which it should fulfil in an efficient way; the force over mass flow ratio should be as high as possible. Therefore, a study is done to find the best geometry to tile the surfaces. The tiling of a surface with polygons is called a tessellation. A tessellation can be performed with various polygons, but a few restrictions are made to increase the efficiency of the actuator surface:

1. The entire actuator surface should be tiled with actuator cells to make optimal use of the available space. This requirement is inherent to a tessellation.
2. To keep the actuator cells and the tessellation of the actuator surface simple it is preferred to use only one geometry, so no combinations of different geometries.

There are three geometries which can tile an entire surface using only this geometry. These are the triangle of Figure 3.3, the square of Figure 3.4 and the hexagon of Figure 3.5. More specifically, the figures show regular tessellation with congruent polygons. Regular means that the sides and angles of the polygon are equivalent and congruent means the polygons which are used for the tiling have the same size and shape. The tessellation can be specified with the Schäfli symbol $\{\mathbf{p},\mathbf{q}\}$ in which **p** indicates the type of polygon (**p**-gon) and **q** indicates the number of polygons coming together at one corner. The Schäfli symbol is written down below the figures. The tessellation is not restricted to be regular. Scaling in a certain direction is an option as well. This is discussed in Section 3.2.2.

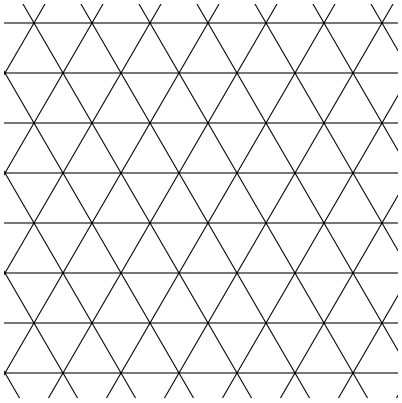

Figure 3.3: Regular tessellation with congruent triangles, Schäfli symbol $\{3,6\}$.

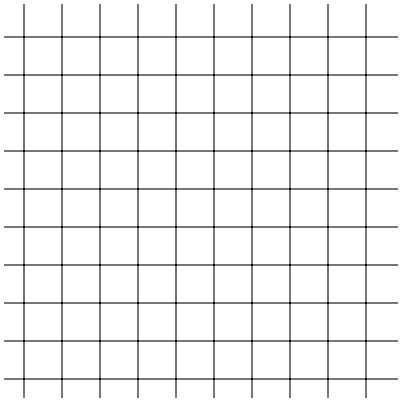

Figure 3.4: Regular tessellation with congruent rectangles, Schäfli symbol $\{4,4\}$.

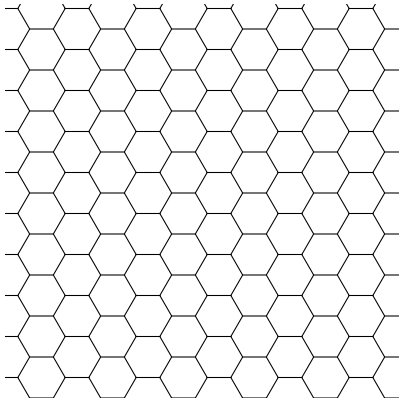

Figure 3.5: Regular tessellation with congruent hexagons, Schäfli symbol $\{6,3\}$.

From the three possible geometries to tile the surface the triangle is disregarded. Tiling an entire surface with only this geometry requires also the flipped version, as can be seen in the figure, and this is not preferred. The two other geometries, the rectangle and the hexagon, will be compared to each other in the next section.

3.2.2. Active Surface

The active surface is designed first. This is done in two optimisation rounds. In the first optimisation round, the geometries are optimised for a force in one degree of freedom. The insights from the first optimisation are used in the second optimisation, which is in two degrees of freedom.

Optimisation: 1-DoF

As a first step the two chosen geometries, namely the square and the hexagon, is optimised for the maximum force over mass flow ratio in one direction. In this optimisation the geometries are regular; the sides and angles of each geometry are equivalent. The geometries have one inlet and one outlet. There are three optimisation variables: α, β and γ. The first two variables are similar to the ones which have been used for the analytical optimisation in 1D. The variable α is a measure for the distance between the inlet- and the outlet groove, relative to the cell length and width, $0 < \alpha < 1$. The variable β is a measure for the fly height above the pocket, relative to the fly height above the dam, $\beta \geq 1$. It can be seen as a measure for the pocket depth. A new variable γ is introduced, $0 < \gamma < 1$. It is a measure for the inlet- and outlet groove length, relative to the distance between the inlet and outlets. The inlets and outlets themselves can either be positioned in the corners or on the edges. The square with the inlet and outlet on the edges and in the corners can be seen in Figure 3.6 and Figure 3.7, respectively. The hexagon with the inlet and outlet on the edges and in the corners can be seen in Figure 3.8 and Figure 3.9, respectively.

The optimisation is done in COMSOL in a dimensionless study using the incompressible flow model. The incompressible model is valid as long as the pressure difference in the thin film is small compared to ambient pressure, which is aimed for in the final design. The geometries occupy an area of 1, pressure inlets have a positive pressure of +1 and pressure outlets have a negative pressure of -1. The zero load condition is then automatically satisfied because of the regular tiling and the inlets and outlets, which have the same dimensions. The geometries are modelled with periodic boundary conditions, such that the surface design is similar to Figure 3.4 and 3.5. All geometries are optimised for the force over mass flow in the positive x-direction. The optimised variables can be seen in Table 3.1.

The variable α is approximately the same for each geometry type and lies around a value of 0.75. The variable β is varying around a value of 2. The variable γ is very small and approaches the lower boundary of

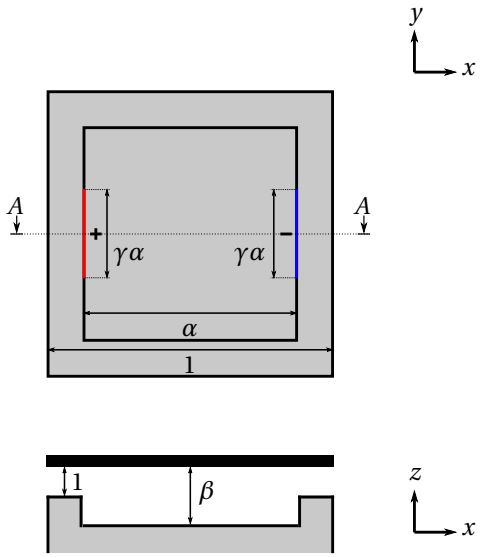

Figure 3.6: Square Edge optimisation with α, β and γ.

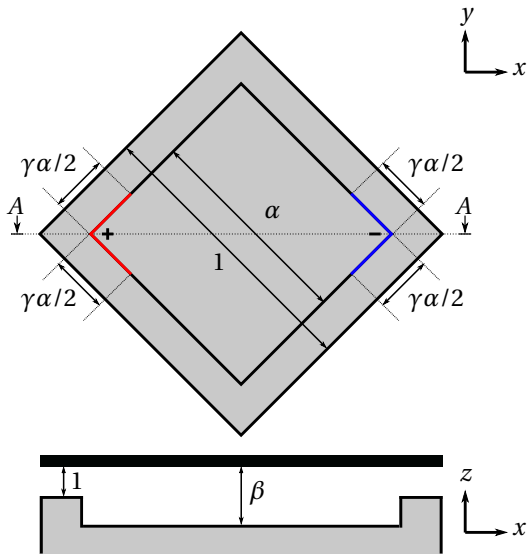

Figure 3.7: Square Corner optimisation with α, β and γ.

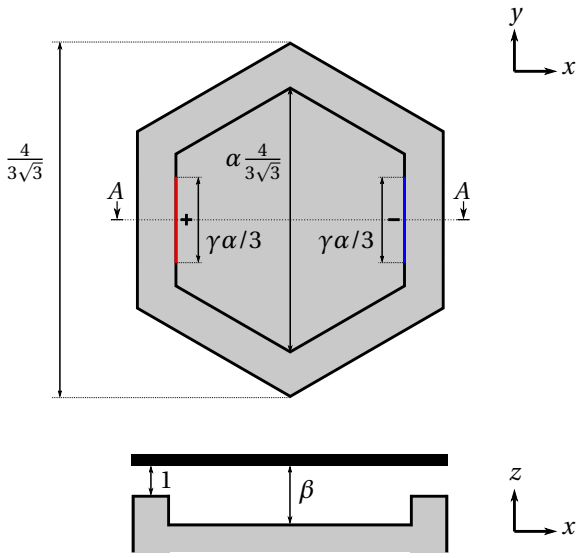

Figure 3.8: Hexagon Edge optimisation with α, β and γ.

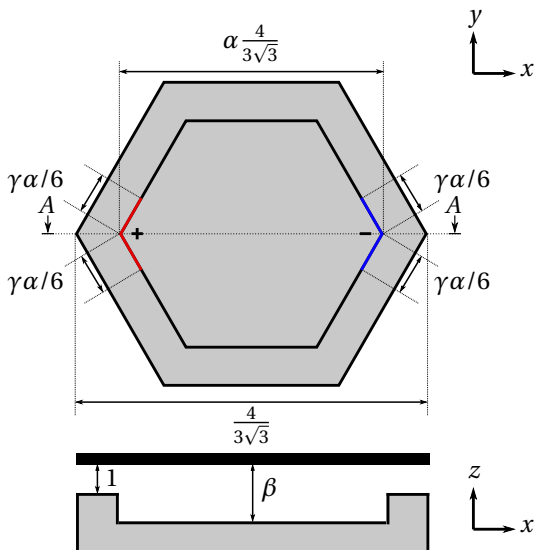

Figure 3.9: Hexagon Corner optimisation with α, β and γ.

0.01, which is set in the optimisation study. The optimisation of the different variables for the Square Edge is visualised in Figure 3.10. This figure shows the optimum for each variable when the two other variables are fixed at the optimisation values from Table 3.1. The optimisation curves of the variables α and β show a clear optimum and the performance ratio decreases rapidly for other values. The influence of γ is considerably less. Nonetheless, it can be concluded that for an optimal performance ratio this variable is as small as possible. The pressure distribution in the Square Edge is visualized in Figure 3.11. It shows two pressure peaks; a positive peak of pressure 1 at the inlet and a negative peak of pressure -1 at the outlet. From the different configurations the square diagonal performs best, followed by the hexagon diagonal. The optimal location for the inlets and outlets is in the corners of the different geometries.

Optimisation: 2-DoF

The first optimisation has given insight in the relevant parameters for a high performance ratio. However, the optimisation has been performed for geometries which are only able to actuate in one DoF. A second optimisation is done in which the geometries are altered such they can actuate in two DoF. To be able to

	α	β	γ	$\overline{F_x}$	$\overline{\dot{m}}$	$\overline{F_x}/\overline{\dot{m}}$
Square Edge	0.74	1.92	0.017	0.18	0.46	0.40
Square Corner	0.76	2.11	0.020	0.20	0.41	0.49
Hexagon Edge	0.74	1.93	0.017	0.17	0.41	0.42
Hexagon Corner	0.75	2.03	0.024	0.17	0.38	0.45

Table 3.1: Optimisation of the different geometries.

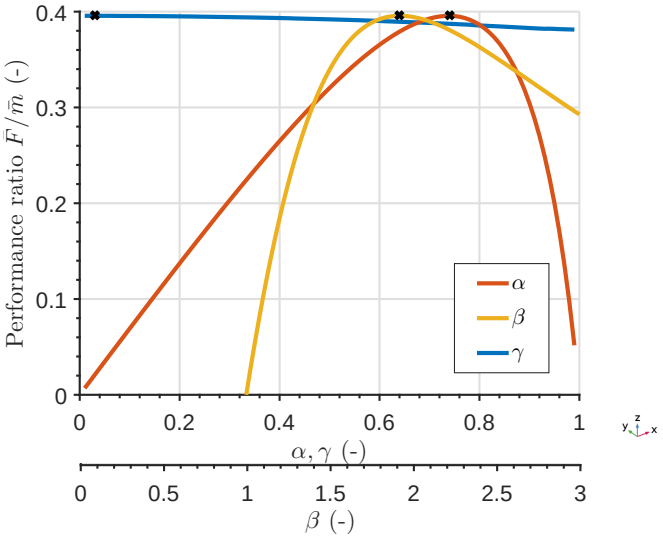

Figure 3.10: Optimisation of the performance ratio of the Square Edge for each variable apart. The two other variables are fixed at their optima.

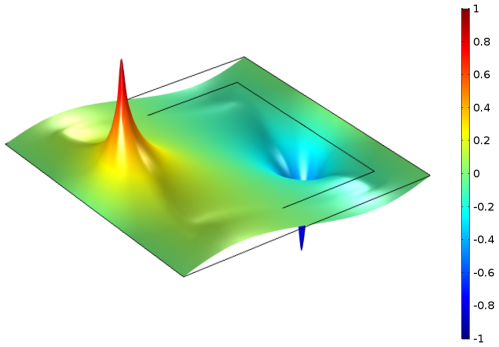

Figure 3.11: Pressure distribution in the Square Edge.

actuate in two DoF one extra inlet or outlet is needed. It makes sense to choose an extra inlet. The inlets and outlets are exposed to ambient air when they are not covered by the substrate. While extra outlets will increase the mass flow to the vacuum pump this is not an issue with an extra inlet. When the pressures at the inlets are different a force in y-direction is realised. The two inlets and one outlet are placed in the geometries, as shown in Figure 3.12-3.15. The variables and shape of the geometries are discussed later in this section. They are modelled as point inlets and outlets as a result of the previous optimisation, which has shown inlets and outlets should be as small as possible for the maximum performance ratio. The first two geometries are a variation on the Square Edge from Figure 3.6. The two inlets are positioned in the left bottom and upper corner, while the outlet can be found at the right edge. The hexagon in Figure 3.14 is a variation on the Hexagon Edge from Figure 3.8 while the hexagon in Figure 3.15 is a variation on the Hexagon Corner from Figure 3.9.

In the first optimisation, the geometries have been tiled using a regular tessellation: the sides and angles of the geometries are equivalent. This is not a fixed requirement and it could be beneficial to stretch the geometries in a certain direction. The performance ratio is defined as the force density over the mass flow density. Looking back at Equation 2.13 of the incompressible analysis in Section 2.3.1, the performance ratio can be written as:

$$\frac{\bar{F}}{\dot{\bar{m}}} = \frac{R_g T}{p_a} \frac{6\eta L}{h^2} \frac{\beta - 1}{\frac{1}{1-\alpha} + \frac{\beta^3}{\alpha}} \tag{3.1}$$

It can be seen that the performance ratio increases when the actuator cell is stretched in the direction of actuation, hereby increasing the actuator length L. This is due to the fact that the force density scales with a factor $1/L$ while the mass flow density scales with a factor $1/L^2$. A new optimisation variable δ is introduced, $\delta > 0$. The geometries are scaled with a factor δ in x-direction and a factor $1/\delta$ in y-direction, hereby preserving the surface area of 1. The scaling is visualised in Figure 3.16. The name of the rectangular geometries is changed to rectangle as they do not have a square shape any more.

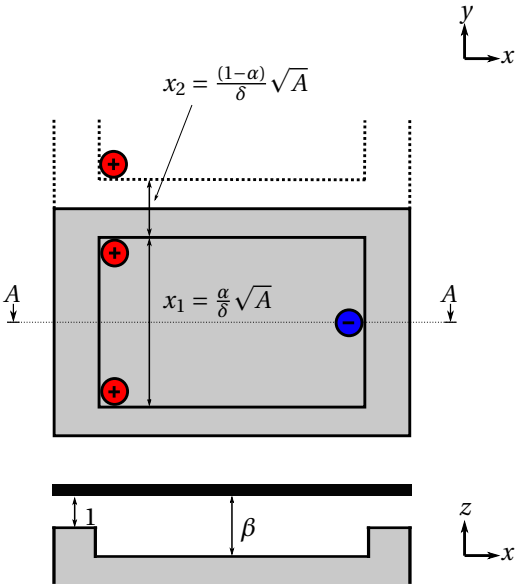

Figure 3.12: Rectangle 1 optimisation for the variables α, β and δ.

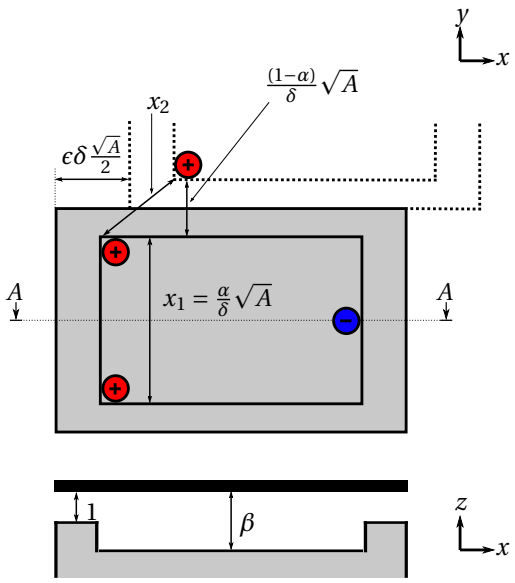

Figure 3.13: Rectangle 2 optimisation for the variables α, β and δ.

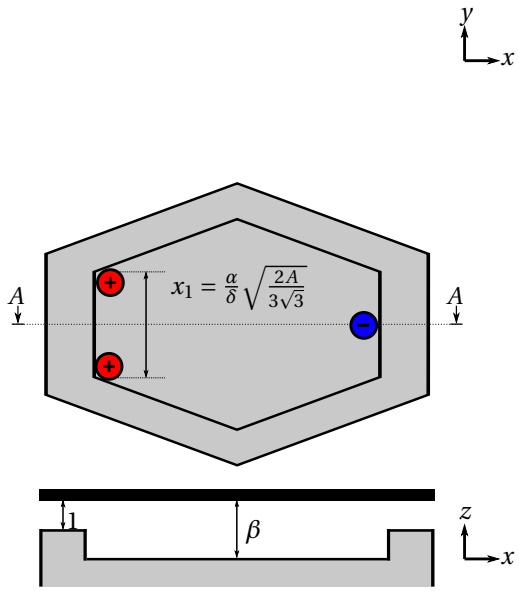

Figure 3.14: Hexagon 1 optimisation for the variables α, β and δ.

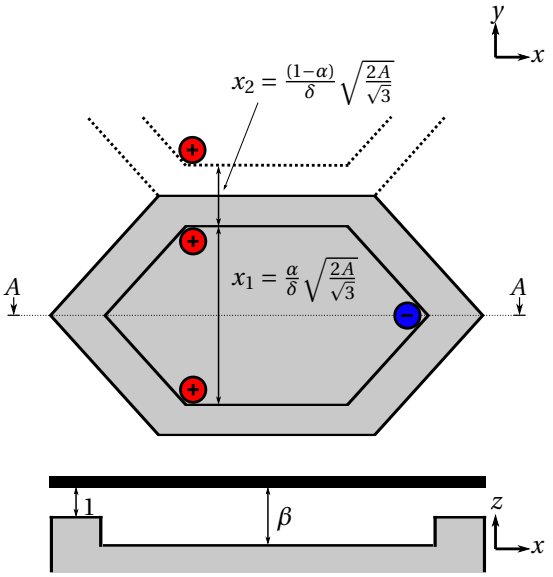

Figure 3.15: Hexagon 2 optimisation for the variables α, β and δ.

In theory, the variable δ is infinitely large, but in practice it is limited by the distance between the inlets for the manufacturability of the manifold and the force in y-direction. Both are discussed in more depth.

Manufacturability

The manifold is the structure beneath the actuator surface and connects the feed pressure and vacuum pressure supplies to the inlets and outlets. The manifold is made out of laser-cut PMMA plates, which are bonded together with double sided tape. The tape is also used to bond the manifold to the air bearing surface. Between the different channels and holes, the tape should be wide enough to prevent leakage. Initial manifold experiments in Appendix G have shown that features should be separated from each other by at least 1.5 mm. The channels and holes in the manifold are dimensioned to have a width/diameter of 2 mm. Therefore, the distance between the inlets should be at least 3.5 mm. This

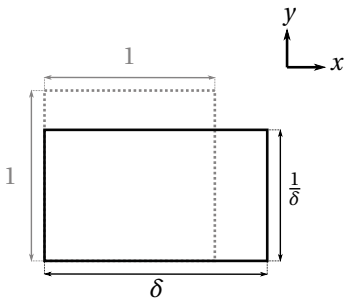

Figure 3.16: The geometries are stretched by a factor δ in x-direction and a factor $1/\delta$ in y-direction.

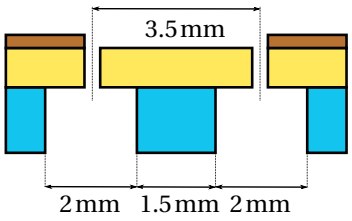

Figure 3.17: Cross-section of a small segment of the manifold (blue) and air bearing surface (yellow/brown). Double-sided tape bonds the manifold and air bearing surface. The inlets should be positioned at least 3.5 mm from each other.

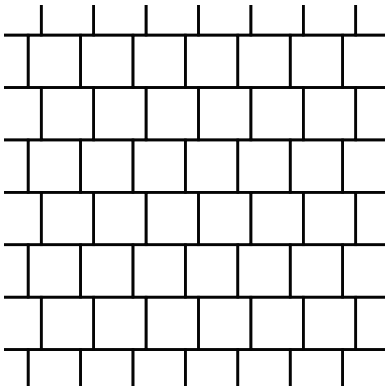

Figure 3.18: The squares or rectangles can also form a tessellation when they are tiled with an off-set with respect to each other.

is visualized schematically in Figure 3.17. Until now, the geometries have been dimensionless. The surface area should be known to find the limit for δ. The surface area is chosen to be 100 mm^2, which is a typical cell area in previous demonstrators [51][49][48]. It means a 100 mm diameter wafer could theoretically cover 78 cells. The variable δ can now be linked to the shortest distance between two inlets. This can be seen in Figure 3.12-3.15. The distance x_1 is a measure for two inlets in the same cell, while the distance x_2 is the distance between two inlets of adjacent cells. For each geometry the critical dimension is determined, along with the corresponding value of δ. For the first geometry, Rectangle 1, the critical dimension is x_2, as indicated in Figure 3.12. The variable δ can be maximum 0.71, which means a contraction instead of a stretch in the direction of actuation. Therefore, another approach for tiling the rectangles is suggested. Instead of the conventional way of tiling, the rectangles could also be tiled with an offset, which is visualised in Figure 3.18. In this way, the rectangles can be stretched in the direction of actuation because the distance between the inlets is increased. A new optimisation variable ϵ is introduced, which can be seen in Figure 3.13. It is a measure for the rectangle shift. Shifting the rectangles with respect to each other is not beneficial for the performance ratio as the pressure distributions of different actuator cells influence each other. An optimum should be found between increasing the performance by the increase of δ, and decreasing the performance by the rectangle shift, as a function of ϵ. It turns out an optimum is reached when x_1 and x_2 are both equal to the critical distance between inlets, which is 3.5 mm. This is the case when δ is equal to 2.14 and ϵ is equal to 0.31. The critical dimension for Hexagon 1 is the distance x_1, which can be seen in Figure 3.14. The maximum value of δ is equal to 1.33. For the last geometry, Hexagon 2 in Figure 3.15, x_2 is the critical dimension, similar to Rectangle 1. The variable δ has a maximum of 0.77, which means this geometry is contracted in the direction of actuation as well, similar to Rectangle 1.

Force in y-direction

The force in y-direction is of less importance than the force in x-direction, which is the transport direction. This is also why all the geometries are optimised for a high performance ratio in x-direction. The aim is to have a performance ratio in y-direction of at least 20% of the performance ratio in x-direction. The geometries are scaled with δ in x-direction and with $1/\delta$ in y-direction, resulting in a decreasing performance ratio in y-direction for an increasing δ. The maximum value of δ is found by the combination of two models. In the first model the performance ratio in x-direction is calculated. The inlet pressures are equal to +0.5. Because the geometries are no longer regular, due to the stretching by a factor δ, the models are solved for satisfying the zero load condition, which results in a certain outlet pressure. In the second model the performance ratio in y-direction is calculated. Only one inlet is used, with a pressure of +0.5. The outlet pressure is found by satisfying the zero load condition again. In both models the variables α, β and ϵ are approximated as respectively 0.75, 2 and 0.31, as taken from the previous optimisation in Section 3.2.2.

All the limits on δ for both the minimal distance between inlets and the performance in y-direction are

listed in Table 3.2. The critical values have been highlighted. It can be seen that the limits on the variable δ are determined by the distance between the inlets for Rectangle 1 and Hexagon 2, and by the minimum force in y-direction for Rectangle 2 and Hexagon 1.

	Distance inlets	$\overline{F_y}/\overline{\dot{m}_y} \geq 20\%$ of $\overline{F_x}/\overline{\dot{m}_x}$
Rectangle 1	0.71	1.49
Rectangle 2	2.14	1.56
Hexagon 1	1.33	1.22
Hexagon 2	0.77	3.21

Table 3.2: Limits on the variable δ. The minimum δ for each geometry is highlighted.

In the second optimisation round for two DoF geometries, the cells from Figure 3.12-3.15 are optimised for the variables α and β. Similar to the first optimisation variable α is the measure for the inlet-outlet distance and the dam width, and variable β is a measure for the pocket depth. The variable δ is taken from Table 3.2; for each geometry the minimum δ is selected. The variable ϵ for Rectangle 2 is equal to 0.31. In this optimisation the pressures at the two inlets are equal to +0.5 and the pressure at the outlet is found by satisfying the zero load condition.

	α	β	δ	ϵ	$\overline{F_x}$	$\overline{\dot{m}}$	$\overline{F_x}/\overline{\dot{m}}$	p^-	$\overline{F_y}/\overline{\dot{m}}$	%
Rectangle 1	0.74	2.01	0.71	-	0.088	0.34	0.26	−0.66	0.25	96
Rectangle 2	0.73	2.16	1.56	0.31	0.15	0.28	0.52	−0.59	0.11	21
Hexagon 1	0.74	2.08	1.22	-	0.12	0.26	0.45	−0.68	0.09	20
Hexagon 2	0.74	1.94	1.07	-	0.07	0.26	0.28	−0.87	0.21	75

Table 3.3: Optimisation of the different configurations. The last column shows the percentage of the performance ratio in y-direction compared to the performance ratio in x-direction. All numbers are dimensionless.

The results of the optimisation can be seen in Table 3.3. The values for α and β are similar to before, around a value of 0.75 and 2, respectively. The small differences with the first optimisation round can be explained by the different modelling of the inlets and outlets (point inlets and outlets instead of grooves) and the influence of the extra inlet on the pressure distribution. The table shows the force density, mass flow and the outlet pressure for satisfying the zero load condition. But most importantly, it shows the performance ratio in x-direction and the performance ratio in y-direction, which is more than 20% of the performance ratio in x-direction for all geometries. The performance ratio in x-direction of Rectangle 1 and Hexagon 2 are equal to 0.26 and 0.28, respectively. These low values can be explained by the low value of variable δ. Rectangle 2 and Hexagon 2 have the highest performance ratios of 0.52 and 0.45, respectively. As these performance ratios are quite close to each other, the choice for the geometry is based on the the distribution of the pressure lines in both tessellations. A better distribution results in less substrate deformations in the actual final demonstrator. The tessellations can be seen in Figure 3.19 and Figure 3.20.

The high pressure lines are shown with the red lines. It can be seen that the pressure lines of the Hexagon 1 tessellation are more distributed over the surface than the pressure lines of the Rectangle 2 tessellation, based on a qualitative measurement. The Hexagon 1 is therefore chosen as the final geometry for the tessellation of the actuator surface. For easy implementation in later models, the optimisation variables are rounded to the values as listed in Table 3.4.

	α	β	δ	ϵ	$\overline{F_x}$	$\overline{\dot{m}}$	$\overline{F_x}/\overline{\dot{m}}$	p^-	$\overline{F_y}/\overline{\dot{m}}$
Hexagon 1 - active	0.75	2.10	1.25	-	0.12	0.26	0.45	−0.68	0.09
Hexagon 1 - passive	0.50	1.00	1.25	-	-	0.082	-	−1.00	-

Table 3.4: Final values of the optimisation variables of Hexagon 1 - active and passive.

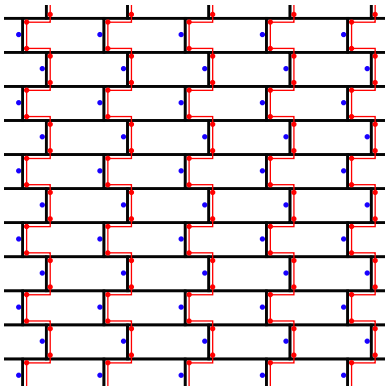

Figure 3.19: Pressure lines Rectangle 2.

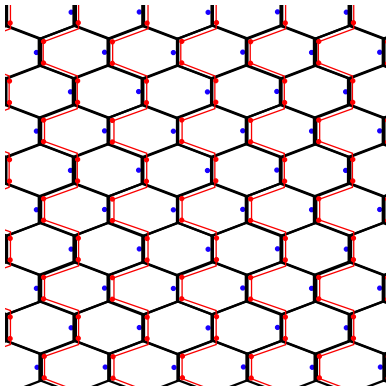

Figure 3.20: Pressure lines Hexagon 1.

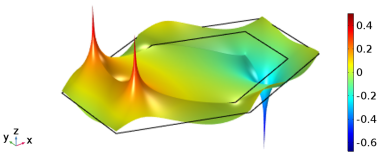

Figure 3.21: Pressure distribution in the final Hexagon 1 geometry.

3.2.3. Passive Surface

In the passive surface, the geometry of the active surface is copied. By removing the pocket in the active cell ($\beta = 1$), a simple air bearing is created. The fly height is the same over the entire geometry. The passive geometry cell is schematically visualised in Figure 3.22. The geometry has one inlet and one outlet. The number of inlets is reduced compared to the active geometry cell, because a force in y-direction is not required. The only function of the passive surface is the levitation of the substrate. The passive geometry is optimised for minimum mass flow. As the shape and dimensions of the passive geometry are identical to the active geometry only the location of the inlet and the outlet are left to vary with. The inlet pressure is fixed at a value of +1. Satisfying the zero load condition results in an outlet pressure of -1, as the geometries are symmetric in x-direction. The distance between the inlet and outlet depends on the variable α. Minimum mass flow is realised when α is equal to 0.5. For this value, the distance between the inlet and the outlet and the distance between the same inlet and the outlet of an adjacent cell are equal; one inlet is positioned exactly in the middle of two outlets. The results of the optimisation are listed in Table 3.4. It can be seen that the mass flow of the passive geometry is considerably less than the mass flow of the active geometry. The pressure distribution in the passive geometry can be seen in Figure 3.23.

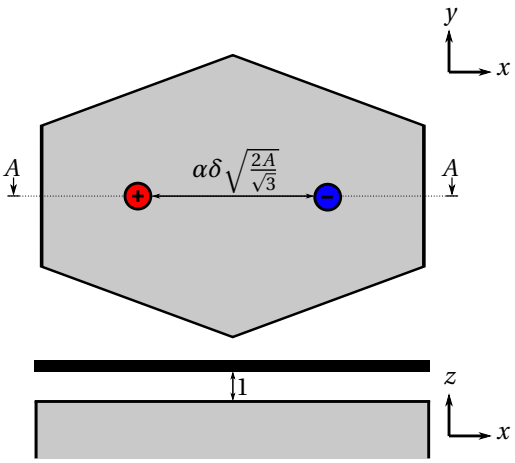

Figure 3.22: The hexagon geometry for the passive surface.

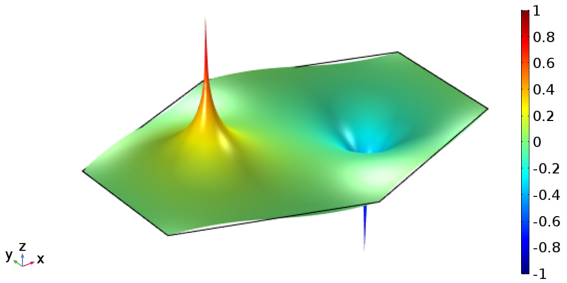

Figure 3.23: Pressure distribution in the hexagon geometry of the passive surface.

3.2.4. Overview

The active geometry and the passive geometry have both been dimensioned. In an earlier stage, it is decided that the transported object is a 100 mm diameter wafer. To make sure the wafer always covers active or passive cells both the active and passive surface should have a surface area of at least 100 mm × 100 mm. However, to

have some safety margins on all sides, the system is designed slightly bigger. The total surface consists out of 170 active cells and 161 passive cells, which can be seen in Figure 3.24. The resulting length and width of the air bearing surface are 284 mm and 144 mm, respectively. The wafer is able to fully cover 64 active or passive cells.

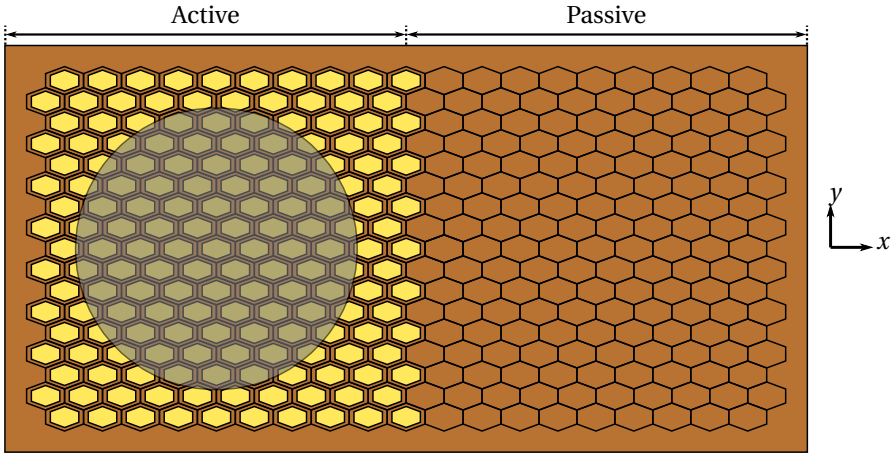

Figure 3.24: Top view of the air bearing surface with the active surface with the pockets on the left and the passive surface on the right. The 100 mm wafer, which is partly transparent visualised to clearly see all cells, fully covers 64 cells of the active surface.

3.3. Restrictions

As already explained in Section 2.2.1, the inlet restrictions are essential for having bearing stiffness. Without inlet restrictions, there is no bearing stiffness. The working principle of air bearing stiffness is explained in Appendix D. The air film stiffness is preferably high. In practice, the air bearing surface is not completely flat. A high air film stiffness will deform the wafer to the shape of the air bearing surface. In this way, it compensates for the possible waviness of the air bearing surface. The flow restrictions are chosen to be orifice restrictions, because of the following reasons:

1. Orifice restrictions ensure a high bearing stiffness compared to other types of restrictions [51].
2. Previous projects [49][20] have used capillaries as inlet restrictions and have experienced problems with integrating the restrictions in their design, as explained in Appendix G. It is believed that orifice restrictions are easier to integrate in the layer approached design. The restrictions, which are basically small holes, can be fabricated directly in the air bearing surface, or in an extra layer. This optional extra layer can be inserted between manifold and the air bearing surface.

In literature, the mass flow of air through an orifice is described by two different formulas. The first one is already discussed in Section 2.5. It is valid for pure inertia flow of a compressible gas [8] and are referred to as ideal orifice flow. For the readers convenience the mass flow equation is repeated here:

$$\dot{m} = \begin{cases} C_\mathrm{d} A p_1 \sqrt{\frac{\kappa}{\kappa-1}\left[\left(\frac{p_2}{p_1}\right)^{2/\kappa} - \left(\frac{p_2}{p_1}\right)^{(\kappa+1)/\kappa}\right]\frac{2}{R_\mathrm{s}T}}, & \text{if } \frac{p_2}{p_1} \geq \left(\frac{2}{\kappa+1}\right)^{\frac{\kappa}{\kappa-1}} \\ C_\mathrm{d} A p_1 \sqrt{\left(\frac{2}{\kappa+1}\right)^{2/(\kappa-1)}\left(\frac{\kappa}{\kappa+1}\right)\frac{2}{R_\mathrm{s}T}}, & \text{if } \frac{p_2}{p_1} < \left(\frac{2}{\kappa+1}\right)^{\frac{\kappa}{\kappa-1}} \end{cases} \tag{3.2}$$

In this equation C_d is the discharge coefficient, which is a number between 0 and 1, A is the passage section area, p_1 and p_2 are the upstream and downstream pressure, respectively, $k = 1.4$ is the specific heat ratio of air, $T = 293\,\mathrm{K}$ is the absolute temperature and $R_\mathrm{s} = 287\,\mathrm{J\,kg^{-1}\,K^{-1}}$ is the specific gas constant for dry air. This orifice flow model states that the flow depends on the pressure ratio up- and downstream of the orifice. If the pressure ratio (p_2/p_1) is larger than or equal to the critical pressure ratio of 0.528 the mass flow is governed by the square root term. If the pressure ratio is smaller than the critical pressure ratio, the flow becomes choked and the mass flow increases linearly with the upstream pressure p_1. The critical pressure ratio depends on the specific heat ratio of air. The second formula for the mass flow of air through an orifice is given by Jobson [23]:

$$\dot{m} = C_\mathrm{d} A \sqrt{\frac{1}{R_\mathrm{s} T}\left(p_1^2 - p_2^2\right)} \tag{3.3}$$

The variables in this equation are similar to the ideal orifice flow in Equation 3.2, but this equation does not assume the flow to become choked.

3.3.1. Dimensioning

In this section, a design guide line for the dimensioning of the inlet and outlets restrictions is made. First, the diameter of the outlet restriction is chosen, such that the flow is limited and can be handled by the vacuum pump. The diameter of the inlet restrictions can then be determined, based on a trade-off between the achievable stiffness and required feed pressure.

Outlet Restrictions

Besides the inlet restrictions, which are important for having bearing stiffness, outlet restrictions are also required to limit the mass flow. Combining the active and passive surface, the system has 331 outlets in total. In the worst case scenario, when there is no substrate, all outlets are exposed to ambient pressure. The restrictions should be small enough to limit the flow to the vacuum pump. The available vacuum pump in the laboratory is a Pfeiffer Hena 60[1] rotary vane pump with a maximum pump speed of 76 $\mathrm{m^3\,h^{-1}}$, which is equal to 0.0211 $\mathrm{m^3\,s^{-1}}$. The company Pfeiffer states that the vacuum pump can be used continuously if the pressure at the pump does not exceed the pressure of 0.8 bar absolute. If this is not the case and the pressure exceeds this limit it is advised to run the vacuum pump for 1 up to 2 hours maximum. Because it is not preferred to use the full pump capacity, it is suggested to aim for 20% of the maximum flow. Using the ideal orifice flow formula from Equation 3.2 and taking the orifice area as the passage area A, the outlet diameter for a certain vacuum pressure can be calculated, which can be seen in Figure 3.25. The mentioned vacuum pressure is the pressure downstream the outlet orifice restriction, which is equal to p_2 in the equation. The pressure p_1 is equal to ambient pressure. The discharge coefficient is taken as 0.8, which is a typical value for orifice restrictions [42].

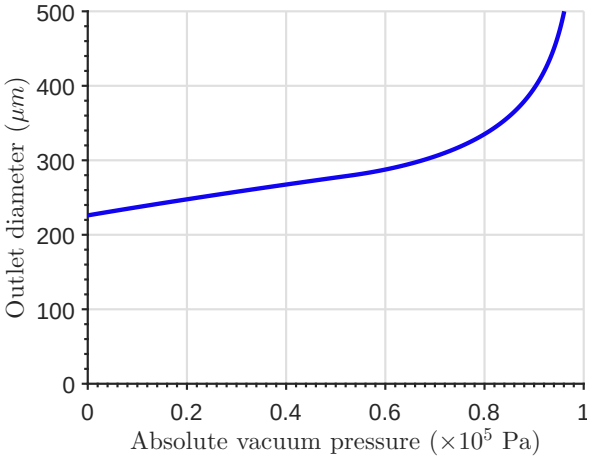

Figure 3.25: Maximum outlet diameter for a given vacuum pressure, such that the vacuum flow is less than 20% of the vacuum pump capacity.

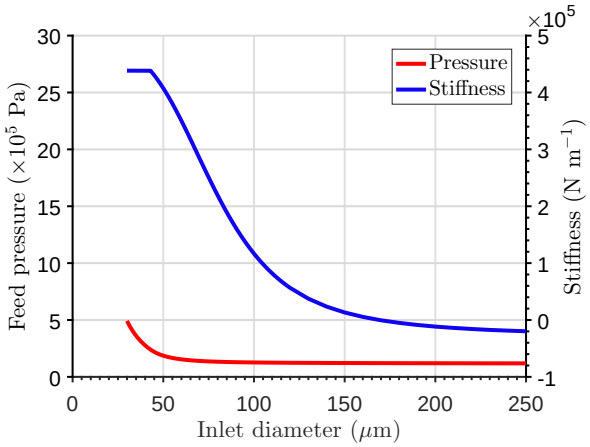

Figure 3.26: Feed pressure and stiffness for a varying inlet diameter.

It can be seen in the figure that from a vacuum pressure of approximately 0.53 bar, when the flow becomes choked, the outlet diameter decreases linearly. The vacuum pressure is chosen to be 0.7 bar, which corresponds to an outlet diameter of 305 µm. At this vacuum pressure the vacuum pump could run continuously, especially because only a fraction of the full pump capacity is used. The diameter of the outlet orifices is chosen to be equal to 300 µm.

[1] https://www.pfeiffer-vacuum.com/productPdfs/PKD02300.en.pdf

Inlet Restrictions

With the outlet diameter known, the diameter of the inlets can be determined. This is done by using the active geometry. In this model the substrate covers the active geometry. The vacuum pressure and the outlet diameter are fixed at 0.7 bar and 300 µm, respectively. The fly height is chosen to be 10 µm, which is a typical fly height in air bearing applications. This results in a pocket depth of $(\beta - 1)\, h$ is 11 µm. The flow through the orifices is assumed to follow the ideal orifice flow model and the orifice area is taken as the passage area A. The required feed pressure for satisfying the zero load condition and the corresponding stiffness per cell are calculated when the inlet diameter is varied. The results can be seen in Figure 3.26. For an inlet diameter of about 43 µm or smaller, the ratio between the positive pressure p^+ and the required feed pressure is smaller than the critical pressure ratio and the flow becomes choked. The stiffness does not increase anymore. The maximum stiffness is equal to $4.4 \times 10^5\,\mathrm{N\,m^{-1}}$, corresponding to a feed pressure of 2.4 bar or higher. It can also be seen that becomes negative for an inlet diameter of about 170 µm or larger. To conclude, it can be stated that the diameter of the inlet restrictions must be chosen as small as possible for achieving the highest stiffness and should at least be smaller than 170 µm to prevent negative stiffness. As a lower limit, the diameter of 43 µm is taken, as the stiffness does not increase any further for smaller inlet diameters. However, it must be noted that these value are only a general guideline, as they are specific for this designed. If the pocket depth, fly height or vacuum pressure is different, these diameters will change. Next to that, the required feed pressure for the chosen inlet diameter must be checked as well.

3.4. Surface Matching

The goal of this project, is the realisation of a transport demonstrator. This demonstrator consists of an active surface and a passive surface, which both consists of separate cells. To achieve a smooth transition between the two surfaces, it is proposed to match the fly height and air film stiffness of the active and passive surface cells. In this section, the approach for matching these parameters, is presented. The fly height and air film stiffness are matched as follows:

1. The vacuum pressure is fixed at 0.7 bar, as presented in Section 3.3.1.
2. The fly height is chosen. It is based on the pocket depth and variable β, which follows from the optimisation study for the optimal performance ratio. Preferably, it is in the order of 10 µm. The fly height is called h_0. To be clear, this is the fly height above the dam.
3. The active surface cells require a feed pressure to lift the substrate to the desired fly height. The combination of feed pressure, vacuum pressure and fly height corresponds to an air film stiffness of the active surface cells.
4. The air film stiffness of the passive surface cells is matched to the air film stiffness of the passive cells, at the desired fly height. As a recap, the expression for the stiffness per unit area for the incompressible flow assumption, is shown (Equation 2.7):

$$\overline{k}(h_0) = -\frac{\partial R_\mathrm{e}(h)}{\partial h}\bigg|_{h=h_0} \frac{R_\mathrm{i} - R_\mathrm{o}}{2\left(R_\mathrm{e}(h_0) + R_\mathrm{i} + R_\mathrm{o}\right)^2}\left(p_\mathrm{s} - p_\mathrm{v}\right) \tag{3.4}$$

   This equation clearly shows the variables, which influence the stiffness:

   - Thin film resistance R_e
   - Inlet restriction R_i
   - Outlet restriction R_o
   - Feed pressure p_s
   - Vacuum pressure p_v

   The thin film resistance can be altered by the dimensions of the geometry, the fly height and the location of the inlets and outlets, which is set by the variable α. The geometry, fly height, and variable α are already fixed. Furthermore, it is preferred to use similar restrictions in the active and passive surface. Therefore, the left over variables to change the stiffness are the feed pressure and the vacuum pressure.

To conclude, the fly height and air film stiffness of the active and the passive surface are matched, by tuning the feed pressure and the vacuum pressure of the passive surface. In this way, the fly height and the static stiffness are matched. The static stiffness is the stiffness at low frequencies.

3.5. Design Plan

In the preceding sections, the conceptual design is presented. The tessellation of the surface is known, and a guideline for the dimensioning of the restrictions is set up. In this section, the design plan is presented. It is proposed to develop two demonstrators. The main difference between the two demonstrators is the realisation of the restrictions. The air bearing surface and the manifold are designed in a similar way.

1. First demonstrator

In the first demonstrator, the orifice restrictions are realised directly in the air bearing surface. This makes the design relatively simple, because it only consists of the manifold and the air bearing surface with the restrictions. However, the combination of pockets with a pocket depth in the order of 10 µm and inlet orifice holes with a diameter in the order of 0.1 mm, is challenging. The inlet restrictions are larger than desired, which is explained in Chapter 5. The first demonstrator is used to validate the numerical models and to gain knowledge about the manufacturing methods to realise a working system. The gained knowledge can be used to develop the second demonstrator. The design of the first demonstrator is presented in Chapter 5.

2. Second demonstrator

The results of the first demonstrator are used to design the second demonstrator. In the second demonstrator, the orifice restrictions are realised in an extra layer, which is placed underneath the air bearing surface. Therefore, the air bearing surface must have holes at the locations of the inlets and outlets, such that the air can flow to the top of the air bearing surface, into the thin film. The system is more complex, but the inlet restrictions can be fabricated with smaller diameters, as will be explained in Chapter 6. This results in an increased air film stiffness. A disadvantage of this design is the introduction of 'dead' volumes at the inlet restrictions. These are created by the holes in the PCB surface, at the location of the inlet restrictions. They have an influence on the stability of the system. Therefore, the stability must be checked in a dynamic analysis, similar as in Section 2.6. The design of the second demonstrator is presented in Chapter 6.

3.6. Conclusion

In this chapter, the transport demonstrator has been designed. As a result of a tessellation study, the cells of the active and passive surface are chosen to be stretched hexagons. They are dimensioned at a surface area of 100 mm^2. The active surface cells are optimised for a high performance ratio and the passive surface cells are optimised for minimum mass flow. Moreover, the flow restrictions are chosen to be orifice restrictions. The outlet restrictions are dimensioned at a diameter of 0.3 mm, to limit the flow to the vacuum pump. The diameter of the inlet restrictions is preferably small, because this is beneficial for the air film stiffness. However, the required feed pressure must be taken into account. The fly height and air film stiffness of the active and the passive surface are matched by tuning the feed pressure and vacuum pressure of the passive surface. It is proposed to develop two demonstrators. In the first demonstrator, the orifice restrictions are drilled directly in the air bearing surface. This demonstrator is used to validate the numerical model. In the second demonstrator, the orifice restrictions are realised in an additional layer beneath the air bearing surface. The smaller restriction diameters result in a higher air film stiffness.

4

Design First Demonstrator

In this chapter, the design of the first demonstrator is presented. This demonstrator is used to validate the numerical models and to gain knowledge about the fabrication of an air bearing system. First, the design overview is presented, which includes the design of the different components. The chapter ends with the theoretical performance of the first demonstrator.

4.1. Design Overview

As mentioned in Chapter 3, the demonstrator consists of three main components: the air bearing surface, the restrictions, and the manifold. The design of each component is discussed in the following section. A render of the design can be seen in Figure 4.1. The figure shows the manifold with the various channels, and the air bearing surface with the pockets and the restriction holes. The restriction holes cannot be observed because they are too small.

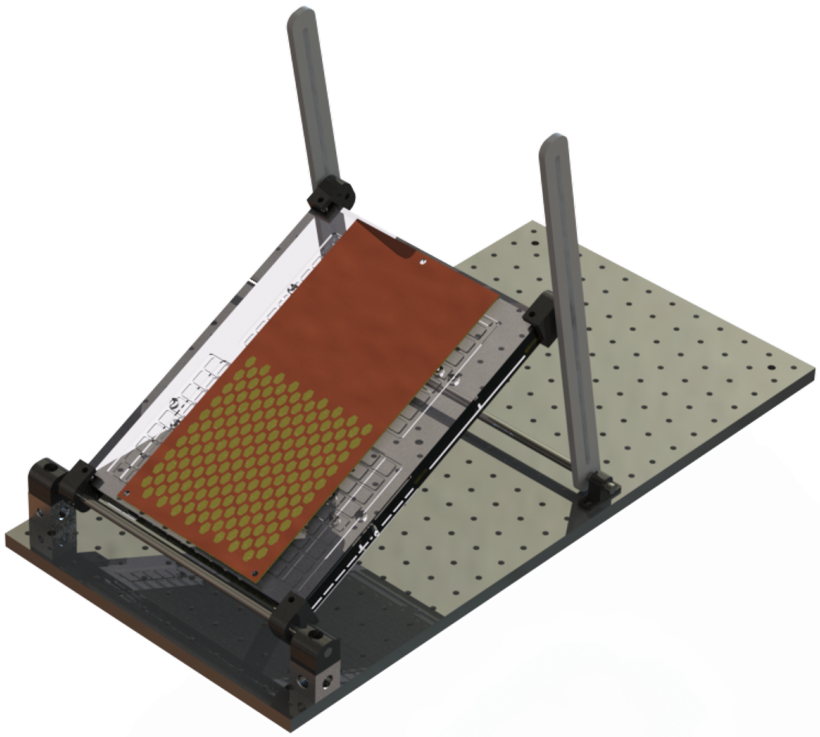

Figure 4.1: Render of the design of the first demonstrator.

4.1.1. Air Bearing Surface

Many different methods have been tried for realising the actuator surface. An overview of the different methods can be found in Appendix G. It is decided to make use of Printed Circuit Board (PCB) production techniques as the final manufacturing method. This technology is usually applied in the fabrication of printed circuit boards, which are used in electronic equipment. A couple of printed circuits boards can be seen in Figure 4.2. However, because the production process and its manufacturing tolerances are well defined, this technique can be exploited to realise an air bearing surface with pockets. By etching away the copper on specified locations, the pockets are created. A big advantage of this method is the freedom in design. The shape of the pockets can be freely chosen. Wesselingh [51] has been the first to use PCB technology to realise an active air bearing system. One of the early prototypes of the step surface actuator, which is presented in Section A.1, consists of a PCB air bearing surface with pockets with a pocket depth of 40 µm. This pocket depth is too large for the demonstrators in this project. The mass flows would be too large and the air film stiffness would be too small. In collaboration with Eurocircuits[1], another type of PCB is chosen. The PCB is manufactured on a separate panel in the "NAKED pool". The production process of this panel is explained in Appendix G. A cross-section of the PCB is shown in Figure 4.3. It consists of a glass-reinforced epoxy laminate base layer, which is named FR4. This is a typical grade designation in printed circuit board technology for being flame resistant. The base material has a top and bottom layer of copper with a thickness of 12 µm. The copper is etched away at the locations of the pockets. In the final step of the production process, the PCB manufacturer applies a gold-nickel surface finish to protect the copper layer. The result is a PCB air bearing surface with pockets with an average pocket depth of 16.5 µm.

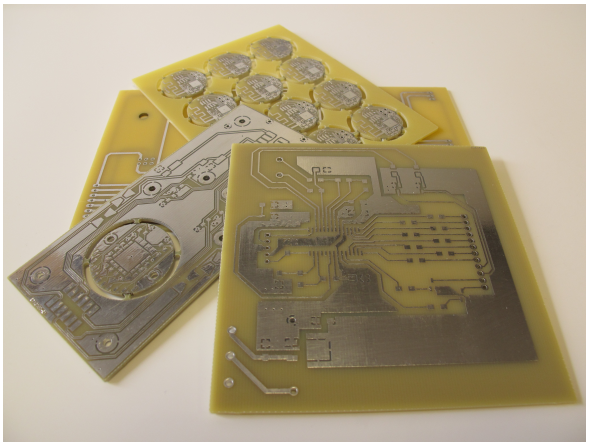

Figure 4.2: Printed circuit boards are normally used for the fabrication of electronics[1].

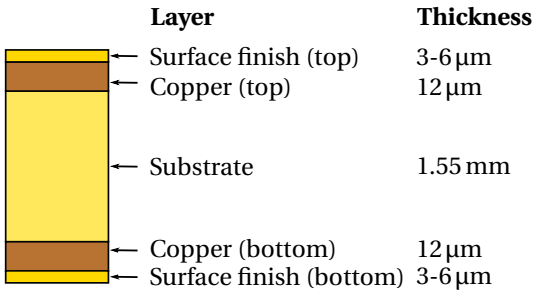

Figure 4.3: Cross-section of the PCB layout. The PCB consists of several thin layers of material.

4.1.2. Restrictions

In the first demonstrator, the restrictions are realised directly in the air bearing surface. Eurocircuits is able to drill small holes in the PCB during the production process. This is convenient, because the demonstrator has more than 800 restriction holes. The PCB manufacturer can drill holes with a diameter down to 0.2 mm. It is physically challenging to drill smaller holes in a 1.55 mm substrate. A rule of thumb for preventing breakage of the drill states that the drilling depth is maximum 6 to 7 times the drilling diameter. The inlets are dimensioned at a minimum diameter of 0.2 mm. It can be seen in Figure 3.26, that the air film stiffness of the active cells is negative for an inlet restriction diameter of 0.2 mm and an outlet restriction diameter of 0.3 mm. To increase the stiffness of the system, the outlet diameter must be increased, in order to reduce the outlet restriction value. The diameter of the outlets is dimensioned at 0.4 mm. The increased outlet diameter results in a larger mass flow to the vacuum pump. For the vacuum pressure of 0.7 bar, the mass flow is 35% of the maximum mass flow of the vacuum pump in the case that all outlets are exposed to ambient pressure. This is not preferred. Therefore, it is decided to only validate the active surface of the first demonstrator. This should be enough to check the validity of the numerical model. By only connecting this surface to the pressure supplies, the total number of outlets is reduced from 331 to 170. The total mass flow through the outlets, when they are all exposed to ambient air, is then equal to 18% of the maximum vacuum pump flow. The modelled

[1] Eurocircuits. Mechelen, Belgium. `http://www.eurocircuits.com/`.

air film stiffness of the active cell and the required feed pressure for the zero load condition are visualised in Figure 4.4. In this plot, the discharge coefficients of the inlets and outlet are equal to 0.8. The pocket depth is fixed at 16.5 µm, as a result of the manufacturing method. Therefore, the fly height above the dam is equal to 15 µm. It can be seen that for an inlet diameter of 0.2 mm the air film stiffness of one cell is equal to 4.60×10^4 N m^{-1}, with a corresponding feed pressure of 1.24 bar. This is still a rather low stiffness compared to the stiffness values in Figure 3.26. The decrease in stiffness is partially explained by the increased pocket depth. The air film stiffness could be increased by increasing the outlet diameter, but this is not preferred due to the large mass flows to the vacuum pump.

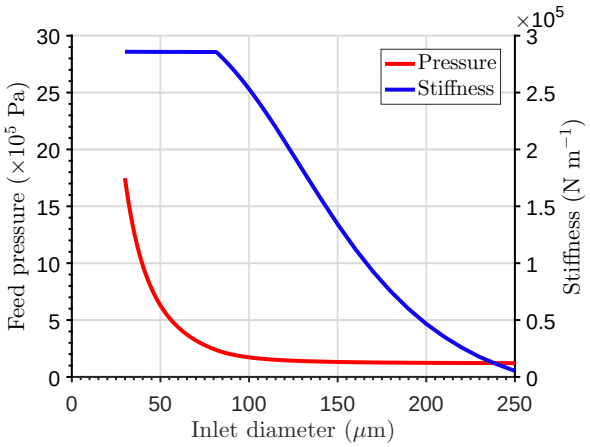

Figure 4.4: Feed pressure and stiffness for the active cell of the first demonstrator.

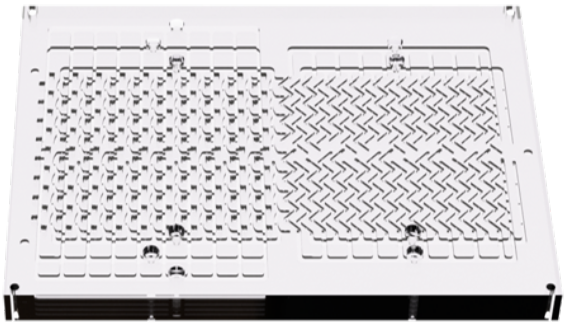

Figure 4.5: A render of the complete manifold, which consists of 8 laser-cut PMMA plates, which are bonded together with 3M double sided tape. The active side (left) has 6 supplies (4× feed pressure and 2× vacuum pressure).

The cross-section of the system with the manifold and the PCB surface can be seen in Figure 3.17. The great advantage of this demonstrator is its simplicity. There are no problems with aligning the small holes in the PCB with even smaller holes in an extra restriction layer. The holes in the manifold can be laser-cut with large enough diameters for easy assembling and aligning of the manifold and the air bearing surface.

4.1.3. Manifold

The manifold is the structure beneath the air bearing surface. It connects the feed pressure and vacuum pressure supplies to the correct inlets and outlets. In Chapter 3, it is already mentioned that the manifold is a stack of laser-cut PMMA plates. Many tests are performed to find a proper way of bonding the PMMA plates. The connection should be leakage free up to pressure differences of a few bar. The best results are obtained with industrial 3M double sided tape. The test results are described in Appendix G. If the tape width is larger than 1.5 mm, it can withstand pressure differences of more than 6.2 bar. The complete manifold, which consists of 8 PMMA plates, can be seen in Figure 4.5. To reduce the possible pressure losses over the various channels in the manifold, it is decided to design them in such a way, that they go from the sides of the manifold to the middle. Therefore, the pressure supplies are located at the sides of the manifold. The active surface on the left has 6 pressure supplies (4× feed pressure and 2× vacuum pressure), and the passive surface on the right has 4 pressure supplies (4× feed pressure and 2× vacuum pressure). The holes in the corners of the manifold are used for aligning the plates during the bonding process, which is also described in Appendix G.

4.2. Theoretical Performance

The theoretical performance of the first demonstrator can be calculated. The transported object is a silicon wafer. The diameter and thickness of the wafer are 100 mm and 525 µm, respectively. The material density of silicon is equal to 2329 kg m^{-3}. The theoretical mass of one wafer is thus equal to 9.6 g. This value is checked by weighing some wafers on a precise weighing scale. For a vacuum pressure of 0.7 bar and a fly height above the dam of 15 µm one actuator cell can provide a viscous traction force on the wafer of 1.39 mN, corresponding to a force per unit area of 13.94 N m^{-2}. The total propulsion force should be in equilibrium with the gravitational force, which is a function of the angle θ between the air bearing surface and the horizon.

The maximum angle of the air bearing surface with respect to the ground is equal to:

$$\theta = \arcsin\left(\frac{\bar{F}}{\rho t g}\right) > 90° \tag{4.1}$$

With a corresponding acceleration of the wafer of:

$$a = \frac{\bar{F}}{\rho t} = 11.4\,\mathrm{m\,s^{-2}} \tag{4.2}$$

In this calculation the wafer is completely covered by actuator cells. In practice this is not possible. The wafer can fully cover 64 actuator cells. The maximum angle θ is equal to 71°, which corresponds to an acceleration of $9.3\,\mathrm{m\,s^{-2}}$. This is less than the acceleration of 1G, which has been set in the requirement. However, for the first demonstrator the acceleration is sufficiently high to demonstrate the transport capabilities, and to validate the model.

4.3. Conclusion

In this chapter, the first demonstrator is designed. The demonstrator consists of three components; the air bearing surface, the restrictions, and the manifold. The air bearing surface is realised by making use of PCB technology. The pockets are created by etching away the copper. The restrictions are drilled directly in the PCB air bearing surface. The inlet restrictions have a diameter of 0.2 mm, which is the smallest diameter Eurocircuits is able to drill. To make sure that the air film stiffness is still positive, the diameter of the outlet restrictions is enlarged to 0.4 mm. The mass flow to the vacuum flow increases, due to the larger outlet restriction diameter. Therefore, only the active surface of the demonstrator is validated. In this case, the air flow to the vacuum pump is well below the 20% of the maximum vacuum pump capacity. The manifold is a stack of laser-cut PMMA plates, which are bonded together with double sided tape. The theoretical performance of the first demonstrator is slightly below the initial requirements, but it is sufficiently high for the validation of the numerical model and the realisation of a convincing demonstrator.

5

Realisation and Validation First Demonstrator

This chapter describes the realisation and validation of the first demonstrator, which is used to validate the numerical model. First, the realisation of the system is discussed, and the different manufacturing methods which have been used are explained. Then, the measurement set-up is introduced and the measurement procedure is presented.

5.1. Realisation

The first demonstrator consists of three important components: the air bearing surface with the pockets, the restrictions in the PCB surface for having flow control, and the manifold for distributing the air from the pressure supplies to the inlets and outlets. The manufacturing of these three components is presented in this section. Although the experimental validation of the numerical model is only done on the active surface, the first demonstrator is realised with the active and passive surface. This simplifies the installation of the second demonstrator, as the same set-up can be used.

5.1.1. Air Bearing Surface

The air bearing surface is manufactured by making use of PCB technology. The pockets are realised by etching away the copper on the PCB plate. More information on the manufacturing method can be found in Appendix G. The pocket depth is estimated to be 16.5 µm. This value must be checked if the system is going to be verified experimentally. Furthermore, in the previous chapters the air bearing surface of the actuator cells, both pocket and dam, are modelled to be flat. The validity of this flat surface assumption must be checked as well. In practice, the air bearing surface has a certain surface texture. The surface texture is the summation of the surface flatness and surface roughness. The flatness is associated with the low frequency surface content and is also called the waviness of the surface. The surface roughness is dominated by the high frequency surface content. The air bearing surface is measured with a Veeco - Bruker Contour GT-K1 white light interferometer using the IXL2.5 lens (2.5 times magnification). This measuring device can measure height differences with nanometre resolution. As the measured surfaces are considerably larger than the viewing area, the stitching function is used to stitch multiple images together. Focusing on two different materials (gold-nickel surface finish and FR4 plastic) represented a challenge. Using green light with a 75% light intensity has proven to be a good trade-off for not overexposing the copper too much and still being able to see the FR4 material in the images. The measurements have been done after bonding the PCB plate to the manifold, as this is the situation in the set-up. Figure 5.1 shows a measurement of the middle of the surface at the transition between the active and the passive surface. The dimensions of the measured rectangle are 40 mm by 25 mm. The hexagon pockets are clearly visible. From the measurement, it is conducted that the average pocket depth is equal to 13 µm, which is a bit less than the expected 16.5 µm. The roughness of the air bearing surface is sub-micrometer. Therefore, the influence of the roughness on the performance of the air bearing surface can be assumed to be negligible. The surface does show something else, which can influence the air bearing behaviour. A wavy pattern can be noticed in both copper and FR4 PCB material. This is better visualised in Figure 5.2, which shows a detailed white light measurement of the air bearing surface. The

dimensions of the measured rectangle are 2.49 mm by 1.87 mm. The waviness is something else than the previously mentioned flatness, which has to do with low frequency surface content. This 'short' waviness, which goes in both x- and y-direction, is most likely caused by the fibres in the PCB material. As the amplitude of the wavy surface is significant compared to the desired fly height, it is implemented in the numerical model. The waviness is characterised with a wave amplitude of 1.3 µm and a spatial wavelength of 1.5 mm in both x- and y-direction.

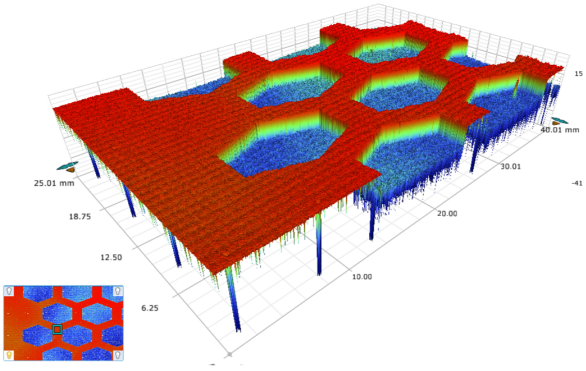

Figure 5.1: A white light interferometer image of the middle of the air bearing surface (gold-nickel surface finish and FR4 PCB material). The pockets are clearly visible in the image.

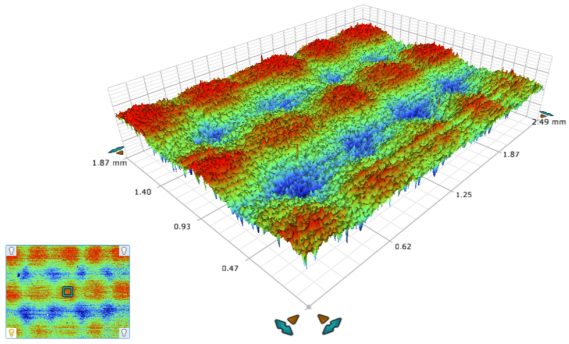

Figure 5.2: A white light interferometer close-up image of the gold-nickel air bearing surface. The wavy pattern in both directions is clearly visible. It has an amplitude of 1.3 µm and a spatial wavelength of 1.5 mm in both x- and y-direction.

The low frequency surface content, or 'long' waviness, has not yet been investigated. The total surface is relatively large compared to the areas, which can be measured by the interferometer. A measurement of the complete surface would take days. Therefore, it has been decided to measure a few lines on the surface, to characterise the flatness. Figure 5.3 shows the lines on which the surface height is measured. The results for the lines in y-direction can be seen in Figure 5.4. The first plot is measured on the active surface and shows the locations and pocket depths of the pockets. The second plot is measured on the passive surface. All plots clearly show a curvature, which is a measure for the flatness of the air bearing surface. The curvature has a peak to peak height difference of approximately 80 µm. Figure 5.5 shows the surface height measurement along the line C_1-C_2. The surface is curved in this direction as well, but the curvature is less than the curvature in x-direction. The largest measured height difference is approximately 40 µm.

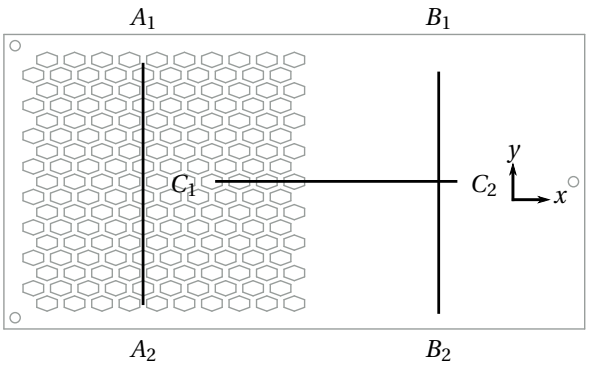

Figure 5.3: A top view of the air bearing surface. The specified lines (A_1-A_2 and B_2-B_2 in y-direction and C_1-C_2 in x-direction) are measured on the white light interferometer.

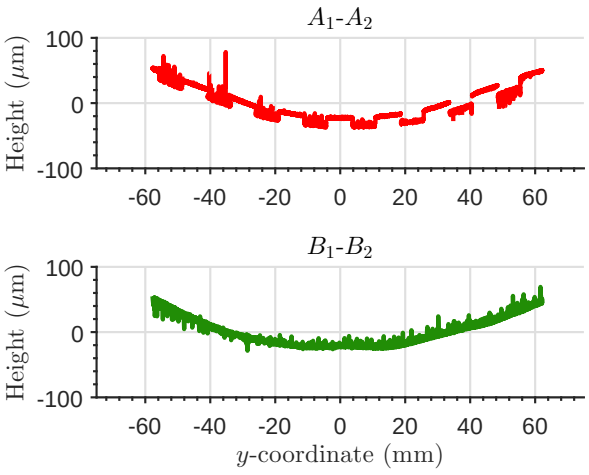

Figure 5.4: These plots show the surface height along the specified lines. A curvature of the surface can be noticed.

The curvature of the air bearing surface is probably caused by the stacking of the PMMA plates of the manifold. As the PCB plate is bonded to the manifold the air bearing surface is curved as well. To compensate for the curvature, a 4 mm thick aluminium plate is added to the system. Three screws in the middle of

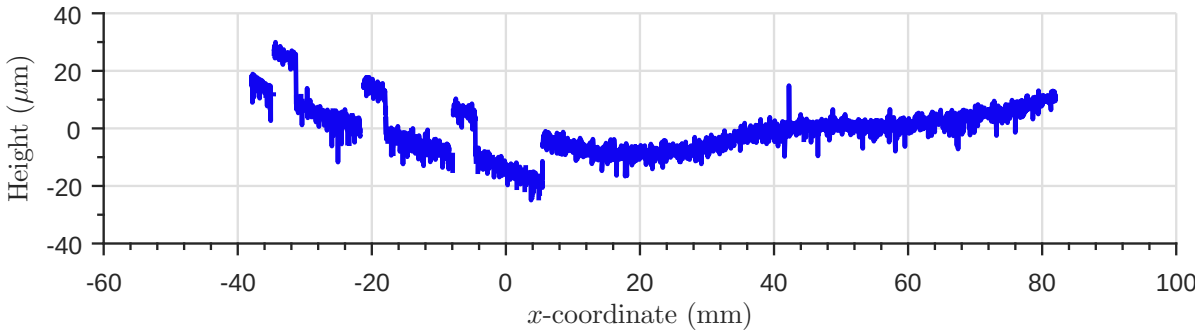

Figure 5.5: Surface height along the line C_1-C_2. The surface is curved towards the middle.

the plate can be used to straighten the manifold. In theory, it would not be necessary to do this, as the air film stiffness should be able to cope with the slight curvatures of the air bearing surface by deforming the wafer. However, from the air film stiffness calculation in Section 4.1.2, it is already known that the air film stiffness of the first demonstrator is rather low. Therefore, a flatter air bearing surface is preferred for the first demonstrator.

5.1.2. Restrictions

The flow restrictions are drilled directly in the PCB surface by the PCB manufacturer. The inlets are dimensioned with a diameter of 0.2 mm, which is the smallest hole diameter the PCB manufacturer can drill, and the outlets have a diameter of 0.4 mm. Flow measurements are performed for both restrictions, to study the mass flow through the orifices as a function of the pressure difference. The measurement set-up is described in Appendix F. The results for the inlet restriction can be seen in Figure 5.6. The ideal orifice model (Equation 3.2) and Jobson orifice model (Equation 3.3) are fitted to the average of the measurements. The orifice area is taken as the passage area A. The discharge coefficient of the ideal orifice model is equal to 0.79, while the discharge coefficient of the Jobson orifice model is equal to 0.64. The ideal orifice model shows the best match and is used in the coming numerical models. The results for the outlet restriction can be seen in Figure 5.7. The discharge coefficient of the ideal orifice flow and Jobson orifice flow are equal to 0.80 and 0.64, respectively. Again, the ideal orifice model shows the best match with the measurements and is used in the coming numerical models.

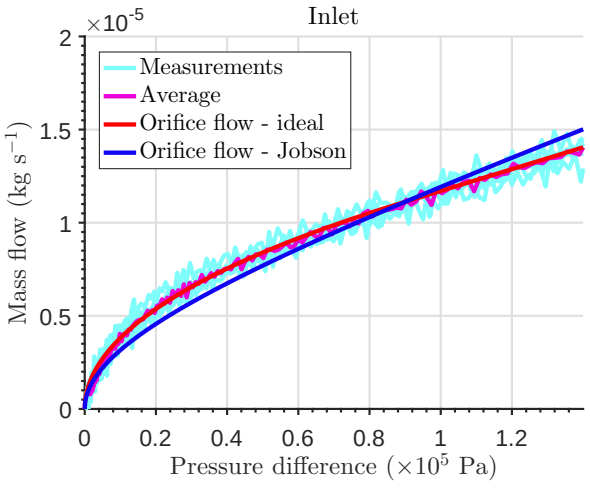

Figure 5.6: Mass flow data of the 0.2 mm inlet restriction.

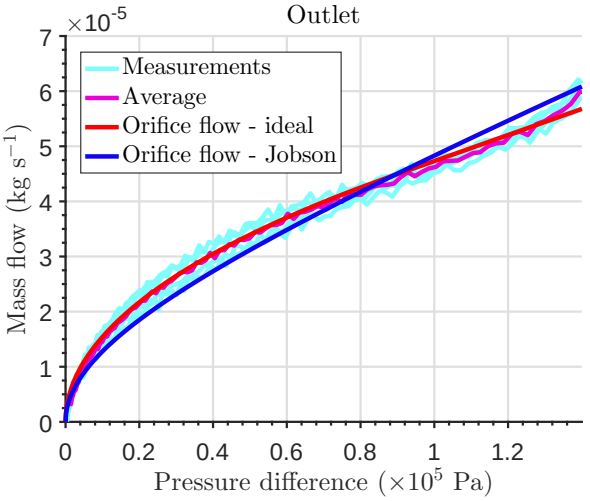

Figure 5.7: Mass flow data of the 0.4 mm outlet restriction.

In reality the discharge coefficient C_d depends on the Reynolds number [8]. The Reynolds number in the orifice is equal to:

$$\mathrm{Re} = \frac{\rho u}{\eta} = \frac{4\dot{m}}{\pi d \eta} \tag{5.1}$$

This could be incorporated in the calculations for determining the discharge coefficients. However, because there is a good match between the measurements and the ideal orifice flow model this is used in further simulations.

5.1.3. Manifold

The manifold is a stack of laser-cut PMMA plates, which are bonded together using 3M double sided tape. This is a very precise process. A detailed description of the process steps can be found in Appendix G. The realised manifold consists of 8 PMMA plates and has a total thickness of about 20 mm. It can be seen in Figure 5.8.

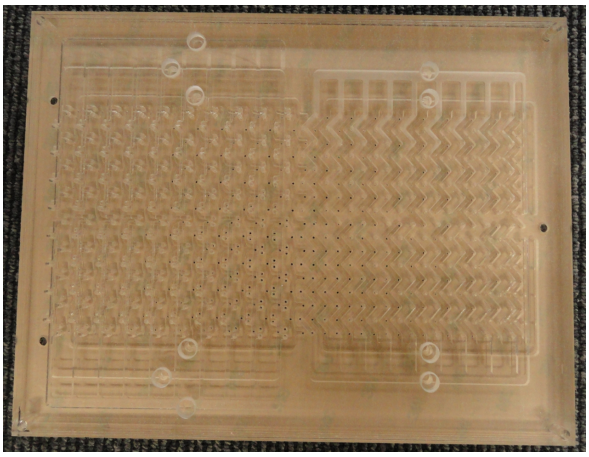

Figure 5.8: A picture of the back-side of the realised manifold. The three dark-coloured holes at the sides of the manifold are used for aligning the PCB plate and the manifold during the bonding process.

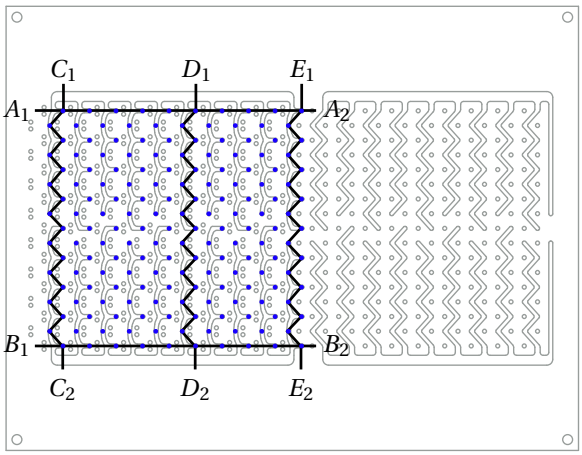

Figure 5.9: This figure shows the channels for guiding the vacuum (grey). The outlets in the active layer are visualised with the blue dots. To characterise the pressure loss in the manifold the vacuum pressure in the two main channels (A_1-A_2 and B_2-B_2) and three side channels (C_1-C_2, D_1-D_2 and E_2-E_2) is measured.

It is interesting to measure the performance of the manifold; the pressure losses over the various turns and channels are analysed. To do this the active side of the manifold is connected to the vacuum pressure supply (on both sides of the manifold). The vacuum channels can be seen in Figure 5.9. The vacuum pressure is measured over the two main channels (A_1-A_2 and B_2-B_2) and three side channels (C_1-C_2, D_1-D_2 and E_2-E_2) by placing a digital pressure sensor (NXP MPX5500DP) over the outlet restriction of the corresponding channel. The various outlets are visualised by the blue dots. The results of the vacuum pressure drop in the main channel can be seen in Figure 5.10. Before the air enters the manifold, the vacuum pressure is equal to approximately 0.72 bar. At the location of the pneumatic connections in the middle of the manifold, the vacuum pressure is the lowest, but there is already a pressure drop of about 0.12 bar. It can be seen that the pressure increases when going further away from the pneumatic connection. There is a pressure loss of about 0.04 bar from the middle of the main channel to the outer sides. Figure 5.11 shows the pressure loss in the side channels. The highest vacuum can be found at the entrance of each side of the channels. Over the length of the channel, a pressure drop of approximately 0.02 bar is measured. Of course, the measured pressure losses are only valid for this specific value of the initial vacuum pressure. However, in general it can be concluded that the pressure drop in the manifold is significant and should be taken into account.

A similar experiment is done to identify the pressure losses of the feed pressure supplies. The pressure drop is far less than the pressure loss of the vacuum pressure. If the pressure below the manifold is equal to 1.4 bar, the pressure drop over the pneumatic connection is equal to 0.02 bar. The pressure drop in the main channels and side channels is less than 0.01 bar.

5.2. Experimental Validation

The first demonstrator is realised to validate the numerical model. The motor function, which is characterised by the actuator force, and the bearing function, which is characterised by the air film stiffness, are measured and compared with the model for different operating conditions.

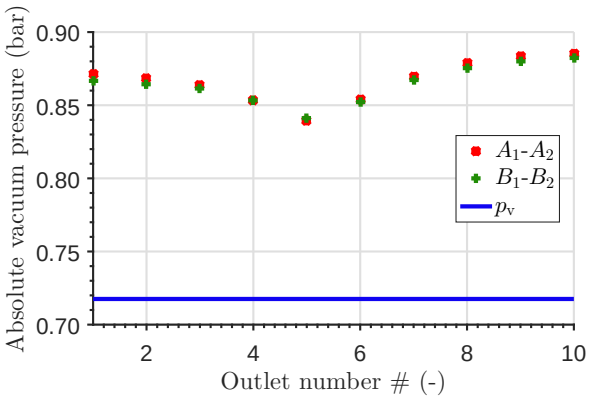

Figure 5.10: Vacuum pressure in the main channels. The initial vacuum pressure p_v is equal to 0.72 bar.

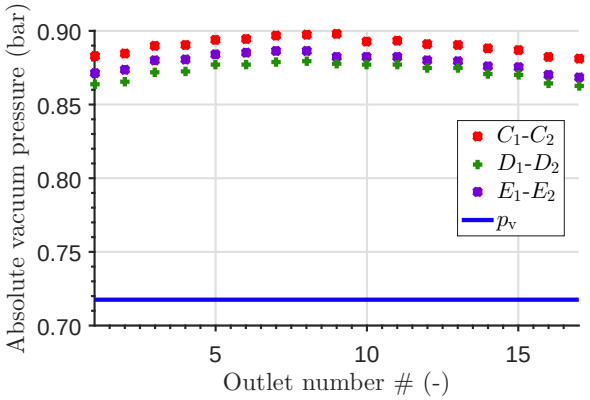

Figure 5.11: Vacuum pressure in the side channels. The initial vacuum pressure p_v is equal to 0.72 bar.

5.2.1. Experimental Set-up

The complete set-up of the first demonstrator can be seen in Figure 5.12. The demonstrator, which consists of the manifold, PCB surface and aluminium plate, is placed in the set-up by making use of several 3D printed connections. The demonstrator is fixed to a metal axis on one side, while it is connected to two sliders on the other side, such that the angle of the demonstrator can be varied. The numerical model is validated in the main transport direction. Therefore, the inlets of the active cells are connected to the same pressure supply.

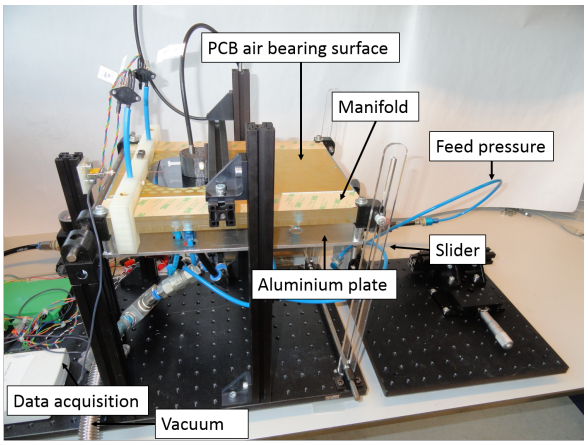

Figure 5.12: The complete measurement set-up. The demonstrator is fixed in a frame of Thorlabs beams and two sliders. The pneumatics are connected on the bottom side of the manifold. An aluminium plate is added to straighten the manifold and air bearing surface.

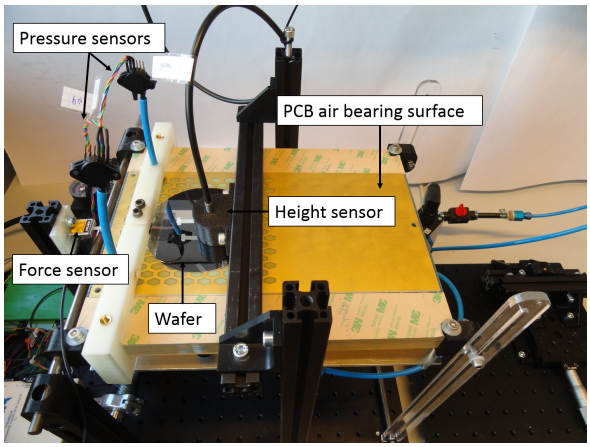

Figure 5.13: Top view of the measurement set-up. The wafer is connected to the force sensor with a thin cord. The pressure sensors and height sensor are fixed in a frame.

Pneumatics

For this set-up, some of the pneumatics of the flow measurement set-up, which is described in Appendix F, is used. The outlets of the cells are connected to the vacuum via the manifold. A manual valve, which is used to set the initial vacuum pressure, is placed in between the vacuum supply and the manifold. The hoses have large diameters to prevent vacuum loss as much as possible. The inlets are connected to the same feed pressure supply. A manual proportional valve is used to set the initial feed pressure. The air then flows through a pressure tank, which is used to level out any pressure perturbations, to a Festo proportional valve (MPPE-3-1/8-1-010B). The feed pressure can be adjusted with the proportional valve by varying the voltage over the valve. In this way different operating conditions can be simulated.

Sensors

To measure the parameters of interest, different sensors are used. They are described below. The locations of the sensors are pointed out in Figure 5.13.

1. Pressure

Two different pressures are measured: the feed pressure upstream the inlet restrictions and the vacuum restriction downstream the outlet restriction. Due to the pressure loss in the manifold it is better not to measure the pressures below the manifold, as this is not an accurate measurement of the actual inlet or outlet pressure. The pressure sensors (NXP MPX5500) are fixed in a 3D printed frame and connected to one of the inlet restrictions and an outlet restriction, on top of the air bearing surface. In this way, the pressure directly below the restriction is measured. Rubber seal rings are used to make sure the connection is leakage free.

2. Fly height

The fly height, which is the fly height above the dams, is measured with a fiberoptic sensor (Philtec D63). The working principle and calibration chart of this sensor can be found in Appendix H. The sensor has a very sensitive near side response and a somewhat less sensitive far side response. The far side region is used, because it is difficult to place the sensor in the range of the near side. In the far range, the response of the sensor is linear from about 0.3 mm to 0.9 mm. The sensitivity in this range is approximately $-2.6\,\mathrm{mV\mu m^{-1}}$. The accuracy of the sensor is within $\pm 0.6\,\mu$m. The sensor is placed in a 3D printed connection, which is fixed in a stiff Thorlabs frame. The 3D printed connection functions as a hood to minimise the influence of external light sources. The sensor measures the fly height in the middle of wafer.

3. Force

A force sensor is used to measure the viscous traction force on the wafer. The sensor is a Futek LSB200 100 g. The sensor signal is amplified with a Scaime CPD RAIL amplifier, such that the sensitivity is equal to $120\,\mathrm{mV mN^{-1}}$. The calibration data can be found in Appendix H. A thin cord connects the wafer to the force sensor. The sensor itself is fixed in a Thorlabs frame. It is carefully positioned to make sure the force is in line with the sensor.

Data Acquisition

The data acquisition is performed with a National Instruments NI USB-6211 DAQ, which is able to sample at 250 ksamples s^{-1}, divided over the number of channels that are measured. This is more than sufficient. The measurements are done at 100 samples s^{-1}.

5.2.2. Measurement Procedure

The measurement procedure for measuring the fly height, force and operating pressures are discussed in this section. The following steps are performed for doing the measurements:

1. The bearing surface is placed horizontal by using a spirit level, to make sure gravity is not influencing the force measurement.
2. The vacuum pressure is set at the desired value with the manual proportional valve.
3. After the vacuum pressure is turned on, a zero reference measurement is done for the height sensor and force sensor. Later measurements are done in reference to these initial measurements.
4. Once the measurement is started the feed pressure is swept by slowly increasing the voltage over the proportional valve. The initial voltage is set at such a value that the wafer is floating freely and does not make contact with the air bearing surface. During the measurement, the feed pressure, vacuum pressure, fly height and force are measured and recorded. The measurement is stopped when the force on the wafer approaches zero.

The measurements are used to study the motor function and bearing function. The viscous traction force as a function of the applied feed pressure and vacuum pressure can be determined and compared with the numerical model. For the validation of the bearing stiffness the measurements are repeated with an additional weight on top of the wafer. The stiffness can then be calculated with the change in load and fly height.

5.3. Results

The results of the measurements can be seen in Figure 5.14-5.17. Each measurement is done for about 110 s. It can be seen that the feed pressure rises from approximately 1.24 bar to 1.40 bar. Due to the rise in feed

pressure, the vacuum pressure and fly height increase as well. The vacuum pressure starts at approximately 0.76 bar and increases to 0.80 bar. The fly height starts at 30 µm and increases to 48 µm. The measured force decreases for an increasing feed pressure. The initial force is equal to 15 mN. When the measurement is stopped the force is equal to 2 mN. All measurements are averaged and the average is fitted with a second order polynomial, which is used for the comparison with the numerical model. First, the measured data is discussed in more depth.

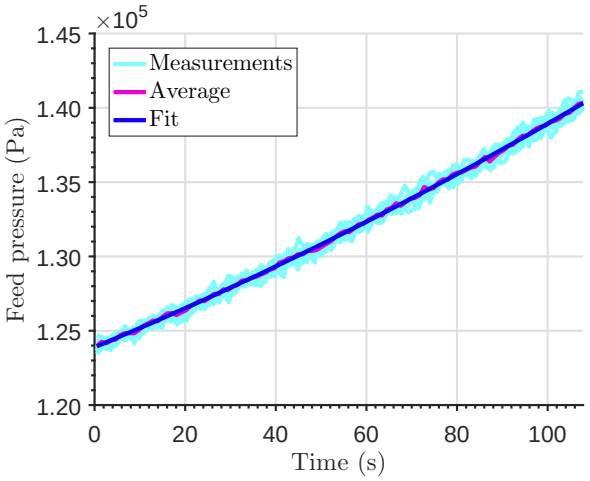

Figure 5.14: The measured absolute feed pressure over time.

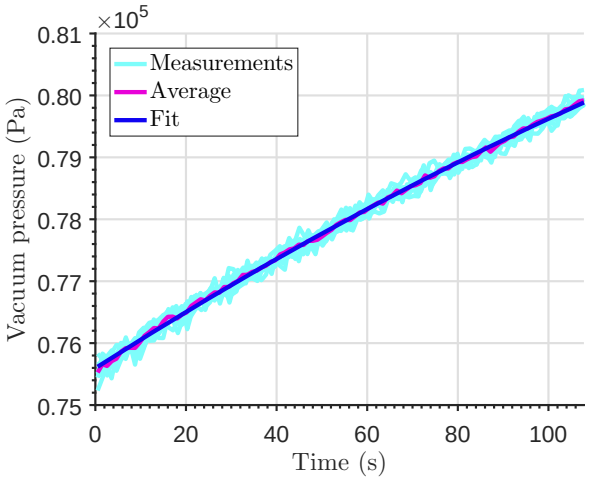

Figure 5.15: The measured absolute vacuum pressure over time.

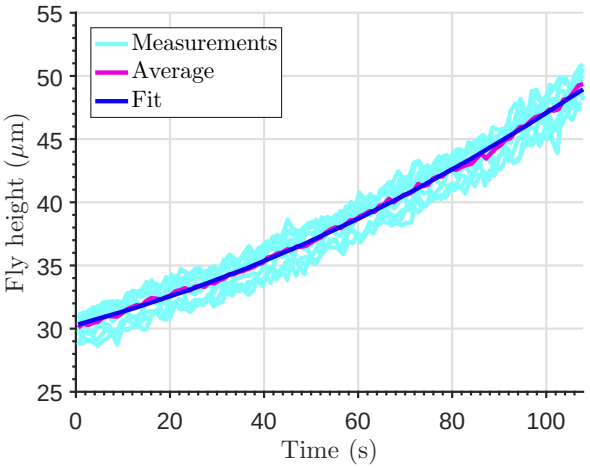

Figure 5.16: The measured fly height (above the dam) over time.

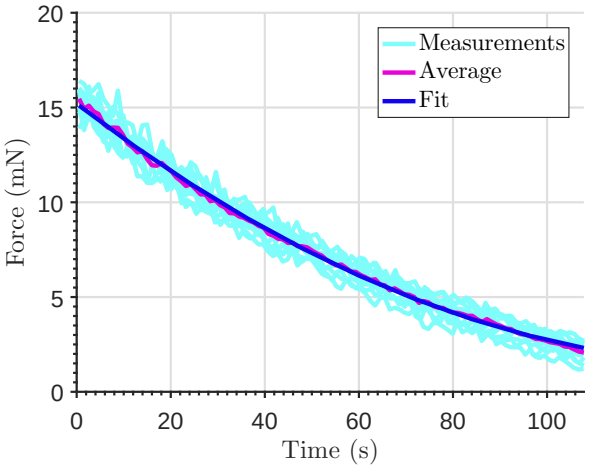

Figure 5.17: The measured force over time.

In practice, it has turned out to be difficult to realise a high vacuum near the manifold. The demonstrator is designed with a vacuum pressure of 0.70 bar. This value has not been reached during the experiments, as can be seen in Figure 5.15. A few causes can be identified. First of all, it is very difficult to transport vacuum. This has already been shown in the characterisation of the manifold, which shows significant pressure drops. With the wafer on top of the air bearing surface, and the feed pressure turned off, the vacuum pressure in the channels of the manifold is approximately 0.70 bar if the vacuum valve is fully open. Lower vacuum pressures have not been reached. The second reason for the relatively high vacuum pressure are the large fly heights, as can be seen in Figure 5.16. Large fly heights result in a large mass flow to the vacuum pump, which makes it difficult to go to very low vacuum pressure levels. It is expected a lower vacuum pressure is reached in the second demonstrator, because of the smaller outlet restriction holes and the ability to fly at lower fly heights. The latter is possible due to the higher air film stiffness.

As said before, the fly heights are larger than expected. It is known from the model in Chapter 3, that the performance of the system is optimal for a β of 2.1. As the average pocket depth is equal to 13 µm, the optimal fly height would be equal to 11.8 µm, which is significantly lower than the realised fly heights. The large fly heights can be explained by the curvature of the manifold, which is not completely removed by the addition

of the aluminium plate. Most likely, the air film stiffness is not high enough to deform the wafer to the air bearing surface. Therefore, the wafer must fly higher to float freely. Something else that can be noticed in the measurement plot of the fly height, is the large spread of approximately ±2 µm in the measurements. The precision of the height measurement is influenced by a couple of variables. First of all, the height reference measurement has turned out to be challenging. Small movements of the wafer influence the height measurement, resulting in an negative off-set of a few microns. Secondly, the measurement is influenced by the variations in vacuum pressure. The vacuum pressure is realised by a vacuum pump, which is situated in the basement of the university. The pump creates a vacuum in a large pressure tank. The pressure in this tank fluctuates, depending on how much vacuum is consumed. As the set-up consumes a relatively large amount of air, the vacuum pressure over the different measurement vary. The fly height is quite sensitive to changes in the vacuum pressure. This can be solved by adding a control loop to the system, which controls the vacuum pressure. Another solution could be to limit the mass flow to the vacuum pump. It is decided to go for the last solution, which is implemented in the second demonstrator. It is expected that the mass flow in the second demonstrator is considerably less, because the diameter of the outlet restrictions is smaller.

The force in Figure 5.17 shows a decreasing trend, which can be explained by the increase in fly height. There is no direct influence of the fly height on the force. However, if the fly height becomes larger, the pressure difference in the thin film decreases and the force becomes smaller. The measurements show a spread of approximately ±2 mN. This can be explained by the large amplification factor of the amplifier, which also amplifies the sensor noise. Another cause are the variations in the force reference measurement. The force reference measurement, which should be zero before and after measuring, shows a variation in the range of ±1 mN.

5.3.1. Motor Function

The motor function is compared with the numerical model. The measured feed pressures and vacuum pressures are inserted in the model, by making use of the curve fit through the averages. The wavy surface of the surface roughness measurements in Section 5.1.1 is modelled as well. The zero load condition is used to calculate the fly height and the corresponding viscous traction force. In the model, the discharge coefficients from the flow measurements and the measured pocket depth of 13 µm are used. The measured and modelled fly height can be seen in Figure 5.18. They are in the same order of magnitude and they follow the same trend line. A constant off-set of about 5 µm can be noticed. The modelled fly height is lower than the measured fly height. The force can be found in Figure 5.19. For the calculation of the modelled force it is assumed that the wafer fully covers 64 cells. The influence of other, not fully covered cells is assumed to be negligible. The measured force is approximately 1/3 of the modelled force. The comparison between the modelled and measured force is not completely fair. One of the reasons for the difference between the modelled and measured force is the difference in fly height. Due to the smaller fly heights in the model, the pressure difference in the thin film is larger, which results in a larger force.

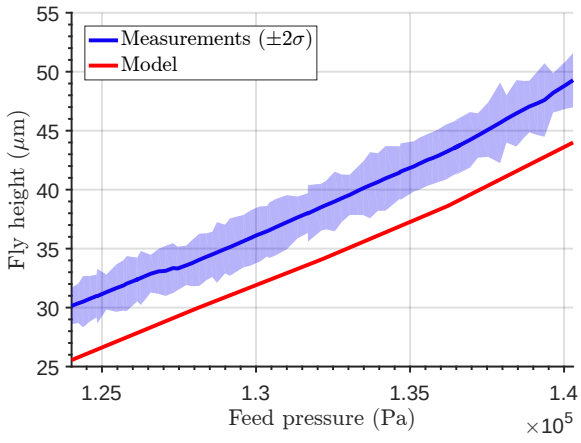

Figure 5.18: The measured and modelled fly height.

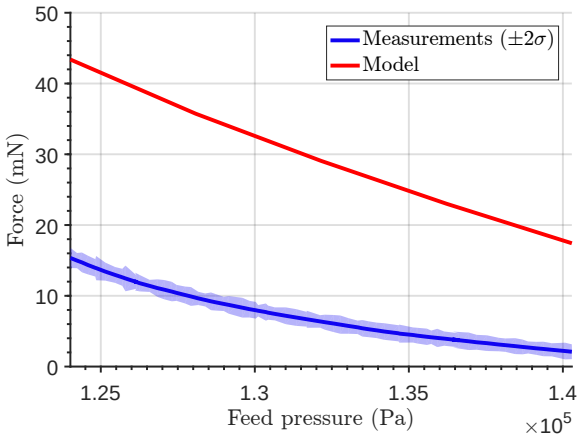

Figure 5.19: The measured and modelled force.

The differences between the model and the measurement can be caused by several factors. First of all, in the model it is assumed the fly height is uniform over the entire surface. Because the fly height is only

measured at one point this assumption, cannot be validated. In reality, the fly height differs due to the curvature of the manifold and the pressure differences over the manifold as a result of the pressure losses. This brings us directly to the second factor of uncertainty, which is the uniformity of the feed pressure and vacuum pressure over the air bearing surface. Earlier in this section, it has already been shown that pressure losses occur in the manifold. While the pressure losses of the feed pressure are small, the vacuum pressure losses are significant and cannot be neglected. To have a more accurate measurement of the pressures they are both measured on top of the manifold. However, the pressure drop from the sides towards the middle of the surface is unknown. The last uncertainty in the model are the flow restriction models. The restrictions are modelled to have the pressure drop over the orifice restriction area. In reality, there is also a pressure drop over the curtain area when the air enters the thin film at the inlet and leaves the thin film at the outlet. The pressure drop can be included in the flow model by lowering the discharge coefficient of the restriction but the exact influence is difficult to predict. The combination of these three uncertainties result in a difference between the measurement and the model. Thus, the discrepancies between the model and the experiment can be clearly explained and related to the fabrication methods. The model shows that the underlying physics are well understood. Therefore, the numerical model can be used to design the second demonstrator.

5.3.2. Bearing Function

Unfortunately, the measurements of the bearing stiffness have not led to any results. The change in fly height, due to the increase in weight, is too small in comparison with the variations of the fly height measurements. This is explained with a calculation of the model, which is valid as there is a reasonable match between the model and the measurements for the motor function. At the initial feed pressure of 1.24 bar and the vacuum pressure of 0.75 bar the fly height in the model is equal to 25 µm. The corresponding stiffness per cell is equal to $7.40 \times 10^4\,\mathrm{N\,m^{-1}}$, which is calculated with the numerical model as well. This is larger than the stiffness, which has been calculated in Section 4.1.2. The difference can be explained by the increase in fly height, which results in a larger pressure difference over the inlet restriction. If it is assumed that only the 64 fully covered cells add bearing stiffness to the system, the total stiffness is equal to $4.73 \times 10^6\,\mathrm{N\,m^{-1}}$. This means that if a mass of for example 200 g is added to the wafer, the fly height becomes 0.41 µm smaller. Obviously, this fly height difference cannot be measured with the current set-up. The variations in the fly height are already in the range of ±2 µm. The accuracy of the height sensor, which is about 0.6 µm, is also too large for what has to be measured.

5.4. Conclusion

The first demonstrator is realised and is used to validate the model. For the realisation of the demonstrator different manufacturing methods have been developed. The manifold is made out of laser-cut PMMA plates, which are bonded together by industrial 3M double sided tape. Pressure losses occur in the manifold, especially for the vacuum, which is difficult to transport. The air bearing surface is manufactured in a PCB plate. The pockets, which are measured to have a depth of 13 µm, are realised by etching away the copper. The inlet and outlet restrictions are drilled directly in the PCB plate. The restriction flow measurements show a close match with the ideal orifice flow. The first demonstrator is installed in the measurement set-up and the relevant variables (feed pressure, vacuum pressure, fly height and force) are measured. The fly height of a freely floating wafer is higher than expected, which is probably caused by the curvature of the manifold and the low air film stiffness. Overall, there is reasonable match between the model and the measurements. The trend line of model and measurement well agree. The measured force is approximately 1/3 of the modelled force. The difference can be explained by the non-uniform pressures and fly height, the uncertainty of the flow restriction model and the mismatch between the modelled and measured fly height. Unfortunately, the bearing function could not be measured, due to the relatively large variations in the fly height measurements, and the limitations of the fiberoptic sensor. Thus, everything is ready for the design of the second demonstrator. The measurement set-up of the first demonstrator can be re-used for doing the measurements on the second demonstrator.

6

Design Second Demonstrator

In this chapter, the design of the second demonstrator is presented. The design is based on the realisation and validation of the first demonstrator, which is presented in Chapter 5. First, the design overview and the realisation of the restrictions are discussed. Then, the theoretical performance is calculated and the stability of the system is checked in a dynamic analysis.

6.1. Design Overview

The second demonstrator consists of three main components, similar to the first demonstrator. These components are the air bearing surface, the restrictions, and the manifold. The main difference between the first and the second demonstrator is the restriction layer. This component is discussed in depth. The air bearing surface and the manifold are designed in the same way as in the first demonstrator, which is described in Chapter 4.1. Therefore, the final design of the second demonstrator is visually similar as the design of the first demonstrator. It is shown in the render in Figure 4.1.

6.1.1. Restrictions

In the second demonstrator, the outlet restrictions are drilled directly in the PCB air bearing surface. They have a diameter of 0.3 mm, as discussed in Section 3.3.1. The PCB manufacturer is able to drill holes down to a diameter of 0.2 mm, so the 0.3 mm holes are certainly feasible. The design guide line from Section 3.3.1 states, that the inlet restrictions should be as small as possible, to achieve a high air film stiffness. Therefore, the inlet restrictions are realised in an additional layer, which is placed underneath the PCB air bearing surface. This can be seen in Figure 6.1. The additional restriction layer has small holes at the location of the inlets, which are the inlet restrictions of the system. The holes in the extra restriction layer are larger at the location of the outlets, such that the 0.3 mm diameter hole in the PCB air bearing surface is the dominant restriction for the outlets. The advantage of the second demonstrator is the larger stiffness and reduced vacuum flow, compared to the first demonstrator. If the stiffness of the air film is larger, it has an increased ability to deform the wafer to the shape of the air bearing surface. It can therefore better compensate for slight curvatures of the air bearing surface. This means that, in theory, the fly height can be decreased which results in a better performance of the system.

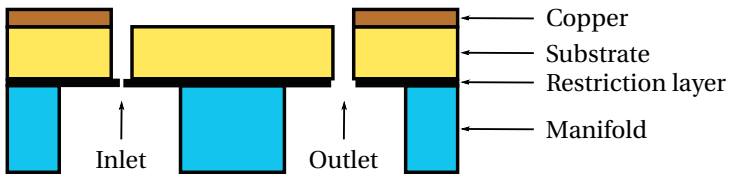

Figure 6.1: Cross-section of the layers of the second demonstrator. An additional layer for the inlet restrictions has been added between the PCB air bearing surface (yellow) and the manifold (blue).

It must be noted, that the extra layer with inlet restrictions does introduce 'dead' volumes at the inlet restrictions. This can be seen in Figure 6.1. The diameter of the holes at the locations of the inlets is chosen

be 0.3 mm as well, in order to have some safety margins in the aligning of the holes in the air bearing surface and the additional restriction layer. The influence of such volumes is presented in Section 2.6.3. The volumes decrease the damping of the air film. The exact influence of the volumes on the dynamic stability in this specific design is investigated in a dynamic analysis in Section 6.3.

Many different methods and materials have been tried to realise the orifice inlet restrictions. They are described in Appendix G. The best results are obtained by laser-cutting the inlet restrictions in a 0.5 mm stainless steel plate (AISI 304). The holes have an average diameter of 0.12 mm. This is not as small as was aimed for, but it is still sufficiently small for achieving a high air film stiffness. The laser-cut inlet restrictions have been tested in an initial restriction measurement, to determine the mass flow through the orifice as a function of the pressure difference. The measurement set-up is described in Appendix F and the results can be seen in Figure 6.2. The measured data shows quite a large deviation of approximately ±15%. This relatively large variation is a result of the laser-cutting. On average the orifice hole have the same diameter, but the production process often leaves burrs at the edges, which influence the effective orifice area. The ideal orifice formula (Equation 3.2) and the Jobson orifice formula (Equation 3.3) are fitted to the average curves of the measured data. The discharge coefficients of the ideal orifice flow and Jobson orifice flow are 0.56 and 0.46, respectively. The Jobson orifice flow clearly better fits the measured data. The 0.3 mm diameter outlet restrictions are tested in the set-up as well. As the final outlet restrictions are drilled by the PCB manufacturer, it is not possible to test those in this phase of the project. To have some initial insight in the discharge coefficient of the outlet restrictions, some 0.3 mm diameter holes have been drilled manually in a piece of 1.55 mm PCB. The mass flow is shown in Figure 6.3. The variance of the measured data is smaller compared to the inlets. The ideal orifice flow and Jobson orifice flow show a reasonable match with the measured data, with a discharge coefficient of 0.66 and 0.53, respectively. The Jobson orifice flow shows the best agreement with the measured data.

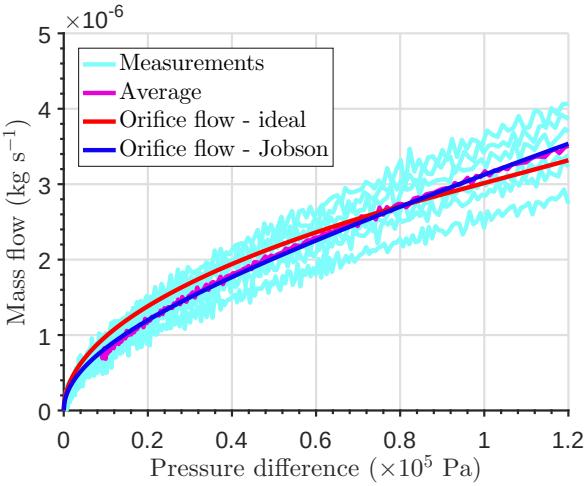

Figure 6.2: Mass flow data inlet restriction.

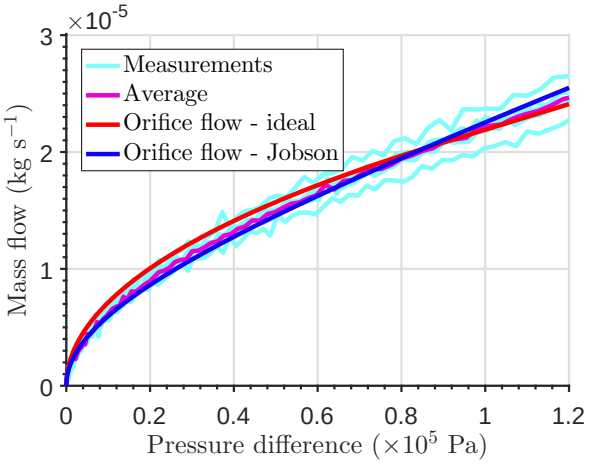

Figure 6.3: Mass flow data outlet restriction.

Using the Jobson orifice formula and the measured discharge coefficient of the outlet restriction, the outlet diameter and the vacuum pump capacity is checked again. The results can be seen in Figure 6.4. The chosen vacuum pressure of 0.7 bar corresponds to a maximum outlet orifice diameter of 353 µm, in order to use maximum 20% of the vacuum pump capacity. This confirms that a diameter of 300 µm is well within the limits. The modelled air film stiffness per cell and the required feed pressure for a certain inlet diameter can be seen in Figure 6.5. In this model, the discharge coefficients of the flow restrictions measurements are used. Furthermore, the pocket depth is equal to 13 µm, which is described in Chapter 5. For the optimal performance ratio, the corresponding fly height above the dam is equal to 11.8 µm. For an inlet diameter of 120 µm, the stiffness per cell is equal to $1.21 \times 10^5\,\mathrm{N\,m^{-1}}$, with a corresponding upstream feed pressure of 1.34 bar. The air film stiffness of the active cells of the second demonstrator is significantly higher than the air film stiffness of the active cells of the first demonstrator. At the fly height of 11.8 µm, the air film stiffness is approximately 10 times larger.

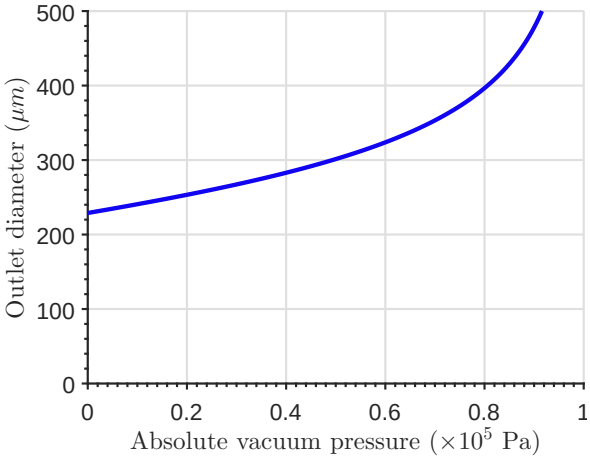

Figure 6.4: Maximum outlet diameter for a given vacuum pressure with Jobson orifice flow, such that the vacuum flow is less than 20% of the maximum vacuum pump capacity.

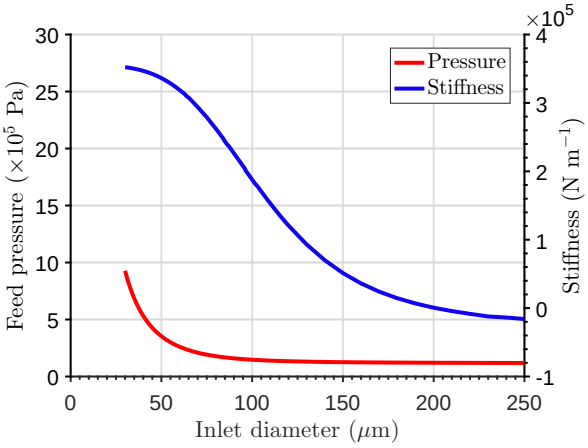

Figure 6.5: Feed pressure and stiffness per cell with Jobson orifice flow.

6.2. Theoretical Performance

Similar as for the first demonstrator, the theoretical performance of the second demonstrator can be calculated. One actuator cell of the second demonstrator, with a pocket of 13 µm, can provide a viscous traction force on the wafer of 1.01 mN, corresponding to a force per unit area of 10.06 N m^{-2}. The maximum angle is equal to:

$$\theta = \arcsin\left(\frac{\bar{F}}{\rho t g}\right) = 57° \tag{6.1}$$

With a corresponding acceleration of the wafer of:

$$a = \frac{\bar{F}}{\rho t} = 8.2\,\mathrm{m\,s^{-2}} \tag{6.2}$$

Again, in practice the wafer can fully cover 64 actuator cells. Taking this into account, the maximum angle θ is equal to 43°, which corresponds to an acceleration of 6.7 m s^{-2}. The performance is worse than that of the first demonstrator, but the comparison is not completely fair. The pocket depth, which has a big influence on the viscous traction force, is decreased from 16.5 µm to 13 µm. Moreover, it is expected that the fly height in the second demonstrator is lower, because of the increased air film stiffness. The lower fly height results in a better performance of the system, because the pressure difference over the thin film restriction is larger.

6.3. Dynamic Analysis

In Section 2.6, it has already been shown that the stiffness and damping in a thin film of air are frequency dependent. In this section, both are determined for the designed geometry of the second demonstrator, by performing a dynamic analysis. Only the active surface cell is analysed, as this design is most sensitive for dynamic instabilities. The influence of the volumes at the inlet restrictions on the dynamic stability is investigated as well.

6.3.1. Perturbed Reynolds Equation

The dynamic analysis is performed by perturbing the Reynolds equation. The perturbation technique in one dimension has been explained in Section 2.6.1. For the two-dimensional situation the analysis is very similar, so the derivation is omitted here. The perturbed Reynolds equation is given by:

$$-\frac{1}{12\eta R_s T}\nabla\left(p_0 h_0^3 \nabla\tilde{p} + \tilde{p} h_0^3 \nabla p_0 + 3 p_0 h_0^2 \tilde{h} \nabla p_0\right) + \frac{1}{R_s T} j\omega\left(p_0\tilde{h} + h_0\tilde{p}\right) = 0 \tag{6.3}$$

In which the nabla operator is equal to $\nabla = \left[\frac{\partial}{\partial x}, \frac{\partial}{\partial y}\right]$. The static solution is given by p_0 and h_0 and the perturbed solution is given by $\tilde{p}$ and $\tilde{h}$. The restriction measurements have shown that the mass flows at the

inlets and outlet can be formulated as:

$$\begin{aligned} \text{inlet: } \dot{m}_\text{i} &= C_\text{d,i} A_\text{i} \sqrt{\frac{1}{R_\text{s} T} \left(p_\text{s}^2 - p^2\right)} \\ \text{outlet: } \dot{m}_\text{o} &= C_\text{d,o} A_\text{o} \sqrt{\frac{1}{R_\text{s} T} \left(p^2 - p_\text{v}^2\right)} \end{aligned} \tag{6.4}$$

In which the pressure p is the pressure in the thin film, downstream the inlet restriction and upstream the outlet restriction, respectively. Using the same procedure as in Section 2.6 the final linearised and perturbed mass flow equations at the inlet and outlet are equal to:

$$\begin{aligned} \text{inlet: } \dot{m}_\text{i,lin} &= \left.\frac{\partial \dot{m}_\text{i}}{\partial p}\right|_{\text{p}_\text{0,i}} \tilde{p} \\ \text{outlet: } \dot{m}_\text{o,lin} &= \left.\frac{\partial \dot{m}_\text{o}}{\partial p}\right|_{\text{p}_\text{0,o}} \tilde{p} \end{aligned} \tag{6.5}$$

The results for the dynamic stiffness and damping can be seen in Figure 6.6 (solid lines). The stiffness at low frequencies is similar to the static stiffness, which is equal to $1.21 \times 10^5\,\text{N m}^{-1}$ for each cell. It increases to a final value of $5.95 \times 10^5\,\text{N m}^{-1}$. The wobble from 1×10^4 Hz to 1×10^6 Hz can be explained by the pocket depth of 13 µm, which introduces a different dynamic behaviour compared to conventional air bearings with flat bearing surfaces, which have been modelled in Section 2.6. The damping starts at a positive value of $64.4\,\text{N s m}^{-1}$ and reduces to zero for high frequencies. At a frequency of approximately 1000 Hz the stiffness starts to increase and the damping starts to decrease.

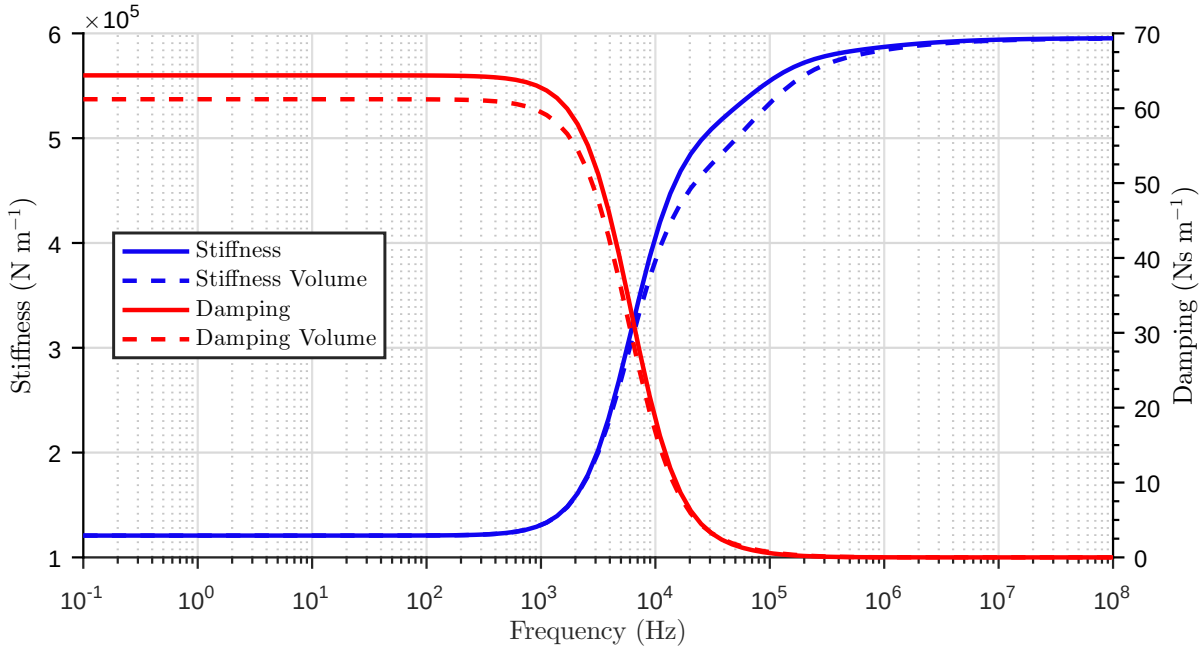

Figure 6.6: Frequency dependent stiffness and damping of the active cell.

6.3.2. Volumes

As mentioned before, the second demonstrator has dead volumes downstream the inlet restrictions, which are introduced by adding the extra steel layer for the inlet restrictions beneath the PCB surface. The volumes are visualised in Figure 6.1. The PCB manufacturer is able to produce holes down to a diameter of 0.2 mm in the 1.55 mm thick PCB. However, initial tests have proven that aligning the holes in the spring steel and the PCB is a complicated procedure. The diameter of the holes in the PCB at the locations of the inlets, is chosen

to be 0.3 mm, similar to the outlet diameter. It is investigated if these volumes cause pneumatic hammer by adding the volumes to the dynamic model. Again, following the same procedure as in Section 2.6 the final linearised and perturbed equation for the mass flow at the inlet including the 'dead' volume is equal to:

$$\dot{m}_{\mathrm{i},2} = \left.\frac{\partial \dot{m}_{\mathrm{i}}}{\partial p}\right|_{\mathrm{p_{0,i}}} \tilde{p} - \frac{V\tilde{p}}{R_{\mathrm{s}}T} j\omega \tag{6.6}$$

The influence of the volume is visualised in Figure 6.6. The stiffness does not change as the static pressure remains constant in the volume. There is a change in damping, however. The damping for low frequencies is decreased from $64.4\,\mathrm{N\,s\,m^{-1}}$ to $61.2\,\mathrm{N\,s\,m^{-1}}$, but it is still positive. Again, the damping reduces to zero as the frequency increases. As the damping is positive for low values of the perturbation frequency, it can be concluded the volumes do not cause pneumatic hammer and the air bearing system is stable.

6.4. Conclusion

In this chapter, the design of the second demonstrator is presented. As the first demonstrator, the second demonstrator consists of three components; the air bearing surface, the restrictions, and the manifold. The air bearing surface and the manifold are similar to those of the first demonstrator. The outlet restrictions are drilled directly in the PCB air bearing surface and have a diameter of 0.3 mm. The main difference can be found in the manufacturing of the inlet restrictions. They are laser-cut in an additional layer of steel and have a diameter of 0.12 mm. The additional layer is inserted between the PCB air bearing surface and the manifold. The air flow to the vacuum pump is well below 20% of the maximum pump capacity, and the air film stiffness is significantly larger than the air film stiffness of the first demonstrator. Therefore, it is expected that the fly heights are lower, which results in larger traction forces on the wafer and a better performance of the system. The extra layer of the inlet restrictions does have an influence on the damping of the air film, but a dynamic analysis shows that the system is still stable.

7

Realisation and Validation Second Demonstrator

This chapter describes the realisation and validation of the second demonstrator. The realisation, measurement set-up, and measurement procedure of the second demonstrator are discussed first. After that, the second demonstrator is validated by comparing the performance of both the active and passive surface with the numerical model. The differences between the measurements and the model are analysed. Lastly, the fly height and air film stiffness of the two surfaces are matched to realise the final demonstrator.

7.1. Realisation

In the second demonstrator, similar to the first demonstrator, three main components can be identified. These are the manifold, the air bearing surface, and the restriction layer. In this section, each component is discussed and the relevant measurements for the characterisation of the components are presented.

7.1.1. Air Bearing Surface

The air bearing surface of the second demonstrator is the same as the air bearing surface of the first demonstrator. Both have been fabricated on the same production panel at the PCB manufacturer. The main difference between the two PCB plates is the diameter of the restriction holes. For the second demonstrator, all the holes are dimensioned with a diameter of 0.3 mm. The pockets are verified to have an average depth of 13 µm, which is similar to pockets of the first demonstrator. The air bearing surface shows the same 'short' waviness, which has been measured in Section 5.1.1. The air bearing surface is measured on the white light interferometer, after bonding it to the manifold. The specifications of the interferometer can be found in Section 5.1.1. To characterise the flatness of the air bearing surface, the surface height is measured on a few lines of the surface. Figure 5.3 shows the lines, on which the surface height is measured. The results of the surface height on the lines in y-direction can be seen in Figure 7.2. The first two plots are measured on the active surface and show the locations and pocket depths of the pockets. The third plot is measured on the passive surface. The air bearing surface is clearly curved in a similar way as the air bearing surface of the first demonstrator. However, the height differences are significantly less. The largest height difference is found in the middle of the air bearing surface and is equal to approximately 30 µm. The decrease in height difference could be caused by the extra steel layer of the inlet restrictions, or a different orientation of the PMMA during the manufacturing of the manifold. Figure 7.3 shows the surface height measurement along the line D_1-D_2. The surface is curved in this direction as well, and the curvature is larger than the curvature in y-direction. The largest measured height difference is approximately 110 µm.

7.1.2. Restrictions

The flow restrictions are the main difference between the first and second demonstrator. In the second demonstrator, the outlet restrictions are drilled directly in the PCB plate by the PCB manufacturer. They have a diameter of 0.3 mm. The inlet restrictions are laser-cut in a plate of 0.5 mm stainless steel, which is done in the workshop (IWS) at the university. The holes have an average diameter of 0.12 mm. The laser-cutter is not really suitable to laser-cut very small holes. However, a workaround has been found. A detailed

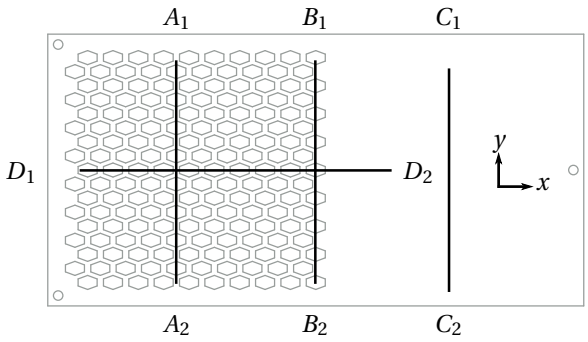

Figure 7.1: A top view of the air bearing surface. The specified lines (A_1-A_2, B_2-B_2 and C_2-C_2 in y-direction and D_2-D_2 in x-direction) are measured on the white light interferometer.

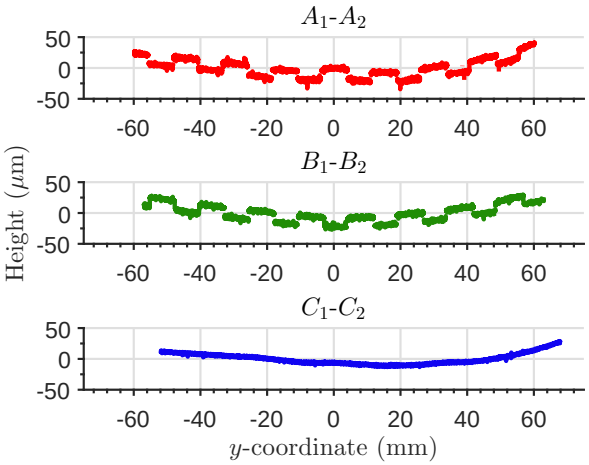

Figure 7.2: These plots show the surface height along the specified lines. A curvature of the air bearing surface can be noticed.

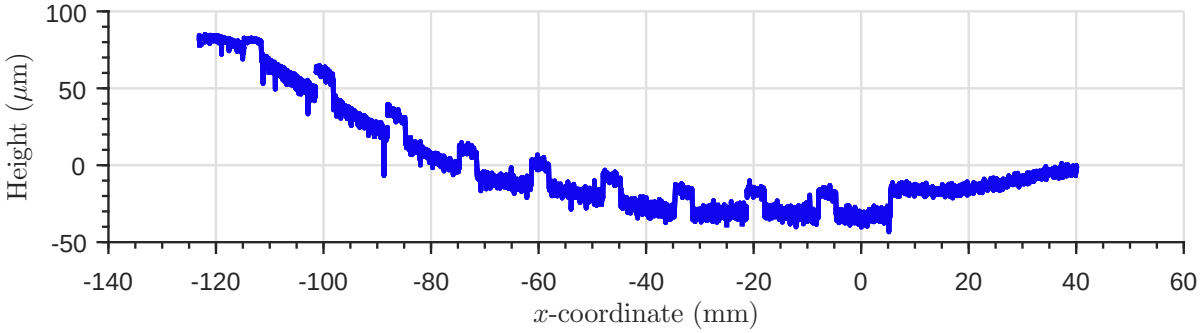

Figure 7.3: Surface height along the line D_1-D_2. The surface is curved towards the middle.

explanation of the fabrication method of these small holes is described in Appendix G. At the location of the outlets, larger holes of 1 mm diameter are laser-cut in the stainless steel. The stainless steel plate and the PCB plate are bonded together with the 3M double-sided tape. The double-sided tape has a very negative effect on the quality of the laser-cut steel. Therefore, the double-sided tape is laser-cut separately on the laser-cutter at industrial design, prior to the bonding process. Both inlets and outlets are tested in the flow measurement set-up, which is described in Appendix F. The tests are performed after the steel plate and PCB plate are bonded together. The results of the flow measurement of the inlet restriction can be seen in Figure 7.4. The measured data shows a spread of ±12%, which is less than the spread in the initial mass flow measurements in Section 6.1.1, but is still significant. The average data of the measurement is fitted with the mass flow data of the ideal orifice formula (Equation 3.2) and the Jobson orifice formula (Equation 3.3). The calculated discharge coefficients are equal to 0.72 (ideal) and 0.59 (Jobson). These values are different than the initial mass flow measurements in Section 6.1.1. The mass flows are larger than expected. The Jobson orifice model shows the best match with the average data and is used in the coming models. The results of the flow measurement of the outlet restriction can be seen in Figure 7.4. The measured mass flow curves lie very close together. The ideal orifice model and Jobson orifice model are fitted with the average data and a discharge coefficient of 0.80 (ideal) and 0.65 (Jobson) is calculated. Again, the Jobson orifice model shows the best match and is used in the coming numerical models.

7.1.3. Manifold

The manifold of the second demonstrator is realised in the same way as the manifold of the first demonstrator. The manufacturing method is explained in Appendix G. The pressure losses in the manifold are studied in both the active and passive surface. It is shown in Chapter 5, that the pressure losses are most severe for the vacuum pressure. Therefore, only the vacuum pressure losses are measured. As the outlet restrictions of the second demonstrator are smaller than the outlet restrictions of the first demonstrator, it is expected that the

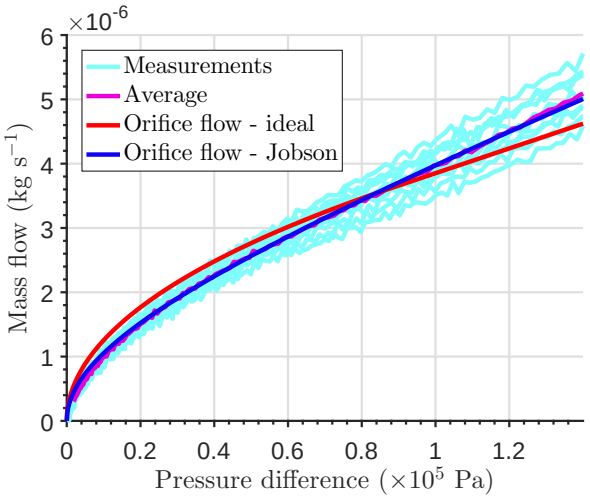

Figure 7.4: Mass flow data of the 0.12 mm inlet restriction.

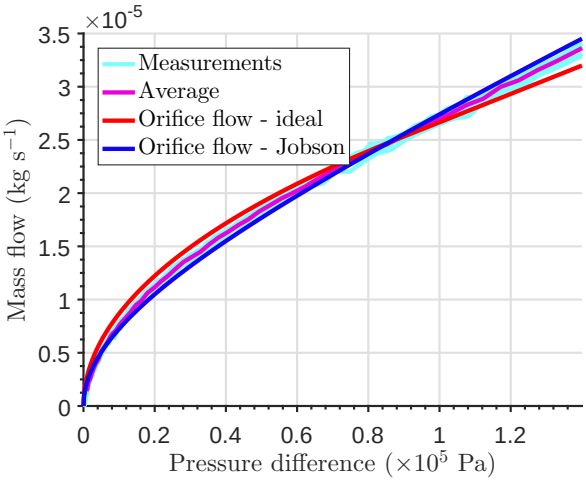

Figure 7.5: Mass flow data of the 0.3 mm outlet restriction.

pressure losses are smaller. The vacuum pressure is measured over the main channels and the side channels, as can be seen in Figure 7.6 for the active surface, and in Figure 7.7 for the passive surface. The results of the vacuum pressure in the main channels of the active surface can be seen in Figure 7.8. The initial vacuum pressure, which is measured below the manifold, is equal to 0.58 bar. Figure 7.8 shows that the pressure loss between the measurement below the manifold and the first outlet restriction is equal to 0.10 bar. The pressure losses in the main channels themselves are approximately 0.02 bar. The pressure losses in the side channels of the active surface can be seen in Figure 7.9. The measured vacuum pressures are slightly different for the side channels, which begin at the same location in the main channels. This means that the manifold is not perfectly symmetric. Differences can be caused if the PMMA plates of the manifold are not perfectly aligned during the bonding. Another cause of the difference can be variations in the tubing towards the pneumatic connections in the manifold. Overall, a pressure loss of approximately 0.01 bar can be identified.

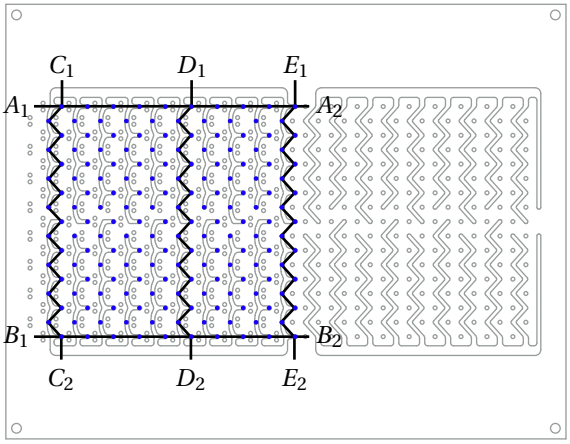

Figure 7.6: The measured channels for the characterisation of the pressure losses in the manifold at the side of the active surface.

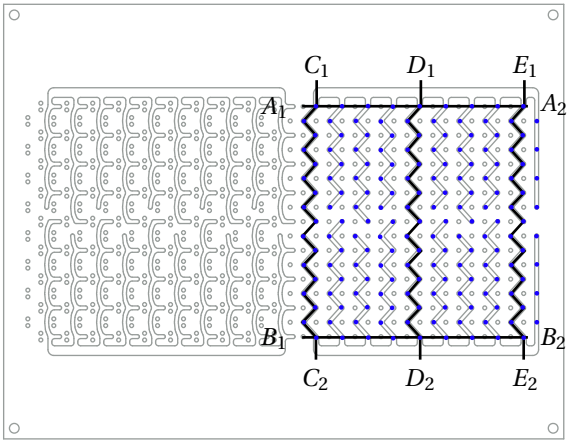

Figure 7.7: The measured channels for the characterisation of the pressure losses in the manifold at the side of the passive surface.

The pressure losses in the main channels of the active surface can be seen in Figure 7.10. The initial vacuum pressure, which is measured below the manifold, is equal to 0.56 bar. The pressure loss between the initial measurement and the first outlet restriction is approximately 0.08 bar, which is less than for the active surface. The pressure losses in the main channels themselves are approximately 0.02 bar, which is similar to the active surface. Figure 7.11 shows the pressure losses in the side channels of the passive surface. Again, the pressures at each side of the manifold are different. It can also be seen that the pressure losses are larger. The pressure losses from the sides to the middle of the manifold are equal to approximately 0.02 bar, which is larger than the pressure losses in the side channels of the active surface. The difference can be

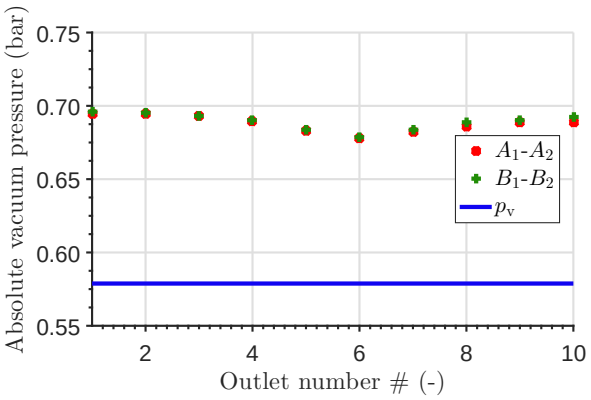

Figure 7.8: Vacuum pressure in the main channels of the active surface. The initial vacuum pressure p_v is equal to 0.58 bar.

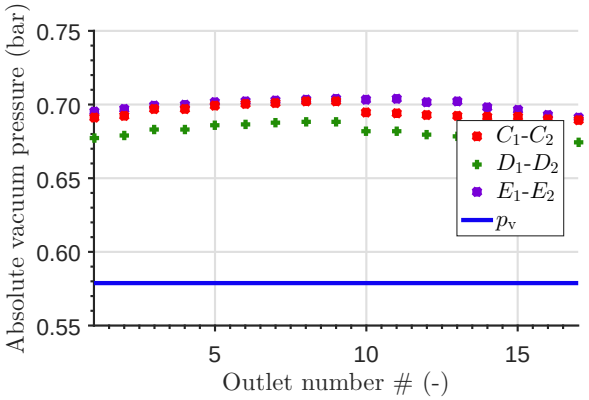

Figure 7.9: Vacuum pressure in the side channels of the active surface. The initial vacuum pressure p_v is equal to 0.58 bar.

explained by the different geometries of the side channels. To conclude, the pressure losses in the main channels and side channels of the active and passive surface, are significantly less than the pressure losses in the first demonstrator. However, they are still present and cannot be neglected.

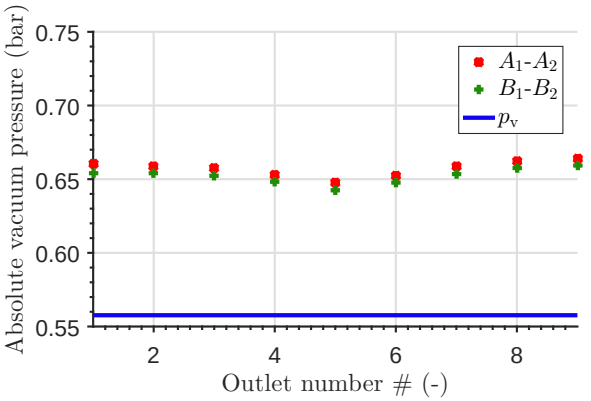

Figure 7.10: Vacuum pressure in the main channels of the passive surface. The initial vacuum pressure p_v is equal to 0.56 bar.

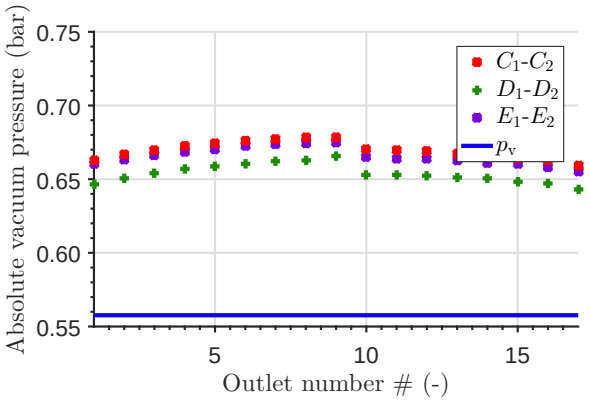

Figure 7.11: Vacuum pressure in the side channels of the passive surface. The initial vacuum pressure p_v is equal to 0.56 bar.

7.2. Experimental Validation

The performance of the second demonstrator are checked and compared to the numerical model. In this section, the set-up and measurement procedure are described. As these are largely the same as for the first demonstrator, the main differences are discussed.

7.2.1. Experimental Set-up

The experimental set-up, which is shown in Figure 7.12, is very similar to the set-up which has been used for the validation of the first demonstrator (Section 5.2). The main difference can be found in the pneumatics. To reduce the variations in feed pressure and vacuum pressure, an extra pressure tank is added to the system. The tanks are placed downstream the proportional valves. In this way, they are able to level out any pressure fluctuations.

In Figure 7.12, the aluminium plate for straightening the air bearing surface is still visible. However, the aluminium plate is not used to straighten the manifold and air bearing surface. The screws to do so are removed. The sensors in the set-up are the same as in the set-up of the first demonstrator. They are described in Section 5.2.1 and the locations are pointed out in Figure 5.13.

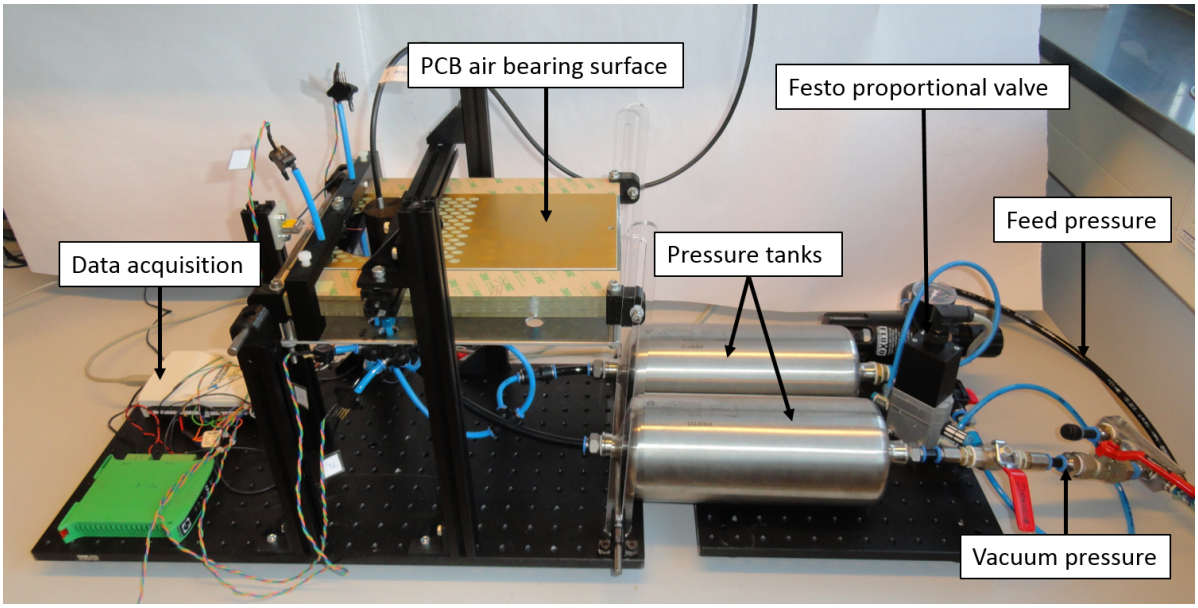

Figure 7.12: Experimental set-up of the second demonstrator.

7.2.2. Measurement Procedure

The measurement procedure is also copied from the first demonstrator. It is described in Section 5.2.2. The feed pressure is slowly increased with the Festo proportional valve, and during the measurement the feed pressure, vacuum pressure, fly height, and force are measured. This is done for both the active surface and the passive surface, which are connected to the pressure supplies one after another. For the latter, the force is irrelevant and is be measured. It is decided to not measure the force in y-direction. This force is irrelevant for showing the proof of concept, in which the fly height and stiffness of the active surface and passive surface are matched. The validation of the system in the main transport direction is more important.

An addition to the measurement procedure is the measurement of the local fly heights. These are measured on the active surface. By moving the height sensor to different locations on the wafer, the local fly height can be mapped.

7.3. Results Active Surface

The results of the measurements of the active surface can be seen in Figure 7.13-7.16. In total, 15 measurements have been performed. They show less variation, which is most likely caused by the pressure smoothening in the pressure tanks. It is useful to mention that, during the measurements, no signs of pneumatic hammer are observed. The wafer has a stable fly height. Therefore, it can be concluded that, at least for this set-up, the dynamic analysis in Section 6.3 is a reliable way to analyse the dynamic stability of the air bearing system. The measurements are done for approximately 120 s. The initial vacuum pressure is set at approximately 0.69 bar, which is lower than for the first demonstrator. The second demonstrator consumes less air, which makes it possible to go to lower vacuum pressures. The wafer starts to float freely at a feed pressure of 1.70 bar. The fly height is then equal to 23 µm, which is another difference with the first demonstrator. Lower fly heights can be achieved in the second demonstrator. This is a result of the higher air film stiffness. The trends of the measured data are similar to the results of the first demonstrator. The feed pressure slowly increases from 1.70 bar to 2.20 bar. The increase in feed pressure results in an increase in vacuum pressure and fly height. The vacuum pressure increases slightly, from about 0.69 bar to 0.74 bar, and the fly height increases from 23 µm to 41 µm. The force shows a decreasing trend. It starts at a value of 32 mN and decreases slowly to 13 mN. The data is averaged and the averages are fitted with a second order polynomial, which will be used in the comparison of the measured data with the numerical model.

7.3.1. Motor Function

The motor function of the active surface is compared with the model. This is done in the same way as has been done for the first demonstrator. The fitted curves of the feed pressure and vacuum pressure are inserted in

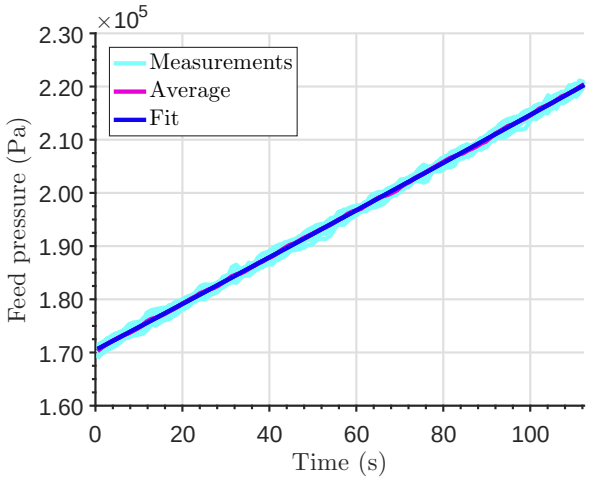

Figure 7.13: The measured absolute feed pressure over time.

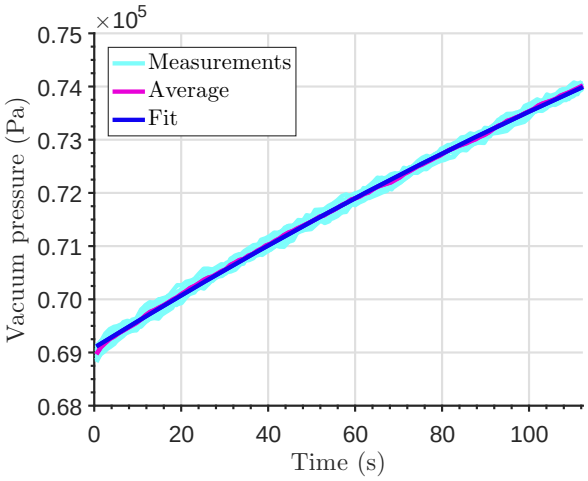

Figure 7.14: The measured absolute vacuum pressure over time.

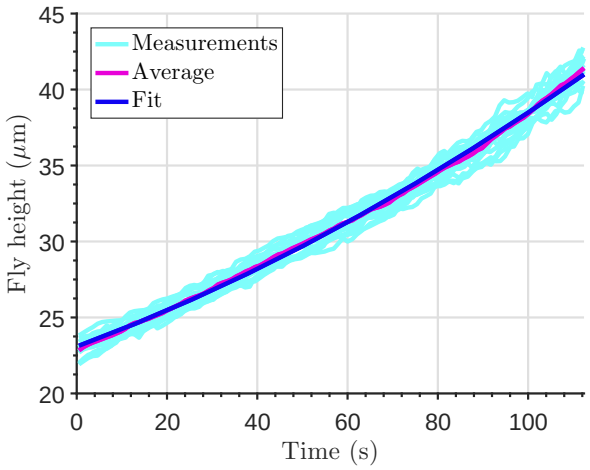

Figure 7.15: The measured fly height over time.

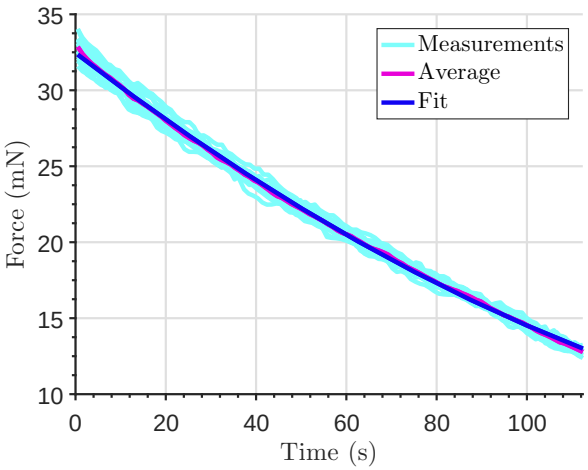

Figure 7.16: The measured force over time.

the numerical model in COMSOL. The zero load condition is used to calculate the fly height. The resulting fly height of both measurement and model can be seen in Figure 7.17. The curves have a difference of maximum 1.5 µm. The trends are not completely the same. The model shows a larger increase in the fly height for higher pressures, in comparison with the measurements. The force of the model and the measurement can be seen in Figure 7.18. The modelled force is calculated by assuming that only the 64 fully covered cells contribute. The lines are closer together than the measurements of the first demonstrator. However, the trend lines differ more. For the lower pressures, the measured force is about 70% of the modelled force at its minimum. The mismatch between the model and the measurements are investigated in Section 7.5.

7.3.2. Bearing Function

Unfortunately, the measurements of the air film stiffness have not been successful. It was expected that the fly height would be more stable, due to the limited vacuum flow and the addition of the pressure tank. Both are true, and the variations in fly height have become less. However, they are still too large for an accurate stiffness measurement. Therefore, the air film stiffness is not measured.

7.3.3. Local Fly Height

The local fly height of the wafer is measured on 25 different points on the active surface. The locations of these points are visualised by the black dots in Figure 7.19. The results can be seen in Figure 7.20. Each fly height is an average of three measurements on each location. The measurements show a relatively large spread of the fly height, which is in the range of 10 µm. A reason for the variations in fly height could be that the air film

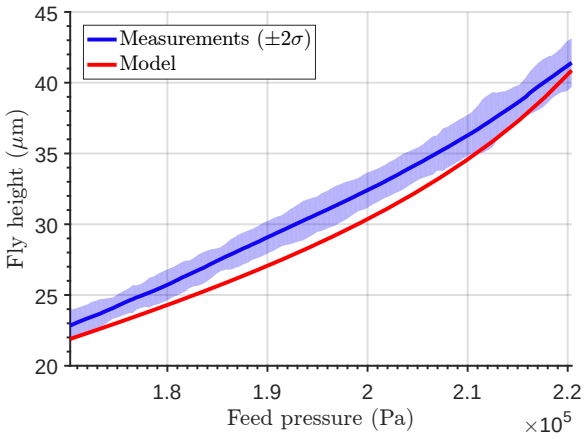

Figure 7.17: The measured and modelled fly height.

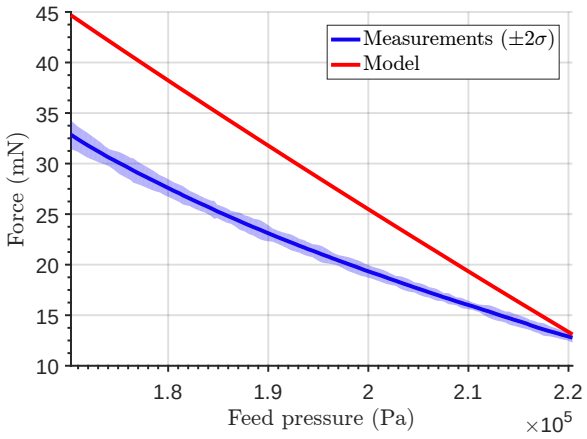

Figure 7.18: The measured and modelled force.

stiffness is not large enough to cope with the curvature of the air bearing surface. Interestingly, the fly height shows a decrease in the middle of the wafer, on the measurement line $(x,0)$. This decrease in fly height can be explained by taking a closer look at the surface roughness measurements of Section 7.1.1. In Figure 7.21, a close-up of the surface roughness measurement on the line A_1-A_2 in Figure 7.1 can be seen. The figure shows that the surface height is slightly larger in the middle of the surface, in comparison with the surface height of the dams on the left and the right. The height variation is in the order of 5 µm. Due to the increase in surface height, the fly height is less in the middle of the wafer. Moreover, two fly height peaks can be noticed in Figure 7.20. They are located on the measurement line $(0,y)$. The peaks can be explained by Figure 7.22. The wafer is located on the active surface. Therefore, the lowest fly heights in x-direction can be found at the edges of the wafer. The combination of the curved air bearing surface, the larger surface heights in the middle of the wafer, and the possible shortage of air film stiffness, result in the fly height profile in Figure 7.20. In previous measurements, the fly height is measured in the middle of the wafer. This corresponds with the coordinate $(0,0)$ in Figure 7.19. Clearly, these measurements do not represent the fly height of the entire wafer. The influence of the varying fly height is studied in Section 7.5.3.

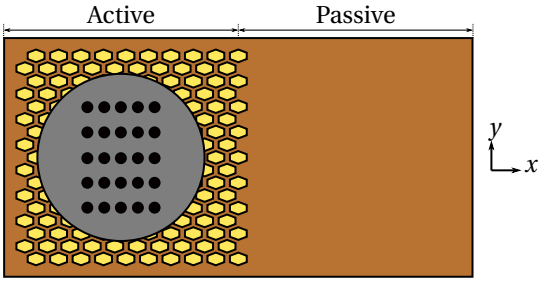

Figure 7.19: Locations of the local fly height measurement, which are indicated by the black dots. The origin of the coordinate system $(0,0)$ is placed at the location of the middle black dot.

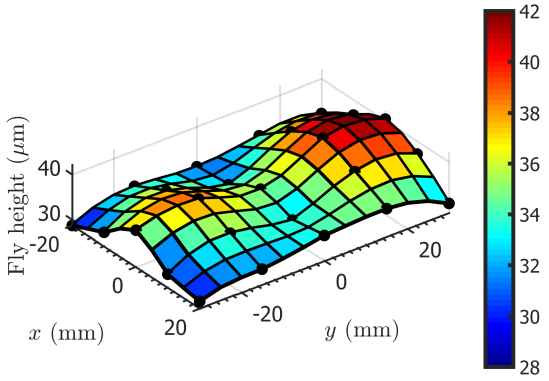

Figure 7.20: Measurements of the local fly height of the wafer.

7.4. Results Passive Surface

The results of the measurements of the passive surface can be seen in Figure 7.23-7.24. The measurements look very similar to the measurements of the active surface. Again, no signs of pneumatic hammer are observed. The measurements are done for approximately 80 s, and the initial vacuum pressure is set at approximately 0.81 bar. The wafer starts to float freely at a feed pressure of 1.48 bar. The fly height is then equal

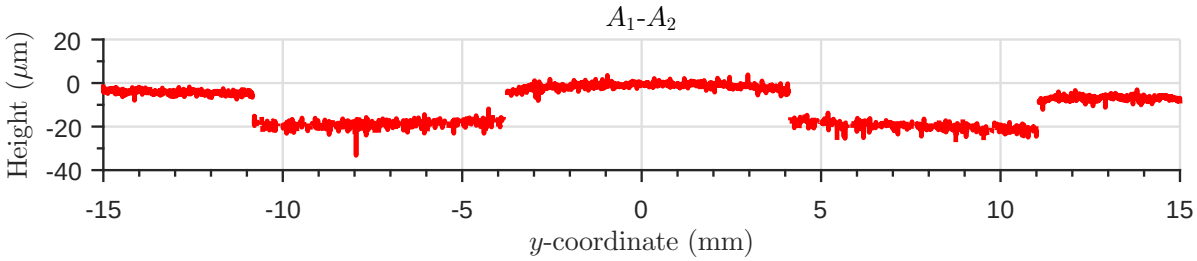

Figure 7.21: Close-up of the surface roughness measurement on the line A_1-A_2 in Figure 7.1.

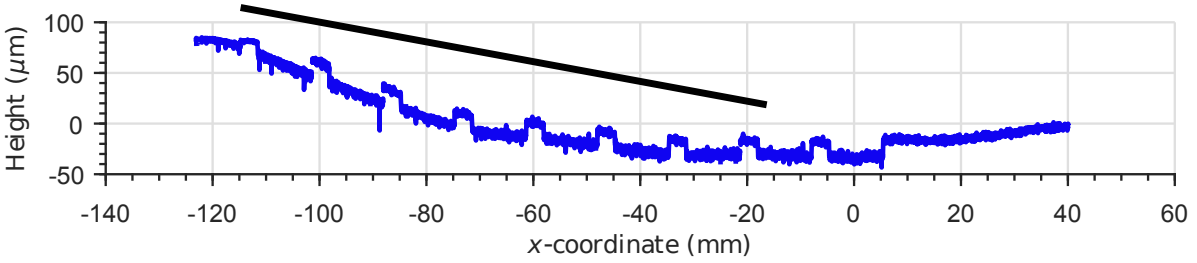

Figure 7.22: Surface roughness measurement on the line D_1-D_2 in Figure 7.1, including the wafer on top of the active surface. The fly height is the lowest at the edges of the wafer.

to 20 µm. The feed pressure increases from 1.48 bar to 1.88 bar. The increase in feed pressure results in an increase in vacuum pressure and fly height. The vacuum pressure increases slightly, from about 0.81 bar to 0.85 bar, and the fly height increases from 20 µm to 27 µm. The data is averaged and the averages are fitted with a second order polynomial. The curves of the feed pressure and vacuum pressure are inserted in the numerical model in COMSOL. The zero load condition is used to calculate the fly height. The resulting fly height of both measurement and model can be seen in Figure 7.26. The curves have a difference of approximately 3 µm and they show the same trend line. Overall, there is a reasonable match between the model and the measurements. Differences between them are investigated in Section 7.5.

7.5. Model Fitting

It is clear from Section 7.3 and Section 7.4, that the model does not fully describe the behaviour of the system. In this section, the differences between the model and the measurement are studied. This is done for the active surface, because for this section the differences for both the fly height and force can be studied. To have a better understanding of the system a sensitivity analysis is done first. The results of this analysis are used in tuning the model, by making use of the method of least squares. Lastly, the influence of the variations in the local fly height of the wafer on the active surface is modelled.

7.5.1. Sensitivity Analysis

In this sensitivity analysis, the influence of small variations of the relevant parameters are investigated. The relevant parameters are the feed pressure p_s, the vacuum pressure p_v, the inlet discharge coefficient $C_{d,i}$, and the outlet discharge coefficient $C_{d,o}$. Each parameter is varied with ±1%. The force and fly height are most sensitive for small changes in the vacuum pressure. This is shown in Figure 7.27 and Figure 7.28. The ±1% variation in vacuum pressure, which is equal to approximately 7 mbar, results in a variation in the fly height of ±1.5 – 3.5%, or ±0.3 – 1.5 µm. The force varies with ±3 – 9%, or ±1.2 – 1.4 mN. The influence of a small variation in the vacuum pressure is significant. In Section 5.1.3, it has already been shown that the vacuum pressure losses in the main channels are in the order of 0.02 bar and the vacuum pressure losses in the side channels are in the order of 0.01 bar. This means, that the maximum pressure difference is in the order of 0.03 bar, which is more than 1.5%. It has an influence on the local fly height of the wafer. The effect of the feed pressure and the discharge coefficients is less significant. The results are shown in Appendix E.2.

It is interesting to see that the trend lines of the measured fly height and force of the first demonstrator are much closer to the modelled curves than the trend lines of the second demonstrator. The main difference between the first demonstrator and the second demonstrator is the diameter of the inlet restrictions. The

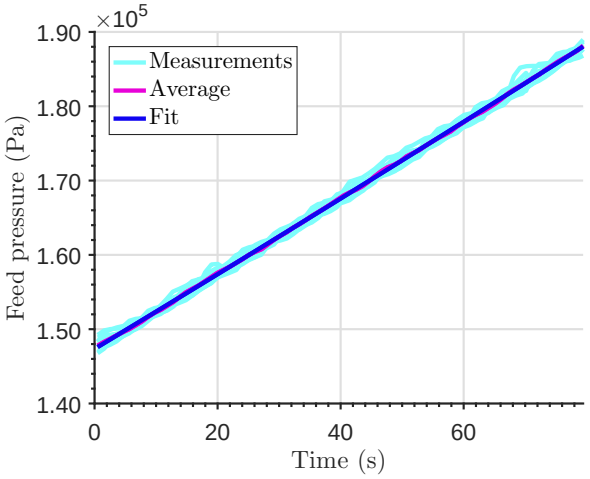

Figure 7.23: The measured absolute feed pressure over time.

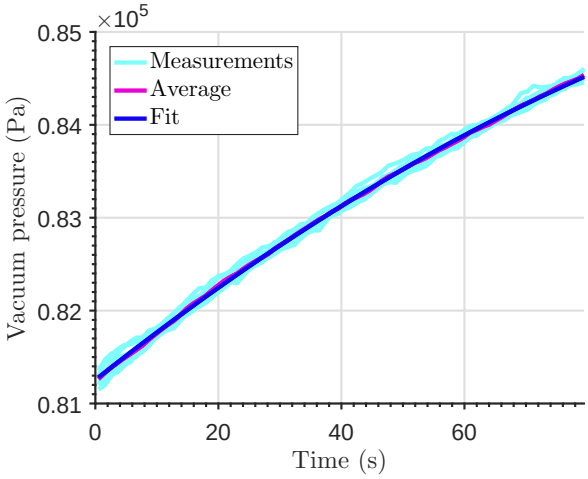

Figure 7.24: The measured absolute vacuum pressure over time.

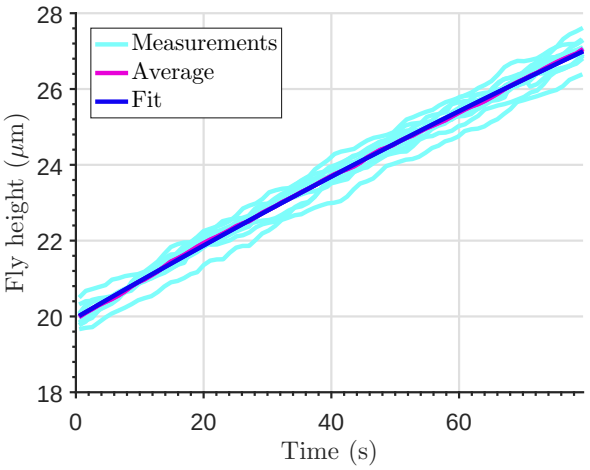

Figure 7.25: The measured fly height (above the dam) over time.

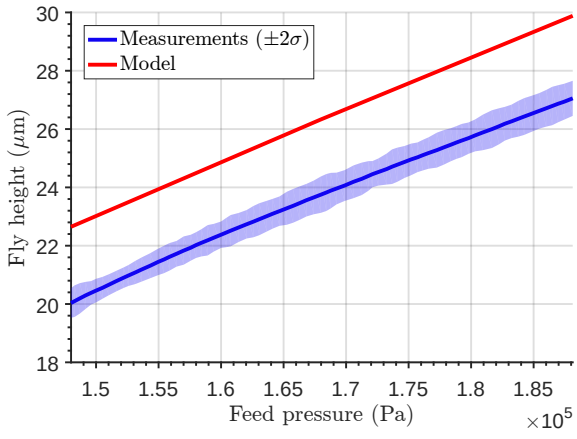

Figure 7.26: The measured and modelled fly height.

inlet restriction flow measurements in Section 7.1.2 show a large spread of ±12%. As the inlet restriction flow measurements of the first demonstrator show much less variation, the difference in trend lines could be explained by the large variations in the inlet restrictions of the second demonstrator. The influence of this variation is analysed in a new study, in which the inlet discharge coefficient is varied with ±12%. The results of the fly height and force can be seen in Figure 7.29 and Figure 7.30, respectively. The influence of a ±12% variation in the inlet discharge coefficient on the fly height and force is enormous. In the case of a larger inlet discharge coefficient, the fly height increases and the force decreases. In the case of a smaller inlet discharge coefficient, the fly height decreases and the force increases. The trend lines for an inlet discharge coefficient, which is 12% smaller than the original, are much closer to the measured trend lines. The absolute differences between the modelled and measured fly height and force do increase. This difference is probably caused by other factors, such as the non-uniform fly heights and vacuum pressure. It is likely that the measured inlet discharge coefficient is not correct. In practice, it is smaller than what is measured.

7.5.2. Least Squares Method

In the previous section, it is shown that the influence of small changes in the vacuum pressure is significant. Moreover, there is an uncertainty in the restriction models, especially in the discharge coefficient of the inlet restrictions. In this section, the model is fitted to the measurement by applying the method of least squares to the force and fly height. The method is well explained in [35]. The discharge coefficient of the inlet is estimated to be 12% lower than the originally value. It is equal to 0.52, instead of 0.59, which is measured in Section 7.1.2. The decrease of the inlet discharge coefficient is a result of the sensitivity analysis in the previous section. The parameters of interest are the discharge coefficients of the outlets and the vacuum

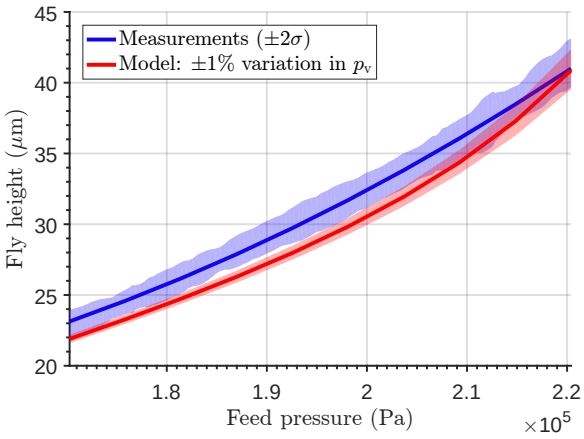

Figure 7.27: Comparison of the fly height of the model and the measurement. The vacuum pressure is varied with ±1%.

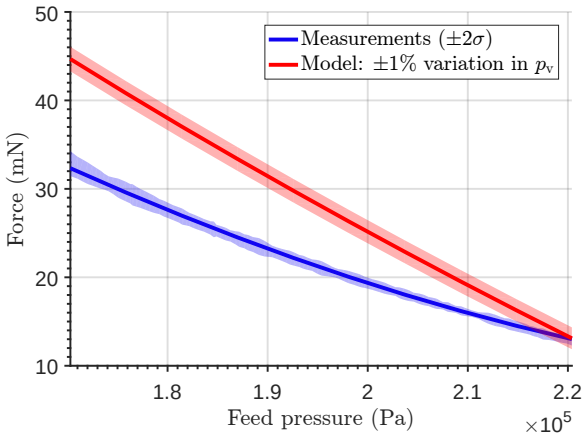

Figure 7.28: Comparison of the force of the model and the measurement. The vacuum pressure is varied with ±1%.

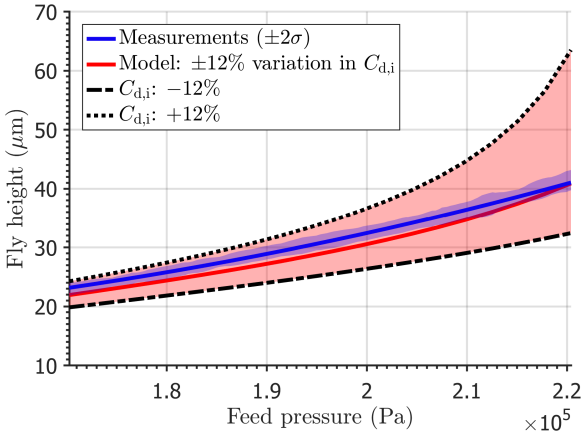

Figure 7.29: Comparison of the fly height of the model and the measurement. The inlet discharge coefficient is varied with ±12%.

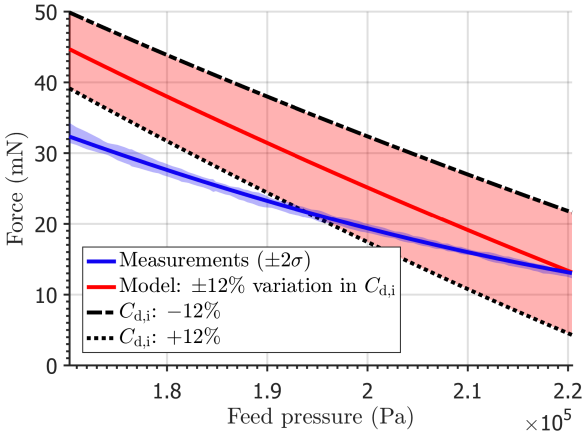

Figure 7.30: Comparison of the force of the model and the measurement. The inlet discharge coefficient is varied with ±12%.

pressure. As the feed pressure losses are small, the measured feed pressures are assumed to be correct. The method of least squares for matching the measured and modelled fly height and force results in a change in outlet discharge coefficient of −0.035 and a change in vacuum pressure of 0.047 bar. The results for the fly height and force are plotted in Figure 7.31 and Figure 7.32, respectively. The red curves are the fly height and force from the model without the results of the method of least squares, but with an inlet discharge coefficient of 0.52. The green curves represent the fly height and force of the model, which includes the change in outlet discharge coefficient and vacuum pressure. It can be seen that the modelled curves of the fly height and force are closer to the measured curves, but still, the trend lines are not completely the same. However, similar to the sensitivity analysis in the previous section, the methods shows that small changes in the relevant parameters have a large influence on the fly height and force.

7.5.3. Local Fly Height

In Section 7.3.3, it is shown that the variations in the local fly height are relatively large. The influence of this variation is unknown. In this section, a height variation is included in the numerical model. Two groups of active cells are modelled. In the first group, which can be seen in Figure 7.33, a curvature in x-direction is applied. The visualised curvature is positive. In the second group, which can be seen in Figure 7.34, a curvature in y-direction is applied. The visualised curvature is negative. In the figures, the fly height in the pockets is larger, due to the pocket depth. Both groups are calculated with a positive and negative curvature. The amplitude of the curvature is equal to 10 µm. The results of the fly height and the force are shown in Figure 7.35 and Figure 7.36, respectively. It can be seen that the curvatures have a significant effect on the fly height. A positive curvature results in a larger fly height and a negative curvature results in a smaller fly

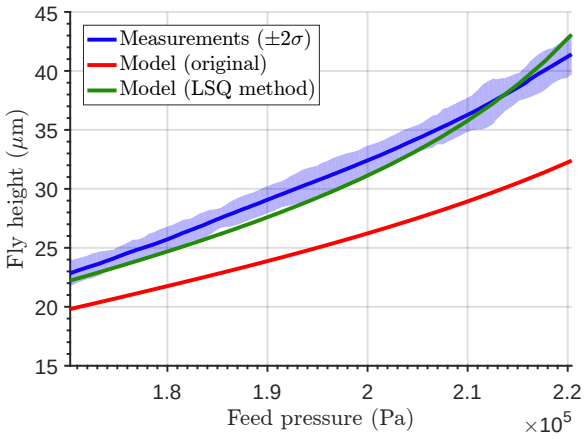

Figure 7.31: Result of the method of least squares for the fly height.

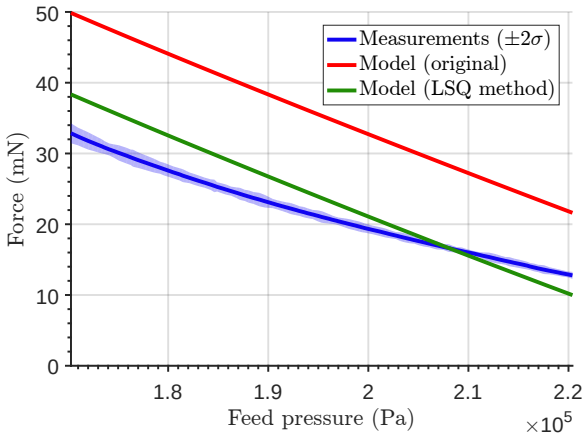

Figure 7.32: Result of the method of least squares for the force.

height. The effect of the curvature in x-direction is larger than the effect of the curvature in y-direction. The influence of the curvatures on the force is less severe. For the curvatures in y-direction, the force shows no change at all. The curvatures do influence the local thin film pressures, but the overall pressure difference between the inlets and the outlets remains constant. Therefore, the force does not change. The curvatures in x-direction have an influence on the force. For both curvatures, the modelled force becomes larger. The effect of a negative curvature more significant greater. Overall, the influence of the curvatures do not have a negative effect on the performance of the system.

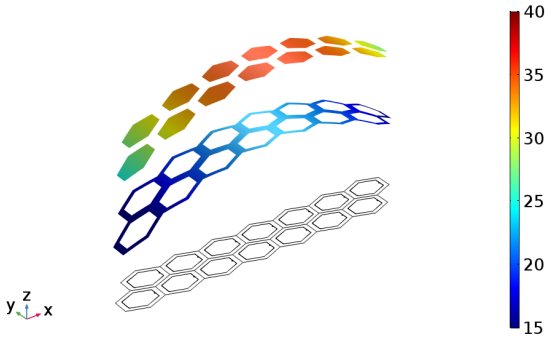

Figure 7.33: Fly height (μm). A positive curvature in x-direction is shown.

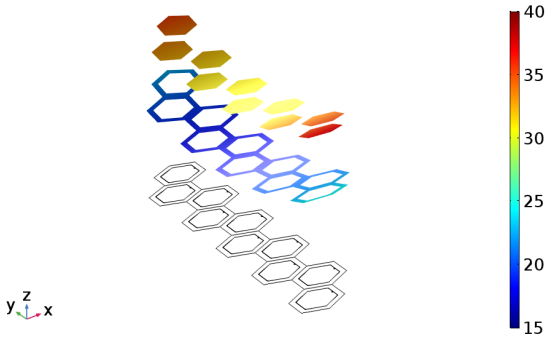

Figure 7.34: Fly height (μm). A negative curvature in y-direction is shown.

7.6. Surface Matching

Both the active surface and the passive surface are measured, and the numerical models are validated. In this section, the fly height and air film stiffness of both surfaces are matched. This is done, as described in the matching approach in Section 3.4. As there is a reasonable match between the model and the measurements, the fly height and air film stiffness of the two surfaces are matched by making use of the numerical model.

1. First, the vacuum pressure is set. If the active and passive surface are both connected to the the vacuum supply, it turns out to be difficult to reach very low vacuum pressure. The lowest vacuum pressure, which can be realised, is equal to 0.75 bar. To have some safety margins, the vacuum pressure is set at 0.8 bar.

2. The next step, is to determine the fly height. Preferably, the fly height is equal to 11.8 μm. at this fly height, the performance ratio of the active surface is the highest. However, from the experiments in Section 7.3 en Section 7.4, it is known that these fly heights cannot be realised. It is decided to match the two surfaces at a fly height of 25 μm.

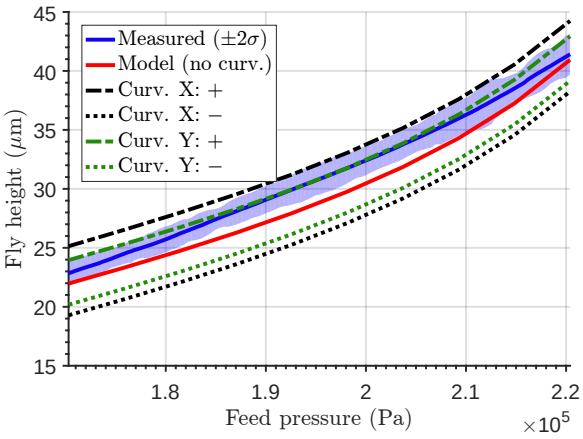

Figure 7.35: The measured and modelled fly height, including positive and negative curvatures in x- and y-direction.

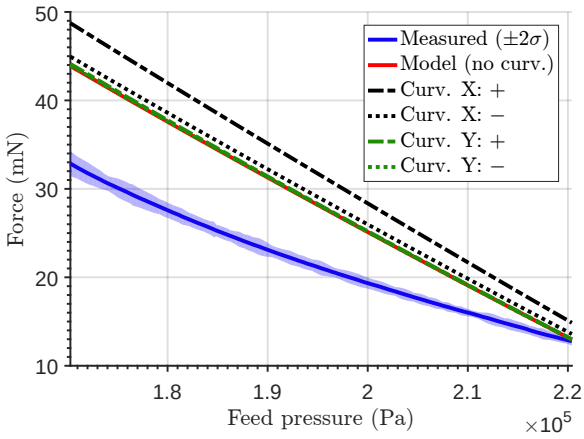

Figure 7.36: The measured and modelled force, including positive and negative curvatures in x- and y-direction.

3. In the active surface cells, a feed pressure of 1.56 bar is required to lift the substrate to the desired fly height of 25 µm. The corresponding air film stiffness of the active cells is $0.85 \times 10^5\,\mathrm{N\,m^{-1}}$ per cell.

4. The feed pressure and vacuum pressure of the passive surface cells are tuned to match the fly height and air film stiffness of the active surface cells. The feed pressure is set at 1.36 bar and the vacuum pressure is set at 0.88 bar. For these pressures, the fly height is equal to 25 µm and the air film stiffness is equal to $0.85 \times 10^5\,\mathrm{N\,m^{-1}}$.

The active surface and passive surface are matched at a fly height of 25 µm. To show that the air film stiffness of the active surface cells and passive surface cells is equal, a dynamic analysis is performed on both surfaces. This dynamic is similar to the analysis in Section 2.6 and Section 6.3. It must be noted that the influence of the volumes downstream the inlet restrictions is neglected, as these volumes only have a influence on the damping. The frequency dependent frequency and damping of the active surface and passive surface are shown in Figure 7.37. The air film stiffness of both surfaces is equal to $0.85 \times 10^5\,\mathrm{N\,m^{-1}}$ per cell for low frequencies. The air film stiffness of the active cells increases to $3.26 \times 10^5\,\mathrm{N\,m^{-1}}$, while the air film stiffness of the passive cells increases to $4.0 \times 10^5\,\mathrm{N\,m^{-1}}$. The air film stiffness of both surfaces are equal up to a frequency of approximately 300 Hz. The damping values at low frequencies are equal to $30.1\,\mathrm{N\,s\,m^{-1}}$ per cell for the active cells and equal to $47.5\,\mathrm{N\,s\,m^{-1}}$ per cell for the passive cells. The damping values approach zero for high frequencies.

The calculated feed pressures and vacuum pressures of the active surface and passive surface, are set manually by tuning the proportional valves in the second transport demonstrator. The demonstrator shows a smooth transition of the wafer. This is based on a qualitative test.

7.7. Conclusion

The second demonstrator is manufactured in a similar way as the first demonstrator. It consists of three main components, which are the air bearing surface, the restrictions, and the manifold. The main difference with the first demonstrator, is the realisation of the inlet restrictions, which are laser-cut in an additional layer of steel. This additional layer is placed beneath the PCB plate. The outlet restrictions are drilled directly in the PCB plate. Both restrictions show a good match with the Jobson orifice flow. The performance of the second demonstrator is measured in the measurement set-up. It shows a better performance than the first demonstrator. The measured fly heights are lower, due to higher air film stiffness and the lower vacuum pressure, which can be realised. The latter is a result of the smaller diameter of the outlet restrictions, which limit the vacuum flow. Because of the lower vacuum pressures and lower fly heights, higher forces can be achieved. The measured forces are in the same order of magnitude as the modelled fly heights, but the trend lines are different. The differences between the measurements and the model are studied in a sensitivity analysis. Small variations in the vacuum pressure have the largest influence on the fly height and force. Furthermore, the influence of the inlet discharge coefficient is studied. A smaller coefficient results in a better

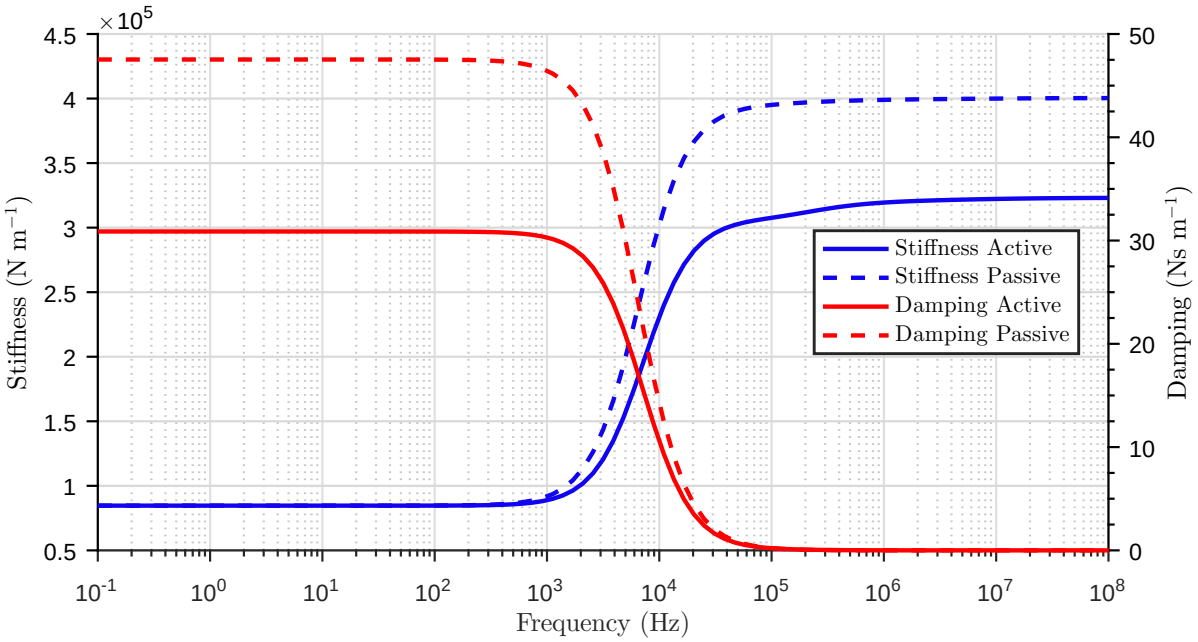

Figure 7.37: Frequency dependent stiffness and damping of both active and passive surface.

match between the trend lines of the measured and modelled fly height and force. As the variations in the inlet discharge coefficient are relatively large, a smaller inlet discharge coefficient is plausible. An even better match between the model and measurement is realised by using the least squares method. The small variations in the outlet discharge coefficient and the vacuum pressure have a large influence on the modelled fly height and force. Finally, the fly height and air film stiffness of the active surface and passive surface are matched by tuning the feed pressure and vacuum pressure of the passive surface. A qualitative test shows a smooth transition of the wafer.

8

Conclusions

The goal of this research is the development of an air-based contactless transport demonstrator. To achieve this goal, two demonstrators are designed, manufactured and tested. In this chapter, the final conclusions that can be drawn from this research are presented. The conclusions are split in three parts: the design, the first demonstrator and the second demonstrator.

Conceptual Design

- The transport demonstrators are designed as a combination of an active surface and a passive surface. It is shown that the mass flow of a passive surface is significantly less than the mass flow of an active surface. A combination of the two surfaces will make the transport demonstrator more efficient in terms of mass flow.

- To exploit gravity, the demonstrator is placed at an angle. By making use of the gravitational force, the system is able to actuate the wafer in two degrees of freedom.

- The active surface and the passive surface consist of cells. A tessellation study is done to find the optimal cell geometry for tiling the surfaces. The cell geometries are optimised for a high traction force over mass flow ratio. Stretched, hexagonally shaped cells show the best performance. This cell geometry is used in both surfaces.

First Demonstrator

- The first demonstrator is designed and manufactured. It is used to validate the numerical model. The demonstrator is designed in a layer approached way, which adds flexibility to the design process. The different layers are the air bearing surface, the restriction layer, and the manifold. Manufacturing methods are developed to realise the different layers of the demonstrator.

- The manifold, which connects the pressure supplies to the inlets and outlets of the system, is made of laser-cut PMMA plates. They are bonded with industrial 3M double-sided tape. The features of the manifold are leakage free up to pressure differences of 6.2 bar. The manufacturing method is a cheap and fast way to manufacture the manifold, but measurements have shown pressure losses over the channels of the manifold in the vacuum pressure.

- The air bearing surface is manufactured by making use of PCB production techniques. The pockets, which have a pocket depth of 13 µm, are created by etching away the copper. The PCB air bearing surface is bonded to the manifold with double-sided tape. Surface roughness measurements have shown that the combination of the stack of PMMA manifold plates and the PCB plate results in an out of plane curvature of the manifold, in x- and y-direction.

- Orifice restrictions are selected as the flow restrictions of the air bearing system. They are drilled directly in the PCB air bearing surface. Flow measurements show a good agreement with the ideal orifice flow model.

- The first demonstrator has been installed in the measurement set-up, and the performance is measured. The fly heights are larger than expected, while the traction forces are smaller than expected. The model and the measurement are in the same order of magnitude and show similar trend lines. Therefore, the model shows that the underlying physics are well understood. The model has a constant off-set compared to the measurements. The air film stiffness could not be measured, because of the large fluctuations in the fly height measurements.

- The differences between the model and the measurements can be explained by the non-uniform vacuum pressure, due to the pressure losses in the manifold. Moreover, the air film stiffness is not high enough to cope with the curvature of the air bearing surface.

Second Demonstrator

- The design of the second demonstrator is similar to the design of the first demonstrator. The main difference is the diameter of the restrictions, which are designed for a higher air film stiffness. The inlet restrictions are laser-cut in an additional layer of steel. The inlet and outlet restrictions show a close match with the Jobson orifice model. However, large variations in the inlet discharge coefficient are measured.

- A dynamic analysis is developed, to model the frequency dependent air film stiffness and damping. The dynamic analysis is used to check the influence of the dead volumes on the dynamic stability. In the demonstrator, there are no signs of pneumatic hammer. The dynamic analysis model has proven to be a proper tool to study the dynamic stability.

- The second demonstrator shows a better performance than the first demonstrator. Due to the higher film stiffness, smaller fly heights and larger traction forces are measured. These are in the same order of magnitude as the model, but the trend lines are different, especially compared to the results of the first demonstrator. The local fly height of the wafer shows variations of approximately 10 µm.

- A sensitivity analysis is done and the method of least squares is applied, to study the differences between the trend lines of the model and the measurement. A much better agreement is found by applying a smaller inlet discharge coefficient and small differences in the vacuum pressure and outlet discharge coefficient in the model. The local fly height variations can be explained by the air film stiffness, which is still not high enough to cope with the curvature of the air bearing surface. The influence of the local fly height variations are studied in a numerical model. They have a large influence on the fly height of the wafer, but do not have a negative influence on the traction force.

- The fly height and air film stiffness of the active surface and the passive surface are matched by making use of the numerical model. The feed pressure and vacuum pressure of the active surface are equal to 1.56 bar and 0.8 bar, respectively. The surfaces are matched at a fly height of 25 µm, and a corresponding air film stiffness of $0.85 \times 10^5\,\mathrm{N\,m^{-1}}$ per cell. The feed pressure and vacuum pressure of the passive surface cells are tuned on this fly height and air film stiffness. They are equal to 1.36 bar and 0.88 bar, respectively. A dynamic analysis shows that the air film stiffness of the active surface and of the passive surface are equal up to a frequency of approximately 300 Hz.

- The feed pressures and vacuum pressures are set in the second demonstrator. A smooth transition of the wafer between the active surface and the passive surface is observed. Based on this qualitative test, the demonstrator shows to be a promising concept to realise a conveying line for thin substrates.

9

Recommendations

In this chapter, the recommendations of this research are presented. The recommendations are focussed on improving the match between the measurements and the numerical model, and involve advice for future transport demonstrators.

- During the experimental validation, problems occurred with realising enough vacuum near the manifold. It has turned out to be quite challenging to transport the vacuum. Significant pressure losses over the channels of the manifold are measured. For a future design, it is recommended to make use of a vacuum chamber, instead of the channels, which have been used in this project. The pressure losses over the vacuum chamber will be far less, compared to the pressure losses over the channels.
- The surface roughness measurements have shown that the the air bearing surfaces have a relatively large out of plane curvature in x- and y-direction. This curvature is caused by the stacking of the PMMA plates. Due to the curvature, the wafer has to fly at a larger fly height to float freely on the thin film of air. The increased fly height results in lower traction forces, which is not preferred. A solution could be to add a flat, stiff, metal plate to the stack of PMMA plates. The manifold and air bearing surface, which are less stiff, will deform to the shape of the metal plate.
- Another issue in the experimental set-up is the correct model of the flow restrictions. The flow restriction measurement is perfect for measuring the flow through a flow restriction, but the actual behaviour of the flow restriction, in combination with the thin film, is unknown. It would be useful to be able to measure the pressures in the thin film. Pressure sensors could be included in the manifold or substrate.
- Actively controlling the feed pressure and vacuum pressure during the measurements would be beneficial for the precision of the measurements. Possible pressure fluctuations in the pressure supplies will be filtered out.
- It is recommended to measure the fly height with another sensor than the fiberoptic sensor. The fiberoptic sensor is sensitive to light contamination and movement of the wafer underneath the sensor. Moreover, the resolution of the fiberoptic sensor is relatively low. It might be an option to use laser triangulation sensors in future fly height measurements.
- The current demonstrators are open-loop systems. Control has not yet been applied. The next step in the realisation of the transport demonstrator is to control the position of the wafer. To realise this, the positions of the wafer should be measured accurately. There are many different sensors, which can be used to detect the position of the wafer. Some examples are vision control [44] and linear sensor arrays. If control is applied, fast computation of the control parameters is essential. The first steps in the design of such a model are presented in Appendix I.
- In the current demonstrators, the mass flow of the system is limited by increasing the restriction values of the outlet restrictions. This is done to limit the mass flow to the vacuum pump. However, the mass flow is still reasonably high. Future designs could actively limit the mass flow to the vacuum pump. This can be done by for example small valves, which are positioned close to the outlet. A combination

with a sensing system, which can detect the position of the wafer, would be perfect. The valves can close the outlets when the wafer is somewhere else.

- The demonstrators in this project are able to actuate the wafer in two degrees of freedom. To simplify the system, some sort of passive alignment of the substrate could be added. The alignment can be air flow based. In this way the cells of the active surface can be optimised for purely actuating the wafer in the main transport direction.
- The flow restriction in this thesis project are orifice restrictions, which are either drilled directly in the PCB air bearing surface, or laser-cut in an additional layer of steel. Another option for realising the flow restriction in a layer approached way, is to make use of a very fine netting/filter. This extra layer can be placed underneath the air bearing surface, similar as the laser-cut steel plate.
- The actual mass flows have not been measured in this project. It will be interesting to see if the modelled mass flows are similar to the measured mass flows. This will improve our knowledge of the system.

A

Contactless Handling Principles

An overview of different technologies of pneumatic contactless handling principles is provided. A survey on pneumatic non-prehensile handling of thin and delicate objects, provided by Laurent [30], has been used as an inspiration. The focus is on air flow based working principles. This means that air, or in general gas, is used as the main tool to handle the object. A thorough review of contactless actuation systems in general has been conducted by Vuong [49]. Besides the pneumatic based technologies for handling objects, including ultrasonic vibrations, it also includes handling principles based on electrostatics and electro-magnetics.

A.1. Air Flow

Thin objects can be handled in a contactless manner by controlling the air flow underneath it. The general principle works as follows. Air is blown from below the substrate. Due to the pressure build-up the substrate is levitated. Depending on the height of the air film (or fly height of the object) and other conditions, such as the geometry, different types of forces can be generated on the substrate. This is very well described in the work of Vuong [49]. An illustration of these different forces can be seen in Figure A.1. The different regions of forces are the air bearing region, the Bernoulli region, the air jet region, and the viscous force region. The latter is visualised in the right drawing of Figure A.1. All principles are discussed in this section.

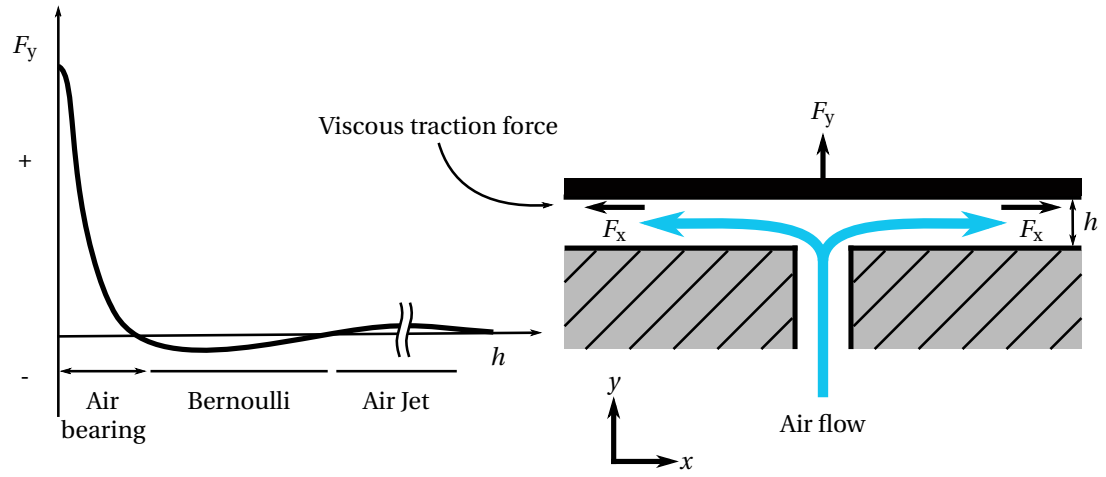

Figure A.1: Four types of forces [49]. The forces or regions can be classified based on the film height between the actuator and the object. For small film heights we are in the air bearing region, characterized by high load capacities. Increasing the film height brings us to negative forces in the Bernoulli region. For even larger film heights the air jet region is found. The last force, based on viscous traction, is not visualized in the graph but can be seen on the right. For this principle the viscous traction force, generated by the air, is explored.

A.1.1. Air Bearing Region

For very small film heights the flow between the object and the system is laminar and the pressure is distributed over the full area of the object. The working principle is similar to that of air-hockey tables, which lift the puck by blowing air from underneath. The air bearing surface can have several pressure inlets and (vacuum) outlets. The shape and geometry of the air bearing surfaces vary a lot. The generated force or load capacity is equal to the pressure integrated over this surface. Very high load capacities can be attained as the system behaves like an air bearing surface. The stiffness is achieved by the inlet restrictions, which is explained in Appendix D. Extra stiffness, damping and controllability in vertical direction can be achieved by adding vacuum to the system, as explained by Devitt [16]. The air bearing surfaces are widely used in for example the LCD and screen industry, for conveying the large glass panels. Different flow restrictions are used, such as porous restrictions [5][38][56], air slits [31] and vortex bearing elements [33]. Also other types of plate and sheet material, and even whole structures can be levitated with this working principle. Companies as New Way Air Bearings [1], Portec [2], and OAV Air Bearings [3], design the conveying surfaces with both porous media and orifices as inlet restrictions. However, it must be stated that with all these different air conveyors only a force in vertical direction is generated. Another type of actuation is necessary to actually convey the objects, which can be gravity, rollers or timing belts for example. For the latter types of actuation, the system is not really contactless anymore. An example of such a system is designed by Pister [39]. This contactless MEMS-based air conveyor uses an electric field to actuate the object. The objects of 1 mm×1 mm size and a thickness varying from 2 µm to 1 mm are levitated on an air cushion of around 20 µm. Forces ranging from 1 to 10 nN have been achieved.

A.1.2. Bernoulli Region

Referring back to Figure A.1, it can be seen that for increasing film heights the generated force becomes negative, which means that the object is pulled towards the system. This phenomena relies on the Bernoulli airflow principle, which states that an increase in fluid velocity is accompanied with a pressure reduction [50]. It results in an attractive force, which is able to lift the object from the top side (corresponding to a negative force F_y in Figure A.1). The Bernoulli principle can be employed in grippers for handling delicate objects. An example of such a gripper based is designed by Davis [12] and is used in the food industry. A variation on the conventional Bernoulli gripper is proposed by Li [32]. This levitating method, called vortex levitation, uses a swirling air flow in the gripper instead of just blowing the air. The vortex flow induces negative pressures at the center of the gripper, which helps lifting the object.

A.1.3. Air Jet Region

By increasing the film height even further the air jet region is reached. Air-jets can be used to convey objects with two different working principles: induced air flows created by an air-jet or inclined air jets. Several papers on the induced air flows are published by Luntz, Moon and Varsos [34][36][46][47]. A similar method is proposed by Delettre [13] and Laurent [28], which can be seen in Figure A.2. Flow is coming out of the surface and the actuation is located in the bottom plate. This bottom plate has, besides the nozzles for the propulsion function, also nozzles for levitating the object, similar to an air bearing surface. The strong vertical air-jets induce a potential air flow which creates a local suction effect. By switching on and off different columns of air-jets an object can be translated. In later publications 2-DoF [15] and 3-DoF [14] systems have been realized, which can move centimeter sized object wits speeds up to 0.22 m s^{-1} and millimeter closed-loop positioning accuracy.

Another and more common way to handle objects with air-jets is to use the concept of inclined air-jets. These air-jets can perform the levitation and propulsion function at the same time. A schematic overview of the working principle can be seen in Figure A.3. A lot of research is conducted on small scale conveyors, which are produced with MEMS technology [24][18][17][55][54][29][43]. Berlin [9] designed a motion control system for handling paper and other thin substrates. It has 1152 pneumatic air-jets, located on a 12" × 12" board and placed above and under the paper. Each air-jet is controlled independently by an electrostatic valve. Typical velocities of 30 mm s^{-1} and a closed-loop positioning repeatability of around 0.025 mm are reached. There is also research on larger scale conveying systems with air-jets. Moon [37] studied the speed of a 300 mm wafer of 127 g weight on a conveying systems with simple inclined air-jets. A maximum speed of around 0.6 m s^{-1}

[1] New Way Air Bearings. Aston, USA. `http://www.newwayairbearings.com/`.
[2] Portec. Aadorf, Switzerland. `http://www.portec.ch/index.htm`.
[3] OAV Air Bearings. Princeton NJ, USA. `http://oavco.com/index.html`.

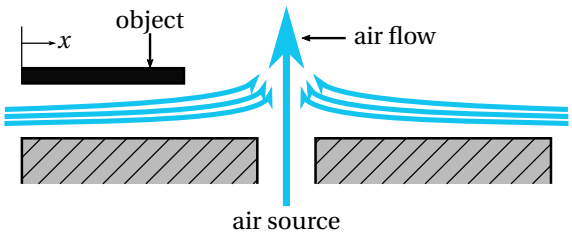

Figure A.2: Schematic cross-section of potential air flow. The air source induces a flow which pulls the object towards the source.

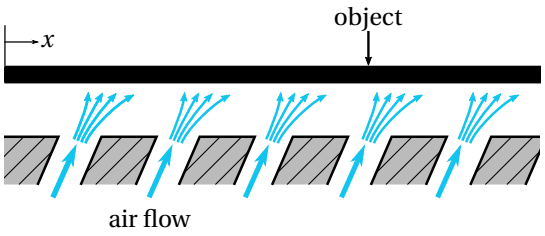

Figure A.3: Schematic cross-section of inclined air-jets. The air-jets provide a levitation and propulsion at the same time.

has been realised. Another more recent study by Dahroug [11] makes use of a modular based conveying systems. Rectangular chucks with air-jets can be placed in different configurations for either positioning, (guided) motion or rotation of objects. For a 150 mm diameter wafer a maximum velocity of $0.62\,\mathrm{m\,s^{-1}}$ has been reached.

A.1.4. Viscous Traction Force

The fourth and last force generated by air is based on the viscous traction force. The viscous traction force, which in air bearings is often said to be negligible, is actually used to actuate an object. Ku [26] was the first to exploit the principle of the viscous traction force. In his design, consisting of 100 capillary glass tubes on a 4 mm×4 mm surface, objects of different size and shape are conveyed. Translating, rotating, positioning and even flipping of the objects is possible. Each capillary has a two-way valve which can be connected to a high pressure or a vacuum. If a high pressure capillary and a vacuum capillary are situated next to each other air will start to flow from high pressure to the vacuum. When the viscous traction force generated by this flow exceeds the friction force the object will start to move. The objects are actuated by moving vacuum lines. The other capillaries are blowing in upward direction to levitate the object.

Within the Mechatronic System Design group of Delft University of Technology, a lot of research is conducted on exploiting the viscous traction force for handling thin substrates. The research is explained in Section 1.2.

B

Reynolds Equation

The Reynolds equation is a two-dimensional differential equation, which describes the pressure distribution in a thin film formed between two bounding surfaces. In this chapter, the history of the Reynolds is discussed, the differential equation is derived and a physical interpretation of its terms is presented.

B.1. History

Beauchamp Tower (1845-1904) was an English inventor and railway engineer. In 1883 he discovered, somewhat by accident, the self-acting lubricating film. Beauchamp Tower built a special test set-up for simulating the conditions in railway axle-boxes, see Figure B.1. In the set-up a shaft was partly immersed in a bath of oil, the so-called oil bath lubrication. The upper half of the shaft was loaded with a weight. Tower found that the friction of the shaft was dependent of the load and the rotational shaft velocity and very low friction coefficients could be reached. In the last phase of the experiment he drilled a hole in the bearing, initially for the supply of lubricating oil. He discovered that the oil would rise in the feed hole and would eventually leak over the top of the bearing surface. He installed a pressure gauge at the location of the drilled hole and measured significant oil pressures.

After this observation the research in the pressure build up in lubrication films took off. Osborne Reynolds developed a theory that the two surfaces might be separated completely and continuously by a thin film of lubrication oil. In 1886 Osborne Reynolds (1842-1912) presented a paper to the Royal Society of London [40]. The paper contains a partial differential equation, which will later be known as te Reynolds equation. It describes the pressure distribution and pressure build up in thin films.

B.2. Derivation

There are multiple ways to derive the Reynolds equation. Two commonly applied methods are the simplification of the Navier-Stokes equation [19] and the analysis of the equilibrium of the viscous shear forces and pressure on a small fluid element. This last method is applied in this section, based on the analysis in [45], [20] and [19]. In Figure B.2 a thin fluid film between two surfaces can be seen. A small fluid element in the thin film with sides dx, dy and dz is analysed in the x-direction, to keep things clear. A similar analysis could be done in the y-direction. The velocities of the element in x-, y- and z-direction are denoted by u, v and w, respectively. Using the assumption of laminar flow an equilibrium of forces in x-direction can be set up:

$$\left(p+\frac{\partial p}{\partial x}dx\right)dydz+\tau dxdy = pdydz+\left(\tau+\frac{\partial \tau}{\partial z}dz\right)dxdy \Rightarrow \frac{\partial p}{\partial x}=\frac{\partial \tau}{\partial z} \tag{B.1}$$

The fluid is assumed to be Newtonian. Newton's law for viscous flow of a Newtonian fluid states:

$$\tau = \eta\frac{\partial u}{\partial z} \tag{B.2}$$

This is inserted in the Equation B.1, yielding:

$$\frac{\partial p}{\partial x}=\frac{\partial}{\partial z}\left(\eta\frac{\partial u}{\partial z}\right) \tag{B.3}$$

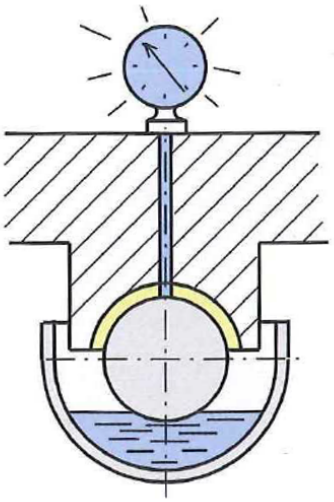

Figure B.1: Test set-up of Beachamp Tower [45].

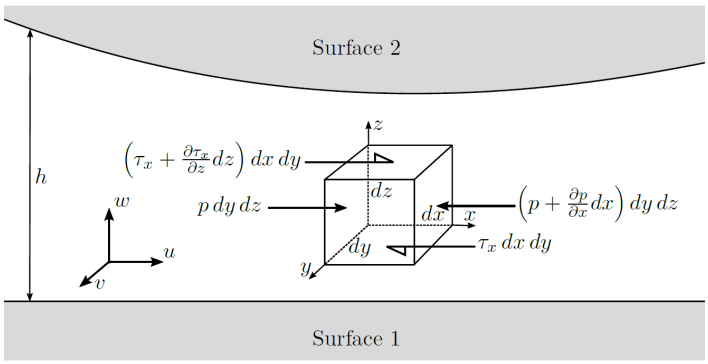

Figure B.2: Equilibrium between the viscous shear forces and pressure force acting on a small fluid element in a thin film [20].

The next assumption is that the viscosity η is constant across the film thickness. Therefore it can be written down in front of the derivative:

$$\frac{\partial p}{\partial x} = \eta \frac{\partial^2 u}{\partial z^2} \tag{B.4}$$

The pressure p is assumed to be constant over the film thickness as well. It is independent of the coordinate z. Two integrations are performed, resulting in a differential equation with two integration constants C_1 and C_2:

$$\frac{\partial p}{\partial x} \frac{z^2}{2} = \eta u + C_1 z + C_2 \tag{B.5}$$

The two integration constants are found by applying the zero slip condition at the lower and upper surface. The velocity of the fluid at the location of the two surfaces is assumed to be equal to the velocity of the surfaces themselves. The resulting two boundary conditions can be written as:

$$\begin{aligned} u(z=0) &= u_1 \\ u(z=h) &= u_2 \end{aligned} \tag{B.6}$$

The boundary conditions are used to find the integration constants C_1 and C_2, which results in the following expression for the fluid velocity:

$$u(x,z) = \frac{1}{2\eta} \frac{\partial p}{\partial x} \left(z^2 - hz\right) + \frac{u_2 - u_1}{h} z + u_1 \tag{B.7}$$

The first term on the right side represents the fluid velocity as a result of the Poiseuille flow, which is pressure driven flow. The last two parts represent the fluid velocity as a result of Couette flow. Couette flow is induced by the relative motion of one surface with respect to another surface. The volume flow per unit length in x-direction can then be found by integrating over the film thickness h:

$$q_x = \int_0^h u(z)\, \mathrm{d}z = -\frac{h^3}{12\eta} \frac{\partial p}{\partial x} + \frac{h}{2} (u_1 + u_2) \tag{B.8}$$

By assuming a constant density over the film thickness, the mass flow per unit length in x- and y-direction can simply be found by multiplying the volumetric flow with the density. This is done for the x- and y-direction:

$$m_{\mathrm{x}} = \rho \int_0^h u(z)\,\mathrm{d}z = -\frac{\rho h^3}{12\eta}\frac{\partial p}{\partial x} + \frac{\rho h}{2}(u_1 + u_2) \tag{B.9}$$

$$m_{\mathrm{y}} = \rho \int_0^h v(z)\,\mathrm{d}z = -\frac{\rho h^3}{12\eta}\frac{\partial p}{\partial y} + \frac{\rho h}{2}(v_1 + v_2) \tag{B.10}$$

The mass flow per unit length in x- and y-direction are known. A mass balance over the small fluid element can be defined. Continuity of flow requires:

$$\frac{\partial m_{\mathrm{x}}}{\partial x} + \frac{\partial m_{\mathrm{y}}}{\partial y} + \frac{\partial}{\partial t}(\rho h) = 0 \tag{B.11}$$

The continuity of flow equation states that the rate of change of the mass of the fluid in the element is equal to the difference in inflow and outflow of mass in x- and y-direction. Using the product rule, the last term can be written down as:

$$\frac{\partial}{\partial t}(\rho h) = \rho\frac{\partial h}{\partial t} + h\frac{\partial \rho}{\partial t} \tag{B.12}$$

The change in film height $\frac{\partial h}{\partial t}$ is affected by two factors:

$$\frac{\partial h}{\partial t} = w_2 - w_1 - u_2\frac{\partial h}{\partial x} - v_2\frac{\partial h}{\partial y} \tag{B.13}$$

The first two terms are the velocity components in z-direction, as a result of the direct movement of the two surfaces. The last two terms are a change in fly height as a result of a velocity component in x- or y-direction when the two surfaces are not parallel to each other, indicated by $(\partial h/\partial x)$ and $\left(\partial h/\partial y\right)$. Only the upper surface, denoted by 2, has been inclined. It is assumed the terms $(\partial h/\partial x)$ and $\left(\partial h/\partial y\right)$ are equal to zero for the first surface, denoted by 1. The expressions for the mass flows m_{x}, m_{y} and the change in fly height $(\partial h/\partial t)$ are inserted in the mass flow balance:

$$\begin{aligned}\frac{\partial}{\partial x}\left(\frac{\rho h^3}{12\eta}\frac{\partial p}{\partial x}\right) + \frac{\partial}{\partial y}\left(\frac{\rho h^3}{12\eta}\frac{\partial p}{\partial y}\right) = \rho\left(w_2 - w_1 - u_2\frac{\partial h}{\partial x} - v_2\frac{\partial h}{\partial y}\right) + \\ \frac{\partial}{\partial x}\left(\frac{\rho h(u_1+u_2)}{2}\right) + \frac{\partial}{\partial y}\left(\frac{\rho h(v_1+v_2)}{2}\right) + h\frac{\partial \rho}{\partial t}\end{aligned} \tag{B.14}$$

This equation is known as the Reynolds equation. The terms on the left give the change in mass flow per unit length in the x- and y-direction, initiated by the terms on the right. These terms are explained in the next section.

B.3. Physical Interpretation

A physical interpretation of the terms of the Reynolds equation is given, based on [19]. First, the Reynolds equation is written down in one DoF (x-direction). The side-leakage terms $\left(\partial/\partial y\right)$ can be removed without any loss of generality [19]:

$$\underbrace{\frac{\partial}{\partial x}\left(\frac{\rho h^3}{12\eta}\frac{\partial p}{\partial x}\right)}_{\text{Poiseuille flow}} - \underbrace{\frac{\partial}{\partial x}\left(\frac{\rho h(u_1+u_2)}{2}\right)}_{\text{Couette flow}} = \underbrace{\frac{\partial}{\partial t}(\rho h)}_{\text{Dynamic effects}} \tag{B.15}$$

The equation consists of three parts. The first part is the Poiseuille term, which describes the mass flow rates due to pressure gradients within the thin film. The second term is called the Couette term and describes the mass flow rate due to surface velocities. Using the product rule the partial derivative in the Couette term can be expanded:

$$\frac{\partial}{\partial x}\left(\frac{\rho h(u_1+u_2)}{2}\right) = \underbrace{\frac{h(u_1+u_2)}{2}\frac{\partial \rho}{\partial x}}_{\text{Density wedge}} + \underbrace{\frac{\rho(u_1+u_2)}{2}\frac{\partial h}{\partial x}}_{\text{Physical wedge}} + \underbrace{\frac{\rho h}{2}\frac{\partial}{\partial x}(u_1+u_2)}_{\text{Stretch}} \tag{B.16}$$

The expansion of the Couette term leads to three distinct actions. The first part is named "density wedge" and is governed by the term $\left(\partial\rho/\partial x\right)$. It describes the mass flow due to a change in the fluid density in the sliding direction. The change in fluid density could be caused by a change in temperature for example. The "physical wedge" term is governed by the change in film height in the sliding direction $(\partial h/\partial x)$. A Couette flow is induced by a sliding motion of one of the surfaces, which forces the fluid in a converging wedge shaped region. The last term is called "stretch" and is governed by the change in velocity in the sliding direction, $(\partial u/\partial x)$. A flow is induced if the bounding surfaces are elongated elastically.

The partial derivative in the dynamic effects term can be expanded as well. In combination with Equation B.13 it can be written as:

$$\frac{\partial}{\partial t}\left(\rho h\right) = \underbrace{\rho\left(w_2 - w_1\right)}_{\text{Normal squeeze}} - \underbrace{\rho u_2 \frac{\partial h}{\partial x}}_{\text{Translational squeeze}} + \underbrace{h\frac{\partial \rho}{\partial t}}_{\text{Local expansion}} \tag{B.17}$$

The expansion results in three distinct terms. The first term, "normal squeeze", is a result of a direct up or down movement of the surfaces in vertical direction. In the absence of sliding, a positive pressure is generated if the film height is decreasing. The second term is related to squeeze as well: "translational squeeze". A translation of the surfaces results in a change in mass flow, if the surfaces are inclined. The last term, "local expansion" is related to the change in density of the fluid over time, which results in a change in flow. The density could be changed by thermal expansion for example.

C

Derivations Theoretical Analysis

In this appendix, the derivations of the theoretical analysis in Chapter 2 are presented. The expressions for the mass flow density, force density and stiffness density are derived step by step. This is done for the passive air bearing cell and the active air bearing cell for both the incompressible and compressible flow situation.

C.1. Air Bearing

The passive air bearing surface is analysed first. It has already been presented in Chapter 2, but as a recap it can be seen in Figure C.1 as well. The figure shows a cross-section of one passive cell, which is dark-coloured. The cell is modelled with an infinite width in the y-direction, pointing out of the paper. The cell has a length L and the inlet is positioned at a distance of αL from the right outlet, $0 < \alpha < 1$. The film height H is constant and equal to the fly height h. The inlet and outlet grooves are assumed to be infinitely small, resulting in a flow path length which is equal to the cell length L. As a last assumption, the outlet restriction is assumed to be negligibly small.

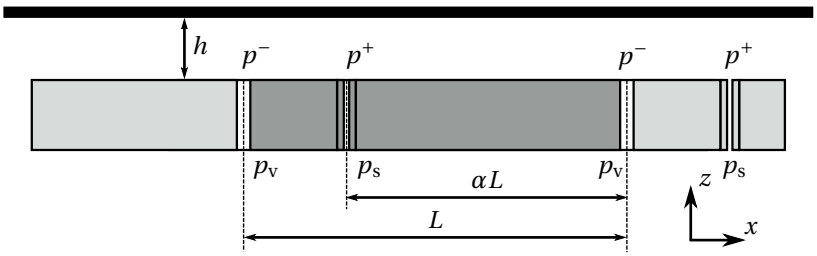

Figure C.1: Schematic cross-section of a passive cell.

C.1.1. Incompressible Flow Case

In the incompressible flow model, the density is assumed to be constant. This is a valid assumption if the pressure difference in the system is relatively small compared to ambient pressure. The constants in the Reynolds equation (Equation 2.1), can be removed and the equation simplifies to:

$$\frac{\partial^2 p}{\partial x^2} = 0 \tag{C.1}$$

As the flow is assumed to be incompressible, the pressure distribution shows a linear decrease from the inlet pressure p^+ to the outlet pressures p^-. This is visualised in Figure 2.3. The location of the inlet is placed at $x = 0$, resulting in the following pressure distribution in the thin film:

$$p(x) = \begin{cases} \frac{p^+ - p^-}{(1-\alpha)L} x + p^+, & \text{for } (\alpha - 1)\, L \leqslant x \leqslant 0 \\ -\frac{p^+ - p^-}{\alpha L} x + p^+, & \text{for } 0 \leqslant x \leqslant \alpha L \end{cases} \tag{C.2}$$

The load capacity can then be determined:

$$\overline{w} = \frac{1}{L}\int_0^L \left(p - p_\mathrm{a}\right) \mathrm{d}x = \frac{p^+ + p^-}{2} - p_\mathrm{a} \tag{C.3}$$

The outlet pressure p^- is substituted with the vacuum pressure p_v, because the outlet restriction is assumed to be negligibly small. The zero load condition from Equation 2.2, which states that the load capacity is equal to zero, is then used to determine the inlet pressure p^+:

$$p^+ = 2p_\mathrm{a} - p_\mathrm{v} \tag{C.4}$$

Motor Function

The motor function of the cell is characterised by the force density. The force density of the passive cell from Figure C.1 is calculated by integrating the shear traction over the cell length L:

$$\overline{F} = \frac{1}{L}\int_0^L -\frac{H}{2}\frac{\partial p}{\partial x}\,\mathrm{d}x = 0 \tag{C.5}$$

The force density turns out to be equal to zero; no in-plane force is generated. Viscous traction forces are created in the left and right x-direction, but the net force is equal to zero as they cancel each other out. The mass flow density can be derived as well, based on Equation 2.4 and the zero load condition of Equation C.4:

$$\overline{\dot{m}} = \frac{p_\mathrm{a}}{R_\mathrm{g}T}\frac{h^3}{6\eta L^2}\left(\frac{1}{1-\alpha} + \frac{1}{\alpha}\right)\left(p_\mathrm{a} - p_\mathrm{v}\right) \tag{C.6}$$

The density ρ is calculated by using the ideal gas law at ambient pressure: $\frac{p_\mathrm{a}}{R_\mathrm{g}T}$. In this equation R_g, is the specific gas constant of air and T is the absolute temperature. The variable α is optimised for minimum mass flow and is equal to 0.5.

Bearing Function

The bearing function of the thin air film has two functionalities: the load capacity and the bearing stiffness. The analogy of flow with electric circuits is useful to determine the bearing stiffness of the system. The circuit can be seen in Figure C.2. The air with feed pressure p_s flows through the inlet restriction R_i, after which the pressure is lowered to the inlet pressure p^+. From there, part of the air flow goes to the left and part of the air flow goes to the right, both to the outlet pressure p^-. The flow resistances R_l and R_r are both dependent on the film height h and can be determined using the Reynolds equation:

$$R_\mathrm{l}(h) = \frac{12\eta L(1-\alpha)}{h^3} \tag{C.7}$$

$$R_\mathrm{r}(h) = \frac{12\eta L\alpha}{h^3} \tag{C.8}$$

As the variable α is equal to 0.5 for minimum mass flow, the flow resistances are equal. There is a small resistance R_o at the outlet of the system. The flow circuit can be simplified to the circuit in Figure C.3. In this circuit $R_\mathrm{e}(h)$ is the equivalent resistance of the resistances R_l and R_r, which are in placed in parallel:

$$R_\mathrm{e}(h) = \left(\frac{1}{R_{\mathrm{l(h)}}} + \frac{1}{R_{\mathrm{r(h)}}}\right)^{-1} = \frac{12\eta L\alpha(1-\alpha)}{h^3} \tag{C.9}$$

The bearing stiffness can be obtained analytically by setting up the system equations from the flow circuit in Figure C.3:

$$p_\mathrm{s} - p^+ = QR_\mathrm{i} \tag{C.10}$$

$$p^+ - p^- = QR_{\mathrm{e(h)}} \tag{C.11}$$

$$p^- - p_\mathrm{v} = QR_\mathrm{o} \tag{C.12}$$

From the equations above expressions for p^+ and p^- can be formulated:

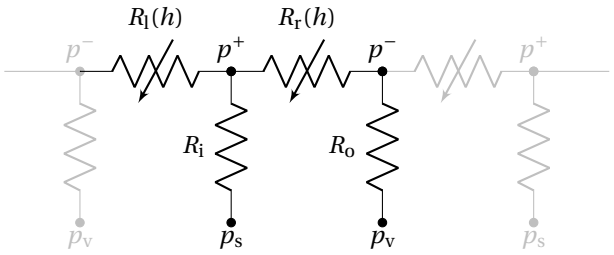

Figure C.2: Flow scheme of one cell (black). The cell is modelled with periodic boundary conditions. It can be copied in both directions, which is shown in grey.

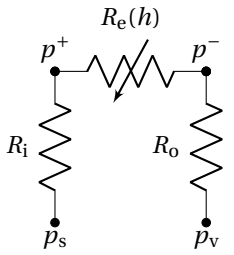

Figure C.3: Simplified flow scheme of one cell (black part in Figure C.2).

$$p^+(h) = \frac{p_s(R_e(h)+R_o)+p_vR_i}{R_i+R_e(h)+R_o} \tag{C.13}$$

$$p^-(h) = \frac{p_sR_o+p_v(R_e(h)+R_i)}{R_i+R_e(h)+R_o} \tag{C.14}$$

As explained in Appendix D, a variation in the fly height will change the pressure distribution, hereby changing the load capacity. The stiffness per unit area at a certain fly height can be calculated by taking the derivative of the load capacity per unit area with respect to the film height h. The load capacity, without the zero load condition, is given by Equation C.3. The pressures p^+ and p^- are inserted in this equation:

$$\overline{w}(h) = \frac{p^+ + p^-}{2} - p_a = \frac{p_s(R_e(h)+2R_o)+p_v(R_e(h)+2R_i)}{2(R_i+R_e(h)+R_o)} - p_a \tag{C.15}$$

$$= \frac{p_s+p_v}{2} + (p_s-p_v)\frac{R_o-R_i}{2(R_i+R_e(h)+R_o)} - p_a \tag{C.16}$$

The stiffness per unit area at a certain fly height can then be calculated by taking the derivative of the load capacity per unit area with respect to the film height h. The outlet resistance R_o is assumed to be small and drops out of the equation, resulting in:

$$\overline{k}\Big|_{h=h_0} = -\frac{\partial\overline{w}(h)}{\partial h}\Big|_{h=h_0} = -\frac{1}{2}\frac{\partial\left(p^+ + p^-\right)}{\partial h}\Big|_{h=h_0} = -\frac{\partial R_e(h)}{\partial h}\Big|_{h=h_0}\frac{R_i-R_o}{2\left(R_e(h_0)+R_i+R_o\right)^2}\left(p_s-p_v\right) \tag{C.17}$$

A positive stiffness is realised if the inlet resistance R_i is larger than the outlet resistance R_o. The stiffness increases if the pressure difference increases. The derivative of the film resistance can be expressed as:

$$\frac{\partial R_e(h)}{\partial h} = -\frac{36\eta L\alpha(1-\alpha)}{h^4} \tag{C.18}$$

The derivative of the stiffness is negative, since the resistance becomes smaller if the fly height increases. The outlet resistance in Equation C.17 is assumed to be small and drops out of the equation:

$$\overline{k}(h_0) = -\frac{\partial R_e(h)}{\partial h}\Big|_{h=h_0}\frac{R_i}{2\left(R_e(h_0)+R_i\right)^2}\left(p_s-p_v\right) \tag{C.19}$$

The resistance $R_e(h_0)$ and its derivative $\frac{\partial R_e(h)}{\partial h}\Big|_{h=h_0}$ depend on the cell geometry. The resistance R_i can be chosen. As the outlet resistance is neglected, it can be removed from the flow circuit in Figure C.3. A new system of equations can be set up:

$$Q = \frac{p_s-p_v}{R_e(h)+R_i} = \frac{p^+-p_v}{R_e(h)} \tag{C.20}$$

The inlet restriction R_i is determined by combining the last system of equations with the zero load condition, $p^+ = 2p_a - p_v$:

$$R_{\mathrm{i}}(h_0) = R_{\mathrm{e}}(h_0)\left(\frac{p_{\mathrm{s}} - p_{\mathrm{v}}}{2\left(p_{\mathrm{a}} - p_{\mathrm{v}}\right)} - 1\right) \tag{C.21}$$

C.1.2. Compressible Flow Case

If the pressure difference in the system becomes larger, the assumptions for incompressible flow are no longer valid and the air density in the Reynolds equation of Equation 2.1 has a high dependency on the film pressure. The density ρ can be written as $\rho = \frac{p}{R_{\mathrm{g}}T}$, assuming it to be an ideal gas. Leaving out the constant terms, the Reynolds equation can be written as:

$$\frac{\partial}{\partial x}\left(p\frac{\partial p}{\partial x}\right) = 0 \tag{C.22}$$

The Reynolds equation for compressible flow results in the following pressure distribution. Again, the location of the inlet is placed at $x = 0$:

$$p(x) = \begin{cases} \sqrt{\frac{\left(p^+\right)^2 - \left(p^-\right)^2}{(1-\alpha)L}x + \left(p^+\right)^2}, & \text{for } (\alpha - 1)\,L \leqslant x \leqslant 0 \\ \sqrt{-\frac{\left(p^+\right)^2 - \left(p^-\right)^2}{\alpha L}x + \left(p^+\right)^2}, & \text{for } 0 \leqslant x \leqslant \alpha L \end{cases} \tag{C.23}$$

The pressure distribution for the compressible flow can be seen in Figure 2.3. There is no longer a linear decrease from the inlet pressure p^+ to the outlet pressures p^-. The load capacity per unit area can be calculated from the Reynolds equation as well:

$$\overline{w} = \frac{2}{3}\frac{{p^+}^2 + p^+ p_{\mathrm{v}} + {p_{\mathrm{v}}}^2}{p^+ + p_{\mathrm{v}}} - p_{\mathrm{a}} \tag{C.24}$$

The load capacity is equal to zero, resulting in the following expression for the inlet pressure p^+:

$$p^+ = -\frac{1}{2}p_{\mathrm{v}} + \frac{3}{4}p_{\mathrm{a}} + \frac{1}{4}\sqrt{-12{p_{\mathrm{v}}}^2 + 12p_{\mathrm{a}}p_{\mathrm{v}} + 9{p_{\mathrm{a}}}^2} \tag{C.25}$$

Motor Function

Similar to the incompressible flow calculations the net force density of the passive cell is equal to zero. The mass flow density is equal to:

$$\overline{m} = \frac{\left(p^+ + p_{\mathrm{v}}\right)}{2R_{\mathrm{g}}T}\frac{h^3}{12\eta L^2}\left(\frac{1}{1-\alpha} + \frac{1}{\alpha}\right)\left(p^+ - p_{\mathrm{v}}\right) \tag{C.26}$$

In which the expression for the inlet pressure p^+ from Equation C.25 can be inserted. For minimum mass flow the variable α is equal to 0.5, similar to the incompressible flow situation. This can be seen in Figure 2.4.

Bearing Function

For the compressible flow situation it is no longer valid to state that the volume flow through each restriction is equal as the density of the air is dependent of the pressure. The mass flow through each restriction is equal and a system of equations can be set up:

$$\dot{m} = \rho Q = \frac{p_{\mathrm{s}}^2 - \left(p^+\right)^2}{2R_{\mathrm{g}}R_{\mathrm{i}}T} \tag{C.27}$$

$$\dot{m} = \rho Q = \frac{\left(p^+\right)^2 - \left(p^-\right)^2}{2R_{\mathrm{g}}R_{\mathrm{e(h)}}T} \tag{C.28}$$

$$\dot{m} = \rho Q = \frac{\left(p^+\right)^2 - p_{\mathrm{v}}^2}{2R_{\mathrm{g}}R_{\mathrm{o}}T} \tag{C.29}$$

The stiffness for the compressible flow is determined numerically. The load capacity per unit area is determined for a small perturbation in the film height, both negative and positive. The stiffness per unit area can then be calculated:

$$\bar{k} = -\frac{\overline{w}_{\mathrm{h}+\delta\mathrm{h}} - \overline{w}_{\mathrm{h}-\delta\mathrm{h}}}{2\delta h} \tag{C.30}$$

C.2. Air Bearing Actuator

A schematic overview of the air bearing actuator can be seen in Figure C.4. The concept is very similar to the passive cell from Figure C.1. The main difference is the varying air bearing surface, which is created by lowering the bearing surface at certain locations, forming so called pockets and dams. The cell has a length L and the inlets and outlets are positioned next to the dams at a distance αL, $0 < \alpha < 1$. The parameter β represents the pocket depth as a factor times the fly height above the dam, $\beta \geq 1$.

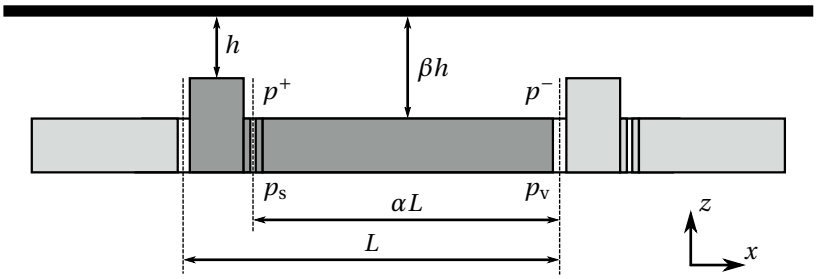

Figure C.4: Schematic cross-section of an active cell: the stepped surface actuator.

C.2.1. Incompressible Flow Case

The Reynolds equation from Equation 2.1 can be simplified to:

$$\frac{\partial}{\partial x}\left(H^3 \frac{\partial p}{\partial x}\right) = 0 \tag{C.31}$$

The film height H is not constant any more, contrary to the passive cell. It depends on the coordinate x and cannot be removed from the equation. However, it does not change the pressure distribution in the cell. The pressure distribution and load capacity are similar to respectively Equation C.2 and Equation C.3. The incompressible pressure distribution in the active cell can be seen in Figure 2.6. Using the zero load condition, the inlet pressure p^+ can be expressed as:

$$p^+ = 2p_{\mathrm{a}} - p_{\mathrm{v}} \tag{C.32}$$

Motor Function

The motor function can be characterised by the force density. Using Equation 2.3 the force density is determined and the inlet pressure p^+ from Equation C.32 is inserted in the equation:

$$\overline{F} = \frac{(\beta - 1)\, h}{L}\left(p_{\mathrm{a}} - p_{\mathrm{v}}\right) \tag{C.33}$$

The difference between the active cell and the passive cell is clear. A net force density is generated, which scales with the pressure difference $p_{\mathrm{a}} - p_{\mathrm{v}}$, the pocket depth $(\beta - 1)\, h$ and the length of the cell L. In addition, the mass flow density for the active cell can be derived:

$$\overline{m} = \frac{p_{\mathrm{a}}}{R_{\mathrm{g}} T} \frac{h^3}{12\eta L^2}\left(\frac{1}{1-\alpha} + \frac{\beta^3}{\alpha}\right)\left(p_{\mathrm{a}} - p_{\mathrm{v}}\right) \tag{C.34}$$

With the expressions for the force density and mass flow density known, the performance ratio can be calculated and the cell can be optimised for a high performance ratio. The result can be seen in Figure 2.7. The highest performance ratio is found for $\alpha = 0.72$ and $\beta = 1.87$.

Bearing Function

The stiffness per unit area for the active cell can be calculated the same way as the passive cell. The only difference with the passive cell is that the flow resistances of the thin film are different:

$$R_{\mathrm{l}}(h) = R_{\mathrm{dam}}(h) = \frac{12\eta L(1-\alpha)}{h^3} \tag{C.35}$$

$$R_{\mathrm{r}}(h) = R_{\mathrm{pocket}}(h) = \frac{12\eta L\alpha}{(\beta h)^3} \tag{C.36}$$

Resulting in an equivalent resistance and its derivative of:

$$R_{\mathrm{e}}(h) = \left(\frac{1}{R_{\mathrm{l(h)}}} + \frac{1}{R_{\mathrm{r(h)}}}\right)^{-1} = \frac{12\eta L\alpha(1-\alpha)}{h^3\left((1-\alpha)\beta^3+\alpha\right)} \tag{C.37}$$

$$\frac{\partial R_{\mathrm{e}}(h)}{\partial h} = -\frac{36\eta L\alpha(1-\alpha)}{h^4\left((1-\alpha)\beta^3+\alpha\right)} \tag{C.38}$$

C.2.2. Compressible Flow Case

After removing the constant terms, the Reynolds equation for the active cell in the compressible flow situation is equal to:

$$\frac{\partial}{\partial x}\left(H^3\frac{p\partial p}{\partial x}\right) = 0 \tag{C.39}$$

Solving the Reynolds equations results in the same pressure distribution and load capacity as the passive cell, which is shown in respectively Equation C.23 and Equation C.24. The pressure distribution is visualised in Figure 2.6. The zero load condition gives the following expression for the inlet pressure p^+.

$$p^+ = -\frac{1}{2}p_{\mathrm{v}} + \frac{3}{4}p_{\mathrm{a}} + \frac{1}{4}\sqrt{-12{p_{\mathrm{v}}}^2 + 12p_{\mathrm{a}}p_{\mathrm{v}} + 9{p_{\mathrm{a}}}^2} \tag{C.40}$$

Bearing Function

Similar to the passive cell, the stiffness of the active cell for the compressible flow situation are determined numerically, according to Equation C.30.

Motor Function

The force density and mass flow density of the active cell can be calculated, using respectively Equation 2.3 and Equation 2.4:

$$\bar{F} = \frac{1}{L}\frac{(\beta-1)h}{2}\left(p^+ - p_{\mathrm{v}}\right) \tag{C.41}$$

$$\bar{\dot{m}} = \frac{\left(p^+ + p_{\mathrm{v}}\right)}{2R_{\mathrm{g}}T}\frac{h^3}{12\eta L^2}\left(\frac{1}{1-\alpha} + \frac{\beta^3}{\alpha}\right)\left(p^+ - p_{\mathrm{v}}\right) \tag{C.42}$$

In both equations the inlet pressure p^+ is taken from Equation C.40. As the force density and mass flow density are known, the performance ratio for the compressible flow situation can be determined and the cell can be optimised for a high performance ratio. The optimal values of α and β are identical to the values which are found in the incompressible flow situation.

D

Flow Control

This chapter describes the working principle of flow control and why it is necessary to have bearing stiffness. After the working principle is explained, the common flow restrictions are discussed.

D.1. Working Principle

Flow control is essential for a stable air bearing system. A simple air bearing is used to explain the working principle. First, an air bearing without an inlet restriction is analysed. The air bearing is visualised in Figure D.1. On the left side of this figure a cross-section of a two-dimensional air bearing, which carries an object, is shown. It is assumed that the air bearing has an infinite width in the out of plane direction (out of the paper). The air bearing is fed with feed pressure p_s. The air flows through the centre to the sides of the air bearing. The pressure, which is plotted above the cross-section, gradually decreases to ambient pressure p_a. Because the average pressure in the air film exceeds the ambient pressure, which acts on top of the object, the bearing has the capacity to carry a load. The load capacity is equal to the integral of the air film pressure over the surface of the air bearing. It is thus dependent on the shape and height of the pressure profile in the air film. A stable air bearing is able to adjust the load capacity according to the applied load. When the load capacity is dependent of the film thickness, bearing stiffness is achieved. This can be well explained by the electric analogy of the air flow on the right side of Figure D.1. The pressures can be seen as the applied voltages, the air flow as the current, the flow resistances as the electric resistances and the ambient pressure as the electric ground. The thin air film is the only resistance in the air bearing. Its resistance value is dependent of the film height: $R_f(h)$. As the feed pressure and ambient pressure are constant, the load capacity of the air bearing is constant. A constant load capacity results in zero stiffness and an unstable air bearing.

Flow control is necessary to ensure that the film pressure varies with the applied load and the air bearing has stiffness. There are several ways to achieve this bearing stiffness, but the most common one is a flow restriction. The cross-section of the air bearing with a flow restriction is visualised in Figure D.2. In this case the air pressure is reduced from feed pressure p_s to the restriction pressure p^+, after which the air flows to the sides of the air bearing. The electric analogy on the right side of Figure D.2 shows an extra resistance R_i: the resistance of the inlet restriction. If the load on the bearing increases, the film height h decreases, resulting in an increased value of the film resistance $R_f(h)$. The restriction pressure p^+ increases, hereby generating a restoring force on the air bearing, which pushes the air bearing upwards. A similar effect can be noticed for a decreasing load. This results in an increasing film height h and therefore a decreasing value of the film resistance $R_f(h)$, resulting in a restoring force, which pulls the object downwards. The air film resistance is now dependent of the applied load and thus the film height, which gives the air bearing stiffness.

D.2. Restrictions

From the previous section it is clear that inlet restrictions are essential for having bearing stiffness. Inlet restrictions control the flow of an air bearing. As said before, there are also other methods to achieve this [41]:

1. Laminar restrictions: such as capillary, slot or annular restrictions.
2. Turbulent restrictions: such as an orifice of any shape.

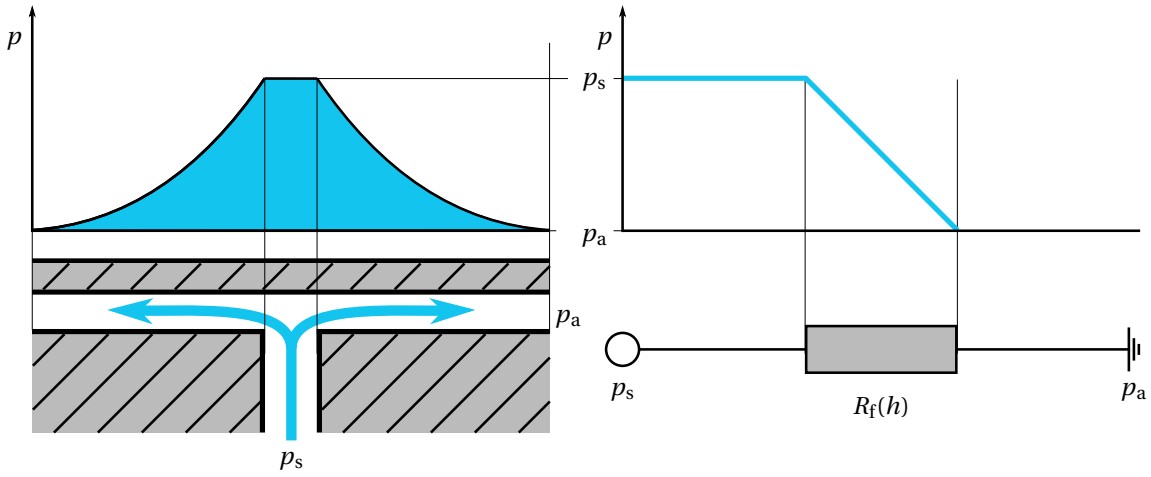

Figure D.1: Left: air bearing surface without an inlet restriction and corresponding pressure decay. Right: flow circuit of the air bearing and corresponding pressure decay.

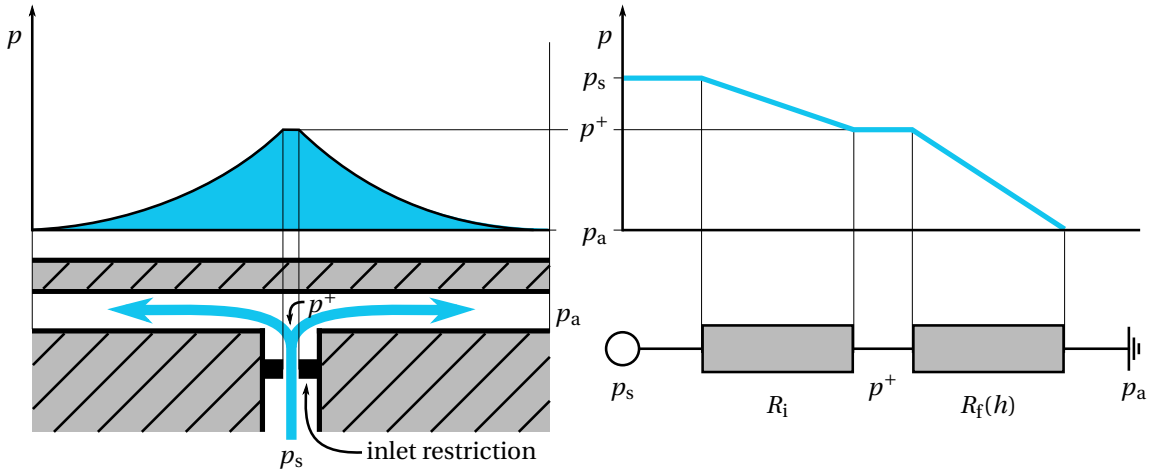

Figure D.2: Left: air bearing surface with an inlet restriction and corresponding pressure decay. Right: flow circuit of the air bearing and corresponding pressure decay.

3. Constant flow control: various valves or pumps.
4. Pressure-sensing valves.
5. Inherent flow control: such as a shallow recess, or inherent annular orifice restrictions.

In this study, only the first two methods (restrictions) are analysed on their performance and how they are modelled, as they are the most commonly applied flow control method in air bearing applications. Furthermore, they are the most suitable for a transport demonstrator because of the ease of manufacturing and low cost. Assuming incompressible flow the pressure drop over a flow restriction can be described by Ohm's law for electric circuits. The pressure drop is determined by the air flow through the restriction:

$$p_1 - p_2 = R\dot{q} \tag{D.1}$$

This is visualised in Figure D.3. The resistance R can be linear or non-linear regarding the pressure difference and is determined by the shape and dimensions of the restriction. The most common restrictions are discussed in more depth. These are the capillary restriction, and the porous restriction. As the orifice restriction is discussed in the main chapters this one is not discussed here.

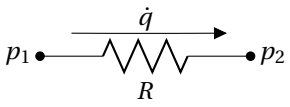

Figure D.3: Pressure drop over a resistance.

D.2.1. Capillary Restriction

A capillary restriction is basically a tube of length l with a round cross-section of diameter d. A schematic of a capillary restriction can be seen in Figure D.4. The flow through a capillary restriction is described by the Hagen-Posuille law [53]:

$$\dot{q} = \frac{\pi d^4}{128 \eta l} \left(p_1 - p_2 \right) \tag{D.2}$$

in which η is the dynamic viscosity. The resistance value can be tuned by varying the length and diameter. The equation is only valid for laminar isothermal viscous conditions, which implies that the Reynolds number should be less than about 2100. The equation applies to tubes where the end-effect losses are negligible. The ratio l/d should be large, preferably over 100. Common methods of making capillary restrictions are tubing, glass capillaries, hole drilling and spark machining. The first two methods are commercially available. The other alternatives are not very practicable because it is difficult to achieve the necessary length to diameter ratio. The biggest advantage of capillary restrictions is the ease of manufacturing them, as a capillary can be made by cutting a commercially available tube of known bore to the desired length. Another advantage is the linear relationship between the flow and the pressures, which makes the modelling relatively easy. However, capillary tube restrictions are not often applied in aero-static bearing applications. Extremely small bore diameters are required, which makes them not very practicable [41]. Wesselingh [51] implemented capillary tubing as inlet restrictions in his air-based actuator for thin substrates. In the final system capillary tubes of 250 µm inner diameter and a length of 16.5 mm are used. All restrictions have been tested on their flow to pressure behaviour and their resistance value. The capillary tubes show a predictable and linear response in the intended operating range and the behaviour of capillaries of the same dimensions is repeatable. However, he discovered that for larger flow rates (>15 kPa pressure difference) the capillary tubes are less suitable. Above this pressure difference the assumption of laminar flow is not valid anymore and the linear relationship between the flow and the pressure difference disappears.

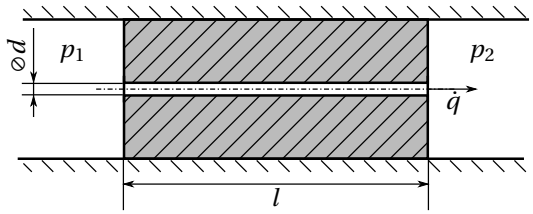

Figure D.4: Cross-section of a capillary restriction.

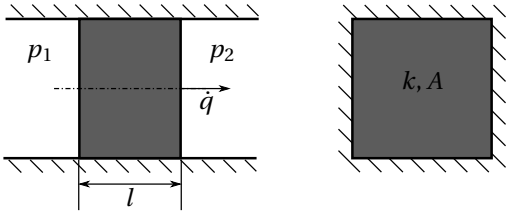

Figure D.5: Cross-section and side view of a porous restriction.

Vuong [49] also implemented capillary tubes in his flowerbed. Commercially available capillary tubes of 0.38 mm inner diameter and 14 mm length have been used. Because the flow in the tubes was found to be purely turbulent the Hagen-Poiseuille could not be used for predicting the resistance values. The restrictions have been dimensioned with an experimental restriction experiment. By using a fitting tool the resistance values have been implemented in the model for more accurate predictions of the system behaviour. Unfortunately, the numerical model and experimental results still show differences. One explanation could be that the capillary restrictions are not identical. The relatively large deviation of ±0.013 mm on the inner diameter of the capillary tubes can result in variations in the resistance values of ±12%. Hoogeboom [20] and Verbruggen [48] have used similar capillary restrictions in their design. They both experienced problems with implementing the capillaries in the set-up. It turned out to be difficult to minimise the volumes downstream the restrictions, which cause pneumatic hammer (dynamic instability).

D.2.2. Porous Restriction

The ideal aero-static design would supply the air evenly over the entire bearing pad. This can be realised by making use of porous restrictions. A porous restriction is a solid block of material with a network of small and tortuous channels running through it. All those channels form an array of very small resistances, which are connected in parallel. A schematic of a porous restriction, both cross-section and side view, can be seen in Figure D.5. The porosity of the material can be achieved in several ways. Metal powder sintering, laser drilling after surface densification by mechanical rolling or porous plastics are some examples. Sintered bronze or sintered carbon are the most commonly applied porous materials. A lot of research has been conducted on air bearing applications which use porous restrictions. A comprehensive overview of these applications and the research on the modelling of the flow through porous media up to 1998 is given by Kwan [27]. Porous restrictions have a higher stiffness and load capacity than other restrictions. Moreover, the damping in porous restrictions is higher and therefore they are generally not subject to pneumatic instabilities [42]. Most researchers use the one-dimensional Darcy's law to describe the flow through a porous medium. This law shows a linear relationship between the volume flow and the pressure difference, assuming incompressible flow:

$$\dot{q} = \frac{kA}{\eta l}\left(p_1 - p_2\right) \tag{D.3}$$

with k the permeability of the medium, A the porous surface perpendicular to the flow direction, η the dynamic viscosity and l the length/thickness of the restriction. The permeability of the medium is the most critical parameter and is highly dependent on the type of process for achieving the porosity. An approximate value of the permeability is given by:

$$k = \frac{\eta_\mathrm{p}}{\tau_\mathrm{p}} d_\mathrm{p}^2 \tag{D.4}$$

with η_p the volume fraction of the voids, τ_p the tortuosity of the channels and d_p the mean pore diameter [51].

E

Extended Studies

In this chapter, the extended studies are presented. In the first section, the extra results of the dynamic analysis from Section 2.6.3 are shown. This is followed by the extra results of the sensitivity analysis from Section 7.5.1.

E.1. Dynamic Analysis

In Section 2.6.3, a two-dimensional, passive air bearing cell is analysed to study the influence of volumes downstream the inlet restriction and the pressure ratio over the inlet restriction on the dynamic stability of the system. The damping is calculated for different combinations of the pressure ratio and the volume. When the damping is negative, the system is dynamically unstable and pneumatic hammer will occur. The analysis in Section 2.6.3 is done for a fixed vacuum pressure of 0.7 bar. In this section, the dynamic analysis is done for different vacuum pressures, such that the influence of this variable on the dynamic stability can also be investigated. The results of the dynamic analysis for a vacuum pressure of 0.5 bar, 0.7 bar and 0.9 bar, can be seen in respectively Figure E.1, Figure E.2 and Figure E.3. The influence of the vacuum pressure is significant. For a vacuum pressure of 0.5 bar the air bearing is only stable for a large pressure ratio, which means a small pressure drop over the inlet restriction. The rule of thumb, which states that the system should be dynamically stable if the volume downstream the inlet restriction is less than 1/20 of the air film volume, is no longer valid [42]. In the case of a vacuum pressure of 0.7 bar the damping increases. This figure is discussed in more depth in Section 2.6.3. The last graph in Figure E.3 shows the damping when the vacuum pressure is equal to 0.9 bar. The values of the damping have increased even more. The system is stable for all the depicted combinations of the volume and the pressure ratio.

In general, it can be concluded that the vacuum pressure has a negative influence on the dynamic stability of an air bearing. A decreasing vacuum pressure will result in a decreasing damping, which increases the chance of pneumatic hammer.

E.2. Sensitivity Analysis

In this study, the measurements and model of the active surface of the second prototype are studied. In Section 7.5.1, the sensitivity of the fly height and force are already shown, as a result of small variations in the vacuum pressure. In this section, the feed pressure p_s, inlet discharge coefficient $C_{d,i}$, and outlet discharge coefficient $C_{d,o}$ are varied with ±1%. The results of the variation in feed pressure are shown in Figure E.4 and Figure E.5. The variation in feed pressure results in a variation of the fly height of $\pm 1.5 - \pm 3.5\%$, or $\pm 0.3 - \pm 1.3\,\mu m$. The variation in force is equal to $\pm 2 - \pm 7\%$, or $\pm 0.8 - \pm 0.9\,mN$. The results of the variation in the inlet discharge coefficient are shown in Figure E.6 and Figure E.7. The variation in the inlet discharge coefficient results in a variation of the fly height of $\pm 1 - \pm 2.5\%$, or $\pm 0.2 - \pm 1\,\mu m$. The variation in force is equal to $\pm 1 - \pm 5.5\%$, or $\pm 0.4 - \pm 0.7\,mN$. The results of the variation in the outlet discharge coefficient are shown in Figure E.8 and Figure E.9. The variation in the outlet discharge coefficient results in a variation of the fly height of $\pm 0.5 - \pm 2\%$, or $\pm 0.1 - \pm 0.8\,\mu m$. The variation in force is equal to $\pm 1 - \pm 5.5\%$, or $\pm 0.4 - \pm 0.7\,mN$.

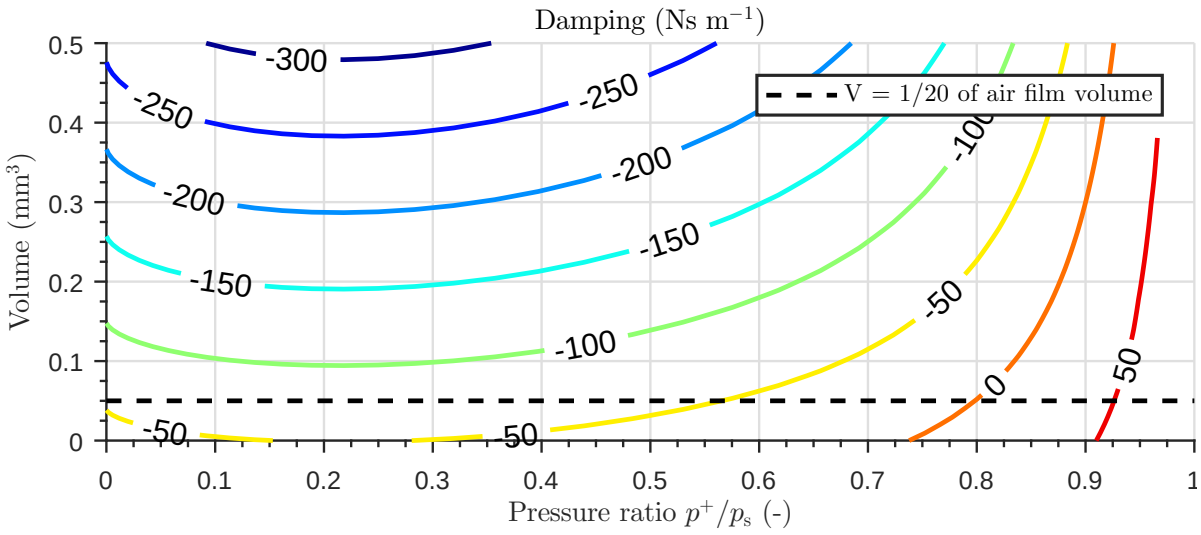

Figure E.1: Damping as a function of the pressure ratio p^+/p_s and the volumes downstream the inlet restriction. The vacuum pressure is equal to 0.5 bar.

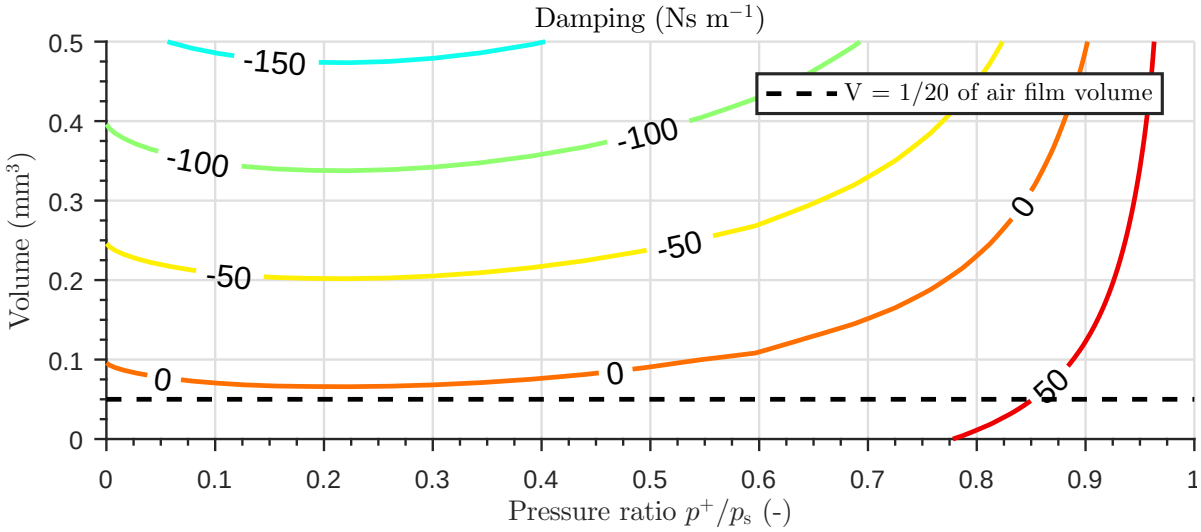

Figure E.2: Damping as a function of the pressure ratio p^+/p_s and the volumes downstream the inlet restriction. The vacuum pressure is equal to 0.7 bar.

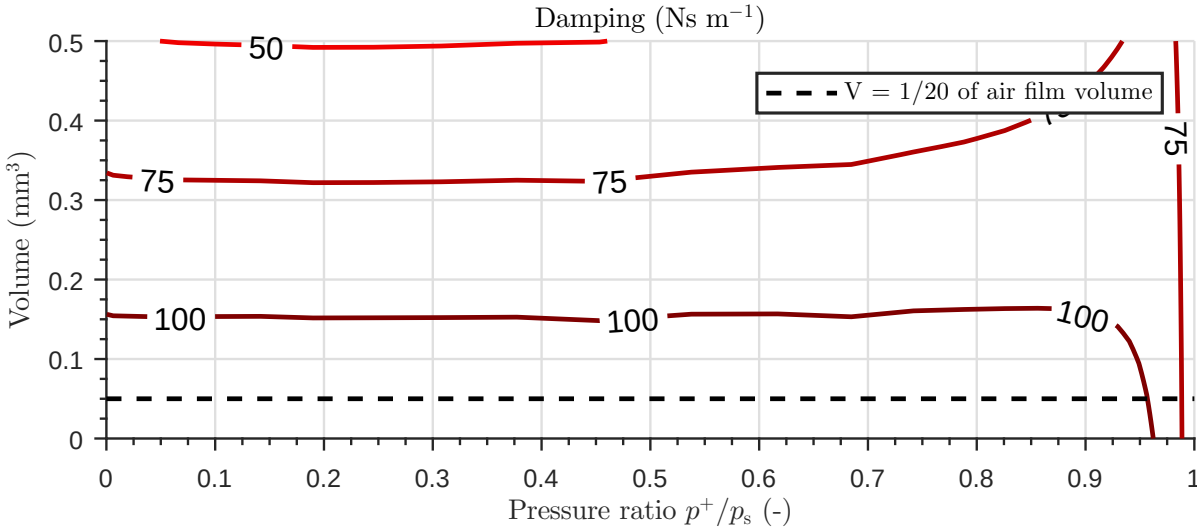

Figure E.3: Damping as a function of the pressure ratio p^+/p_s and the volumes downstream the inlet restriction. The vacuum pressure is equal to 0.9 bar.

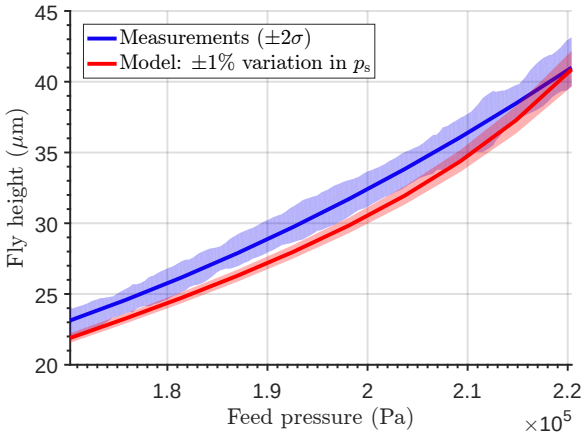

Figure E.4: Comparison of the fly height of the model and the measurement. The feed pressure is varied with ±1%.

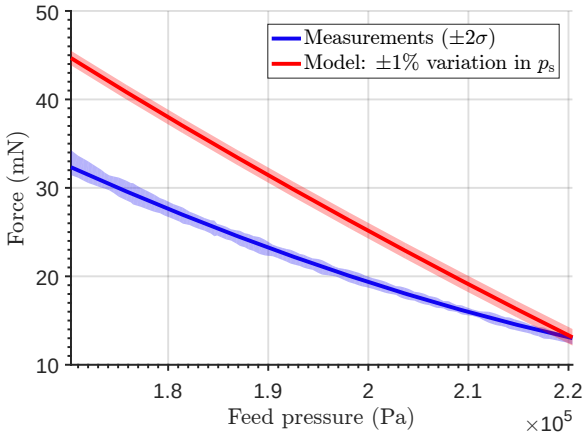

Figure E.5: Comparison of the force of the model and the measurement. The feed pressure is varied with ±1%.

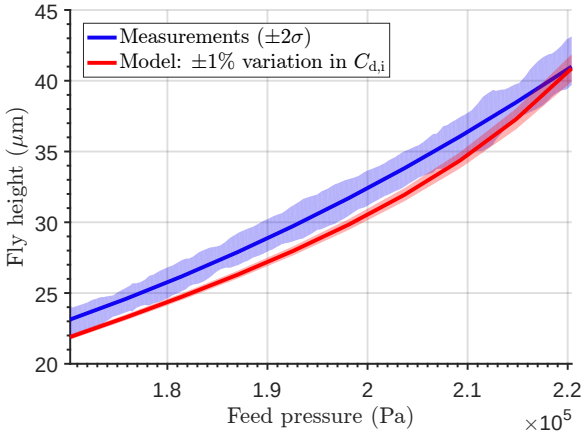

Figure E.6: Comparison of the fly height of the model and the measurement. The inlet discharge coefficient is varied with ±1%.

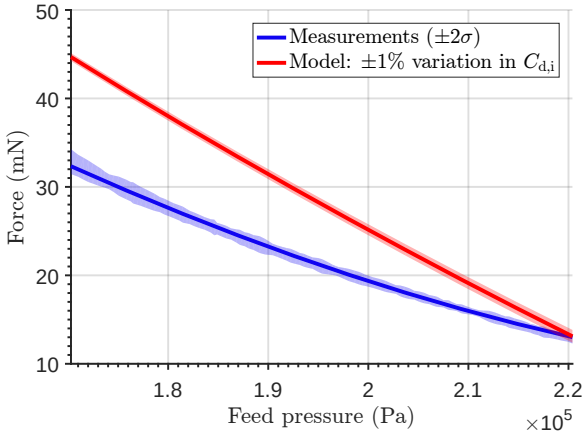

Figure E.7: Comparison of the force of the model and the measurement. The inlet discharge coefficient is varied with ±1%.

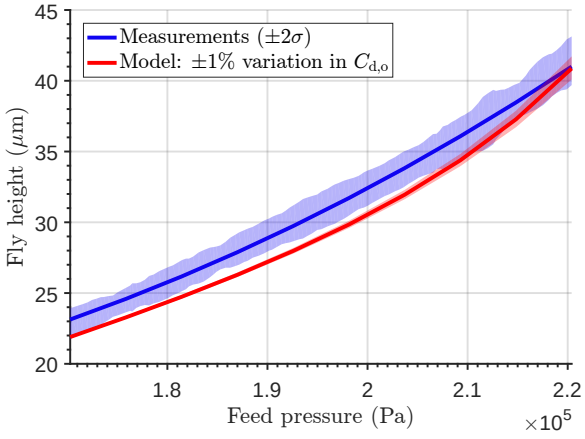

Figure E.8: Comparison of the fly height of the model and the measurement. The outlet discharge coefficient is varied with ±1%.

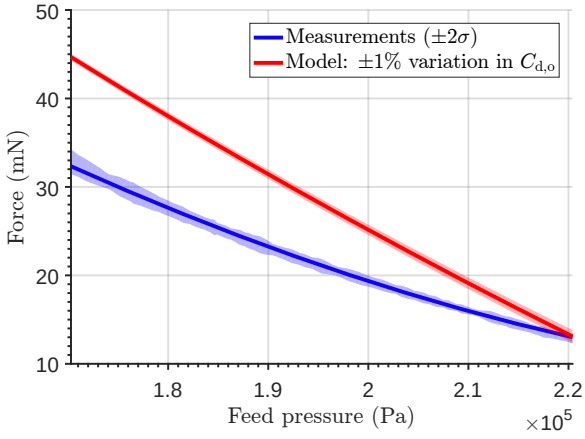

Figure E.9: Comparison of the force of the model and the measurement. The outlet discharge coefficient is varied with ±1%.

F

Restriction Measurement

For this thesis, many restriction measurements have been performed to investigate the mass flow through a flow restriction as a function of the pressure difference. The experiment is quite easy to set up and is described in this chapter.

F.1. Method

The mass flow through the orifices is measured by making use of a 2 l Festo pressure tank and a NXP MPX 5700DP differential pressure sensor with 7 bar pressure range. The set-up can be seen in Figure F.1. First, the pressure is set at a certain pressure with the proportional valve, which can be adjusted manually. The tank is filled with air at this pressure by closing the second valve (valve 2) and opening the first valve (valve 1). The first valve is then closed and the second valve is opened. The air in the tanks flows through the restriction to ambient pressure. By measuring the pressure upstream the restriction the mass flow can be determined.

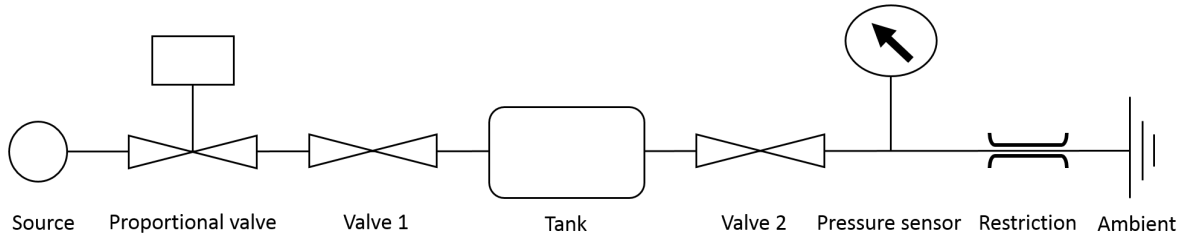

Figure F.1: Schematic of the restriction measurement [48].

The mass of air inside the tank follows from the ideal gas law and the fixed 2 l volume:

$$m = \rho V = \frac{pV}{R_s T} \tag{F.1}$$

The mass flow can then be determined by taking the derivative of the mass over time, assuming constant volume and temperature:

$$\dot{m} = -\frac{\partial p}{\partial t}\frac{V}{R_s T} \tag{F.2}$$

The mass flow through the restriction can thus be determined with a single pressure sensor. The data acquisition has been accomplished in LabVIEW and a USB-6211 (16-bit) DAQ device.

F.2. Restriction Integration

The biggest challenge in the restriction measurement is to include the restriction in the flow circuit such that the system is completely leakage free. Two methods have been developed to achieve this. The first method is used for the restriction measurement of the orifices, which are laser-cut by the precision laser

(Appendix G.2.2). The laser is also used to lase-cut a circle with a diameter of 4.6 mm around the previously laser-cut orifice. The result is a disk with the orifice in the centre. The disk can be placed in a 4 mm Festo connection, which can be connected to the pressure tank. The Festo connection has been adjusted slightly in a lathe. Some rubber o-rings make sure everything is leakage free. The connection can be seen in Figure F.2 and F.3. The second method has been developed to measure flow restrictions in a plate. The plate can be clamped by the device, which can be seen in Figure F.4 and F.5. Rubber o-rings seal everything and a tube can be connected on top of the device.

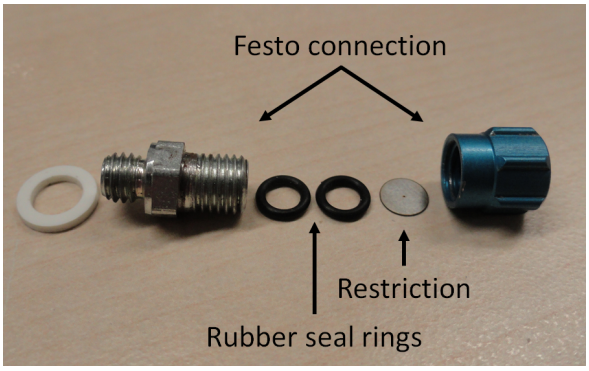

Figure F.2: The components of the Festo connection for including the laser-cut orifice in the flow circuit.

Figure F.3: The full assembly of the Festo connection.

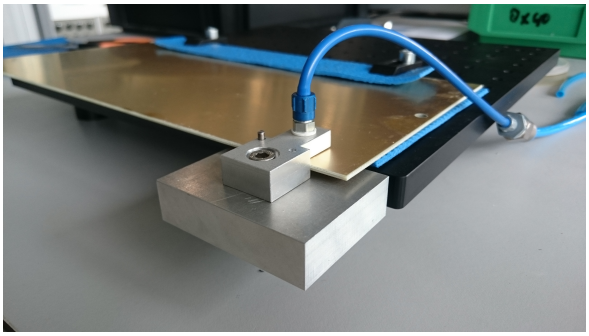

Figure F.4: The clamping device is used to measure the restrictions in the PCB surface.

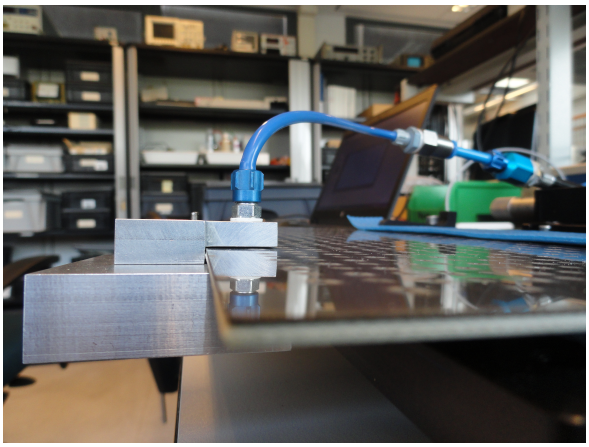

Figure F.5: The clamping device is used to measure the restrictions in the steel, which is already bonded to the PCB surface.

G

Manufacturing

During this project, a lot of knowledge on manufacturing methods has been developed. This has been documented such that other students can make use of it in future projects. For this thesis, a transport demonstrator has been manufactured. The complete transport demonstrator consists of three main parts: the manifold, the restrictions and the air bearing surface. The manufacturing method of each component is discussed in depth.

G.1. Manifold

The main function of the manifold is to connect the pressure supplies to the correct inlets and outlets. Leakage from one channel to another should be prevented. It is suggested to make use of a layered approach. The manifold can be build up from different layers as well. The aim is to find a simple, fast and cheap manufacturing method. Wesselingh [51] created his aluminium manifold in a CNC milling machine. As the manifold for this project consists of more layers and the milling is deemed to be relatively expensive, this is not the preferred solution. Vuong [49] 3D printed his manifold, which is a cheap way of manufacturing. However, he faced problems with removing all the support material in the small channels and therefore this manufacturing method is not preferred. Vagher [44] built a manifold using Poly Methyl Meth Acrylate (PMMA) plates, which is seen as the most promising manufacturing method. The air channels and holes can be easily laser cut in the PMMA. While the manufacturing of the air channels and holes is very easy, the bonding of the PMMA plates is a challenge, as it should be leakage free. The bonding of PMMA plates is a trending topic in the microfluidic fabrication sector as PMMA plates are a cheap alternative for the silicon-based materials. The bonding of the plates is the final and most important step in the manufacturing process. A nice overview of different bonding techniques can be found in [7]. Thermal bonding, UV-assisted bonding, solvent bonding, microwave bonding and friction spot welding are examples of conventional bonding techniques. For many of these techniques special equipment is needed, like hot embossing machines for thermal bonding and high intensity UV-lamps for UV-assisted bonding. Different bonding methods have been tried and will be discussed.

G.1.1. Ethanol

A relatively simple alternative for bonding PMMA plates has been suggested by Bamshad [7]. In this bonding process a thin layer of pure ethanol is dispersed between two PMMA plates. The plates are then pressed together by simple paper clamps and the whole assembly is heated to 74° for 10 minutes. At this temperature the thin film of ethanol is able to dissolve some of the PMMA material. The ethanol evaporates and the monomers of the PMMA plates are connected to each other. A big advantage of this technique is the sequence of applying the ethanol and the heating of the plates. If the plates are positioned incorrectly with respect to each other or the solvent has not reached all parts of the plates, the first step of applying the ethanol can be repeated. This is not possible with conventional glues or tapes.

The thermal assisted bonding technique with ethanol has been tried with a few small samples. A strong bond is realised. Bigger PMMA plates are more difficult to bond for two reasons. First of all, it is quite hard to make sure that the ethanol film covers the entire surface. Secondly, the heating of the plates is an issue. Be-

cause of the lack of a fan-assisted oven, which is required when working with flammable gasses like ethanol, the heating is performed by placing the plates in hot water. This becomes more cumbersome when the plates become bigger. As an alternative it has been found in [21] that a mixture of 80% ethanol and 20% demi-water is able to solve PMMA at room temperature. This could potentially solve the heating problem. Some small tests have been performed. The bonding is realised but unfortunately the ethanol mixture cracks the PMMA at certain locations in the plates due to high material stresses. The cracking is probably not an issue at higher temperatures (74°) because then the PMMA is a bit more flexible.

G.1.2. Conventional

Because the experiments with ethanol have not been successful, some conventional solvent bonding techniques are tried. Vagher [44] tested several adhesives (Kombi Plastic, Loctite 9492 Epoxy Hysol), chemicals (Dichloromethane) and tapes (3M double-sided Foam Tape 4026, commercial double-sided tape and 3M double-sided transfer tape 7955MP) for the bonding of the plates and tested small manifolds for leakage. He states that the tested manifolds with 3M double-sided tape are completely leakage free and are able to withstand really high pressure difference as well. In this project the initial experiments with 3M double-sided tape have not been successful. Many air bubbles are trapped between the plates. An experimental study has been performed for finding a method in applying the tape in a proper way and limiting the amount of trapped air bubbles. The best results are realised by pressing the plates together with a mechanical press, after the tape has been applied. The mechanical press pushes the air away and forces the tape to bond the PMMA plates. As a result, only very tiny air bubbles are left. The steps for bonding two PMMA in a proper way is described below.

1. As a first step, clean the PMMA plates on which you want to apply the tape. Isopropanol and a cleaning wipe are used to remove any dust or fat. Something like toilet paper works as well, but make sure that no bits of paper are left.

2. Cut the tape to an appropriate size and remove the first liner. The tape should be applied in a rolling manner, such that no air bubbles are trapped between the tape and the PMMA. You can use your fingers or a wall paper roller to press the tape directly on the PMMA during the rolling movement, see Figure G.1 and G.2.

Figure G.1: Apply the tape in a rolling manner.

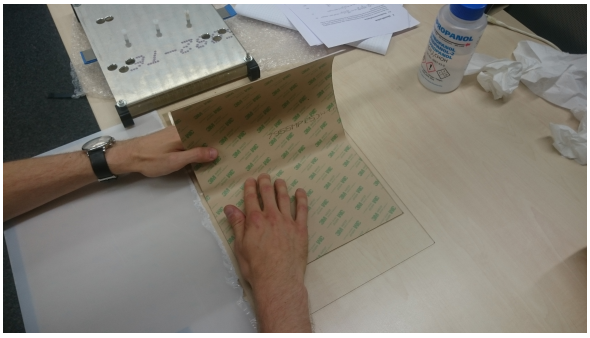

Figure G.2: Use your fingers to press the tape on the PMMA.

3. When the tape is applied, you can laser cut the plates. The laser cutter at 3mE (IWS) has a known drift. If you have to laser cut a large amount of features, like in this project, the laser cutter will be millimetres off target when it is finished. The laser cutter at Industrial Design does not have this drift and is therefore preferred. For aligning the plates in later steps of this bonding process, it is very useful to include additional holes in the corners of your design. For my design, holes of 5 mm diameter and corresponding guiding screws have been used.

4. The next step is to tap the holes for you pneumatic connections. Most of the Festo equipment uses a G1/8 thread. For this connection you have to laser cut holes with a 8.8 mm diameter.

5. Wait for at least 24 hours to let the tape settle. 3M has confirmed that the air is able to propagate through the adhesive and second liner. This means that any present air bubbles will disappear over time, resulting in a stronger connection.

6. Now it is time to bond the plates together. Clean the surface of the second PMMA plate with isopropanol as well. Remove the second liner of the 3M tape (Figure G.3). You can use the guidance screws to align the plates. Clap the plates onto each other and press the plates together (Figure G.4).

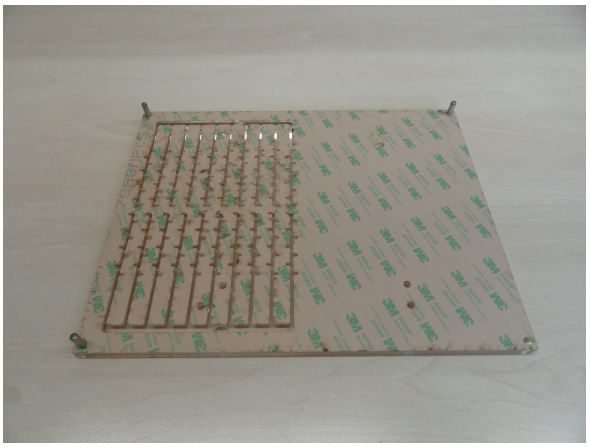

Figure G.3: Remove the last liner of tape.

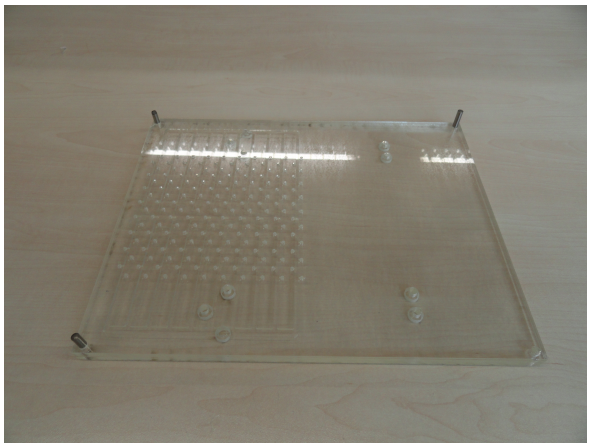

Figure G.4: Use guidance screws to align the plates.

7. The last step is to remove the air bubbles. Put the stack of plates under the mechanical press (IWS), see Figure G.5. It is advised to place a flat plate or a piece of rubber on top of the stack of plates to avoid deformations of the PMMA. I have used a yoga mat for this (Figure G.6), on both sides of the PMMA. Lower the press and apply sufficient pressure. Do this on every part of the stack until only very tiny air bubbles are left. You can clearly see in Figure G.7 that the air bubbles are removed at the location where pressure has been applied on the plates. The final manifold can be seen in Figure G.8.

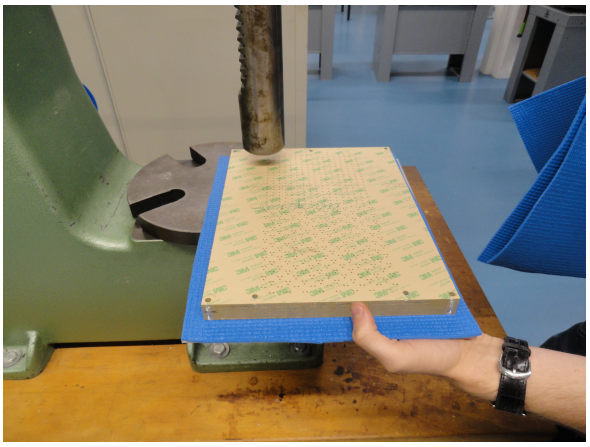

Figure G.5: Use the mechanical press at IWS to press the plates together.

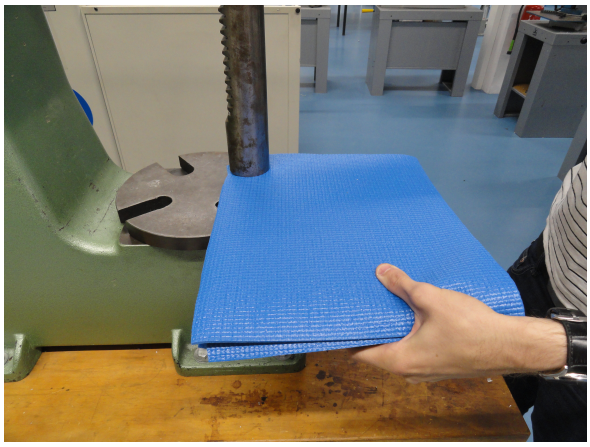

Figure G.6: It is advised to use some sort of rubber material between the press and the PMMA to prevent damage to the plates, which easily crack.

G.1.3. Measurements

In order to have a better quantification of the maximum pressure difference, a couple of tests have been performed, in which the maximum pressure difference over a feature in the manifold has been measured. The features, which are called restrictions, are based on the geometries of the manifold and different types of restrictions are tested: channel to channel, channel to hole and hole to hole, see Figure G.9, G.10 and G.11. The width w is a measure for the tape width. The last two restrictions do not have true holes, because it is not possible to realise these in a test manifold with only a few layers and it is preferred to keep the manifolds simple. As the smallest restriction is in the direction of the circular shape, it is believed that it is a good representation of a hole. The test manifolds consist of two 5 mm outer base plates with the pneumatic connections and a 3 mm inner plate with the channels for guiding the air flow. The air flow channels have a width of 2 mm.

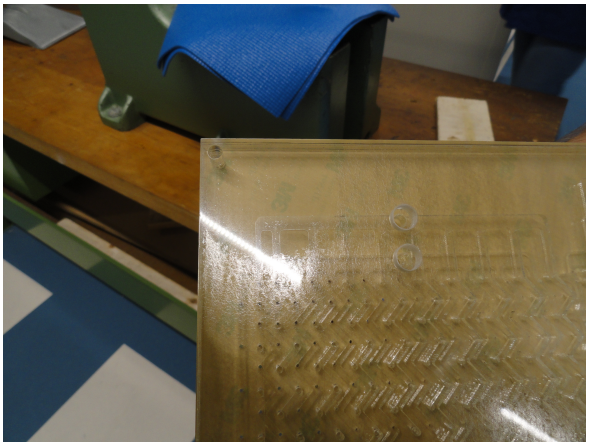

Figure G.7: The before and after applying pressure picture.

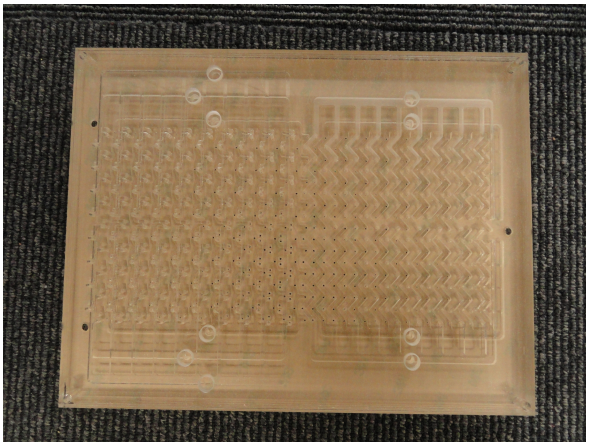

Figure G.8: The total manifold of eight plates.

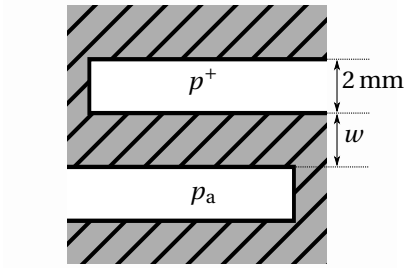

Figure G.9: channel to channel manifold.

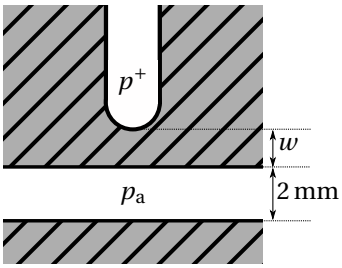

Figure G.10: Hole to channel manifold

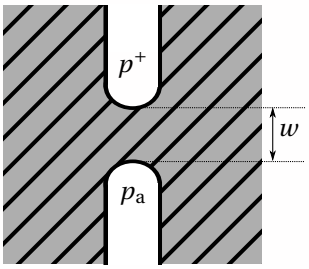

Figure G.11: Hole to hole manifold.

In the measurement set-up, the pressure is slowly increased with a proportional valve, until leakage occurs. The maximum pressure difference is recorded. The channels are partly filled with coloured water, which makes it easy to see if a leakage occurs. The coloured channels can be seen in Figure G.12. Restrictions with different tape widths w have been tested.

Results

The channel to channel restriction is basically a beam structure with double sided tape on both top and bottom side. It is the weakest restriction, because the beams tend to bend if the pressure difference increases. The tested restrictions have a beam length of 27 mm. Leakages occur when the beam breaks, due to the pressure difference. The results of the pressure differences for varying beam thickness values can be seen in Figure G.13. The measurements show a general trend in which the pressure differences increase linearly with the thickness of the beam. For the smallest beam thickness of 1 mm, a pressure difference of 1.9 bar is reached, while the thickest beam of 3 mm fails at approximately 4.5 bar. Some of the measurements are coloured in red because leakages occurred at the supply pressure connection. These measurements are not used in the calculation of the linear regression line. It must be noted that the beams tend to bend significantly while increasing the pressure difference. This already starts at a pressure difference of approximately 0.9 bar for the thinnest beam of 1 mm. All the beams break in the corners, at which location the bending moment is largest, before the double sided tape fails. As the measurement does not indicate when the double sided tape fails it is only relevant for this specific beam length.

The experiments for the channel to hole restriction and hole to hole restriction do not show any sign of leakage up to a pressure difference of 6.2 bar. Larger pressure differences are not realised, because 7.2 bar is the maximum pressure in the laboratory. In general, it can be concluded that is not preferred to have long channel with pressure differences close to each other because of the bending of the beams. The double sided tape is in this case not the limiting factor. For small restrictions such as the channel to hole and hole to hole restriction very high pressure differences can be applied, at least up to 6.2 bar.

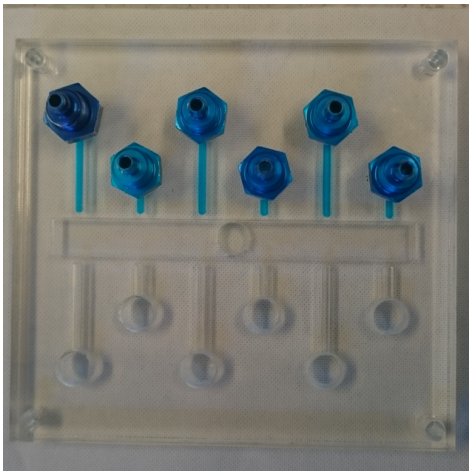

Figure G.12: Manifold for testing the channel to hole restriction.

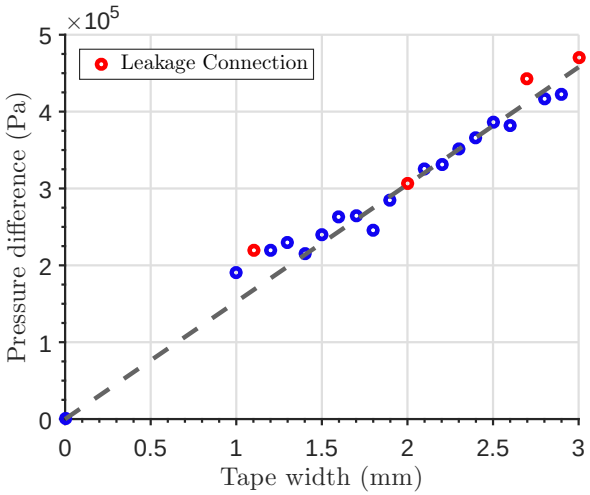

Figure G.13: Results of channel to channel restriction.

G.2. Restrictions

It is decided to use orifice restrictions in the demonstrator. The restrictions can be fabricated by creating small holes in a layer of material. The outlet restrictions have a diameter which is larger than 0.2 mm and can therefore be drilled in the PCB by Eurocircuits. The inlet restrictions have a diameter which is preferably smaller, in the range of 0.1 mm. It would be very convenient to also create the inlet restrictions in the PCB, but the diameter of the inlet restrictions and the thickness of the PCB make this challenging. Therefore, the inlet restrictions are created in an extra layer of material, which can be inserted between the manifold and the PCB. A fabrication method must be found, which is able to manufacture a large amount of very small holes in a repeatable way.

G.2.1. Drilling

The conventional way of making holes in a sheet of material is drilling. Drilling can be done down to diameter of 0.1 mm. These drills break easily and it is almost impossible to drill such holes manually. A possibility would be to drill the holes on a CNC machine. Unfortunately, it proved to be hard to find a timeslot in the busy schedule of DEMO and the employee workshop of 3mE. Besides that, a cheaper solution is preferred.

G.2.2. Micro-laser

A cheap way to realise holes is by making use of laser cutting. The faculty of Precision and Microsystems Engineering has a micro-laser which is equipped with a 15 W Talon laser. This laser has a laser spot of 15 µm and is able to laser cut fine details and features. Many tests in 0.1 mm thick spring steel have been done with this laser. The spring steel is chosen because of its well-defined thickness and flat surface. The normal way of fabricating a circular hole by laser cutting is defining a circle, which can be seen in Figure G.14. The hole is realised by drilling the circle. The drilling number and drilling step determine the number of circles in the same plane and the distance between them. The drilling step is set to the laser spot size of 15 µm and the drilling number is set to 3. The material will be removed level by level, which is defined by the number of levels and the step in z-direction (out of plane, into the spring steel). Typical values for 0.1 mm spring steel are 4 levels and a z-step of 0.25 mm. In each level, three circles will be laser cut. It has been discovered that laser cutting the circular holes in this way does not work, because the holes are too small. The laser does not finish the full circle: the end point and start point on a circle do not match. This results in a hole in which some material is left. To solve this problem the circle is replaced by a spiral, as can be seen in Figure G.15. When using the spiral shape, circular holes can be realised. The settings for the drilling can be found in Figure G.16. The internal laser frequency should match the firing rate, which is set in de drill settings. Make sure to click the green check marks in the laser settings.

Due to the the laser spot size and the used settings the final hole has an outer diameter of 140 µm on top. The final hole diameter at the bottom of the plate is equal to 90 µm. A close-up of the backside of the orifice can be seen in Figure G.17. The difference in diameter between the front- and backside can be explained by

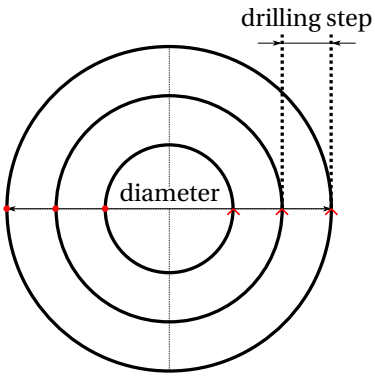

Figure G.14: Typical way for laser cutting circular holes. In each level three circles will be laser cut (drill number is equal to three). The drilling step is the distance between the circles. The laser starts at the red dot and the red arrow shows the direction in which the circles are laser cut.

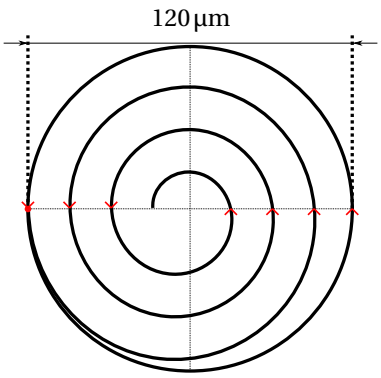

Figure G.15: To realise nicely shaped circular holes a spiral shape is used. The laser starts at the red dot and laser cuts the spiral in the direction of the red arrows. The distance between the lines at the horizontal axis is equal to the laser spot size. As the spiral consists out of one shape the drill number can be set to 1.

the so-called taper angle of the laser, which is approximately equal to 15°. Due to the thickness of the material the laser cannot reach the entire circle at lower levels. Therefore, the hole is tapered.

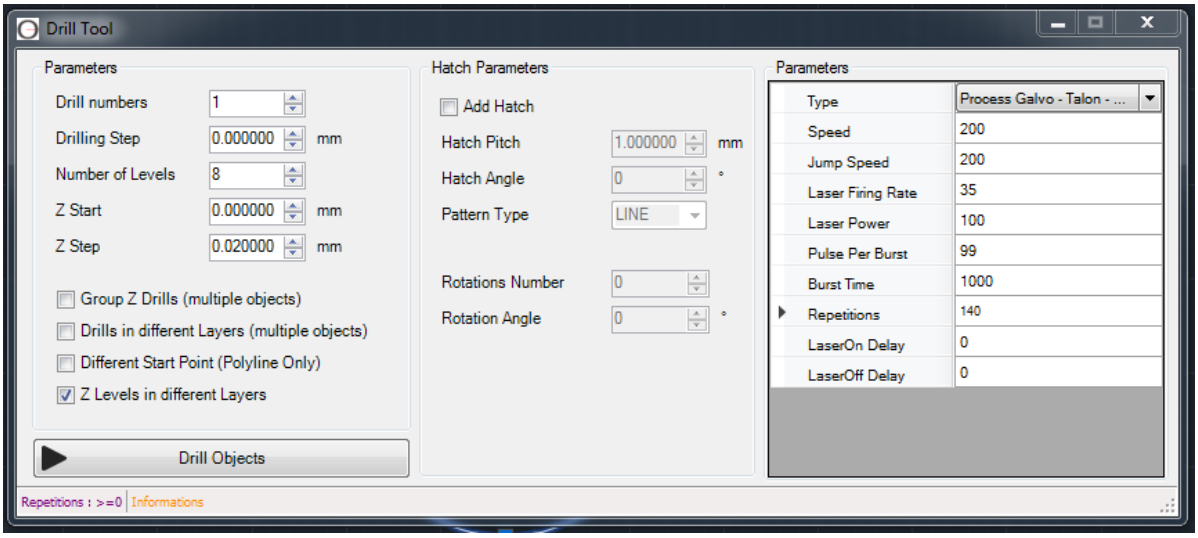

Figure G.16: Setting for the drilling.

The laser-cut orifice are tested in the flow measurement set-up, which is described in Appendix F. The mass flows, as a function of the pressure difference, can be seen in Figure G.18. The two orifice models (ideal and Jobson) are fitted to the average mass flow data, resulting in a discharge coefficients of 0.86 for the ideal orifice flow and 0.70 for the Jobson orifice flow.

The precision laser is able to laser-cut very nice well-defined orifice restrictions, but unfortunately it also has some downsides. One of the big disadvantages of the precision laser is the small working area. It is able to reach material within a 64 mm diameter circle. This area is considerably smaller than the area of the demonstrator. If the micro-laser is used to laser cut all the holes the spring steel plate must be re-positioned many times. Alignment becomes an issue and turns out to be really difficult. Another issue is the laser time. It takes about 30 seconds to laser-cut one orifice. As the final system has more than 500 inlets, it will take a long time to laser-cut them all. Therefore, this fabrication method is not preferred, despite the good quality of the orifices holes.

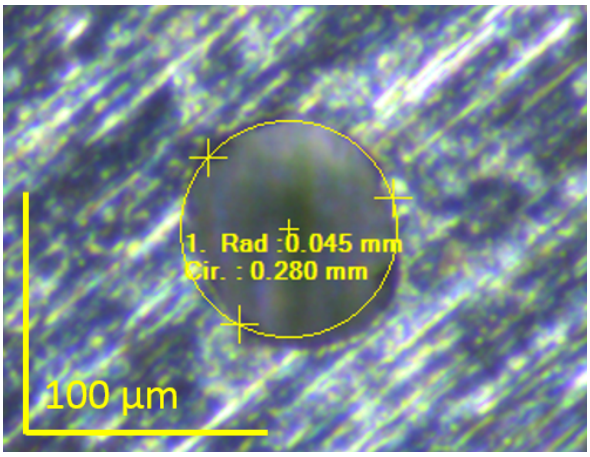

Figure G.17: Close-up of the backside of a orifice, which is laser-cut by the precision laser.

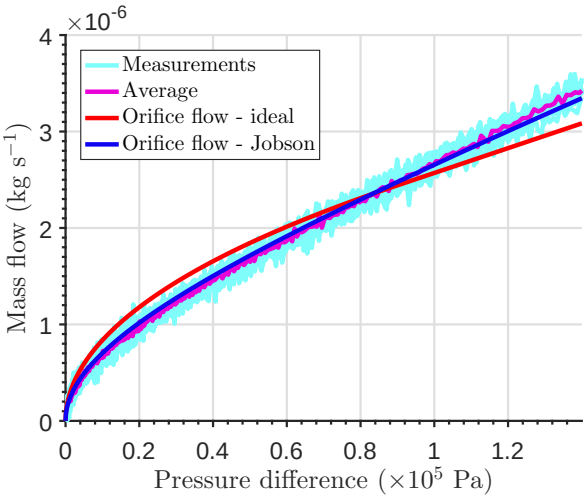

Figure G.18: Mass flow data inlet restriction.

G.2.3. Laser

The micro-laser produces very nice results, but the limited working area of the laser is a problem. It is suggested to use another laser, which has a larger working area. The laser at IWS (Lion Laser 1200 metal) meets this requirement. However, it is not really suited for the fabrication of small holes. The laser spot size has a diameter of approximately 0.1 mm. As the final holes size is equal to the laser spot size, the laser should only laser cut at one single point. This has turned out to be a problem because it is not possible to upload single points in the software of the laser. A workaround has been found. Instead of points small lines of 0.02 mm are drawn, as can be seen in Figure G.19. The frequency of the laser is set to 1 Hz, which is very low. The laser will start with one laser pulse at the beginning of the line. Because the frequency of the laser is so low, it is already at the beginning of the next line when the second laser pulse is fired. In this way the laser will laser cut single point in the material. The settings for the laser can be seen in Table G.20. Nice results have been achieved with 0.5 mm stainless steel (AISI 304). A close-up of the front side of the orifice hole can be seen in Figure G.21. The front side of the orifice is the side which faces the laser during the laser cut process. The hole diameter is equal to approximately 0.20 mm. The back side of the orifice hole can be seen in Figure G.22. The quality of the back side is less nice than that of the front side, due to backfiring of the laser. Small pieces of metal (burrs) are left at the edges. They will influence the mass flow through the orifice, but unfortunately it is almost impossible to remove them. The average diameter of the orifice holes is found to be equal to 0.12 mm.

Figure G.19: Small 0.02 mm lines are drawn for generating the DXF. Because of the low frequency the laser only fires one pulse at the beginning of each line, at the location of the red dot. The result is a pattern with holes.

Setting	Value	
Frequency	1	Hz
Time (laser)	10	ms
Power	75	%
Speed	32	$mm\,s^{-1}$
Time	0.1	s

Figure G.20: Settings for the Lion Laser.

G.3. Air Bearing Surface

The air bearing surface is the top surface of the layered design. It should be a flat surface with a low roughness and hexagonal pockets with a pocket depth in the order of 10 µm. The combination of the relatively large flat surface and the small pocket depth is a challenge for the fabrication and different methods have been tried. A relatively cheap and easy manufacturing method is aimed for. Wesselingh [51] developed multiple prototypes

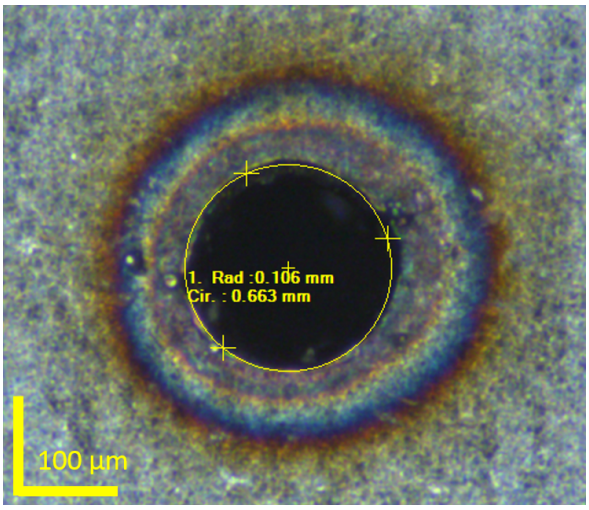

Figure G.21: Close-up of the front-side of a orifice, which is laser-cut by the IWS laser.

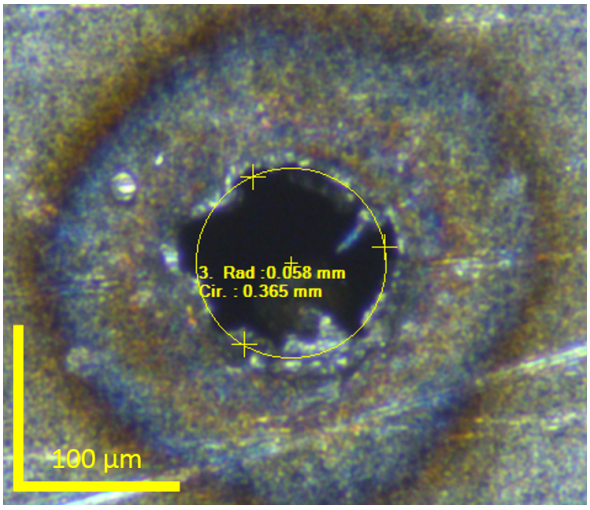

Figure G.22: Close-up of the back-side of a orifice, which is laser-cut by the IWS laser.

for the realisation of his final demonstrator: the step surface actuator. The first prototype he developed used PCB production techniques to manufacture the air bearing surface. The copper on the fibreglass substrate is used as dams and the pockets are etched away. A final pocket depth of 40 µm has been realised, which consists out of a 35 µm copper layer and a 5 µm surface finish. Two later prototypes of Wesselingh were designed for modularity and interchangeability. He tested different manufacturing techniques. The goal was to find a flat plate with well-defined pocket depths:

Sinker electrical discharge machining
The substrate is bended because of the internal stresses, which are caused by the removal of pockets on only one side. The price for a single plate is €800,-. The pocket depth has been verified at several locations and is equal to 10 µm.

Etching
Etching has been performed on low-cost steel and expensive stress relieved steel. Only the latter one is usable because it does not suffer from bending. The cost is €400,- for 10 plates and the pockets have a depth between 10 and 11 µm.

Electro-forming
The plates which are manufactured by electro-forming are grown on a mandrel from a nickel-cobalt alloy, resulting in a virtually stress free product. The pockets are etched away in a subsequent step. The cost is €600 for 10 plates. The pocket depth measurements are between 10 and 12 µm. However, the plate thickness shows variations of 5 µm across the plate.

Laser ablation
The quotation for laser ablation was €4000 for a single plate and thus too expensive. Wesselingh gives laser ablation as a recommendation for future projects as it can theoretically reach sub-micrometer accuracies and a very good surface finish.

Wesselingh concluded that the best results can be achieved by electro-forming. This method results in the best surface finish and the scratch-resistant nickel-cobalt alloy is a benefit as well. Using the 15W Talon Laser at the university laser ablation has been tested as well. Many materials, including spring steel, silicon, glass and aluminium, have been tested. However, it proved to be hard to find the correct settings. The surfaces are rough and the pocket depths do not have well-defined depths.

A method for manufacturing the air bearing surfaces must be selected. As the surface area in this project is considerably larger than the surface area of the prototype of Wesselingh [51], these investigated methods are deemed too expensive. The laser ablation does not give satisfying results. Therefore, the PCB surface is considered to be the most elegant solution. The PCB can be ordered at Eurocircuits, which is the usual PCB supplier of the university. To be able to provide the customers PCB's at a low price they work with certain

pools. Each pool has its own specifications such as number of layers, surface finish and copper layer thickness. Eurocircuits tries to place as many customer PCB's on one panel to make the price per PCB piece lower. The panel goes through the pool and in the final step the PCB's are separated from each other. The most basic pool is a 2-layer PCB, which is sufficient for this project. This PCB consists of a base substrate with a copper layer at the top and at the bottom. The typical process steps for the manufacturing of a single layer PCB will be explained. A detailed explanation can be found on the website of Eurocircuits[1].

1. Basis
The process starts with the selection of the base material, which consists out of a base substrate of epoxy resin and glass fill (reinforced fibreglass) and a copper layer on top and bottom. The thickness of the base layer and copper layers can be chosen. The standard is a 1.55 mm base layer with 35 µm copper layers.

2. Drilling
In this step the holes for the leaded components and via holes are drilled, the so called plated through (PTH) holes. In a later step the via holes will connect the outer copper layers together.

3. Imaging
In the clean room the copper is cleaned and coated with a layer of photo-sensitive film (photo-resist). The photo-resist is then hardened with powerful UV-lamps, which shines through the photo-mask, to define the copper pattern. The unhardened photo-resist is removed.

4. Plating
The next step is electro-plating the board with copper. In this process, an additional layer of 20-25 µm copper is added to the walls of the previously drilled holes to connect the outer copper layers. An additional aspect of the plating process is that the copper surfaces on top and bottom will also have the extra layer of copper. As a last step a thin layer of thin is plated onto the copper.

5. Etching
In the etching step the photo-resist is removed. The unwanted copper (without the layer of thin) is then etched away. The designed copper pattern remains.

6. Surface finish
To protect the copper a surface finish is applied. First, nickel is chemically deposited onto the copper. Then a thin coating of gold is applied in the same way over the nickel. The surface finish has a thickness of 3-6 µm.

7. Profiling
In the last step the non-plated through (NPTH) holes are drilled and the PCB's are separated from each other. The NPTH holes do not have the copper layer on the inner wall, which means the drill diameter is the final hole diameter. The profiling is usually done using a 2 mm drill but can also be done by V-scoring in which the panel is cut.

Due to the plating, the final copper layer thickness is increased by 20-25 µm. This means that the pocket depth will be larger and this is not preferred. As the plating of the holes is not required for this project it has been decided to fabricate the PCB on a separate panel. The base material is chosen to be 1.55 mm and the copper layer thickness is 12 µm. Because of the surface finish, the final pocket depth will be approximately 16.5 µm. The holes at the inlets and outlets will be drilled in the last step. The complete panel can be seen in Figure G.23. The panel is filled with four plates (2x prototype 1 and 2x prototype 2). The panel is shared with someone else, from whom the lower designs with the circles are.

G.4. Useful Commands

The final design is a relatively large surface with many holes. To handle this geometry efficiently some programs have been written to automatically draw the different features. As a help for future projects some useful commands have been written down here.

[1] `http://www.eurocircuits.com/making-a-pcb-pcb-manufacture-step-by-step/`

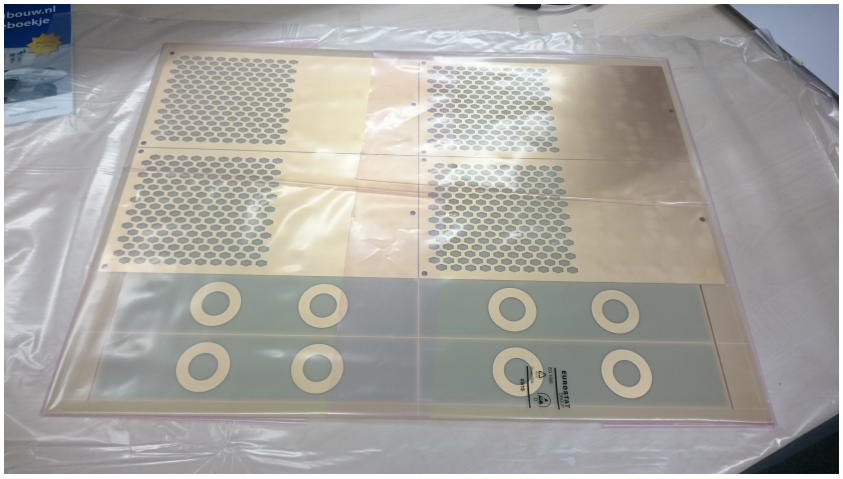

Figure G.23: The PCB's are ordered in a separate pool at Eurocircuits to prevent the extra layer of copper in the plating step.

G.4.1. AutoDesk EAGLE

The PCB is designed in the program AutoDesk EAGLE. In this program designs can be drawn manually, but this is very inconvenient if the design has many holes and the dimensions need to be accurate. The command line can be used for commands and has been very useful for the drawing of the PCB. The coordinates of the coordinates of the hexagons are taken from a DXF file, which is generated by COMSOL. The coordinates are imported into MATLAB by a small function found on the MathWorks website: "f_LectDxf". The coordinates of the drill holes are calculated in MATLAB using the geometry variables. Matlab is then used to generate a text file with all the commands, which are necessary to draw the design in EAGLE. The following commands have proven to be very useful for drawing the different features:

- `POLYGON (x1 y1) (x2 y2) (x3 y3) (x4 y4) (x5 y5) (x6 y6);` (for drawing the hexagons)
- `LINE (x1 y1) (x2 y2) (x3 y3) (x4 y4);` (for drawing the outer borders of the PCB and copper surface)
- `HOLE D (x1 y1);` (for creating a hole with diameter `D`)

Other useful commands are:

- `GRID MM;` (the grid is normally dimensioned in inches. This command changes the unit to mm)
- `CHANGE POUR CUTOUT;` (for not having copper at the enclosed geometry)
- `CHANGE POUR SOLID;` (for having copper at the enclosed geometry)
- `CHANGE WIDTH 0;` (the width of the wire should not influence the shape)
- `RATSNEST;` (for creating the polygon pour)
- `CHANGE LAYER TOP/BOTTOM/DIMENSION;` (for switching layers)

G.4.2. AutoDesk AutoCAD

The micro-laser at the faculty uses AutoCAD for drawing geometries. As the spiral geometry is very inconvenient to draw in AutoCAD it is automated using a script. The `SCRIPT` command is able to import commands from a ".scr" file. The command can be written down in a text editor program like Notepad. The file must be saved using the ".scr" extension. The two main commands are given below:

- `OSNAPCOORD 1` (this makes sure that the keyboard entries override the object snap settings. The object is drawn at the specified coordinates and does not snap to the nearest known point.)
- `PLINE x0,y0 A D` θ `(x1 y1) (x2 y2) (x3 y3) (x4 y4) (x5 y5) (x6 y6) (x7 y7) (x8 y8)` (A polyline is used for drawing the spirals. It starts at the position `x0,y0` and from there an arc is drawn with a diameter `D` in the direction of θ to the next point `x1,y1`. It then just continuous with similar curves to the next point.)

H

Sensors

In this chapter, the working of the sensors is explained and the calibration measurements are presented. First, the optic height sensors is discussed. After that, the force sensor is described.

H.1. Height Sensor

A height sensor is used to measure the fly height of the wafer. It should be able to measure tens of micrometers with at least micrometer resolution. The measurement has to be contactless, such that the wafer can float freely. In the system air is flowing with high velocities below the wafer. If the air is cleaned and filtered it will not charge the wafer. However, if the air has impurities the wafer is possibly charged. Therefore, a capacitive height measurement is not applicable in this case, as the charges of the wafer will disturb the measurement. It is suggested to make use of a fiberoptic sensor. This sensor is not sensitive to possible charges of the wafer. Other advantages of this sensor are the ability to measure the distance on a relatively small surface area and the ability to measure basically any surface by manually tuning the gain factor. A disadvantage of this sensor is the sensitivity to external light sources. This effect is minimised by making use of a hood in which the sensor is placed. The 3D printed hood can be seen in the pictures of the measurement set-up in Section 5.2.1. The sensor is a Philtec Model D63. The basic working principle of the sensor can be seen in Figure H.1. The sensor emits light, which reflects on the surface of the object which is measured. The distance between the sensor and the object depends on the amount of reflected light which is measured by the detector. A typical measurement curve can be seen in Figure H.1 as well. The sensor has a sensitive near side with a linear sensitivity of approximately $100\,\mathrm{mV\mu m^{-1}}$ in the range of $18\,\mu\mathrm{m}$ to $43\,\mu\mathrm{m}$ and a somewhat less sensitive far side with a linear sensitivity of approximately $-2.6\,\mathrm{mV\mu m^{-1}}$ in the range of 0.3 mm to 0.9 mm. In total, two sensors are tested by making use of a Thorlabs micrometer stage with a 0.01 mm resolution. The results are shown in Figure H.2. Each curve in this graph is an average of three measurements. The company Philtec has provided us with the calibration charts and data. As the measured curves show the expected behaviour the data from the calibration charts can be used safely. The first sensor (serial number D1716) has a near side sensitivity of $104.9\,\mathrm{mV\mu m^{-1}}$ in the range of $10.2\,\mu\mathrm{m}$ to $30.5\,\mu\mathrm{m}$. The second sensor (serial number D1719) has a near side sensitivity of $102.2\,\mathrm{mV\mu m^{-1}}$ in the range of $17.8\,\mu\mathrm{m}$ to $35.6\,\mu\mathrm{m}$. The calibration charts show the same far side sensitivity of $-2.87\,\mathrm{mV\mu m^{-1}}$ in the range of 0.2 mm to 1.0 mm.

H.2. Force Sensor

The force sensor measures the viscous traction force on the wafer. As the forces are in the order of tens of mN a sensitive sensor is required. Unfortunately, such a sensor was not available at the university at the time of doing this thesis project. Therefore, a Futek 100 g sensor is used, which is able to measure up to 1 N. By amplifying the signal a reasonable resolution is achieved. The calibration of the sensor can be seen in Figure H.3. In combination with the amplifier the sensor has a sensitivity of $8.36\,\mathrm{VmN^{-1}}$.

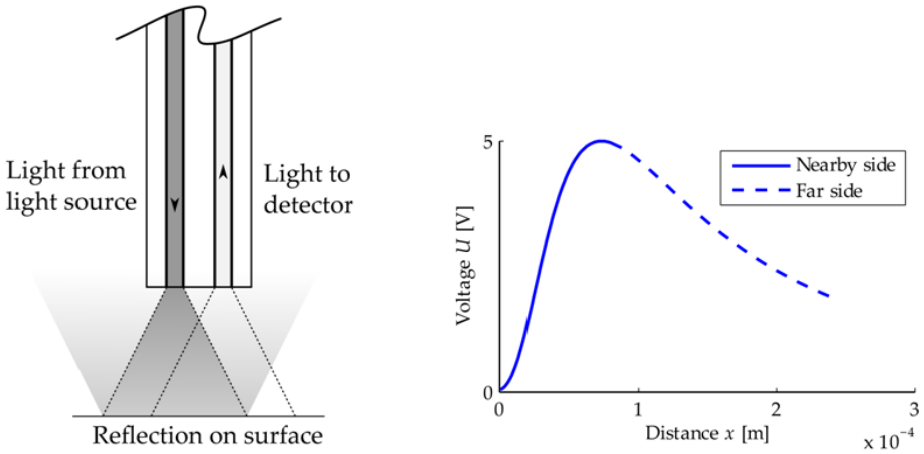

Figure H.1: Figure from [22]. The sensor emits light, which reflects on the surface of the object. The amount of reflected light that is measured by the detector is a measure for the distance between the sensor and the object. The sensor has high sensitive near side and a somewhat less sensitive far side.

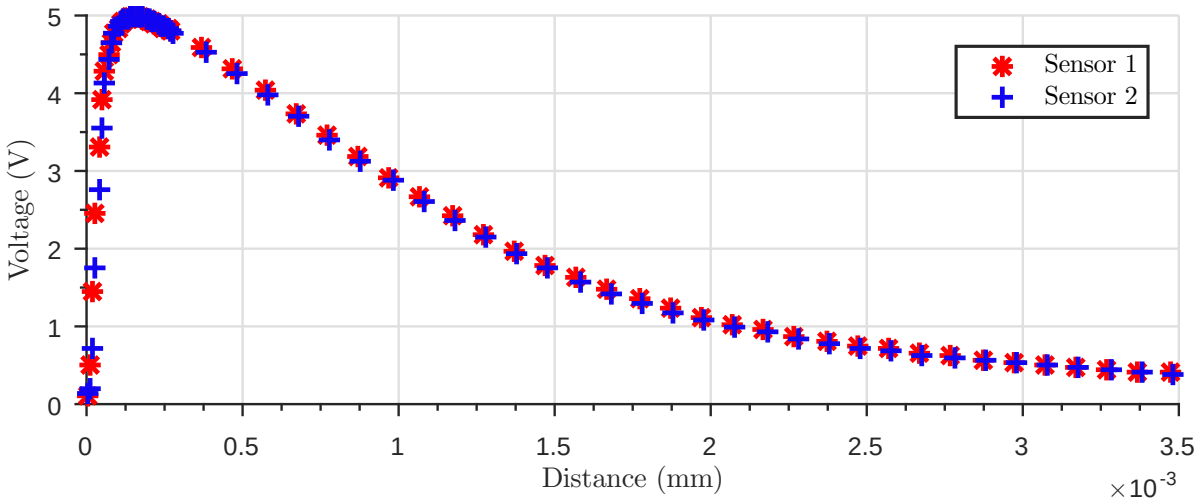

Figure H.2: The results of the tested sensors. Each curve is an average of three measurements.

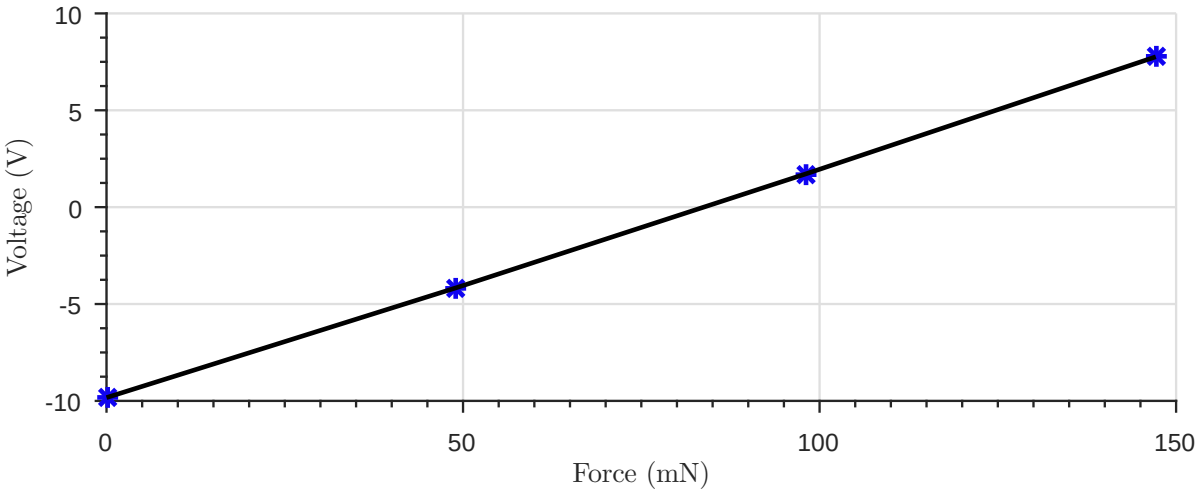

Figure H.3: Calibration of the force sensor. It has a sensitivity of $8.36\,\mathrm{V\,mN^{-1}}$.

Lumped Restrictions Model

The realised demonstrator is an open-loop system; control has not been applied yet. The position of the wafer can be controlled by controlling the feed pressure and vacuum pressure with proportional valves. Controlling the position of the wafer is out of the scope of this project. However, the first steps of the controller design have already been done. A good knowledge of the system behaviour is essential for designing the controller. For proper feed forward control, a model should be developed to calculate the required actions of the controller. This model could be made in COMSOL [2], but the calculations in this software package are relatively slow and not useful for real time calculations. In this appendix, the model is made by making use of the electric circuit analogy, which has been introduced in Appendix C. To show the working principle of this model, the active surface of the second prototype is modelled. Only the cells of the active surface, which are covered by the wafer, are taken into account. The performance of the model is compared with the measurements on the active surface of the second prototype and the corresponding COMSOL model.

I.1. Circuit

The flow circuit of the active surface can be seen in Figure I.1. The 64 fully covered cells are modelled as a network of flow restrictions, which are connected with each other. The 64 fully covered cells are connected in parallel with the supply pressures, which means that each restriction in Figure I.1 represents the summation of the restrictions of the 64 fully covered cells. The flow circuit can also be called a lumped restrictions model.

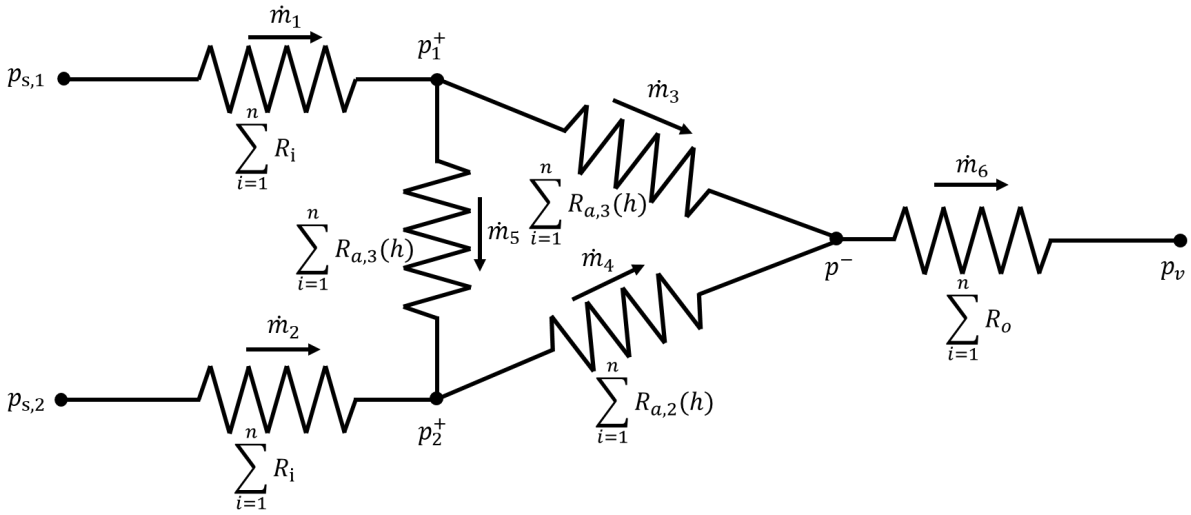

Figure I.1: Flow circuit of the active surface. The variable n in the summations is the number of fully covered cells, which is equal to 64.

The pressures $p_{s,1}$, $p_{s,1}$ and p_v are respectively the feed pressures upstream the inlet restrictions and the vacuum pressure downstream the outlet restriction. The inlet restrictions are indicated with the symbol R_i and the outlet restriction is shown with the symbol R_o. The air flows through the inlet restrictions into the

thin film. The thin film of the active cells consists of three flow restrictions. They all depend on the fly height of the wafer. Restriction $R_{a,1}(h)$ is the flow restriction between pressure p_1^+ of the first inlet restriction to pressure p^- of the outlet restriction. Restriction $R_{a,2}(h)$ is the flow restriction between pressure p_2^+ of the second inlet restriction to pressure p^- of the outlet restriction. And lastly, restriction $R_{a,3}(h)$ is the flow restriction between pressure p_1^+ of the first inlet restriction to pressure p_2^+ of the second inlet restriction or the other way around, depending on the direction of the mass flow. There are six different mass flows in total. The mass flows $\dot{m}_1$ and $\dot{m}_2$ are the mass flows through the inlet restrictions, the mass flows $\dot{m}_4$, $\dot{m}_4$ and $\dot{m}_5$ are the mass flows in the thin film and mass flow $\dot{m}_6$ is the mass flow through the outlet restrictions.

The restrictions of the air film are determined experimentally in COMSOL. The fly height is varied and the restriction values are calculated as follows::

$$R_{a,1}(h) = \frac{1}{2R_s T \dot{m}_3}\left(\left(p_1^+\right)^2 - \left(p^-\right)^2\right) \tag{I.1}$$

$$R_{a,2}(h) = \frac{1}{2R_s T \dot{m}_4}\left(\left(p_2^+\right)^2 - \left(p^-\right)^2\right) \tag{I.2}$$

$$R_{a,3}(h) = \frac{1}{2R_s T \dot{m}_5}\left(\left(p_1^+\right)^2 - \left(p_2^+\right)^2\right) \tag{I.3}$$

The calculated restriction values are used to fit an experimental curve, which is an exponential function with four terms:

$$R = ae^{bh} + ce^{dh} \tag{I.4}$$

The fly height h is the dependent variable and the data is fitted by tuning the coefficients a, b, c and d for the three different flow restrictions in the thin film. The results can be seen in Figure I.2. The restriction values of $R_{a,1}$ and $R_{a,2}$ are similar, as is expected from the symmetry in the active surface cells. The restriction value of $R_{a,3}$ is somewhat smaller. This has to do with the shorter distance between the two inlets, in comparison with the distance between an inlet and an outlet. Furthermore, it can be noticed that the restriction values have a finite value for very small fly heights. This is caused by the pockets in the active surface cells. They will always cause a flow in the active cells, even if the fly height is equal to zero.

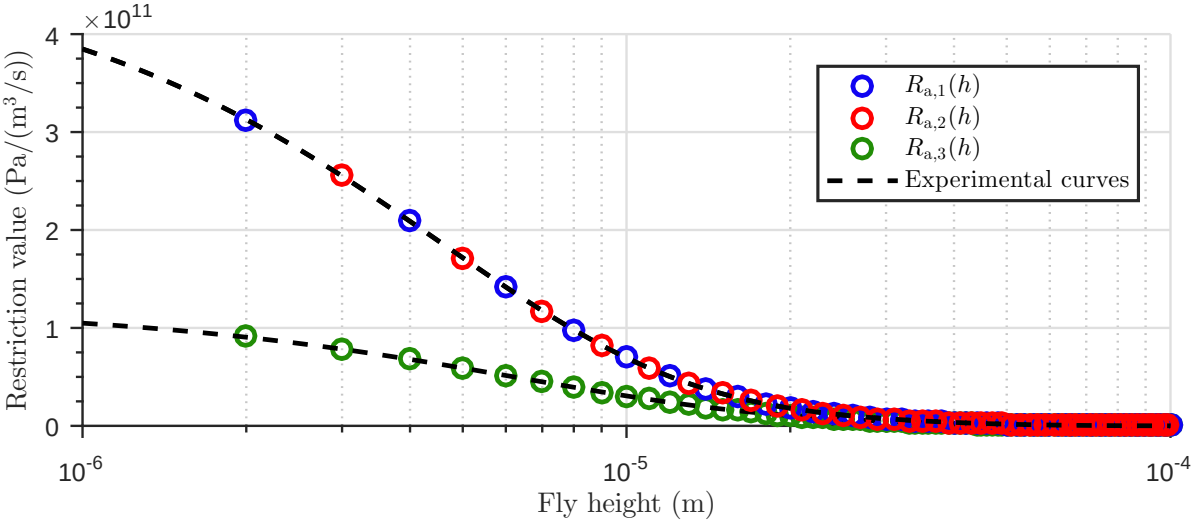

Figure I.2: Resistance air film and fitted model.

To be able to find the correct fly height, the zero load condition should be applied. Looking back at Section 2.2.1, the zero load condition can be calculated by setting the load capacity minus ambient pressure equal to zero. The load capacity can be calculated with the surface integral of the thin film pressure. For the incompressible flow assumption the load capacity is simply the average pressure in the thin film pressure. The load capacity in the compressible flow is slightly more complex. In this model the incompressible flow assumption is not valid. The formulation for the load capacity cannot be calculated analytically. However,

as an approximation of the load capacity the average thin film pressure can still be calculated as a certain combination of the three pressures in the thin film. The zero load condition is written as:

$$W = \frac{ap_1^+ + ap_2^+ + (3-2a)p^-}{3} - p_a = 0 \tag{I.5}$$

The parameter a depends on the location of the inlets and outlet, but also on the fly height of the wafer. If all inlets and outlets are positioned in the corners and the incompressible flow assumption is used, the parameter a would be equal to 1. The parameter a is calculated in COMSOL for different fly heights. The results can be seen in Figure I.3. It can be seen the parameter varies between 0.85 and 0.89. The final model will be compared with the measurements on the active surface, which are presented in Section 7.3. The fly heights in this measurement are in the range of 20 to 40 µm. The parameter a will therefore be approximated at the fly height of 30 µm, with the value of 0.88.

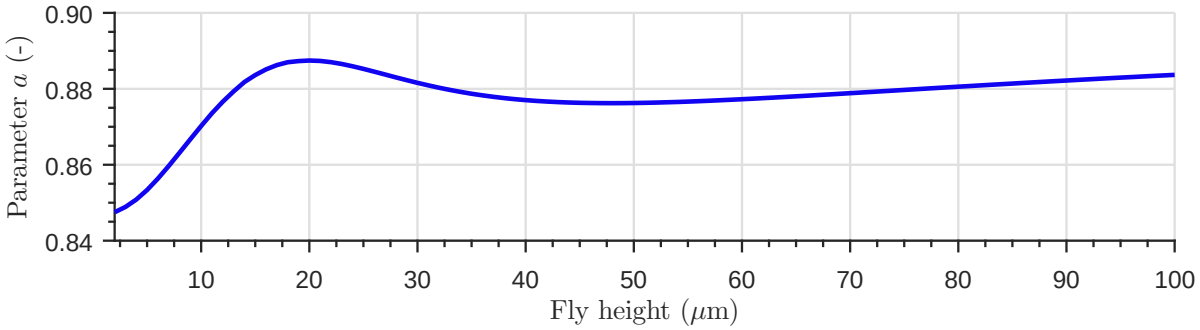

Figure I.3: Parameter a for different fly heights.

In Figure I.4, the zero load capacities for two different values of the parameter a are shown. Ideally, the zero load capacity would be equal to zero for all fly heights. This is not the case, but the difference between the curves is significant.

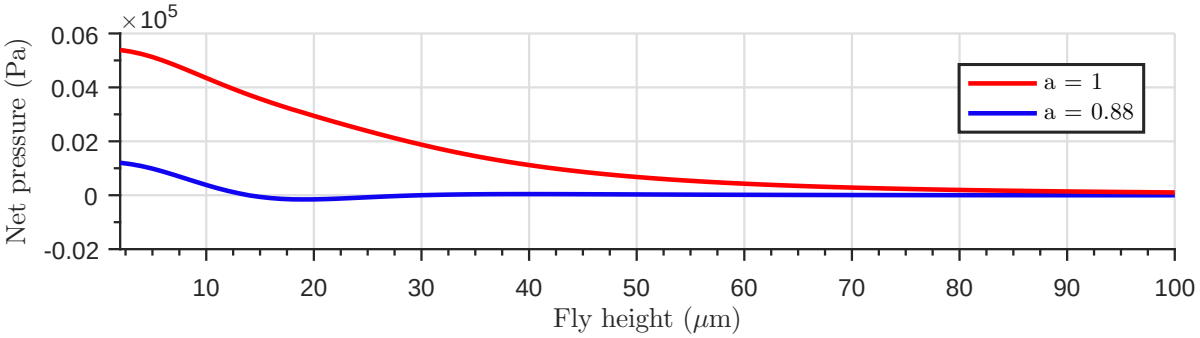

Figure I.4: Zero load capacities for two different values of the parameter a.

I.2. Model

The complete model consists of 10 equations and 10 unknown variables, which makes it a system of non-linear equations. These equations are the 6 mass flow equations through the flow restrictions, 3 mass flow equilibrium equations at the bifurcation points and the zero load condition equation. They can be written as follows:

$$\dot{m}_1 - nC_{\mathrm{d,i}}A_{\mathrm{i}}\sqrt{\frac{1}{R_{\mathrm{s}}T}\left(p_{\mathrm{s},1}^2 - \left(p_1^+\right)^2\right)} = 0 \qquad \text{(I.6)}$$

$$\dot{m}_2 - nC_{\mathrm{d,i}}A_{\mathrm{i}}\sqrt{\frac{1}{R_{\mathrm{s}}T}\left(p_{\mathrm{s},2}^2 - \left(p_2^+\right)^2\right)} = 0 \qquad \text{(I.7)}$$

$$\dot{m}_3 - \frac{n}{2R_{\mathrm{s}}R_{\mathrm{a},1}(h)T}\left(\left(p_1^+\right)^2 - \left(p^-\right)^2\right) = 0 \qquad \text{(I.8)}$$

$$\dot{m}_4 - \frac{n}{2R_{\mathrm{s}}R_{\mathrm{a},2}(h)T}\left(\left(p_2^+\right)^2 - \left(p^-\right)^2\right) = 0 \qquad \text{(I.9)}$$

$$\dot{m}_5 - \frac{n}{2R_{\mathrm{s}}R_{\mathrm{a},3}(h)T}\left(\left(p_1^+\right)^2 - \left(p_2^+\right)^2\right) = 0 \qquad \text{(I.10)}$$

$$\dot{m}_6 - nC_{\mathrm{d,o}}A_{\mathrm{o}}\sqrt{\frac{1}{R_{\mathrm{s}}T}\left(\left(p^-\right)^2 - p_{\mathrm{v}}^2\right)} = 0 \qquad \text{(I.11)}$$

$$\dot{m}_1 - \dot{m}_3 - \dot{m}_5 = 0 \qquad \text{(I.12)}$$

$$\dot{m}_2 - \dot{m}_4 + \dot{m}_5 = 0 \qquad \text{(I.13)}$$

$$\dot{m}_6 - \dot{m}_3 - \dot{m}_4 = 0 \qquad \text{(I.14)}$$

$$\frac{ap_1^+ + ap_2^+ + (3-2a)p^-}{3} - p_{\mathrm{a}} = 0 \qquad \text{(I.15)}$$

The variable n is the number of fully covered cells, similar as in Figure I.1. The mass flow through the inlet and outlet restrictions is described by the Jobson orifice flow. The unknown variables are the thin film pressures p_1^+, p_2^+ and p^-, the mass flows $\dot{m}_1$, $\dot{m}_2$, $\dot{m}_3$, $\dot{m}_4$, $\dot{m}_5$ and $\dot{m}_6$ and the fly height h. The boundary pressures $p_{\mathrm{s},1}$, $p_{\mathrm{s},2}$ and p_{v} are set by forehand. The system of non-linear equations is solved by making use of a non-linear solver in MATLAB (`fsolve`) with the Levenberg-Marquardt algorithm. The algorithm is provided with a realistic initial guess and for faster computation, the objective gradients are specified analytically.

I.3. Results

As said before, the performance and accuracy of the developed model are compared with the measurements on the active surface of the second prototype and the corresponding model of Section 7.3. The parameters of the models are the same. The 120 µm diameter inlets have a discharge coefficient of 0.59 and the 300 µm outlets have a discharge coefficient of 0.65. The average feed pressures and vacuum pressures of the measurements are inserted in the model. The model is used to calculate the corresponding fly height, which is based on the zero load condition. The results can be seen in Figure I.5, which shows the fly height versus the feed pressure. The lines of the COMSOL model and the lumped model are not identical, but are close together. The lumped model is a good approximation of the finite element model in COMSOL. The difference between the two models can be explained by the approximation of the variable a and the way in which the thin film restrictions are determined. The latter are an approximation of the actual thin film restriction.

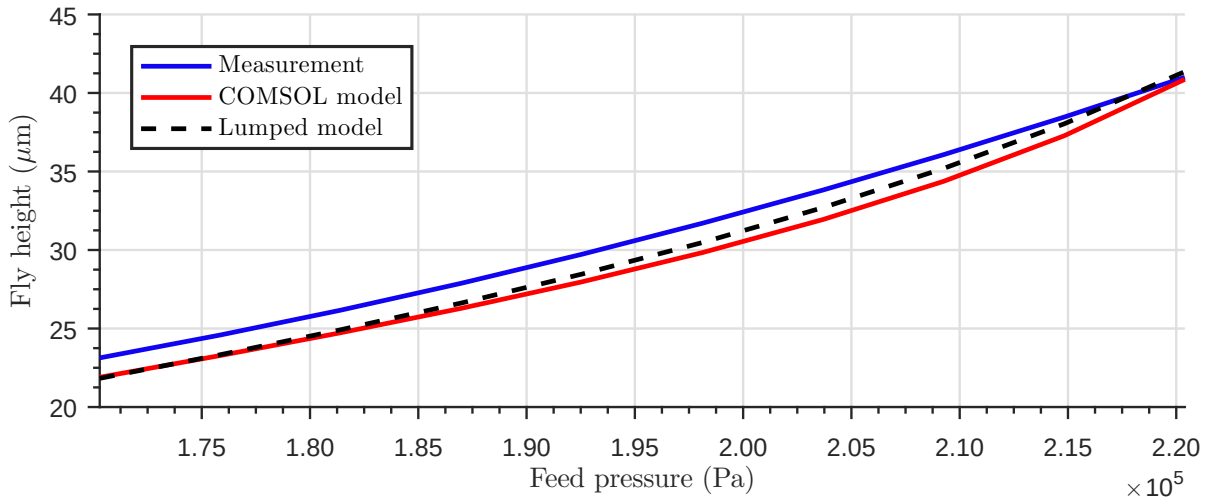

Figure I.5: Fly height as a function of the feed pressure.

The biggest difference between the finite element model in COMSOL and the lumped model is the computational time. If the COMSOL model is coupled to MATLAB via the Livelink program, 100 calculations take 186 s in total. This is very slow, especially compared to the lumped model, which takes 2.6 s for 100 runs. Overall, the lumped restrictions model shows to be promising method for applying feed forward control in a controller. The method is considerably faster than the finite element model in COMSOL. It can be further approved by implementing a fly height dependent parameter a in the model.

Bibliography

[1] International Technology Roadmap for Photovoltaic - Results 2015. (October), 2016.

[2] COMSOL Multiphysics 5.2a, 2017.

[3] International Technology Roadmap for Photovoltaic - Results 2016. (July), 2017.

[4] F. Al-Bender. On the Modelling of the Dynamic Characteristics of Aerostatic Bearing Films: from Stability Analysis to Active Compensation. *Precis. Eng.*, 33(2):117–126, 2009.

[5] K. Amano, S. Yoshimoto, M. Miyatake, and T. Hirayama. Basic Investigation of Noncontact Transportation System for Large TFT-LCD Glass Sheet used in CCD Inspection Section. *Precis. Eng.*, 35(1):58–64, 2011.

[6] M. Arghir, M.-A. Hassini, F. Balducchi, and R. Gauthier. Synthesis of Experimental and Theoretical Analysis of Pneumatic Hammer Instability in an Aerostatic Bearing. *J. Eng. Gas Turbines Power*, 138(February 2016), 2016.

[7] A. Bamshad, A. Nikfarjam, and H. Khaleghi. A New Simple and Fast Thermally-Solvent Assisted Method to Bond PMMA – PMMA in Micro-Fluidics Devices. *J. Micromechanics Microengineering*, 26:12, 2016.

[8] G. Belforte, T. Raparelli, V. Viktorov, and A. Trivella. Discharge Coefficients of Orifice-Type Restrictor for Aerostatic Bearings. *Tribol. Int.*, 40(3):512–521, 2007.

[9] A. Berlin, D. Biegelsen, P. Cheung, M. Fromherz, D. Goldberg, W. Jackson, B. Preas, J. Reich, and L.-e. Swartz. Motion Control of Planar Objects Using Large-Area Arrays of Mems-Like Distributed Manipulators. In *Micromechatronics*, 2000.

[10] S. Carey, D. M. Knotter, E. Ooms, J. Boersma, and A. E. Nijmegen. Yield Impact of Backside Metal-ion contamination. *Solid State Phenom.*, 187:287–290, 2012.

[11] B. Dahroug, G. J. Laurent, V. Guelpa, and N. Le Fort-Piat. Design, Modeling and Control of a Modular Contactless Wafer Handling System. *Robot. Autom. (ICRA), 2015 IEEE Int. Conf.*, pages 976–981, 2015.

[12] S. Davis, J. O. Gray, and D. G. Caldwell. An End Effector Based on the Bernoulli Principle for Handling Sliced Fruit and Vegetables. *Robot. Comput. Integr. Manuf.*, 24(2):249–257, 2008.

[13] A. Delettre, G. J. Laurent, and N. L. Fort-piat. A New Contactless Conveyor System for Handling Clean and Delicate Products Using Induced Air Flows. In *Int. Conf. Intell. Robot. Syst.*, pages 2351–2356, 2010.

[14] A. Delettre, G. J. Laurent, N. L. Fort-piat, and C. Varnier. 3-DOF Potential Air Flow Manipulation by Inverse Modeling Control. In *IEEE Int. Conf. Autom. Sci. Eng.*, pages 926–931, 2012.

[15] A. Delettre, G. J. Laurent, and N. Le Fort-Piat. 2-DOF Contactless Distributed Manipulation using Superposition of Induced Air Flows. *IEEE Int. Conf. Intell. Robot. Syst.*, pages 5121–5126, 2011.

[16] A. J. Devitt. The Physics of Glass Flotation, 2009.

[17] Y. Fukuta, Y. A. Chapuis, Y. Mita, and H. Fujita. Design, Fabrication, and Control of MEMS-Based Actuator Arrays for Air-Flow Distributed Micromanipulation. *J. Microelectromechanical Syst.*, 15(4):912–926, 2006.

[18] Y. Fukuta, Y. Mita, M. Arai, and H. Fujita. Pneumatic Two-Dimensional Conveyance System for Autonomous Distributed MEMS. *TRANSDUCERS 2003 - 12th Int. Conf. Solid-State Sensors, Actuators Microsystems, Dig. Tech. Pap.*, 2:1019–1022, 2003.

[19] B. J. Hamrock, S. R. Schmid, and B. O. Jacobson. *Fundamentals of Fluid Film Lubrication*. Marcel Dekker, New York, 2 edition, 2004.

[20] R. P. Hoogeboom. Design and Experimental Validation of Low Stiffness Aerostatic Thrust Bearings. Technical report, Delft University of Technology, 2016.

[21] R. Hoogenboom, C. Remzi Becer, C. Guerrero-Sanchez, S. Hoeppener, and U. S. Schubert. Solubility and Thermoresponsiveness of PMMA in Alcohol-Water Solvent Mixtures. *Aust. J. Chem.*, 63:1173–1178, 2010.

[22] F. K. Horsman. A Hybrid Inertial Sensor for Measuring Absolute Displacement. Technical report, Delft University of Technology, 2016.

[23] D. Jobson. On the Flow of a Compressible Fluid through Orifices. 1954.

[24] S. Konishi and H. Fujita. A Conveyance System using Air Flow Based on the Concept of Distributed Micro Motion Systems. *J. Microelectromechanical Syst.*, 3(2):54–58, 1994.

[25] M. E. Krijnen. Control System Design for a Contactless Actuation System. Technical report, Delft University of Technology, 2016.

[26] P. Ku, K. T. Winther, H. F. Stephanou, and R. Safaric. Distributed Control System for an Active Surface Device. *IEEE Int. Conf. Robot. Autom.*, 4:3417–3422, 2001.

[27] Y. B. P. Kwan and J. Corbett. Porous Aerostatic Bearings - an Updated Review. *Wear*, 222(2):69–73, 1998.

[28] G. J. Laurent, A. Delettre, and N. Le Fort-Piat. A New Aerodynamic-Traction Principle for Handling Products on an Air Cushion. *IEEE Trans. Robot.*, 27(2):379–384, 2011.

[29] G. J. Laurent, A. Delettre, R. Zeggari, R. Yahiaoui, J. F. Manceau, and N. L. Fort-Piat. Micropositioning and Fast Transport using a Contactless Micro-Conveyor. *Micromachines*, 5(1):66–80, 2014.

[30] G. J. Laurent and H. Moon. A Survey of Non-Prehensile Pneumatic Manipulation Surfaces: Principles, Models and Control. *Intell. Serv. Robot.*, 8(3):151–163, 2015.

[31] H. G. Lee and D. G. Lee. Design of a Large LCD Panel Handling Air Conveyor with Minimum Air Consumption. *Mech. Mach. Theory*, 41(7):790–806, 2006.

[32] X. Li, K. Kawashima, and T. Kagawa. Analysis of Vortex Levitation. *Exp. Therm. Fluid Sci.*, 32(8):1448–1454, 2008.

[33] X. Li, Y. Nakamura, M. Horie, and T. Kagawa. An Experimental Investigation on the Quasi-Static Flotation Transport of a Glass Substrate Using Vortex Bearing Elements. *J. Flow Control. Meas. Vis.*, 2013(April):6–12, 2013.

[34] J. Luntz and H. Moon. Distributed Manipulation With Passive Air Flow. *Intell. Robot. Syst. 2001. Proceedings. 2001 IEEE/RSJ Int. Conf.*, 1:195–201, 2001.

[35] S. Miller. The Method of Least Squares and Signal Analysis. Technical report, Brown University, 1992.

[36] H. Moon and J. Luntz. Distributed Manipulation of Flat Objects with Two Airflow Sinks. *IEEE Trans. Robot.*, 22(6):1189–1201, 2006.

[37] I. H. Moon and Y. K. Hwang. Evaluation of a Wafer Transportation Speed for Propulsion Nozzle Array on Air Levitation System. *J. Mech. Sci. Technol.*, 20(9):1492–1501, 2006.

[38] N. Oiwa, M. Masuda, T. Hirayama, T. Matsuoka, and H. Yabe. Deformation and FlyingHeight Orbit of Glass Sheets on Aerostatic Porous Bearing Guides. *Tribol. Int.*, 48:2–7, 2012.

[39] K. Pister, R. Fearing, and R. Howe. A Planar Air Levitated Electrostatic Actuator System. *IEEE Proc. Micro Electro Mech. Syst. An Investig. Micro Struct. Sensors, Actuators, Mach. Robot.*, pages 67–71, 1990.

[40] O. Reynolds. On the Theory of Lubrication and its Application to Mr. Beauchamps Tower's Experiments, including an Experimental Determination of the Viscosity of Olive Oil. *Proc. R. Soc. London*, pages 191–202, 1886.

[41] W. Rowe. *Hydrostatic, Aerostatic and Hybrid Bearing Design*. Elsevier/Butterworth Heinemann, 2012.

[42] A. H. Slocum. *Precision Machine Design*. Society of Manufacturing Engineers, 1992.

[43] T. Takaki, S. Tanaka, T. Aoyama, and I. Ishii. Position/Attitude Control of an Object by Controlling a Fluid Field using a Grid Pattern Air Nozzle. *Proc. - IEEE Int. Conf. Robot. Autom.*, pages 6162–6167, 2014.

[44] E. P. Vagher. Contactless Passive Transport of Thin Solar Cells. Technical report, Delft University of Technology, 2016.

[45] A. van Beek. *Advanced Engineering Design: Lifetime Performance and Reliability*. TU Delft, Delft, 2009.

[46] K. Varsos and J. Luntz. Superposition Methods for Distributed Manipulation using Quadratic Potential Force Fields. *IEEE Trans. Robot.*, 22(6):1202–1215, 2006.

[47] K. Varsos, H. Moon, and J. Luntz. Generation of Quadratic Force Fields from Potential Flow Fields for Distributed Manipulation. *Proc. - IEEE Int. Conf. Robot. Autom.*, 2005(April):1021–1027, 2005.

[48] N. Verbruggen. Air-Based Contactless Positioning of Thin Substrates. Technical Report July, Delft University of Technology, 2017.

[49] P. H. Vuong. *Air-Based Contactless Actuation System for Thin Substrates*. PhD thesis, Delft University of Technology, 2016.

[50] C. Waltham, S. Bendall, and A. Kotlicki. "Bernoulli" Levitation. *Physics (College. Park. Md).*, page 12, 2002.

[51] J. Wesselingh. *Contactless Positioning Using an Active Air Film*. PhD thesis, Delft University of Technology, 2011.

[52] J. Wesselingh, J. W. Spronck, R. A. J. Van Ostayen, and J. Van Eijk. Contactless 6 DoF planar positioning system utilizing an active air film. *Proc. 10th Int. Conf. Eur. Soc. Precis. Eng. Nanotechnology, EUSPEN 2010*, 1(June):417–420, 2010.

[53] F. M. White. *Fluid Mechanics*. McGraw-Hill, New York, 7th edition, 2011.

[54] R. Yahiaoui, R. Zeggari, J. Malapert, and J. F. Manceau. A MEMS-Based Pneumatic Micro-Conveyor for Planar Micromanipulation. *Mechatronics*, 22(5):515–521, 2012.

[55] R. Zeggari, R. Yahiaoui, J. Malapert, and J. F. Manceau. Design and Fabrication of a New Two-Dimensional Pneumatic Micro-Conveyor. *Sensors Actuators, A Phys.*, 164(1-2):125–130, 2010.

[56] W. Zhong, X. Li, G.-l. Tao, B. Lu, and T. Kagawa. Theoretical and Experimental Investigation on Optimization of a Non-Contact Air Conveyor. *J. Cent. South Univ.*, 23(2):353–361, 2016.